Glacial Dispersion at the Canadian Malartic Gold Deposit

by

Caroline Emily Taylor

A thesis
presented to the University of Waterloo
in fulfilment of the
thesis requirement for the degree of
Master of Science
in
Earth Sciences

Waterloo, Ontario, Canada, 2024

Author's Declaration

This thesis consists of material all of which I authored or co-authored: see Statement of Contributions included in the thesis. This is a true copy of the thesis, including any required final revisions, as accepted by my examiners.

I understand that my thesis may be made electronically available to the public.

Statement of Contributions

I am the sole author of Chapters 1 and 4, which were written under the supervision of Dr. Martin Ross and were not written for publication.

This thesis has two chapters (Chapters 2 and 3), which are intended for publication; this work is part of the NSERC-CMIC Footprints multidisciplinary project and has benefited greatly from multiple collaborators.

Chapter 2:
Dr. Stéphane Perrouty (Laurentian University) supervised my fieldwork and helped collect measurements and samples in the study area.

Robin Taves (University of Waterloo) produced all samples, data, and results from 2015. She also helped process samples collected in 2016 (dry sieving, washing clasts, and identifying clasts).

Neera Sundaralingham (Western University) helped collect measurements and samples in the study area.

Chapter 3:
Dr. Philip Lypaczewski (University of Alberta) and Dr. Benoit Rivard (University of Alberta) processed clasts and provided hyperspectral imaging data and photos.

Dr. Perrouty produced the contours (minimum curvature interpolation) for the tracer till clast distribution data. He also helped identify clast mineralogy and texture using SEM-EPMA and provided photos.

Dr. Gema Olivo (Queen's University) helped identify clast mineralogy and texture using optical microscopy.

James R. Clark (McGill University) helped investigate W-enriched rutile grains and their efficacy as indicator minerals.

Abstract

A novel drift prospecting approach detected components from previously established bedrock footprints at the world-class Canadian Malartic gold deposit within the site's surrounding Quaternary sediments. The measured glacial dispersion of footprint components is significantly more extensive than the largest bedrock footprint. This new method could apply to similar high-tonnage disseminated gold deposits and other deposits with similar features.

Drift prospecting methods included ice flow indicator mapping, surficial sediment sampling and characterization, particle size distribution analyses, till matrix geochemistry (major oxide, minor, and trace elements), glacial clast lithology, gold grain counts, and petrography. Our novel approach combined hyperspectral imaging analyses with petrographic analyses targeting glacial granules and pebbles.

Within the study area, the direction of past ice flow phases evolves from ~210º to ~150º; it dominates towards ~170º. Multivariate analysis of till matrix major oxide geochemistry links clusters of samples to bedrock geology and postglacial processes. Till clast lithologies link to bedrock type. The spatial distribution of till matrix minor and trace element geochemical values reveals glacial dispersal trains for Au, Ag, Rb, W, and potentially Ba; however, glacial dispersal trains for Cs, Mo, Pb, and Sr are unclear (all listed elements have been previously reported as footprint components). Multivariate analyses of till matrix minor and trace element geochemistry link clusters of samples to footprint components (Mo has the highest first principal component positive loading in the relevant cluster), bedrock geology background values, and postglacial processes. Sand-sized gold grain counts from till and their morphology link to the phengitic white mica bedrock footprint associated with the deposit.

Hyperspectral imaging analysis of bulk glacial clasts reveals dispersal extents that are significantly larger than the extent of the phengitic white mica footprint in bedrock (i.e, the most extensive bedrock footprint at the Canadian Malartic gold deposit). 4-8 mm tracer till clasts produce a dispersal extent 7.0-13.5 times larger while 2-4 mm tracer till clasts produce a dispersal extent 4.5-8.4 times larger than the bedrock footprint. Further, petrographic analyses of 42 highly phengitic 4-8 mm clasts classify 14 clasts as showing mineralogy and rock texture similar to the host quartz-monzodioritic, granodioritic, and meta-sedimentary rocks at the deposit. One of these clasts is mineralized with gold like the mineralization at the Canadian Malartic deposit, and this is the first reported instance of finding a mineralized clast using this novel technique.

The Quaternary dispersion relative to the previously established bedrock footprints at the Canadian Malartic gold deposit is significant. Ongoing hyperspectral imaging and petrographic analyses of similar clasts may demonstrate numerous practical applications to exploration campaigns seeking other Canadian Malartic-type gold deposits or other deposits with similar characteristics.

Acknowledgements

I would like to thank Dr. Martin Ross for his unfailing support and invaluable guidance.

I would also like to thank Dr. Martin Ross' research group for their inspiration and support.

Also, thank you to Dr. Brian Kendall and Dr. Robert Linnen for being on my committee and for their steadfast support and helpful comments at all times.

I would like to extend a personal thank you to James Taylor for making this possible.

I would also like to thank the University of Waterloo for being my home away from home.

Special thanks to Neera Sundaralingham for her companionship in digging for till (and for saving my fieldbook!!!).

Finally, I am grateful beyond words to the CMIC Footprints collaboration and the partners at the Canadian Malartic Mine for providing this opportunity.

This work was funded by the NSERC-CMIC Footprints research project. This thesis is NSERC-CMIC Footprints contribution #233.

Dedication

First and foremost, this thesis is dedicated to my son Sandy, who is and always will be more precious than any gold out there.

I also dedicate my work to Jimmy Kimmel and his crew because we all need laughter and sanity.

Additionally, my work goes out to the Meiselas brothers Blue-Eyed Prof Ben (who sees the world through a democratic lens), Jordy, Brett, and everyone else at the Meidas Touch Network (too many to name). Thank you all for the invaluable work that you do!

This also goes out to Enrique Noppadopulous, a.k.a. @EnNopp112, for streaming. Prayge RNG

Finally, this work is dedicated to Chef Gordon Ramsay and Musician Stromae. Thank you both for the inspiration to dance when it storms.

Table of Contents

List of Figures

List of Tables

List of Abbreviations

AAS - Atomic Absorption Spectrometry

AGB – Abitibi greenstone belt

CMIC – Canada Mining Innovation Council

DEM – Digital elevation model

GLBO – Glacial Lake Barlow-Ojibway

HIA – Hyperspectral Imaging Analysis

HMC – Heavy mineral concentrates

ICP-MS – Inductively-Coupled Plasma Mass Spectrometry

ICP-OES – Induction Coupled Plasma-Optical Emission Spectroscopy

LIS – Laurentide Ice Sheet

Ma – Mega-annum

masl – Meters above sea level

NSERC – Natural Sciences and Engineering Research Council of Canada

PC – Principal Component

PCA – Principal Component Analysis

PGE – Platinum Group Element

QA/QC – Quality Assurance/ Quality Control

QGIS – Quantum Geographic Information System

SEM-EPMA – Scanning Electron Microscopy with Electron Probe Microanalysis

SWIR – Short-wave infrared

USD – United States dollar

VMS – Volcanogenic massive sulfide ore deposit

XRD – X-ray diffraction

Malartic, 2016

CHAPTER 1: Motivation, Background & Thesis Overview

1.1. Research Motivation

Extensive and complex Quaternary sediments, which cover 20% of the continental surface in the northern hemisphere (Ehlers & Gibbard, 2007), routinely impede mineral exploration and prospecting efforts; however, drift prospectors take advantage of these glacial sediments to identify glacially eroded, transported, and deposited geochemical anomalies, mineral indicators, and mineralized boulders, and use the record of past ice flow dynamics to trace these signals back to their bedrock sources (Dilabio, 1990; Fulton, 1995; Shilts, 1996). The power of using glacial sediments, such as subglacial till or glaciofluvial deposits, for prospecting has been recognized for decades (Prest, 1915; Shilts, 1976; Saarnisto, 1990) and drift prospecting techniques have improved considerably since the late 1980s, with great successes in prospecting for gold and diamonds, as well as for other precious and base metals (Averill, 2001; Thorleifson, 2017; McClenaghan & Paulen, 2018).

In recent years, several advances have been made that allow better fingerprinting of indicator minerals (McClenaghan et al., 2023). Still, the potential exists to further expand the usefulness of drift prospecting by tracing new types of mineralization or their surrounding alteration assemblages. Such advances may prove particularly important for the Abitibi greenstone belt (AGB), which is historically one of the richest areas in Canada for mineral resources and continues to hold valuable exploration potential in the 21st century despite the extensive mining history in the region. The AGB contains multiple different styles of mineralization with diverse base and precious metals, including volcanogenic massive sulfides (VMS), magmatic Ni-Cu-PGE, orogenic Au, and porphyry Au deposits (Hufford, 2015 and references therein), as well as diamondiferous kimberlites (McClenaghan et al., 2017). During the 20th century, the AGB had more than 145 mines producing precious metals (Veillette et al., 2005). Notably, approximately 70% of the country's gold mines are located within the Abitibi Gold Belt, which runs from Timmins to Val D'Or and represents Canada's richest endowment of gold. During that time, this globally important gold belt was estimated to have produced approximately 130 million ounces of gold valued at $39 billion (at $300 USD per ounce) (McClenaghan, 2001).

1.1.1. Case Study at the Canadian Malartic Gold Mine

The Canadian Malartic gold deposit was "re-discovered" in 2004 by Osisko Exploration Ltd. as an Archean porphyry gold system within the AGB that met the criteria for open-pit mining after underground mining operations had ended in the 1980s (Wares & Burzynski, 2011). This junior exploration company landed a world-class deposit with their innovative strategy of targeting characteristics of porphyry gold systems, despite the area being considered an exhausted brownfield, using mainly a public governmental geoscientific database (Wares & Burzynski, 2011). This "re-discovery" was missed by previous regional exploration efforts such as the Cadillac Project and subsequent analyses (LaSalle et al., 1975; LaSalle et al., 2005), which focused on glacial sediments and a regional gold rush in the 1980s (Veillette et al., 2005), which focused on drilling through surficial cover to bedrock. This example shows that while prospectors are still discovering new deposits in the AGB, innovation is key to ongoing successful prospecting in drift-covered (and heavily mined) areas.

The Canadian Malartic mine was selected as one of three nationally important sites to be part of the NSERC-CMIC Mineral Footprints Research Network (hereafter referred to as "Footprints") to identify and constrain as many footprints as possible by bridging geological, geophysical, petrophysical, geochemical, mineralogical, and surficial prospecting disciplines (Lesher et al. 2017). As a case study, it is a world-class gold deposit (>18.6 Moz Au indicated, inferred, and historical) (Gervais et al., 2014) that exemplifies numerous exploration challenges, which crosscut multiple prospecting methods, as well as the ongoing resource potential of the Abitibi Gold Belt within the AGB.

There is a wealth of background knowledge regarding general drift prospecting and the study area's geologic framework, including previous prospecting efforts. The following sections review this information, establish relevant background, and conclude by highlighting knowledge gaps and important research questions. The final section presents an overview of this thesis. The main goals of this thesis are to develop a detailed understanding of the till composition and dispersal patterns around Malartic and to test new innovative techniques to identify and trace secondary alteration footprints within glacial sediments.

1.2. Drift Prospecting State of Knowledge

This section establishes relevant background regarding dynamic glacial ice, glacial sediment characteristics, glacial tracer dispersion from a deposit, field and data collection strategy, and a summary of current gold drift prospecting techniques.

1.2.1. Glaciation & Ice Flow Indicators

Large ice sheets formed and extended into mid-latitudes during the glaciations of the Middle and Late Pleistocene (~0.8-0.011Ma) (Ehlers & Gibbard, 2007), as shown in **Figure 1.1**. The global Last Glacial Maximum (LGM) occurred between about 27 and 21 cal ka BP (Mix et al., 2001; Hughes and Gibbard 2015), a time interval when most of Canada's landmass was covered by the Laurentide, Cordilleran and Inuitian ice sheets (Dyke et al., 2002; Dalton et al. 2020).

There is a complex interplay between the many factors that drive the ice sheet dynamic in response to energy and mass balance fluxes. Our understanding of subglacial dynamics has shifted from simplistic "steady-state" models (Boulton, 1996) to models that capture complex spatiotemporal variability by accounting for basal pressure and sliding, sediment rheology, and polythermal glacier hydrology (Glasser & Bennett, 2004; Irvine-Fynn et al., 2011; Trommelen et al., 2013). Also, ice-divide migration and the nature and degree of ice-streaming can be fundamental in controlling the behaviour of an ice sheet (Ross et al., 2009; Hodder et al., 2016; Paulen, 2017). Ice sheet thickness is also an important factor as it determines the degree of influence of topography on ice flow direction, which can be particularly critical at local scales (McMartin & Paulen, 2009). Local ice flow records may differ from regional trends in ice flow; therefore, it is imperative to map local ice flow indicators as part of surficial sediment exploration programs while collecting field samples.

Glacial ice is dynamic, and rock material embedded in the sole of a sliding glacier creates erosional features on bedrock through frictional processes (Prest, 1983; McMartin & Paulen, 2009). Certain features like striations and grooves provide information about ice flow direction (Rea, 2007). In many cases, the erosional ice flow record is complex, with evidence of shifting ice flow directions in the form of crosscutting features or other characteristics (e.g. Parent et al. 1995). The correct identification and interpretation of erosional features is thus of primary importance in drift prospecting endeavours because it provides critical information about the direction of ice flow phases and thus of glacial sediment transport (Hirvas & Nenonen, 1990; McMartin & Paulen, 2009). Working with dispersal trains alone would be challenging, especially in areas of complex patterns and ice flow history.

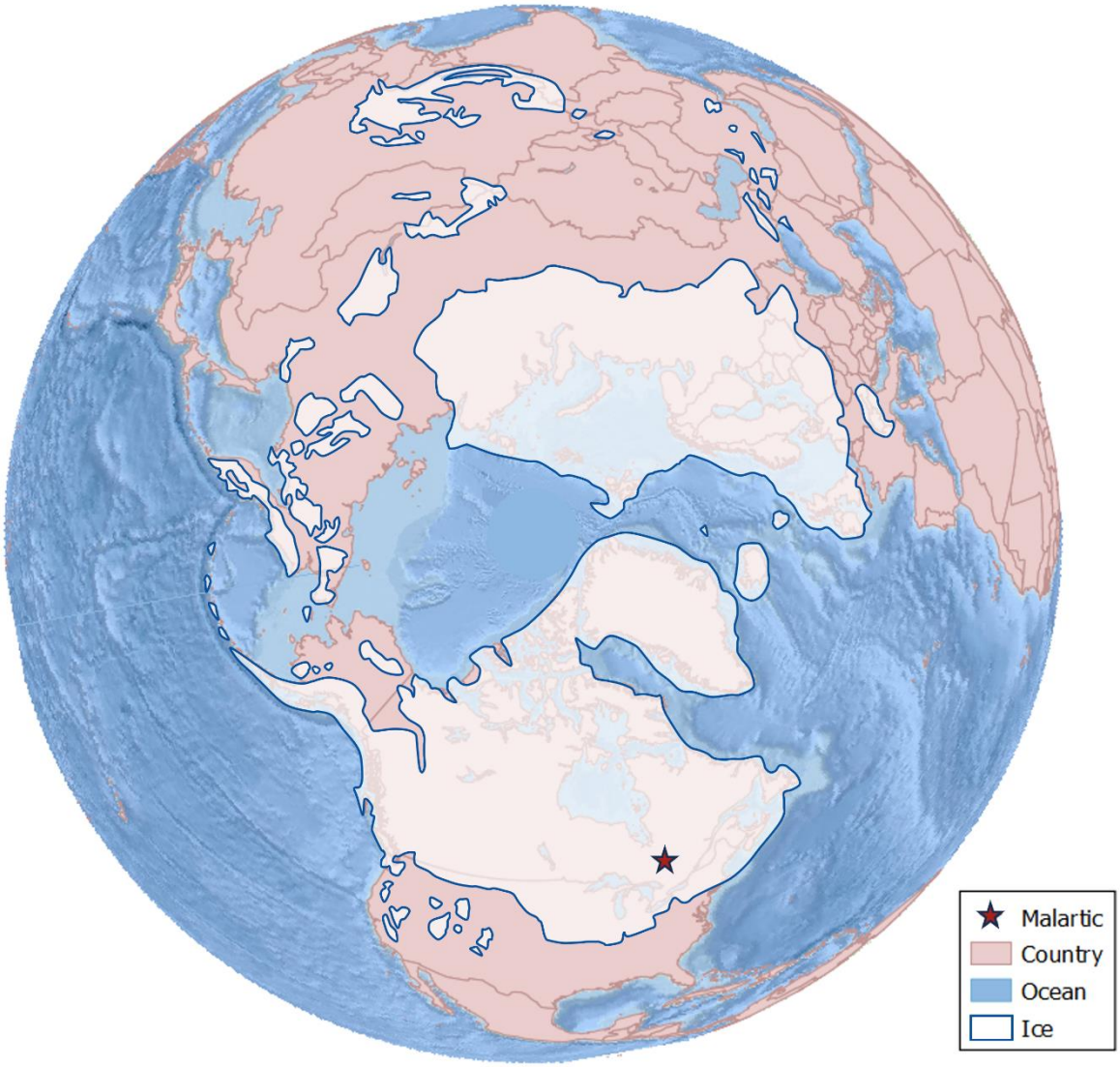

Figure 1.1 Polar view of the northern hemisphere showing ice coverage (white polygons) during the Last Glacial Maximum, with the location of Malartic, Canada, indicated by a red star. Modified after McClenaghan & Paulen (2018), original in Ehlers & Gibbard (2007). Ocean basemap is from Esri (https://services.arcgisonline.com/ArcGIS/rest/services/Ocean/World_Ocean_Base/MapServer).

1.2.2. Glacial Sediment Characteristics & Implications for Drift Prospecting

There are different types of glacial sediments, which can be broadly categorized as being formed in (1) ice-contact environments, either as a direct product of ice mechanical processes (e.g. primary till) or by the internal meltwater drainage system (e.g. ice-contact glaciofluvial), and (2) in the proglacial environment (e.g. glaciofluvial, glaciomarine, glaciolacustrine) where their 'glacial' nature tends to diminish with increasing distance to the ice margin (Menzies & Ross, 2022). Each category includes a variety of sediment facies associated with different processes, which ultimately translates into different degrees of utility as tracer sources for drift prospecting.

The word "till" is first attributed to Geikie (Geikie, 1863) to describe glacial deposits characterized by a stiff clay matrix filled with clasts of all sizes, ranging up to boulders in Scotland. Till is a type of diamicton (Flint et al., 1960), meaning it is unconsolidated sedimentary material that is composed of a wide range of grain sizes (as defined by Wentworth (1922)), characteristically from rock flour up to large, glacially transported erratics. This wide range of grain sizes in till means that different grain size fractions represent different mixes of input sources due to differences in processes that led to their formation, and thus have the potential to preserve different types of indicators and pathfinders, which is referred to as textural partitioning (Shilts, 1971, 1996; Menzies, 2023).

Till is the most useful surficial material for drift prospecting for numerous reasons. Till is made from direct glacial bedrock erosion and by re-entrainment of pre-existing sediment by flowing ice. As such, till has the potential to contain chemical and mineral indicators of a range of mineral deposits that intersect the bedrock surface and may be used in conjunction with ice flow indicators to locate deposits of interest (Shilts, 1976; Hirvas & Nenonen, 1990; Saarnisto, 1990; McClenaghan & Paulen, 2018). On the Canadian Shield, bedrock was generally available to subglacial erosion during the last glaciation due to relatively thin and discontinuous pre-existing sediment cover, allowing abrasion and quarrying processes (Rea 2007) to occur across large surface areas. Quarrying (Iverson, 2012) is more effective than abrasion for eroding bedrock and producing till. Conditions favorable for quarrying include water pressure fluctuations in a linked-cavity system over irregular jointed bedrock. These conditions typically form before the drainage system evolves into a well-organized channelized system, whereby small channels are captured by larger, low-pressure ones (Benn and Evans 2010). This dendritic system formed in association with the late-stage ice flow phases. During those late phases, ice became thinner, and erosion was probably limited to abrasion of the stoss-side of bedrock bumps and the remobilization of previously deposited till.

Till is commonly widespread and deposited in sheets. It can occur in a single layer or as stacks of unique layers with the possibility of other interbedded sediment layers. Individual till sheets can be classified broadly based on their characteristics and genesis (e.g. Dreimanis 1989), with end-members

identified as lodgement till, deformation till, gravity flowtill, and melt-out till. Evans (2018) provides a comprehensive account of the current understanding of till sedimentology. Till units can be distinguished based on physical characteristics such as colour, grain-size distribution, clast lithology, clast orientation (till fabric) and degree of consolidation (Dreimanis, 1989), but seemingly physically identical till sheets can sometimes be discriminated in terms of their dominant provenance based on till matrix geochemistry (Wang, 2018).

A single till sheet can record a single ice flow direction and related sedimentary cycle, or it can contain evidence of ice-flow shift during its formation in the form of a shift in composition from changing input sources. “End member” tills are the simplest products of erosion, transport, and deposition by glacial ice moving in a single direction, and they are useful for constraining sediment provenance and ice flow phases (Stea & Finck, 2001). “Hybrid” tills represent material that one or more ice flow phases have reworked. Their characteristic components can be understood in terms of a gradient between compositional overprinting and inheritance, i.e. a mixture of features from the most recently recorded glacial cycle and those from earlier glacial phases, respectively (Stea & Finck, 2001; Stone & McMillan, 2013; Trommelen et al., 2012; Trommelen et al., 2013). Ice flow shifts and readvances can reshape till substrates into depositional landforms. Relict and palimpsest glacial depositional landforms are common in glacial landscapes, and although they can be complex to unravel, they are invaluable sources of information in reconstructing ice flow history to understand glacial dispersal (Stea, 1994; Kleman & Borgstrom, 1996; Gauthier et al., 2019).

To better understand observed till dispersal patterns, it is essential to understand how geologic material transforms into till. Comminution describes the action of breaking parent material into smaller particles, and much work has been done to investigate this process during the production of till (Slatt, 1972; Haldorsen, 1978; Haldorsen, 1981; Jari, 1995; Caracciolo et al., 2012). Dreimanis and Vagners (1971) introduced the concept of “terminal grades,” which is the observation that rock type determines the final grain size of the comminuted material. Comminution occurs subglacially at the ice-bed interface of a glacier, a.k.a its traction or basal zone. In contrast, it is a minor process within the basal debris-rich ice (englacial) zone (Boulton, 1978), where frictional processes between particles are reduced. However, many indicator minerals may be released into the till matrix of subglacial traction till directly from abrasion of bedrock or after short down-ice transport. They may acquire frictional wear patterns without changing their grain size significantly. Porewater pressure and till dilatancy play an important role in the amount of frictional stress particles will experience during subglacial transport, which explains the occurrence in some tills of fragile particles such as shell fragments (McMartin et al., 2019) or delicate coatings or rims around certain mineral grains (Kelley et al., 2019). As a result, basal till contains a significant fraction of autochthonous (i.e. proximal) material, whereas till that is sourced from englacial

or supraglacial sediment contains a significant fraction of allochthonous (i.e. distal) material (Dreimanis, 1989); therefore, drift prospectors should identify and sample basal till whenever possible to draw stronger inferences regarding local bedrock. The pivotal work on using glacial sediments for drift prospecting is attributed to Shilts (1971). Much work has been done to develop the understanding of dispersal patterns in terms of tracer train or fan morphology and their relationship to ice flow (Shilts, 1976; Dilabio, 1990; Shilts, 1996; Broster et al., 1997), attenuation (i.e. "half-distance" length) (Strobel & Faure, 1987), and inheritance versus overprinting (i.e. relict and palimpsest dispersal patterns, and glacial smearing) (Stea, 1994; Parent et al., 1996; Stea & Finck, 2001).

Commonly used fractions and typical drift prospecting analyses for those fractions are summarized in **Table 1.1**. Notably, pebbles (2 mm – 64 mm) have not been established as tracers in drift prospecting.

Table 1.1 Summary of surficial sediment grain size categories (Wentworth, 1922) and prevailing analyses in drift prospecting.

Fraction	Size (mm)	Traditional Drift Prospecting Analyses
Silt and Clay	<0.063	Major and trace elements
Sand	0.063 - 2	Heavy minerals
Pebbles	2 - 64	None
Cobbles and Boulders	>64	Mineralization and alteration

Glaciofluvial sediments are mostly sourced from debris-rich ice and till present along englacial and subglacial meltwater pathways. Glaciofluvial sediments commonly contain imbricated clasts and other primary sedimentary structures (e.g. dunes, ripples), which may be mapped to determine the direction of subglacial meltwater flow. These sediments are commonly found as sorted, positive relief features such as eskers, which may be long, sinuous and narrow (e.g. Benn & Evans, 2010), with a relatively thick unsaturated zone (i.e. deposit above the water table). Fine-grained silt and clay material may be readily washed away by flowing water; however, heavy sand-sized indicator minerals that are resistant to oxidation (e.g., common in the unsaturated zone) may be further concentrated in ice-contact glaciofluvial deposits and may thus be found naturally concentrated within large eskers, which is the case, for example, with certain kimberlite indicators; eskers have been successfully used in prospecting for diamonds (McClenaghan et al., 2002). Other heavy mineral indicator grains have the potential to be utilized in a similar way (Cummings et al., 2011). Esker sediments, therefore, hold potential as being a valuable source of tracer minerals and clasts for drift prospectors because their material is relatively

washed and sorted, with the added benefit of being readily identifiable and accessible topographic features that extend over vast distances, such as throughout the Canadian Shield (Prest, 1983; Fulton, 1995). However, indicators sensitive to oxidation conditions and/or concentrated in finer sediment fractions may be lacking in glaciofluvial sediments.

Glaciolacustrine sediments are produced by settling in a glacial lake. They are typically well-sorted, with ice-contact features such as embedded ice-rafted debris (e.g. dropstones), and are also commonly laminated due to seasonal (a.k.a. varves) or other cyclical controls (e.g. Benn & Evans, 2010). Glaciolacustrine sediments from a large lake basin are not directly useful in drift prospecting because they represent sorted detrital sediments which have entered the lake as either buoyant sediment plumes or density currents from multiple input sources, which broad lake currents and other processes may have also redistributed. This setting has led to important sediment compositional dilution and mixing, which makes these sediments uninteresting from a drift prospecting perspective. However, identifying these sediments in the field is critical as some proximal facies may be diamictic and could be misinterpreted as primary till, especially from small drillcores, which could create issues in the analysis and interpretation of results in drift prospecting. Understanding the evolution and distribution of glaciolacustrine sediments is thus a component of a full understanding of a region's glacial history, essential to making effective drift prospecting strategic decisions in the field and well-informed subsequent interpretations of results.

1.2.3. Data Collection Strategy

Field sampling strategies must be chosen based on a project's goals and the nature of the target material. Sampling surveys can use a wide variety of techniques depending on location, the purpose of the survey (e.g. regional vs property scale or detailed targeting), the ore deposit type of interest, the exploration team's expertise, equipment, budget, and time constraints. The most effective distribution of surficial sample sites also depends on the distribution of target material and the complexity of the glacial history, as well as the dispersion characteristics of target indicators (McMartin & Campbell, 2007; McClenaghan & Paulen, 2018). Ideal field sample sizes are determined based on the analytical method, grain size fraction, and minerals that are being targeted for analysis. Either hand excavation or drilling is used to carry out surficial sediment sampling. McClenaghan et al. (2013) provide an overview of available techniques and appropriate sample targets and sizes for subsequent analyses.

Techniques such as soil, stream sediment, groundwater, vegetation sampling (Sibbick & Fletcher, 1993; Salminen & Tarvainen, 1995; Anand et al., 2007; Lintern et al., 2013) and even training dogs to detect sulphur gases from mineralized boulders (Valkama, 2011), have all been used successfully in prospecting on their own or in conjunction with practices from other established disciplines such as

geophysics, structural geology, lithogeochemistry, etc. Many techniques are commonly integrated, depending on the nature of the survey.

Sample size requirements for till matrix geochemical analyses are small (1-3 kg) (McClenaghan et al., 2013; McClenaghan, 2017), are commonly collected with percussion drilling or by hand excavation and can be performed at changing depths to target particular stratigraphic units or at a constant depth for a regional survey (McClenaghan, et al., 2013; Salminen & Tarvainen, 1995; Sarala, P. & Nykanen, 2017). The sampling strategy can be augmented with portable x-ray fluorescence spectrometry (pXRF) in the field by focusing on areas with potential anomalies and by prioritizing samples for subsequent analyses (McClenaghan, 2017 and references therein; Geological Survey, 2017). McClenaghan (2017) provides an overview of the evolution of geochemical analyses as well as the modern situation and summarizes the applicability of these techniques to prospecting for VMS, magmatic Ni-Cu-PGE, orogenic Au, porphyry Cu, IOCG, and kimberlite deposits.

Till matrix fine fraction geochemical analyses are particularly well-suited to exploration for deposit types where the main ore minerals are relatively soft and friable (i.e., they disintegrate readily during glacial transport). As outlined by McClenaghan (2017), the silt and clay (<63 µm) size fraction is the most used fraction for geochemical analysis for several reasons. In practice, it is readily obtainable from till samples by the simple process of sieving. Further, it strikes the best balance in terms of the strength of an anomalous signal; the next grain size up begins to incorporate fine sand-sized quartz and feldspar grains that dilute anomalies while using clay alone (<2 µm) may produce a stronger anomaly but is also more time consuming to prepare. Clay-sized particles are susceptible to hydromorphic dispersion, which may produce patterns unrelated to glacial transport (Rose et al., 1979), thus complicating interpretation. Identifying and tracing a geochemical signal in the clay fraction can be challenging. For instance, the signal can be diluted. If the mineralized source is disseminated, as is the case at the Canadian Malartic deposit, its geochemical signal in till silt and clay may be subtle and too difficult, if not impossible, to distinguish an indicator signal from background values. Further, in a resource-rich brownfield area, as is also the case with the Canadian Malartic deposit, stronger signals from neighbouring yet different deposit types may also obscure a potentially subtle signal.

In general, indicator minerals are resistant and are traditionally associated with mineralization. When using gold grains as indicators, their quantity, morphology and composition can be used to vector toward their source deposit (McClenaghan, 2005). Sand-sized, exotic heavy mineral grains are collected from 10-15 kg till samples (McClenaghan et al., 2023) that are first sieved based on grain size and then separated using one of various techniques such as settling based on gravity in a dense fluid, with a centrifuge, shaker table, or based on ferromagnetic properties. Heavy mineral concentrates (HMC) are searched under a microscope, and indicator grains are identified by eye and hand-picked with tweezers.

Grain mounts can be made for XRD or microprobe analyses. The limitations of this conventional approach are that it requires large sample sizes, is time-consuming, expensive, prone to human error, and can only be used on sand-sized indicators with visually distinct characteristics. New technologies are emerging to computer automate and refine this task and can identify smaller indicator minerals, but they are still preliminary (Girard et al., 2021). Geochemical surveys may be faster and less expensive than indicator mineral surveys.

1.2.4. Gold Prospecting

Various drift prospecting techniques have been used successfully to vector towards gold deposits. Geochemical analyses on till matrix have established elements such as Au, As, B, Bi, Co, Cu, Fe, Te, and W as tracers for gold (Salminen & Tarvainen, 1995; Salminen, 1995, as cited by Sarala et al., 2009; McClenaghan, 2001; Sarala et al., 2009; Taivalkoski et al., 2015). Sand-sized heavy minerals such as grains of gold, sulphides (e.g., cinnabar, arsenopyrite, chalcopyrite, galena), tellurides, scheelite, tourmaline, cassiterite, barite, and rutile, among others, have all been used as indicators for gold deposits (Plouffe, 2001; McClenaghan, 2005; McClenaghan & Cabri, 2011; Taivalkoski et al., 2015). Changes in gold grain morphology, which ranges from “pristine” to “modified” to “reshaped,” and composition have also been used to get insights into potential transport distance (Dilabio, 1991). Using mineralized boulders (and cobbles) predates all other techniques, and Prest (1911) is credited with the first account of such a dispersal plume in North America. These established techniques utilize most size fractions available in glacial sediments, but the information available in the pebble fraction has not yet been used to its full potential.

1.3. Geological Framework of the Study Area

This section establishes regional and local bedrock geology and resource potential. It explores study area physiography, modern hydrology, surficial geology, and regional glacial history in terms of erosional and depositional records, including the evolution of Glacial Lake Barlow-Ojibway.

1.3.1. Bedrock Geology and Resource Potential

The AGB lies on the boundary between Ontario and Quebec in Canada, as shown in **Figure 1.2**. Regionally, the AGB is an Archean granite-greenstone belt comprised of volcanic and siliciclastic rocks that occur in broad, east-west trending lithological units that are intruded by dominantly intermediate to felsic intrusions, with a few minor mafic to ultramafic intrusions. Volcanic rocks are the oldest in the region, and intrusive rocks are ~10–30 myr younger (Jackson & Cruden, 1995). Sedimentary rocks are either Archean or Proterozoic. Archean rocks occur in alternative bands of units interstratified with volcanic rocks, and sometimes these boundaries occur along fault zones, but not always. Two regional fault zones, which structurally control the bulk of the ore deposits in the area, are the Larder Lake-Cadillac fault zone (LLCfz) and the Porcupine-Destor fault zone (PDfz) (Hufford, 2015 and references therein; Bedeaux et al., 2017). Crustal-scale fault zones generally cross the region in east-west running, boudin-like segments and occasionally divide lithological units. The AGB is posited to have been formed by arc-trench migration (Jackson & Cruden, 1995), which accounts for alternating volcanic and sedimentary units, intrusions, repeated deformation events, and general younging to the south.

The Canadian Malartic deposit is a word-class, large-tonnage, low-grade stockwork disseminated Archean gold deposit (De Souza et al., 2015), and it is considered a world-class deposit (>18.6 Moz Au indicated, inferred, and historical) (Robert & Poulsen, 1997; Gervais et al., 2014). It is located within the Pontiac sub-province, south of the boundary with the Abitibi sub-province, but its genesis is structurally controlled by the Cadillac-Larder Lake deformation zone (De Souza et al., 2015; Perrouty et al., 2017); therefore, the Canadian Malartic deposit is considered as part of the AGB system for this work. Mineralization is associated with a felsic intrusion and subsequent potassic (K) alteration and is primarily hosted in meta-sedimentary rocks, with a small amount of ore found within the cap of the intrusion (Helt et al., 2014; De Souza et al., 2015). In addition to the potassic alteration, Helt et al. (2014) observed carbonatization, both of which led to gains of K, Ca, S (mainly as pyrite), as well as large gains of Ba, Cd, W, Pb, As, Sb, Bi and Mo, and very large gains of Ag, Te, and Au. Similarly, De Souza et al. (2015) noted that the Au-ore was typified by quartz-carbonate stockwork veins and disseminated pyrite characterized by Au-Te-W-S-Bi-Ag±Pb±Mo metals.

Malartic is located approximately 30 km west of Val D'Or, within the Abitibi gold belt. Initial geologic assessments observed two types of ore bodies, one associated with greywacke and one with pegmatite (Derry, 1939; Gunning & Ambrose, 1940). After a history of underground mining that ended in the 1980s, this site was deemed an 'exhausted' brownfield and abandoned until it was 'rediscovered' in 2004 as a potential open pit mine with an innovative strategy of targeting characteristics of porphyry gold systems by using a public governmental geoscientific database (Wares & Burzynski, 2011). **Figure 1.3** shows detailed bedrock geology within the study area, with mines/ore bodies labelled in **Table 1.2**.

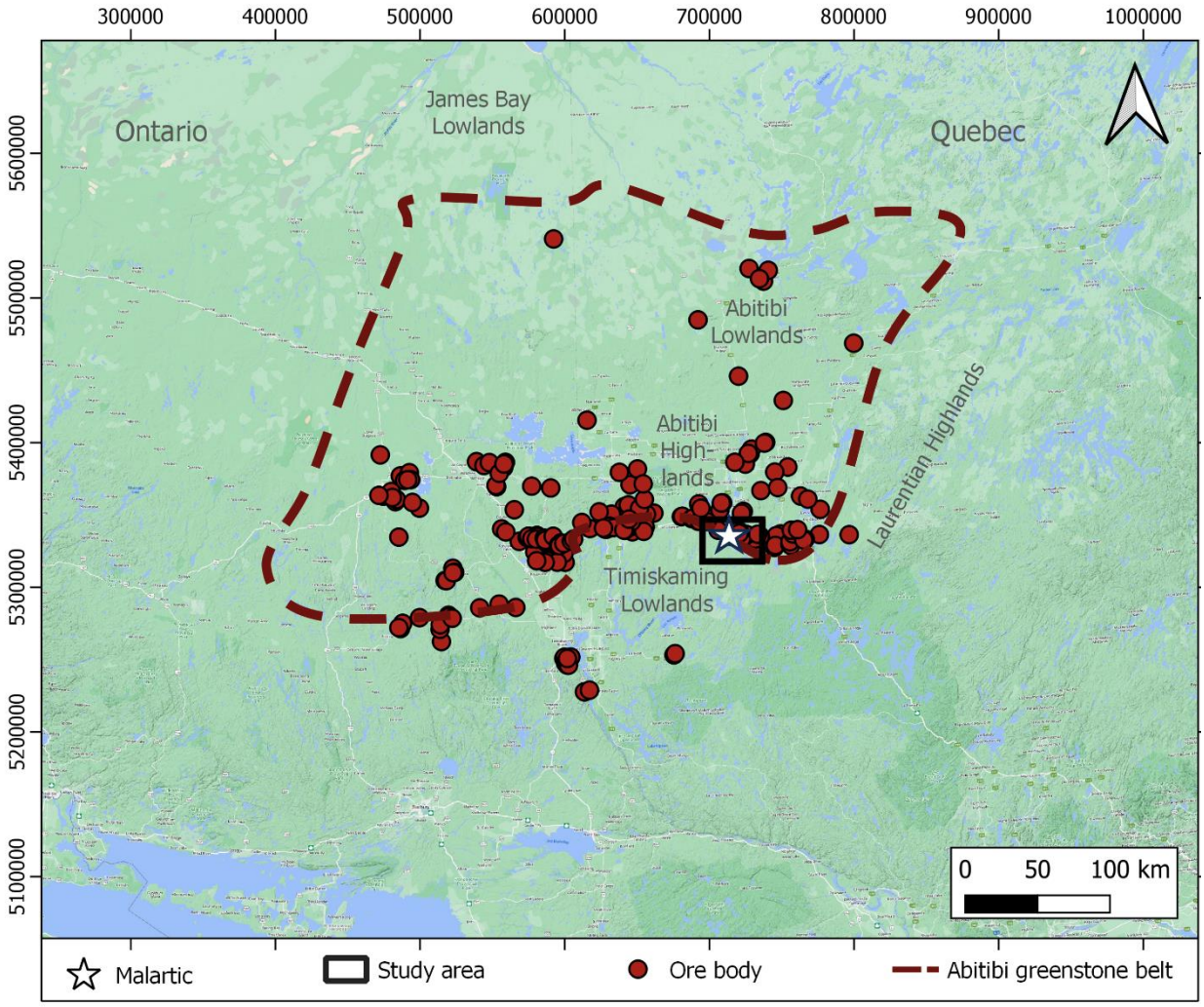

Figure 1.2 Full extent of the Abitibi greenstone belt (dashed red line) and its location between Ontario and Quebec in Canada, with the location of Malartic (white star), the study area (black rectangle), and identified ore deposits (red circles) (modified after Hufford (2015), original in Thurston et al. (2008)). The main physiographic features are labelled. Ore bodies are from SIGEOM (https://sigeom.mines.gouv.qc.ca/signet/classes/I1108_afchCarteIntr). Terrain basemap is by Google (2015). Coordinate system: NAD 83, UTM zone 17N.

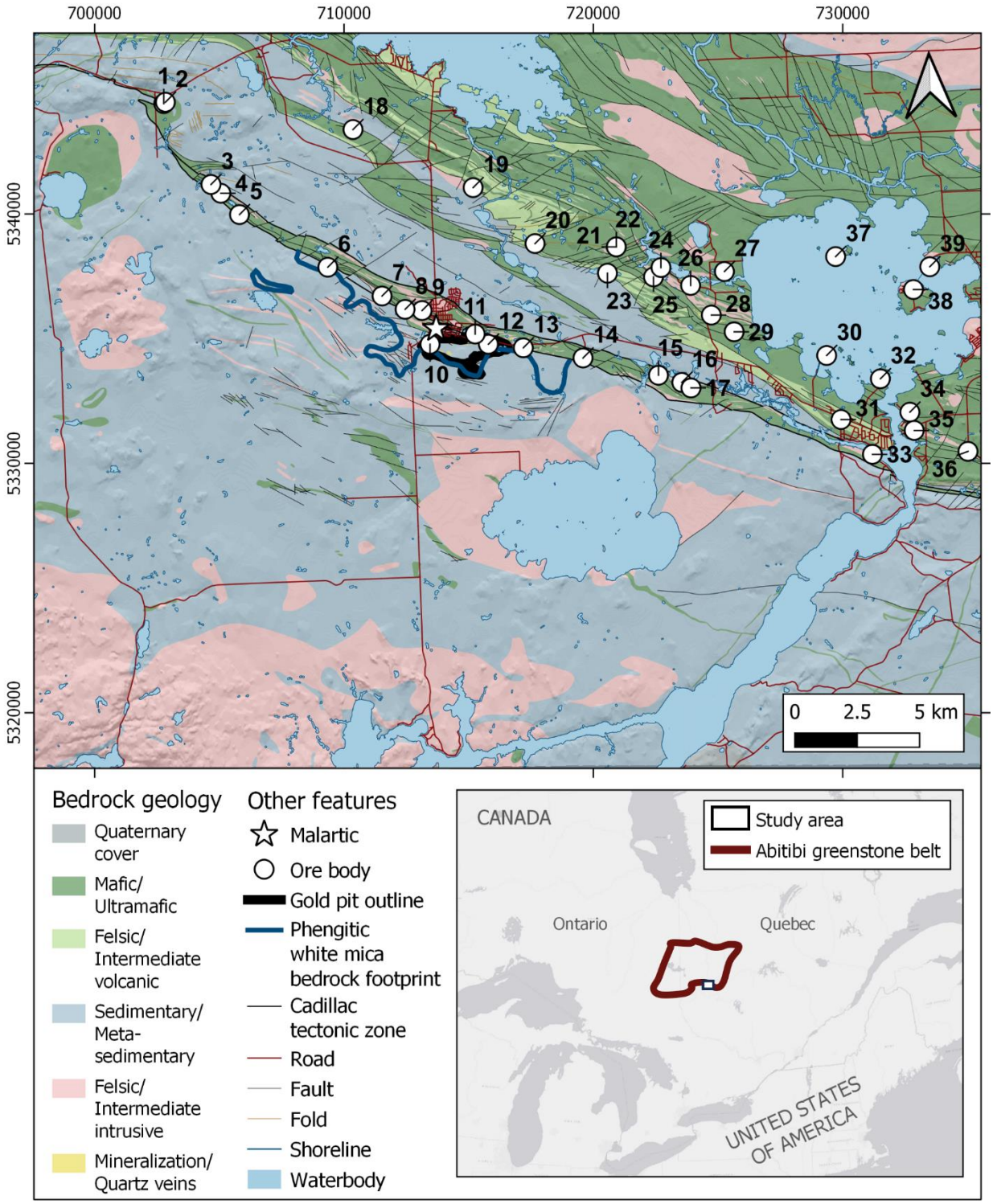

Figure 1.3 Bedrock geology within the study area. The gold pit outline and phengitic white mica bedrock footprint are after Lypaczewski et al. (2019). The extent of the Abitibi greenstone belt is modified after Hufford (2015), original in Thurston et al. (2008). Waterbodies and hillshade are from Natural Resources Canada (https://maps.canada.ca/czs/index-en.html). Bedrock geology, ore bodies, Cadillac tectonic zone, roads, faults, folds, and shorelines are from SIGEOM (https://sigeom.mines.gouv.qc.ca/signet/classes/I1108_afchCarteIntr). Labels for ore bodies are provided in **Table 1.2**. Coordinate system: NAD 83, UTM zone 17.

Table 1.2 Mine/ore body names within the study area, as labelled in **Figure 1.3**. (SIGEOM (https://sigeom.mines.gouv.qc.ca/signet/classes/I1108_afchCarteIntr)).

Label - Mine/Ore Body	
1 - Lapa Cadillac (Zulapa)	21 - Mineralized Zone No 8
2 - Lapa	22 - Malartic Hygrade (Principal/Orion)
3 - Pan-Canadian	23 - Camflo
4 - Pan-Canadian No 2	24 - Kierens (First Canadian)
5 - Pan-Canadian No 1	25 - Gold Hawk
6 - Parbec Malartic (Zone Du Camp)	26 - Norlartic
7 - East Amphi	27 - Callahan (Amlartic)
8 - Western Porphyry Zone	28 - Marban
9 - Fourax Shear Zone	29 - Little Long Lac
10 - Canadian Malartic	30 - Kiena
11 - Barnat (Sladen)	31 - Audet Property (Elmac)
12 - East Malartic	32 - Mine Shawkey
13 - Odyssey[a]	33 - Quebec Explorers
14 - Rand Malartic (New Senator Rouyn)	34 - École
15 - Malartic Gold Fields No 2	35 - Goldex (and Ormico Zone GE)
16 - Malartic Gold Fields No 1	36 - Joubi
17 - Chabela	37 - Wesdome (Western Quebec)
18 - Malrobic (North Malartic)	38 - Siscoe (Maufort)
19 - Audet Zone	39 - Siscoe Extension
20 - Black Cliff - Vinray (Abior)	

[a]Location from Agnico Eagle (2021)

1.3.2. Physiography and Modern Hydrology

Physiography encompasses the natural environment of an area. For prospecting purposes, but also this research, it is important to understand the ecozone and topography to optimize fieldwork and to be aware of their potential influence on the interpretation of results, such as increasing topographic controls at the end stages of deglaciation (McMartin & Paulen, 2009). Also, it is important to account for hydrologic gradient when conducting geochemical analyses because a regional drainage network will permeate the geologic framework of a region and interact with its geochemical and physical properties. As a result, the dispersal patterns of soluble salts and aqueous geochemical species (for example, Cu) may be influenced by water flow (Rose et al., 1979).

The area's glacial history has largely determined the physiography of the AGB. The area is characterized as the Boreal Shield (Wiken et al., 1996), meaning a combination of deciduous and coniferous forest interspersed with lakes and wetlands, generally representative of the Canadian Shield. The AGB is dominated by the flat, low relief of the Abitibi Lowland, and the main positive relief feature is the Abitibi Highlands, which is characterized by a band of rounded bedrock hills running approximately east-west (**Figure 1.2**). The Abitibi Highlands have hills with elevations up to 500 masl. It houses the watershed divide between the St. Laurence River hydrographic basin, which slopes southward to the Timiskaming lowland, and the James Bay basin, which slopes northward to the Abitibi lowland. This region is also bounded in the southeast on a northeast running diagonal with the Laurentian Highlands (an earlier peneplain with elevations 400 – 600 masl). While the Laurentian Highlands are not part of the AGB, the Abitibi Highlands used to be part of the same peneplain (Veillette et al., 2005). **Figure** 1.4 shows the detailed topography of the study area.

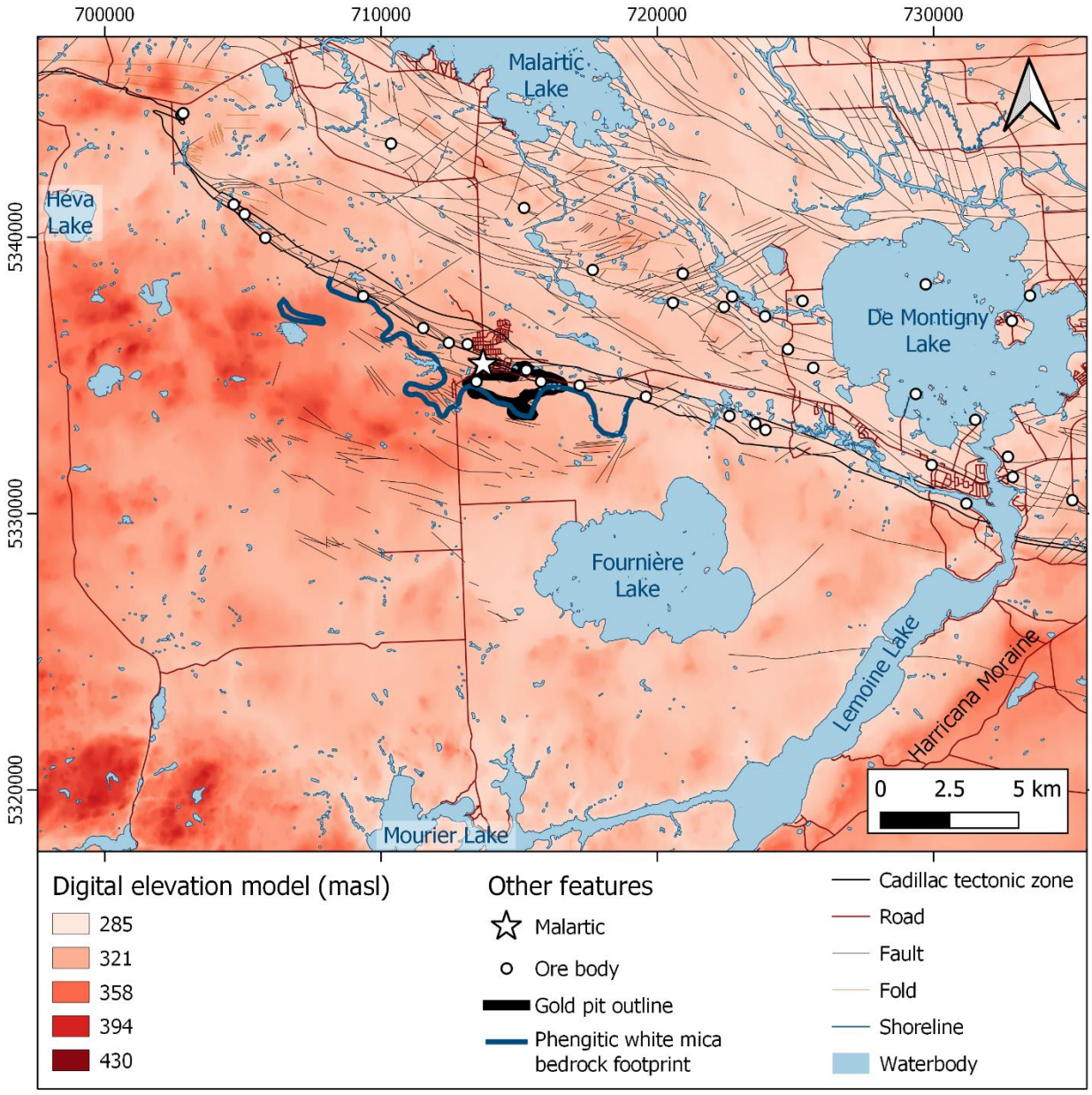

Figure 1.4 Digital elevation model (DEM) of the study area. The gold pit outline and phengitic white mica bedrock footprint are after Lypaczewski et al. (2019). Waterbodies are from Natural Resources Canada (https://maps.canada.ca/czs/index-en.html). Ore bodies, Cadillac tectonic zone, roads, faults, folds, and shorelines are from SIGEOM (https://sigeom.mines.gouv.qc.ca/signet/classes/I1108_afchCarteIntr). Coordinate system: NAD 83, UTM zone 17.

1.3.3. Surficial Geology

Quaternary deposits are ubiquitous throughout the AGB and have been mapped extensively (Veillette et al., 2003). The study area contains sporadic bedrock outcrops, subglacial till, glaciofluvial sediments, glaciolacustrine sediments, alluvial sediments, and postglacial organics, as shown in **Figure 1.5**.

Bedrock outcrops are positive relief features associated with higher elevations and make up the Abitibi Highlands (**Figure 1.2**). Spatially, they are associated with continuous and then discontinuous till sediments, glaciolacustrine deltaic or shallow-water sediments (as opposed to deep-water sediments), and glaciofluvial (esker and subaqueous fan) sediments.

Throughout the AGB, till is distributed predominantly within the Abitibi Highlands. Discontinuous or continuous sandy and silty till from Paleozoic carbonate rocks, derived from the James Bay Lowland, and non-calcareous Precambrian rocks are found within the AGB and north of the study area (Bonham-Carter, 2005). In the study area, discontinuous or continuous sandy tills are from non-calcareous Precambrian rocks (Veillette, 2004).

Glaciofluvial sediments lie throughout the AGB in long strands that trend north-south, with some exceptions, and are subdivided into moraines, eskers and subaqueous fans, and undifferentiated sediments and ice-contact sediments. An evolving glacial meltwater system connected to GLBO created these sorted sand and gravel deposits. Although they account for ~5% of the surficial area, the combined length of the eskers alone is approximately 1400 km (Veillette et al., 2005).

Glaciolacustrine sediments characterize the regional landscape by being the most abundant type of surficial cover. Within the study area, glaciolacustrine sediments are subdivided into deep-water, deep-to-shallow (i.e. transitional), and shallow-water sediments. The deep-water sediments are primarily clay and silt, while the shallow-water deposits are mainly sand and gravel. The deep-water facies are typically characterized by well-sorted and laminated fine-grained material with minor amounts of sand and occasional larger clasts (i.e. dropstones) and are distributed extensively below an elevation of 320 m (Veillette, 1994; Roy et al., 2015; Veillette et al., 2005). North of the drainage divide, the thick laminated sediments are interpreted as varves associated with lake depths of 40 m or more (Veillette et al., 2005). Shallow-water sediments are associated with deltaic sediments, produced in areas where subglacial meltwater (associated with esker production) entered the glacial lake.

Postglacial alluvial sediments are generated by modern floodplains and are found edging streams. However, there are minor paleo-floodplain deposits within the AGB (e.g. the largest example of paleo-floodplain alluvial deposits is found north of Lake Timiskaming) (Veillette et al., 2005).

Organic deposits are associated spatially with glaciolacustrine sediments. This postglacial unit made of peat and muck has generally accumulated on poorly drained glaciolacustrine sediments throughout the AGB and the study area.

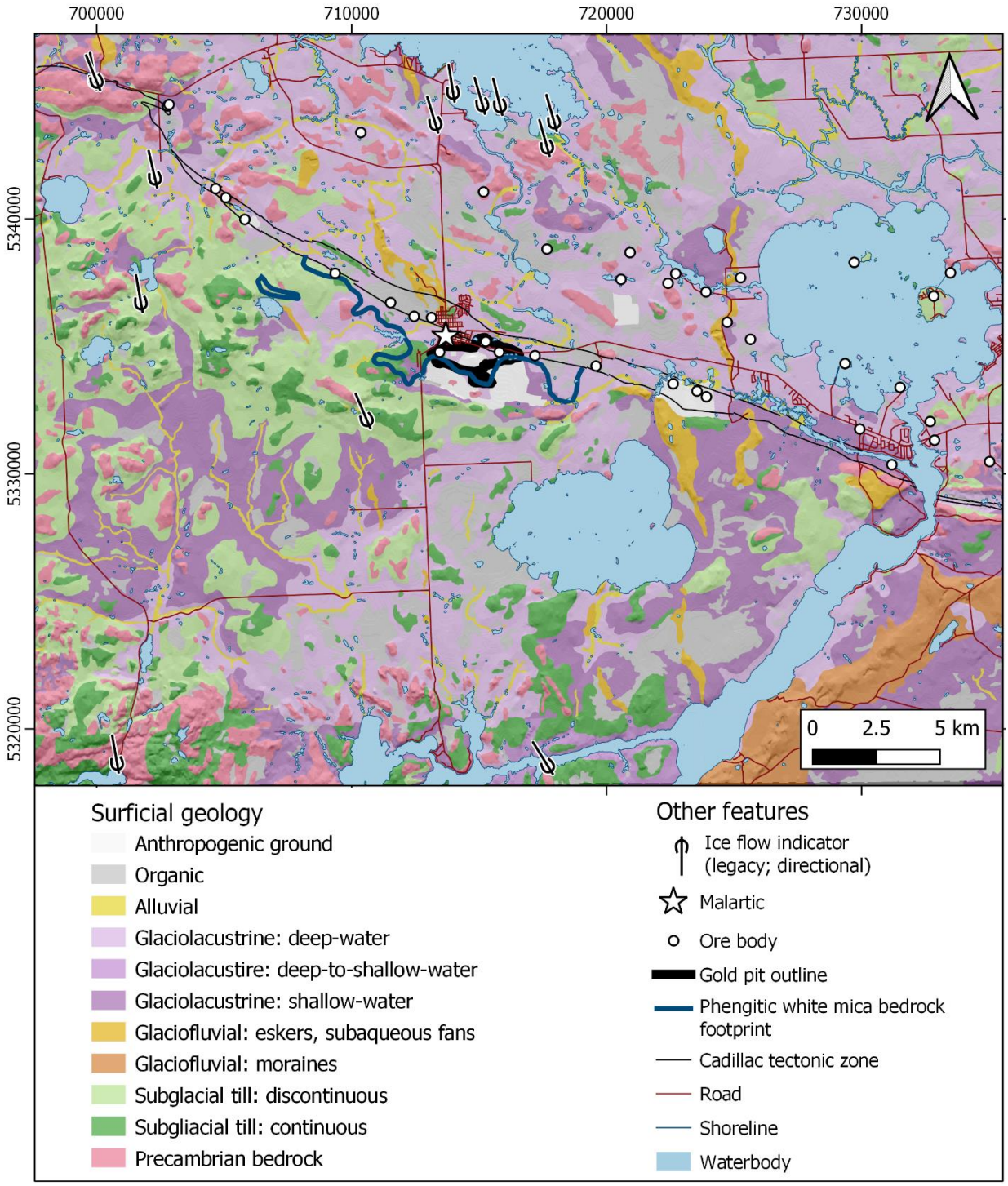

Figure 1.5 Surficial geology and a hillshade elevation model within the study area around the Canadian Malartic Mine. The simplified surficial geology map and the location of Malartic were generated using data from the GSC MITE project (Bonham-Carter, 2005). The gold pit outline and phengitic white mica bedrock footprint are after Lypaczewski et al. (2019). Waterbodies and hillshade are from Natural Resources Canada (https://maps.canada.ca/czs/index-en.html). Legacy ice flow indicators, ore bodies, Cadillac tectonic zone, roads, and shorelines are from SIGEOM (https://sigeom.mines.gouv.qc.ca/signet/classes/I1108_afchCarteIntr). Coordinate system: NAD 83, UTM zone 17N.

1.3.4. Regional Glacial History

The study area's modern landscape and the characteristics of its surficial deposits stem from the greater region's glacial history, and their genesis can be understood in terms of broader trends in the erosional and depositional records on a larger scale. This subsection reviews the erosional and depositional records on the scale of the AGB.

1.3.4.1. Erosional Record

During the last glaciation, the Laurentide Ice Sheet (LIS) waxed, waned, and sometimes covered the AGB. Basal sliding of the LIS sculpted bedrock extensively and produced erosional marks that were preferentially preserved in volcanic and sedimentary rocks relative to more resistant granitic and gneissic rocks (Veillette & McClenaghan, 1996; Veillette et al., 2005). Throughout the AGB, Veillette and McClenaghan (1996) recorded data from over 3000 striated outcrop surfaces that preserved evidence from at least two distinct ice flows and established the chronological ice flow history based on crosscutting striated rock surfaces. Seven separate ice flow phases were identified. Erosional ice flow indicators in the region show evidence for an oldest northwestward ice flow phase, followed by a counterclockwise shift in ice flow directions, which is consistent with reconstructions in adjacent regions, including northern Ontario (Thorleifson et al., 1993; Veillette et al., 2017) and around the James Bay Lowlands (Veillette et al., 1999). The established ice flow history within the study area is summarized by an initial and more regionally dominant phase to the southwest, followed by a counterclockwise shift and subordinate flow to the southeast (Veillette, 1989, 2004). **Figure 1.6** presents the ice flow history based on this erosional record, and **Table 1.3** details each flow.

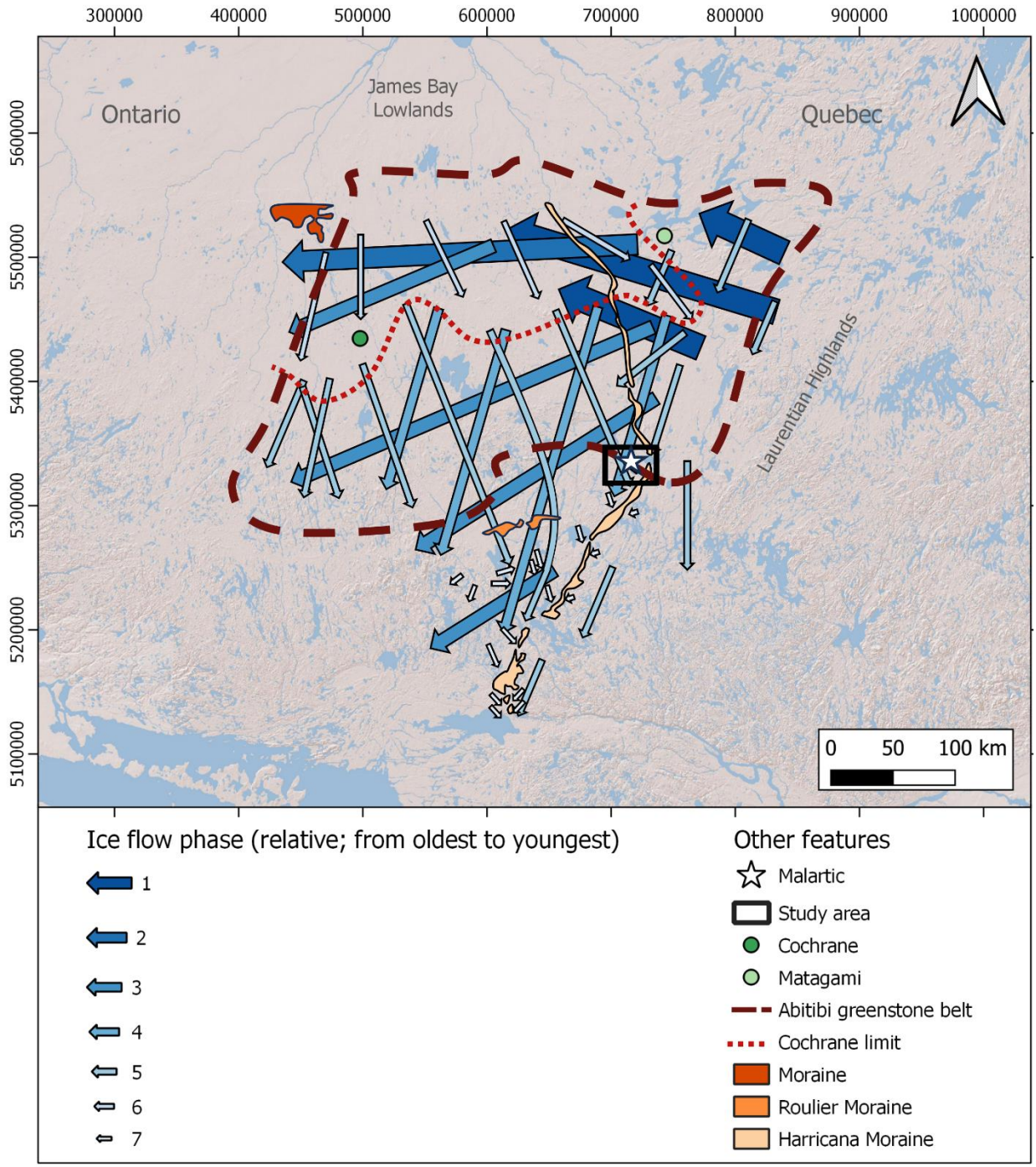

Figure 1.6 Summary of the ice flow history within most of the Abitibi greenstone belt. The seven ice flows' relative age, direction, and location are represented by arrows (ranging from dark blue to light blue for oldest to youngest, respectively). The relative size of these arrows corresponds to the extent of the regional influence of the ice flow, meaning that the influence of an ice flow becomes increasingly local as the size of its arrow decreases. A red star represents the location of Malartic. Modified after Veillette et al. (2005), original in Veillette & McClenaghan (1996). **Table 1.3** details each flow. The extent of the Abitibi greenstone belt is modified after Hufford (2015), original in Thurston et al. (2008). Shaded relief is from Esri (https://server.arcgisonline.com/ArcGIS/rest/services/World_Shaded_Relief/MapServer). Coordinate system: NAD 83, UTM zone 17N.

Table 1.3 Summary of ice flow history within the Abitibi Greenstone Belt (Veillette & McClenaghan, 1996; Veillette et al., 2005), as shown in **Figure 1.6**.

Flow	Azimuth (º)	Notes
I (oldest)	290-315	Rare striations, limited to the James Bay basin, north of latitude 49º N. Interpreted as occurring during the LIS's early phase (growth) of the Labrador Sector, part of which flowed from the Quebec Highlands towards Hudson Bay.
II	260-270	Rare striations, mainly in the north end of the AGB and west of the Harricana Moraine, are found on lee-sides of stoss-lee geomorphic features (e.g. *roches moutonées*) from flow V. Interpreted as occurring during the mature phase of the LIS, before deglaciation.
III	230-250	Like flow II, but with more abundant striations throughout the central and southern portions of the AGB. Interpreted as occurring during the mature phase of the LIS, before deglaciation.
IV	190-220	Significant transport of glacial debris over long distances. Interpreted as occurring during early deglaciation in response to an ice margin opening south of the region.
V	160-230, complex	Produced the present-day Quaternary landscape despite transporting glacial debris over relatively short distances due to its short duration of approximately 2000 years. Two main directions converged and produced the interlobate Harricana Moraine.
VI	130-200	Found north of the Cochrane limit produced by the Cochrane surges (i.e. ice sheet readvancing into proglacial Lake Ojibway), which occurred during late-stage deglaciation.
VII (youngest)	Complex	Minor flows with significant local topographic controls from the final stage of deglaciation.

1.3.4.2. Depositional Record & Evolution of Glacial Lake Barlow-Ojibway

Throughout the region of the AGB, natural exposures along rivers and lakes reveal its stratigraphy but are limited to the most recent glacial cycle (Veillette et al., 2005). Anthropogenic activities such as drilling holes down to bedrock and other excavations provide evidence of earlier interglacial and glacial sediments. The general sequence of events based on the regional stratigraphic framework is that till deposition dominates during full glaciation and is overlain locally by glaciofluvial deposits during deglaciation, followed by glaciolacustrine deposition upon ice margin retreat, which can be seen distinctly during the last glacial cycle and is interpreted as ice sheet advance and retreat coupled with regional flooding by Glacial Lake Barlow-Ojibway (GLBO). **Figure 1.7** shows a composite Quaternary stratigraphic column for the AGB region.

The main till sheet that covers most of the AGB is the Matheson Till, which is exposed in natural sections on river and lake banks. It represents the main unit of the last glaciation, mostly the late Wisconsinan or Marine Isotope Stage 2 (~25-10ka). The Cochrane Till is a younger till sheet and it is only found within the limit of the late-stage Cochrane ice readvances (Hardy 1977; Veillette et al. 1991; Veillette et al. 2017). The Cochrane Till is in the north-central part of the AGB (beyond the study area), and was deposited within a short interval (~9-8.7 cal ka) that was before the collapse of the ice mass over southern Hudson Bay (Dalton et al. 2020).

Veillette et al. (2005) provide a detailed analysis of regional and local markers throughout the AGB and evidence for a shift in the Matheson Till. The three sources of regional carbonate marker erratics and dropstones in the AGB are the Hudson Platform (Paleozoic rocks), the Churchill Province in Hudson Bay (Proterozoic rocks), and the Lake Mistassini basin (Proterozoic rocks). Changes in rock flour composition in till and glaciolacustrine deposits occur due to carbonate input from the Hudson Platform, and the distribution of carbonate markers constrains the timing and extent of the Cochrane surges. If there is an input from one or more carbonate sources into sediments, this will affect the pH of water that may flow through the sediments, affecting ion mobility. Calcareous rock flour is an important component in the Matheson Till, Cochrane Till, and the glaciolacustrine sediments found in the northwestern part of the AGB (Veillette & McClenaghan, 1996; Veillette et al., 2005); however, significant carbonate markers are not expected in the study area's Matheson Till nor glaciofluvial sediments.

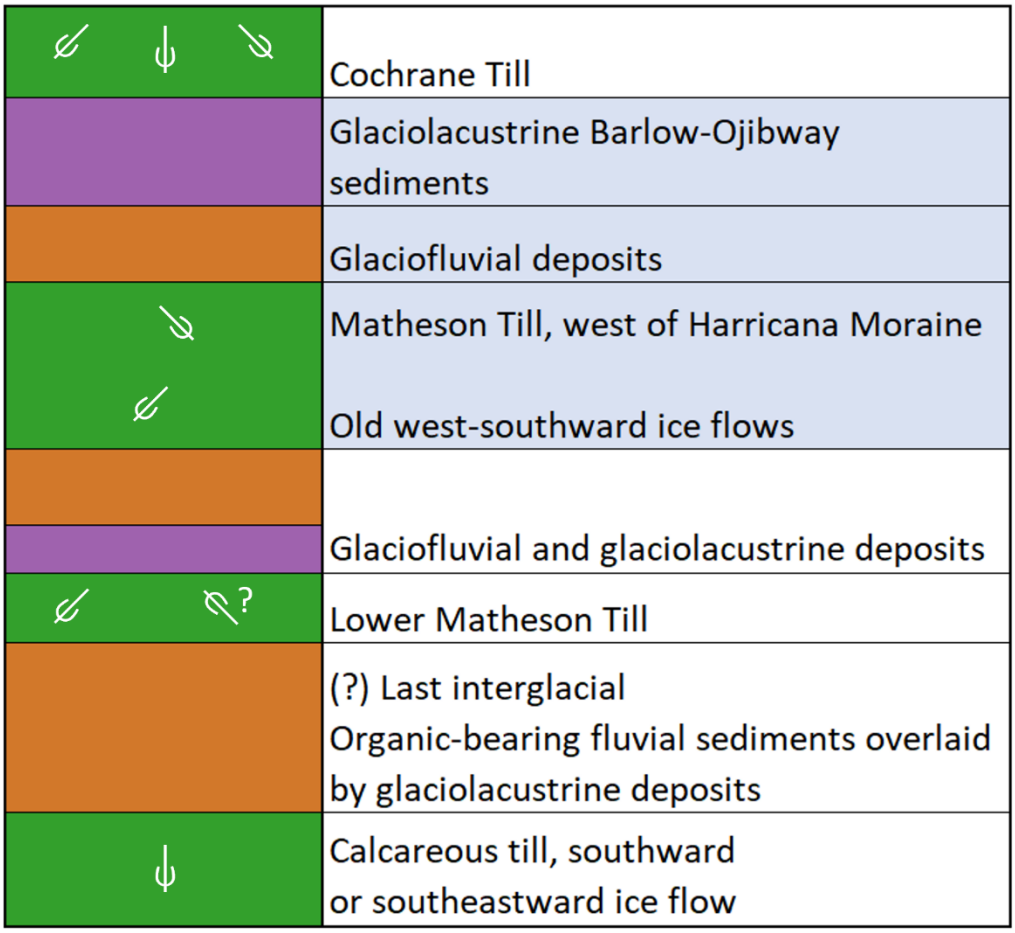

Figure 1.7 Composite Quaternary stratigraphic column for the Abitibi Greenstone Belt (AGB) region, Quebec and adjacent Ontario areas showing the relative order and proportion of units. The sedimentary sequence most likely encountered within the study area is highlighted (light blue). The Cochrane Till is limited to the north of the AGB region, outside the study area. Rare sediments from the previous glacial cycle have been uncovered during anthropogenic drilling and other excavations, comprising the column's lower portion. Modified after Veillette et al. (2005), original in Veillette & McClenaghan (1996).

Glaciofluvial deposits are stratigraphically posited between the Matheson and Cochrane tills. The most prominent depositional feature of glaciofluvial origin is the interlobate Harricana Moraine (**Figure 1.6**), which is thought to have been formed between two retreating lobes, one to the northwest and one to the northeast, of this sector of the LIS (Hardy, 1976; Brennand et al., 1996). Another moraine, the Roulier Moraine, is thought to have been formed at an ice-frontal position of the lobe that retreated to the northwest (Veillette et al., 2005) (**Figure 1.6**). Veillette et al. (1999) provide a detailed review of the evolution of the Quebec-Labrador sector of the LIS that covered this region, and the updated ice margin retreat chronology is detailed in Dalton et al. (2020).

The glaciofluvial deposits are stratigraphically overlain by sediments of Glacial Lake Barlow-Ojibway (**Figure 1.7**). The evolution of GLBO is a key component of the most recent glacial history of

the AGB and its resulting surficial sediments, and it laid the foundation for the area's modern-day hydrologic system. GLBO is so called because it represents the maximum extent of an amalgamation of two ice-contact glacial lakes that were otherwise separated by the drainage divide within the Abitibi Highlands (Antevs, 1925) (**Figure 1.8**). Glacial Lake Barlow (GLB) evolved within the southern watershed (Wilson, 1918), while Glacial Lake Ojibway (GLO) evolved within the northern watershed (Coleman, 1909 as cited by Veillette,1994), which corresponds to the bulk of the area in the AGB.

GLBO was formed from meltwater from the LIS, akin to Glacial Lake Agassiz (i.e. GLBO's counterpart in central North America). At one stage during deglaciation, GLO and Glacial Lake Agassiz were combined (Lepper et al., 2011; Roy et al., 2015; and references therein) provide detailed analyses of the evolution of Glacial Lake Agassiz in terms of lake stages, outlets, and changes in routing events). From its maximum extent, GLBO drained to the north via a breach near the upper reach of the Harricana River, and it drained to the south via a breach near the upper reach of the Kinojevis River (Veillette, 1994; Veillette et al., 2005).

Vincent & Hardy (1979) and Veillette (1994) provide detailed analyses of GLBO's evolution by mapping raised shorelines, among other lines of evidence, and conclude that there were three main stages. Veillette (1988), Richard & Larouche (1989), and Richard et al. (1989) constrain the chronology of deglaciation. Roy et al. (2015) investigated the late-stage phases of GLO, whose final drainage occurred at approximately 7600 PB (Barber et al., 1999) into the Tyrrell Sea (i.e. modern-day Hudson Bay). This event is linked with Ice Flow IV (**Figure 1.6**), which shaped the modern glacial landscape throughout the AGB.

The development of a well-organized drainage system in the form of conduits and tunnels in the ice, along the bed, or the interlobate zone also caused several local deviations (Flow VI) from the main regional flow direction, especially in the vicinity of the Harricana interlobate zone. The latter was a large conduit for meltwater, which led to the formation of the prominent Harricana moraine (McClenaghan and Veillette 1996; Veillette 2005). The late-stage flow on the eastern side of the Harricana interlobate zone was to the SW. In contrast, ice was flowing to the SE on the western side of the interlobate zone because ice converged towards the lateral lobe margins due to local ice surface topography and inward ice creep in the low-pressure conduit.

The town of Malartic is within the Abitibi Highlands, north of the drainage divide (**Figure 1.8**). Modern regional groundwater flow is generally to the northeast in the vicinity of Malartic (Roy, 2013), which may have modified glacial dispersion patterns of mobile geochemical pathfinders in the till at depth (in the saturated zone); therefore, aqueous species in susceptible media may be dispersed northeastwards by groundwater and surface water.

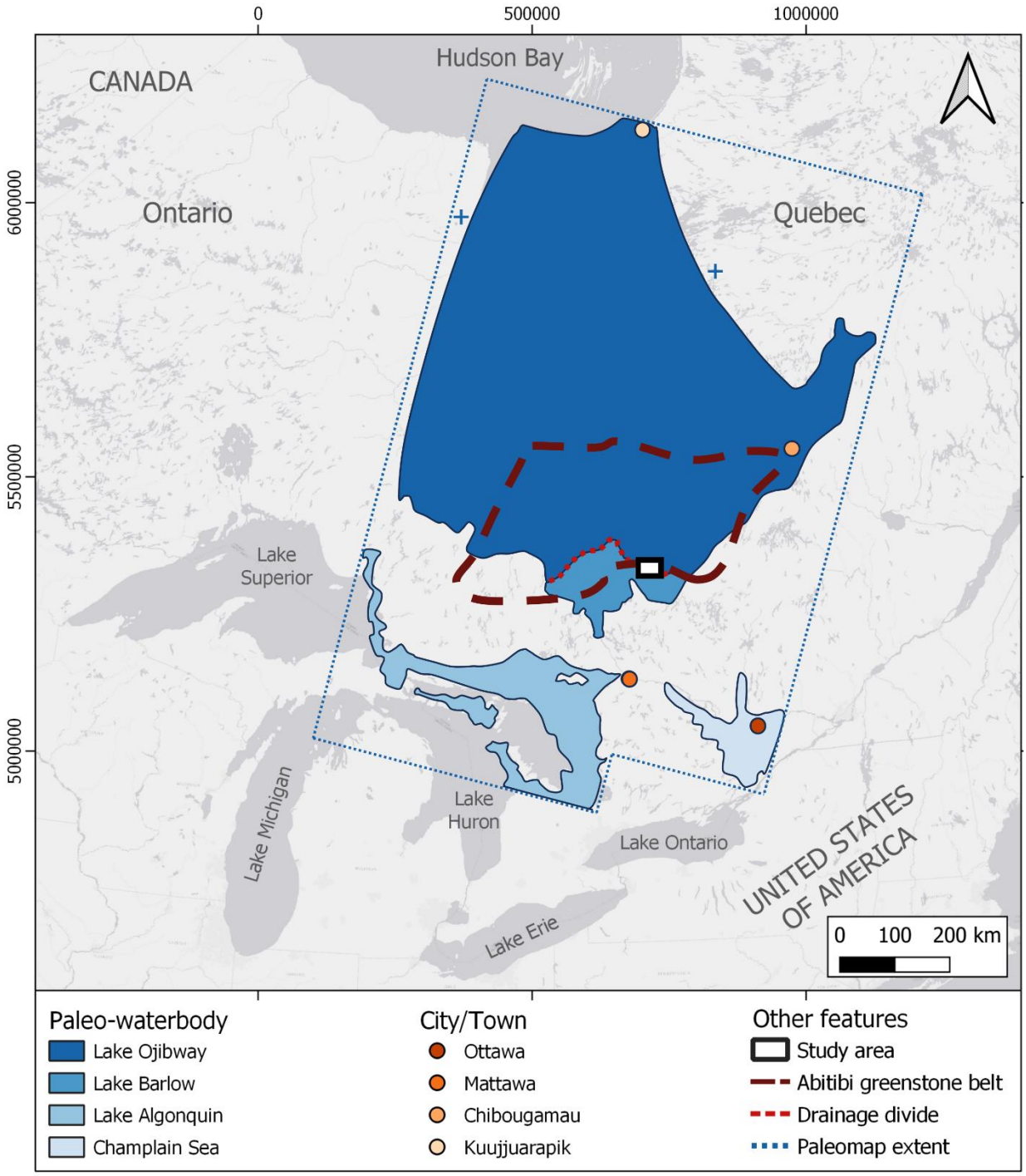

Figure 1.8 Full extent of Glacial Lake Barlow-Ojibway during deglaciation, compared with the maximum extents of Glacial Lake Algonquin and the Champlain Sea (maximum extents not coincident). Malartic is located north of the drainage divide, within the study area, and present-day groundwater in the local area continues to flow northwards towards James Bay. Modified after Veillette (1994); original map by Prest et al. (1968). The extent of the Abitibi greenstone belt is modified after Hufford (2015), original in Thurston et al. (2008). Shaded relief is from Esri (https://server.arcgisonline.com/ArcGIS/rest/services/World_Shaded_Relief/MapServer). Coordinate system: NAD 83, UTM zone 17N.

1.4. Previous Research at the Canadian Malartic Gold Deposit

1.4.1. NSERC-CMIC Footprints Project Results

The inter-disciplinary Footprints collaboration has identified over 60 previously unknown footprint components and vectors in bedrock (Lesher et al., 2017). In bedrock, the smallest halo identified thus far is for whole-rock lithogeochemistry of ore-related elements (e.g., Au, Ag, Te, W, Mo, etc.) (Lesher et al., 2017)) and approximately corresponds to the outline of the open pit (~3 km²). In contrast, the largest haloes are the white-mica and biotite mineral chemistry in metasedimentary and intrusive rocks and the biotite alteration in mafic dykes (up to 60 km²) (Lypaczewski et al., 2019; Perrouty et al., 2019). Lypaczewski et al. (2019) used hydrothermal alteration micas as an effective proxy for gold in drill cores and to expand the ~3 km^2 planar Canadian Malartic open pit gold mine to a 12 km by 3 km footprint alteration halo in bedrock (**Figure 1.3**, **Figure** 1.4, **Figure 1.5**). Their rapid and cost-effective approach to imaging Au-related alteration, as opposed to mineralization, identified relative degrees of hydrothermal alteration, an example of a footprint that effectively vectors toward mineralization.

1.4.2. Surficial Exploration

A large sampling survey in 1971-1973, conducted by the *Ministère de l'Énergie et des Ressources Naturelles du Québec*, collected around 7000 sediment samples throughout the Abitibi-Temiskaming region (Natural Resources Canada, 2019). Taves (2015) performed a preliminary assessment of the legacy data for 436 samples in and around the area of Malartic and demonstrated geochemical levelling between two datasets. Taves (2015) noted two serious concerns regarding the data's fitness: the lack of information regarding the analytical digestion method used to produce geochemical measurement values and the indiscriminate labelling of all sample material as till in the Cadillac Data. Taves (2015) showed clear evidence that in several areas within the sampling grid, laminated glacial lake mud was observed overlying and draping bedrock in the field; clearly, till is lacking in these areas, which means that the 'till' geochemical database contains an unknown number of results from glaciolacustrine sediment samples, which are generally diluted in most elements of interest. Combining measurements from glaciolacustrine sediment samples with till samples has implications in determining the correct background level of the dataset and integrating that data with the new data from the current project.

Taves (2015) also collected surficial till samples and conducted preliminary testing on the efficacy of W (from W-enriched rutile) and Au as geochemical tracers in the till matrix and applied hyperspectral imaging analysis to glacial pebbles. She concluded that using these techniques holds potential and warrants further investigation with better sample coverage of the area around Malartic.

1.5. Knowledge Gaps and Important Research Questions

The well-established use of geochemical elements, indicator grains, and mineralized boulders and cobbles from surficial sediments in exploration demonstrates unique advantages and limitations stemming from their specificity. Till matrix can be geochemically complex, and anomalies may be difficult to interpret. Sometimes, fine-grained indicator minerals may be diluted and mixed to a degree that prevents their identification from geochemical results. Advanced statistical techniques may be required to isolate a specific signature, discover a process (e.g., alteration), and separate the anomalies from the normal compositional variations (Grunsky, 2010). Individual indicator mineral grains may undergo regional transport. They can be probed to reveal a unique signature associated with a specific source of interest, which makes it possible to identify and fingerprint contrasting sources across an area or to determine the mineralization potential of the source. However, current techniques rely on visually identifiable characteristic properties of indicator grains, which must be large enough (i.e. sand-sized) to correctly identify. Mineralized cobbles and boulders preserve host-rock mineral assemblages, which can be valuable in constraining source-bedrock lithology, but boulders are not always present in sufficient quantity at the surface.

An overview of these techniques revealed a size fraction that does not receive much attention: the granule and pebble fractions, which have yet to be utilized beyond general pebble lithology to identify major bedrock sources to constrain provenance and the extent of glacial transport (Broster, 1986; Dilabio, 1990; Trommelen et al., 2013). Further, it is challenging to identify mineralization-related alteration instead of working with deposit indicators because alteration-related minerals may not be well known or difficult to identify in the till matrix (Bustard 2016). However, there is significant potential in shifting the focus from searching for indicator signs of mineralization to exploring resource-related alteration in till and glaciofluvial sediments because the exploration target becomes much larger. It can also open new applications of drift prospecting to trace ore deposits whose mineralized zone does not intersect the bedrock surface. The few case studies about this type of application showed promising results for deep uranium deposits (e.g. Earle 2001). Still, to my knowledge, no equivalent studies have been done for tracing alteration related to gold mineralization.

The Canadian Malartic deposit embodies challenges associated with traditional drift (and other) prospecting techniques. At the start of Footprints, the Canadian Malartic deposit eluded established prospecting methods despite its high-tonnage. Also, because of its disseminated low-grade nature, it had an elusive geophysical signal. Its geographically unconstrained and partly defined alteration haloes with mineralization characterized by very fine gold grains (diameters on average 10 µm and rarely >30 µm) (Helt et al., 2014) represent an important challenge, and it is also located in an extensive brownfield region populated with historical and active mines that further complicates its detection. In addition, the

area is covered by widespread surficial sediments, including glaciolacustrine sediments that limit surficial till sampling surveys. Finally, there is an insufficient quantity of boulders within the study area to apply boulder tracing techniques.

Interesting research questions include determining which components of till (or other glacial sediments) may preserve footprints and comparing the dispersion patterns and extent of different footprints to one another. **Figure 1.9** summarizes previously established footprints at the Canadian Malartic gold deposit (Lesher et al., 2017) and the potential for Quaternary dispersion as established by Taves (2015).

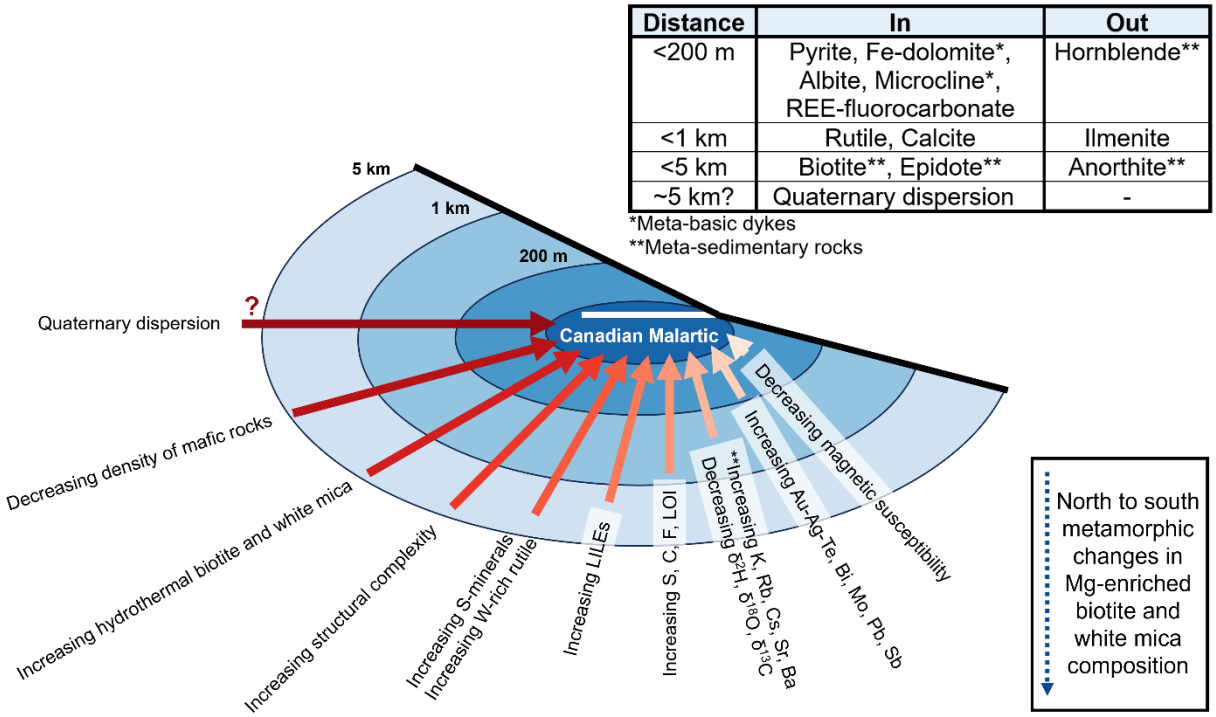

Figure 1.9 Schematic shows previously established footprints at the Canadian Malartic gold deposit (modified after Lesher et al., 2017), as well as the potential for Quaternary dispersion (Taves, 2015).

1.6. Thesis Hypothesis & Objectives

This research posits that several of the diagnostic features that define 'Canadian Malartic' footprints in the near-surface bedrock also occur as detectable secondary (detrital) footprints in glacial sediments due to past glacial erosion, transport, and deposition around Malartic, Quebec.

The hypothesis is based on three main assumptions: (1) bedrock along the Canadian Malartic footprint was available to glacial erosion (i.e., it was not completely covered by pre-existing sediments of a different provenance); (2) sufficient erosion took place to produce dispersal patterns in till, and dilution from up-ice rock sources was limited; and (3) there has been insignificant overprinting by groundwater action on potential tracers.

The two specific objectives of the thesis are: (1) to establish the main dispersal trains down-ice of the Canadian Malartic deposit based on existing techniques such as indicator minerals of gold mineralization and key geochemical pathfinders and (2) to assess the feasibility and efficacy of hyperspectral imaging analysis techniques applied to glacial pebbles to trace alteration footprints and delineate secondary dispersal footprints of alteration down-ice of Canadian Malartic-type deposits.

Despite well-established regional knowledge about ice flow history, deglacial events and surficial sediments in the study area, it was deemed necessary to add to this body of data and knowledge to further constrain local ice flow directions as well as to improve descriptions of sedimentological properties and composition of glacial sediments, especially till. Previous work concluded that a single till sheet occurs at the surface in the study area, i.e., the Matheson Till (Veillette et al., 2005), but this needs to be further assessed in this study. The mineralogical assemblages related to the ore deposit and its surrounding alteration footprint are central to this research because they determine the indicator minerals and geochemical pathfinders that must be targeted and investigated in glacial sediments.

1.7. Structure of Thesis Chapters

The chosen structure of this thesis is to facilitate preparation for a future submission to a journal. This thesis is divided into four chapters: Chapters 1 and 4, which are not written for publication, and Chapters 2 and 3, which are intended for publication.

Chapter 1 (i.e., current chapter) presents research motivation, current drift prospecting state of knowledge, the geological framework of the study area, previous research at the Canadian Malartic gold deposit, knowledge gaps and important research questions, thesis hypothesis and objectives, and this description of the structure of the thesis.

Chapter 2 establishes fieldwork and preliminary sample processing methodology, augments and refines the local erosional and depositional record with new observations and investigates the primary characteristics of subglacial till in the area. This work constrains local dispersal pattern interpretation and the identification of anomalies in till in the following chapters.

Chapter 3 applies existing drift prospecting techniques to search for footprint components and vectors in till by investigating till matrix geochemistry and heavy mineral grain counts. It also builds on existing results from Footprints. It applies a novel technique based on hyperspectral imaging analysis, which has successfully identified footprint components and vectors in bedrock (Lypaczewski et al., 2019) to pebbles from till.

Chapter 4 summarizes the work, highlights important research contributions, and lists opportunities for future work and recommendations.

CHAPTER 2: Ice Flow & Glacial Sediment Records of the Canadian Malartic Mine Area: Implications for Glacial Dispersal from a World-Class Gold Deposit

2.1. Introduction

Glacial dispersal trains of indicator minerals and geochemical pathfinder elements from mineralized zones in bedrock are routinely characterized in mineral exploration (Shilts, 1976; Dilabio, 1990; McClenaghan & Paulen, 2018), which requires an understanding of the regional and local glacial geology. As explained in Chapter 1, this study focuses on the Canadian Malartic gold deposit, which is a unique low-grade world-class deposit (>18.6 Moz Au indicated, inferred, and historical) (Robert & Poulsen, 1997; Gervais et al., 2014) found in Canada's Abitibi Gold Belt, within Quebec's previously glaciated Precambrian shield terrain. This chapter describes and interprets the glacial geology record to provide the foundation for detailed dispersal train analysis down-ice of the Canadian Malartic deposit and surrounding alteration halo.

An understanding of local ice flow dynamics of the Laurentide Ice Sheet needs to be coupled with surficial sediment analyses to then use tracers within subglacial till and glaciofluvial deposits as vectors towards a mineral deposit (Shilts, 1976; Hirvas & Nenonen, 1990; Saarnisto, 1990; Cummings et al., 2011; McClenaghan & Paulen, 2018). Ice flow indicators must be identified and measured where possible to determine ice flow direction and relative chronology of flow phases (Lowell et al., 1990), which provides information about possible sediment entrainment directions and is essential when tracing geochemical and mineral anomalies back to their source. Glacial landforms and sediment characteristics are also important as they give insights into sedimentary processes such as erosion, sediment entrainment and deposition. Characterizing the overall texture and composition of surficial sediments is also essential to determine bedrock provenance, investigate the potential effects of physical sediment characteristics on composition, and is critical to identify anomalies related to mineralization.

This chapter thus describes evidence related to ice flow directions and the main glacial sediment types and characteristics. It reconstructs evolving glacial dynamics of the Laurentide Ice Sheet in the study area. This chapter also discusses implications for drift prospecting from sampling strategies to the prediction and interpretation of dispersal patterns of compositional tracers of Canadian Malartic-type gold deposits.

2.2. Linking Past Ice Flow to Modern Landscapes

Glacial records vary in complexity, but they are typically fragmented, creating a mosaic of sediment and landform assemblages formed at different times, which may have also been reworked to variable extent by younger events (Stea & Finck, 2001; Trommelen et al., 2012; Stone & McMillan, 2013). Glacial features may thus be 'inherited' from older events and variably 'overprinted' by younger events. One important effect of this on the composition of glacial sediments is that they tend to be of mixed provenance due to ice flow shifts over time. As such, mapping many kinds of ice flow indicators and analyzing the physical and chemical components of glacial sediments is essential to unravelling a detailed glacial history of a region and how that explains the composition and related mixed provenance of glacial sediments.

Ice flow indicators are preserved physical alterations to bedrock or sediments produced by the movement of warm-based glacial ice and occur over a wide range of scales as erosional or depositional features. These indicators can be used to determine the presence of one or more past ice flow phases and associated flow direction, to establish the relative chronology of the phases to one another, which can be used to trace ore-related anomalies in glacial sediment back to their source (Prest, 1983; Hirvas & Nenonen, 1990; Stea & Finck, 2001; Veillette, 2004b; McMartin & Paulen, 2009).

Erosional ice-flow indicators on bedrock outcrops include a group of features that are found on abraded bedrock surfaces, such as small-scale striae, rat tails, chatter marks, gouges, crescentic fractures, and P-forms. Bedrock can also be sculpted at an intermediate scale, forming *roches moutonnées*, whalebacks, rock drumlins, and irregular over-deepenings (Benn & Evans, 2010). Certain features, such as grooves and striations, are straight lines created by abrasion of debris-rich basal ice as it was sliding on bedrock (Rea, 2007). Ice flow was thus parallel to these linear features, but other information, such as the shape of the outcrop, is usually required to determine the down-ice direction. *Roches moutonnées* are especially useful because they have a distinctive stoss (up-ice) and lee (down-ice) shape that establishes ice flow direction from striations on the landform's abraded stoss side. Further, relict features such as striations from earlier ice flow phases are commonly crosscut by younger features or identified on protected lee-side surfaces and are essential in establishing ice flow chronology (Veillette et al. 1999).

Landform-scale ice flow indicators include streamlined landforms that develop in bedrock or sediments with or without a bedrock core; in some cases, down-ice of a bedrock knob (e.g. crag-and-tails) (Benn & Evans, 2010). Additionally, the orientation of elongated particles (macro and micro fabrics) in subglacial traction till provides useful information about the direction of shear during subglacial sediment transport, which is often used to infer ice flow direction at time of till deposition, especially in areas where there is a paucity of accessible bedrock outcrops and thick exposed tills (Benn, 1995; Menzies et al., 2006; Gauthier et al., 2019; Roman, 2019). Similarly, glaciofluvial clast fabric analyses provide

information about the direction of pressurized subglacial water flow and can be linked to the reconstruction of ice sheet dynamics and evolution (Delaney, 2001).

Dynamic glacial ice shapes a landscape by eroding underlying material via abrasion (striation and polishing) that produces fine material for till matrix and by quarrying that produces boulders and many of the matrix-supported clasts in till (Rea, 2007; Benn & Evans, 2010). The till matrix amalgamates proximal and mixed distal sources (Dreimanis, 1990). As such, the till matrix can be challenging to analyze because of its complicated evolutionary history. In contrast, larger clasts such as pebbles, cobbles, and boulders are generated predominantly by quarrying and provide a sample of the bedrock lithologies of the source region(s), which reduces the complexity of the interpretation of their provenance and can produce rock samples of target ore material. Another consideration is substrate control, meaning the competence or friability of the input subglacial material. For example, more friable rock, such as limestone, which also tends to be jointed and fractured, is far more prone to widespread quarrying and abrasion, whereas relatively competent rock, such as crystalline granitic rock with lower fracture density, is more resistant to abrasion and far more resistant to quarrying (Iverson 2012; Bukhari et al., 2021).

Within the study area, the regional till is generally discontinuous, crosscut by a few eskers, and glacial lake deposits cover the surface extensively, particularly north (up-ice) of the Malartic gold deposit (**Figure 1.5**). Also, Abitibi eskers within the Glacial Lake Barlow-Ojibway basin tend to be of lower amplitude (subdued landform) than eskers unmodified by proglacial and later shoreline processes; subaqueous fans of sand and silt covered their coarse gravel and cobble cores from the transition of subglacial meltwater flowing in conduits to openings into the regressing glacial lake, which was a change from relatively high hydrostatic pressure to relatively low hydrostatic pressure conditions. Subsequent wave action during lake lowering phases may have further reworked esker flanks, along with postglacial wind erosion and paludification (Veillette et al., 2005).

Linking the evolution of this study area to its present landscape is essential to decipher ore-related anomalies from background measurements in sediments and then trace them back to their source.

2.3. Methods

Fieldwork was necessary to collect ice flow indicator measurements and surficial samples and was conducted over two seasons; the first field season was the basis of the Undergraduate thesis work completed by Taves (2015), and the second season was completed in 2016 (by the author). The purpose of the second field season was to map different types of local ice flow indicators and to collect additional surficial till samples to increase the spatial coverage around the deposit, increase sampling density nearer the deposit, and constrain background measurements. Fieldwork in 2016 increased the study area from 90 km^2 to 340 km^2.

Primary sediment sample processing (i.e. drying, archiving, and dry sieving) was completed at the Applied Quaternary Geosciences Research Laboratory at the University of Waterloo. Grain size distribution and variations in clay content were used to characterize sediments (Wentworth, 1922) and assess the potential for geochemical partitioning in the clay fraction (Shilts, 1995). Till matrix major oxide geochemistry and clast lithology were analyzed to constrain local till composition (Stea & Finck, 2001) and general provenance (Broster et al., 1997; Veillette et al., 2005; Trommelen et al., 2013; Rice, 2020). A flowchart (in the **Appendix**) summarizes research steps and results.

2.3.1. Ice Flow Indicator Mapping

The field strategy was to search for ice flow indicators on outcrops that were accessible from the regional highway, which produced a North-to-South running transect of the study area, as well as from a few additional sites on secondary roads and accessible powerlines. Measured features include small-scale indicators such as striations, grooves, chatter marks, crescentic gouges, lunate fractures, polishing, plucking, and outcrop-scale landforms such as *roches moutonnées*. These features are bedrock's main glacial erosional indicators identified and described across the Abitibi (Veillette et al., 2003). Relative chronology of ice flow phases was determined where possible based on stoss-lee and crosscutting relationships using established methods detailed in several publications (Klassen & Bolduc, 1984; Lundqvist, 1990; Parent et al., 1995; Veillette and Roy, 1999; Rea et al. 2000; Veillette, 2004b; Paulen et al., 2013; Rice et al. 2019). Oriented ice flow indicator measurements within the study area are displayed using QGIS (QGIS Development Team, 2020). The abundance and orientation of measurements for new and legacy data are shown on rose diagrams, which were created in Python 3 (Van Rossum & Drake, 2009) using Pandas (McKinney, 2010), Numpy (Harris et al., 2020), Matplotlib (Hunter, 2007), Mplstereonet (Kington, 2020), and Seaborn (Waskom et al., 2014).

Additionally, strike and dip measurements were collected for imbricated platy clasts within an esker deposit and plotted as great circles and poles to planes on an equal area stereonet (Allmendinger et al., 2012) to constrain the direction of subglacial meltwater flow at that location. Density contours around

the poles were produced using a modified Kamb method with exponential smoothing (Vollmer, 1995). The plunge and bearing of each pole were found and used to calculate the orientation tensors for the plunge, azimuth, and normalized eigenvalues. The normalized eigenvalues were used to calculate the elongation index, isotropy index, and residual value. Then, the plunge and bearing of the V1 pole were calculated and a ternary diagram was used to characterize the fabric (i.e. isotropic vs. girdle vs. cluster). The V1 pole was plotted against all poles and the density contours. The V1 pole was converted to its corresponding planar surface (semi-circle on the stereonet), and both were then plotted against all clast AB-planes. All Jupyter notebooks are available in the **Appendix**.

2.3.2. Surficial Sediment Sampling & Characterization

Potential surficial sample sites were identified by using a regional surficial geology map (Veillette, 2004a). Till is discontinuous and is also partially covered by younger sediments. Surficial till samples thus had to be collected from every accessible surficial till patch to minimize the clustering of sample locations. No suitable surficial till sampling sites were found north of Malartic, which would have provided useful data to establish background composition up-ice of the deposit; however, good sites were found away laterally from the main predicted dispersal area and should provide useful background compositional data.

During sampling, till material was identified for sampling based on the presence of glacially polished, striated, and faceted (i.e. "iron-shaped") clasts (Evans & Benn, 2004) in stiff, poorly-sorted material. Whenever possible, till was sampled from below the B horizon (in the B/C or C horizon) to decrease the likelihood of post-depositional reworking and leaching (**Figure 2.1**) (Hirvas & Nenonen, 1990; McMartin & Campbell, 2007). The C horizon was accessed by excavating a small section using a clean, non-painted shovel. A clean plastic shovel was then used to sample the till, which helps minimize potential issues for till matrix geochemistry. The degrees of oxidation in till samples were characterized as "Unapparent," "Slight," or "High" based on sample colour in field photos and notes (**Figure 2.1 a** to **c**). In contrast, glaciolacustrine sediment material was light grey, clast-poor, and typically laminated (rhythmites); it was encountered regularly during attempts to recover till in areas of discontinuous till coverage (**Figure 2.1d**), where it commonly underlies postglacial organic matter.

Glaciofluvial material was identified based on sorted, rounded, imbricated clasts with minimal fines within the cores of diagnostic yet subdued, esker landforms (Veillette, 2005). These esker sediments record varying past depositional regimes and modern sedimentological processes that demark their outer boundaries (**Figure 2.2 a** and **b**). Samples of finer gravelly sand facies were selected for indicator mineral analysis, while coarser pebble-rich facies were selected for hyperspectral imaging analysis. Strike and dip of imbricated esker gravel clasts were measured with a compass.

Elevation data was extracted by unit type from a digital elevation model of the study area using QGIS (QGIS Development Team, 2020) to better characterize the surficial units. Then, histograms were created in Python to explore the distribution of unit type by surficial area and their relationship to elevation.

2.3.3. Particle Size Distribution

Surficial samples were first air-dried in an oven at 60ºC for 24 to 48 hours. Once dry, samples were poured through an open-bin riffle splitter, and ¼ of each sample was archived. Samples were dry-sieved by hand using standard sieves and then with a shaker table (**Figure 2.2c**) to produce various size fractions for subsequent analyses (see flowchart in **Appendix**). The sieved fractions were weighed to a precision of ±0.01g and bagged separately (**Figure 2.2d**).

A subsection of till samples regularly spaced throughout the study area underwent a more detailed grain size analysis. Cumulative weight percent values for dry sieve data were calculated by normalizing the weight of each fraction by the total weight of that sample and converting it to a weight percent value and then to a cumulative weight percent value. All samples had a recorded measurement at the 2 mm grain size boundary, so the distribution of the measurements at that boundary was used to categorize relative sample texture. Samples within the first quartile (including the boundary) were called "fine," those within the interquartile range were called "medium," and those within the last quartile (including the boundary) were called "coarse." The spatial distribution of the subsection of samples was investigated using QGIS (QGIS Development Team, 2020). Gradistat software (Blott & Pye, 2001) was used to characterize sample type by textural group.

The grain size distribution of the <63 µm silt and clay fraction was analyzed with laser diffraction particle sizing and was performed using a Fritsch Analysette 22 laser diffractometer (Lavallab, 2020) on the same subsection of till samples. The instrument software measures particle size frequency and presents results by particle size intervals, each defined by low, mid, and high size values in µm. The mid-size values of each interval were chosen for plotting and analyzing particle size distribution. A value of 72 µm was used as the maximum grain size diameter boundary to account for the fact that the preceding sieving technique measures the intermediate (*b* axis) of grains (because elongated particles can pass through the mesh in their elongated orientation) whereas the laser technique measures diffraction patterns created by randomly oriented suspended fine particles in motion as they pass through a laser beam; therefore, laser results for the <63 µm dry sieved fraction of samples may show >63 µm sized particles. The laser diffractometer generated cumulative frequency data. Laser diffraction particle sizing data was also collected for all Pionjar (i.e., portable, hand-held drill) till samples (all data for samples from 2015 were collected by Taves (2015)).

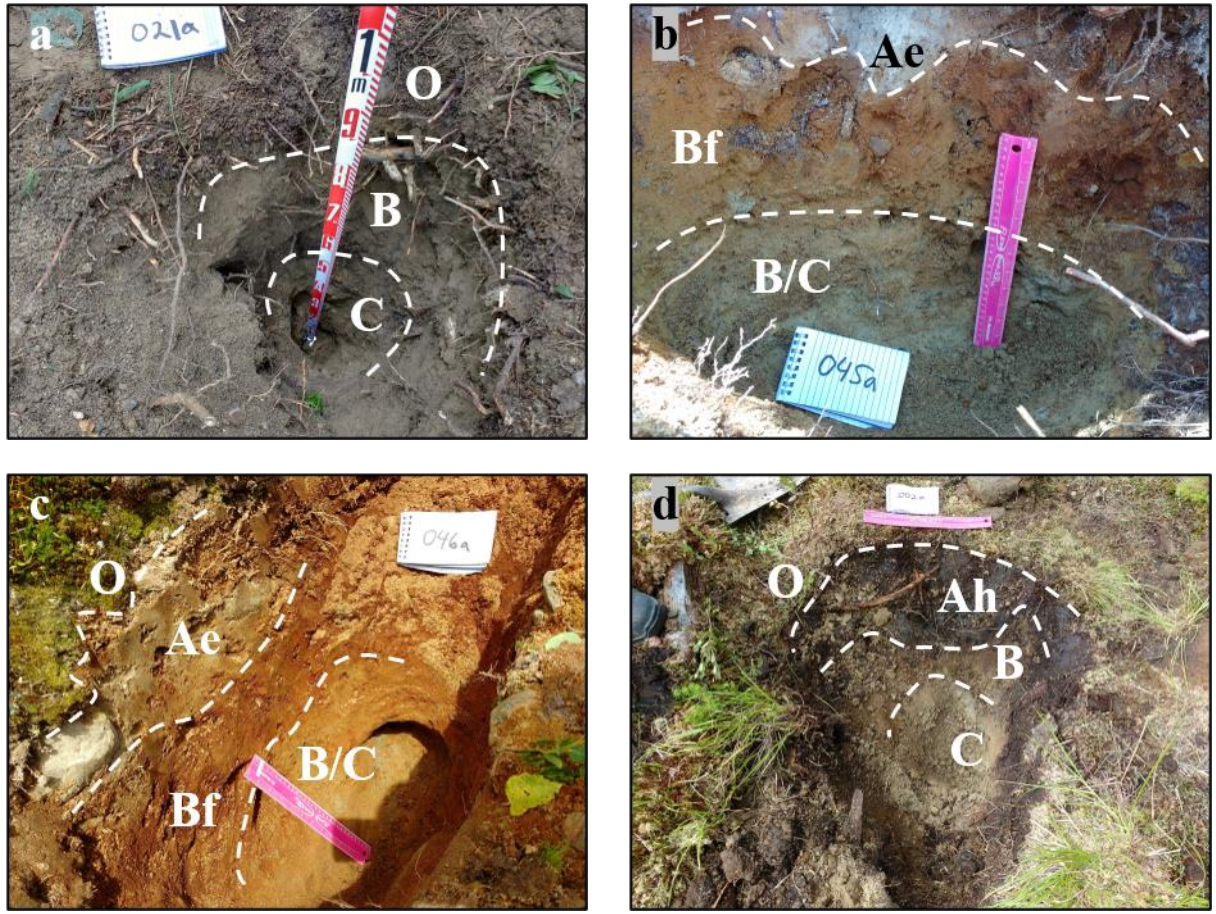

Figure 2.1 Examples of sample sites and their soil horizons (Soil Classification Working Group, 1998). (a) is from site CT-021a and shows a till with an unapparent degree of oxidation. (b) is from site CT-045a and shows a slightly oxidized till. (c) is from site CT-046a and shows a more oxidized till. (d) is from site CT-002a and shows glaciolacustrine mud in an area mapped as discontinuous till coverage (Veillette, 2004a).

Abbr: Ae – topsoil eluviated in clay/Fe/Al/organics, Ah – topsoil enriched with organic matter, B – subsoil, Bf – subsoil enriched with amorphous Fe/Al/organics, C – parent material, O – organic layer.

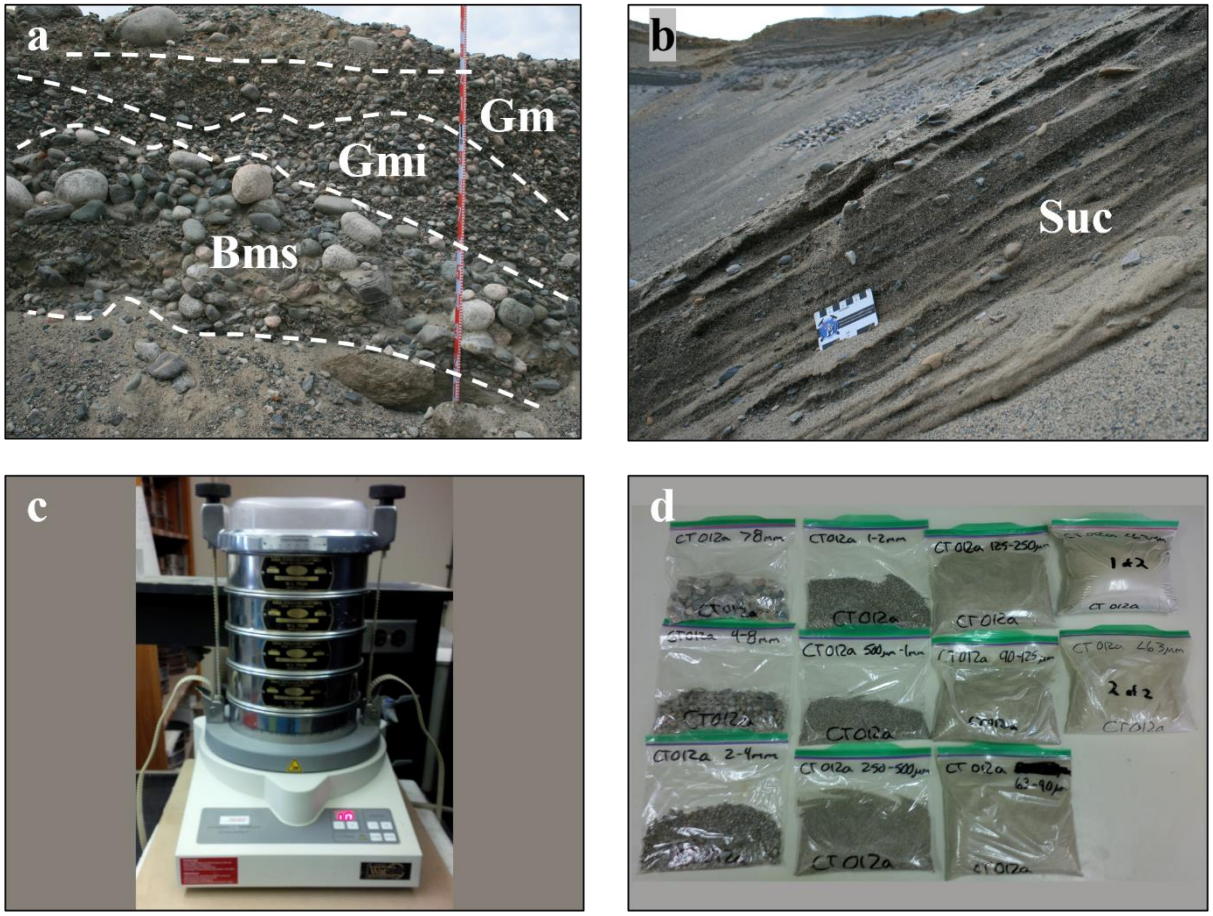

Figure 2.2 Glaciofluvial (esker) deposits in the Malartic study area and preliminary sediment sample processing. (a) is from site CT-013 and shows a cross-section of esker deposits within a sand and gravel pit. The clast-supported gravel facies were selected for imbrication measurements to determine the paleocurrent direction of subglacial water flow. Average clast size varies between units, as does the proportion of matrix material, which indicates varying depositional conditions (i.e., larger clast sizes indicate more energetic flow regimes). The white dashed lines trace unit boundaries. (b) is from site CT-015 and shows modern grain flow laminations with reverse-graded bedding caused by grains avalanching down the gravel pit slopes, which mark the outer boundary of the core esker deposits. (c) A stack of sieves separates till sediment by grain size on a mechanical shaker. (d) Final grain size fractions of till sample CT-012a.

Facies codes: Bms – matrix-supported (massive) boulders; Gm – clast-supported, massive gravel; Gmi – clast-supported, massive (imbricated) gravel; Suc – upward coarsening sand.

2.3.4. Till Matrix Major Oxide Geochemistry

Following Shilts (1996), the influence of geochemical partitioning was assessed by using <2 µm in grain size diameter as the boundary between silt and clay particles (as opposed to <4 µm diameter as defined by Wentworth (1922)). The silt-to-clay ratio was calculated using collected laser diffraction data by finding the ratio of total silt frequency to total clay frequency, and the range of values was inspected with a box plot to assess the variation in clay content.

Till matrix geochemical data collection was performed at the Saskatchewan Research Council Geoanalytical Laboratory in 2015 and 2016 with the 'ICPMS1 Sandstone Exploration Package' (https://www.src.sk.ca/sites/default/files/files/resource/SRC_Geoanalytical_Services_Schedule_Nov20.pdf). The ICPMS1 package was chosen for multi-element analysis because 'sandstone' better approximates the metamorphosed Pontiac greywackes and associated till, which dominate the study area, as opposed to the alternative 'Basement' package, which is better suited for mafic or felsic igneous rocks.

Till matrix (<0.063 mm) was separated and analyzed for major oxide compounds by Inductively Coupled Plasma – Optical Emission Spectroscopy (ICP-OES) following total digestion. Total digestion was achieved by heating the pulp in ultrapure $HF/HNO_3/HClO_4$ until dry and then dissolving the residue in dilute ultrapure HNO_3.

Quality assurance and quality control (QA/QC) were conducted following Piercey (2014) (see **Appendix**). Major oxide data from till samples were investigated using Python 3 (Van Rossum & Drake, 2009) with Pandas (McKinney, 2010), Seaborn (Waskom et al., 2014), and Matplotlib (Hunter, 2007). Till matrix composition was constrained with summary statistics and boxplots. Lithogeochemical values (Perrouty et al., 2019; Gaillard et al., 2020) for felsic rocks, metasedimentary rocks, and mafic dykes (unaltered, altered, and mineralized in each case) within the study area were used to guide the interpretation of surficial major oxide geochemical results. Principal component analysis (PCA) was used for dimensionality reduction, in concert with k-means clustering as an unsupervised classification technique (Grunsky, 2010; Wang, 2018), to investigate till matrix compositional variations, excluding MnO (to explore 8 major oxide variables with 72 samples) by using SciPy (Virtanen et al., 2020) and scikit-learn (Pedregosa et al., 2011). The spatial distribution of k-means clusters was mapped using QGIS (QGIS Development Team, 2020).

2.3.5. Glacial Clast Lithology

Pebble counts were completed on randomly selected clasts per sample by mixing 4-8 mm clasts, quartering the mixture, and selecting the nearest 200 clasts by hand (Rice, 2020). Randomly selected clasts from the >8 mm fraction were added if needed to reach 200 total clasts. Clasts were sorted based on visual inspection with a hand lens and a binary microscope. Clasts were sorted into the categories "quartz fragments," "meta-sedimentary clasts," and "intrusive clasts" (subdivided into "Felsic," "Intermediate," and "Mafic").

QA/QC was completed using a scatterplot to assess the precision of field duplicates from 2016 (including samples from different depths at the same site) and shows that pebble counts are precise to within 10% (**Appendix**).

Clasts from surficial till samples from 2015 were sorted by Taves (2015). Slightly different sorting schemes were applied (Taves used a "miscellaneous" category); therefore, the counts from 2015 were normalized by setting matching categories ("intrusive clasts," "meta-sedimentary clasts," and "quartz fragments") to 100% (see **Appendix** for normalized counts and photos of sorted samples). The abundance and distribution of clasts by category were plotted as proportional dot diagrams using QGIS (QGIS Development Team, 2020).

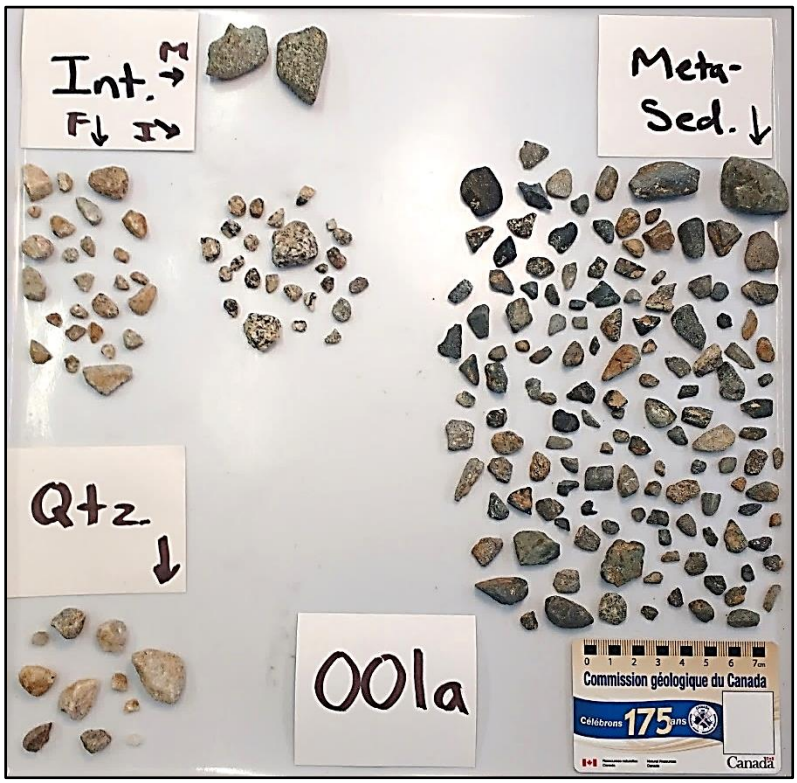

Figure 2.3 Classification of 200 surficial till clasts (4-8, >8 mm) by lithology for sample 001a.
Abbr: F – felsic, I – intermediate, Int – intrusive, M – mafic, Meta-sed – metasedimentary, Qtz – quartz fragment.

2.4. Results and Interpretation

Table 2.1 summarizes ice flow indicator measurements and surficial sample details collected during the two field seasons. **Figure 2.4** presents all data collection sites from both field seasons.

Due to limited till coverage in the study area, most samples were taken south-southwest of the Canadian Malartic Mine, which introduced a spatial bias in the sampling; however, it was considered reasonable for the study to proceed because the general south-southwest direction is one of the recognized regional down-ice directions (Veillette, 1986; Veillette, 2004a) and was expected to be an important dispersal area. It was also considered reasonable to use samples that were collected at a lateral distance away from the main predicted dispersal area to determine background compositional data levels.

Table 2.1 Summary of collected field measurements and samples.

Measurement/ Sample Type	# of Measurements/ Samples	Dry Sample Weight (kg)	Sample Depth Start (m)
2016			
Ice Flow Indicator	42	-	-
Esker Clast Fabric	50	-	-
Surficial Till	40	1.4 - 5.1 ($\bar{x}$ = 3.0)	0.1 – 0.8 ($\bar{x}$ = 0.40)
Surficial Esker	6	2.1 – 7.1 ($\bar{x}$ = 5.3)	-
2015[a]			
Surficial Till	18	8.8 - 15.5 ($\bar{x}$ = 12.6)	0.28 – 0.95 ($\bar{x}$ = 0.44)
Surficial Esker	4	8.9 – 9.7 ($\bar{x}$ = 9.3)	-
Portable Drill Till	14	-	1.34 – 13.10 ($\bar{x}$ = 4.69)

[a]Collected by Taves (2015)

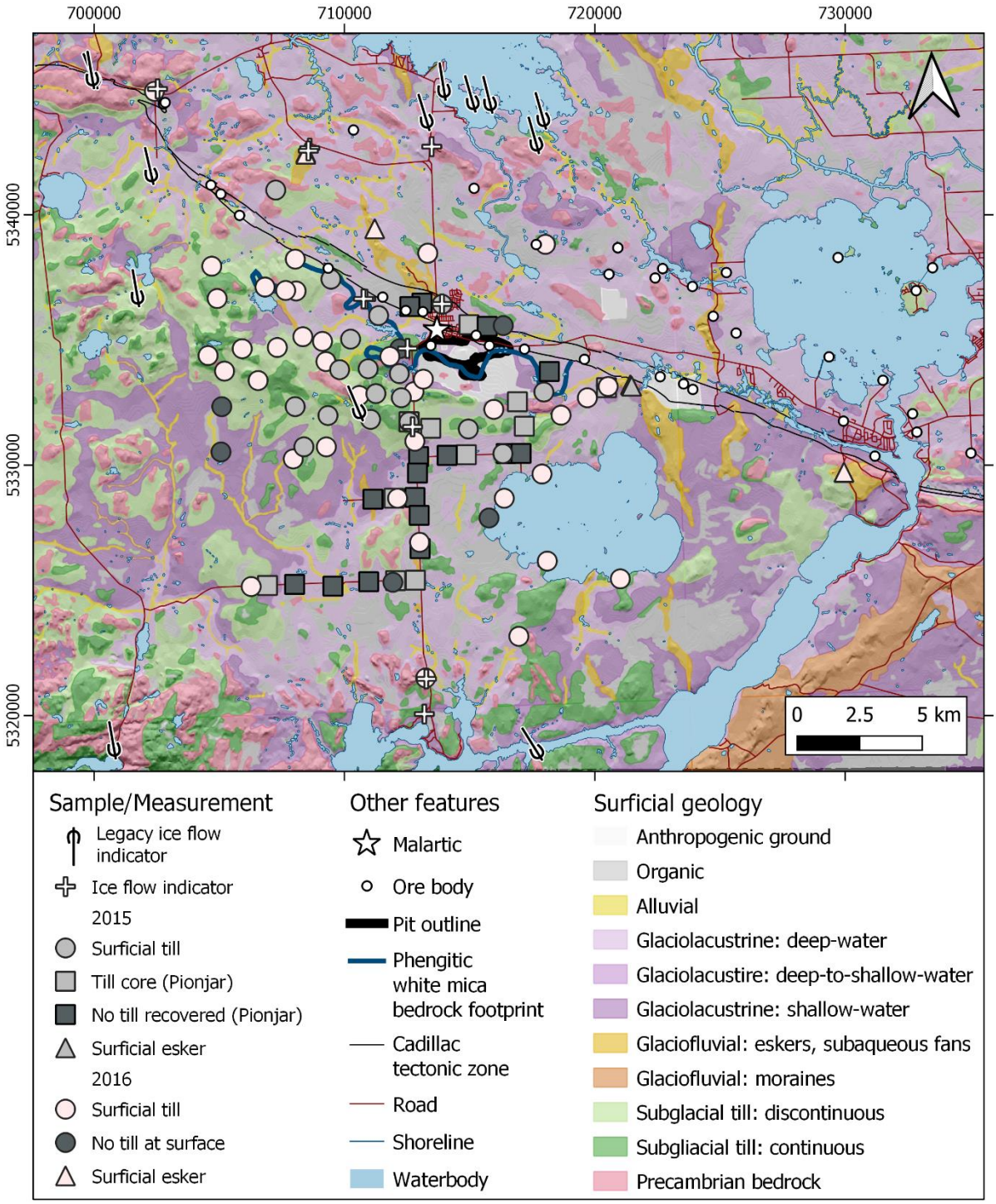

Figure 2.4 Distribution of all data collection stations in the study area around the Canadian Malartic Mine on surficial geology and a hillshade elevation model. Samples from 2015 are from Taves (2015). The simplified surficial geology map was generated using data from the GSC MITE project (Bonham-Carter, 2005). The gold pit outline and phengitic white mica bedrock footprint are after Lypaczewski et al. (2019). Waterbodies and hillshade are from Natural Resources Canada (https://maps.canada.ca/czs/index-en.html). Legacy ice flow indicators, ore bodies, Cadillac tectonic zone, roads, and shorelines are from SIGEOM (https://sigeom.mines.gouv.qc.ca/signet/classes/I1108_afchCarteIntr). Coordinate system: NAD 83, UTM zone 17N.

2.4.1. Local Ice & Subglacial Water Flow Directions

Forty-two erosional ice flow indicators and their orientations were noted at twelve stations; **Figure 2.5** shows field examples, and **Table 2.2** summarizes all ice flow indicator measurements. Feature orientations range from 148º to 213º, and there is evidence of two distinct flow phases at three sites where it was possible to establish relative chronology. In each case where more than one phase was apparent, the flow of the older phase was westward of that of the younger phase.

Details regarding observed relative chronology at three sites are presented herein. At site 16-CT-014, younger striations, chatter marks, and gouges ($\bar{x}$ = 173º) dominate a polished outcrop; however, careful examination revealed older instances of chatter marks ($\bar{x}$ = 190º) that were overprinted and crosscut by the younger indicators on the same surface (**Figure 2.5a**). At site 16-CT-016, two generations of striations were identified on a single surface, with abundant examples in the younger generation ($\bar{x}$ = 170º) and rare examples in the older generation ($\bar{x}$ = 190º). At site 16-CT-024, younger striations and friction cracks ($\bar{x}$ = 158º) were identified on an older, glacially-sculpted quartz outcrop that had deep crescentic gouges and a lunate fracture ($\bar{x}$ = 166º) (**Figure 2.5b**). It follows that an older flow shapes an outcrop, and then a younger flow overprints that outcrop (Lundqvist, 1990).

Figure 2.6 shows rose diagrams with collected azimuthal measurements by feature category. Small-scale features are oriented from ~190º to ~160º, with most oriented ~170º (**Figure 2.6a)**. Landform-scale features are oriented from ~210º to ~150º with most oriented ~170º (**Figure 2.6b).** **Figure 2.7** shows rose diagrams for legacy data (**Figure 2.7a**) and all available data within the study area (**Figure 2.7b**). Legacy features are oriented from ~180º to ~150º, with most oriented from ~170º to ~160º (**Figure 2.7a**). All features combined are oriented from ~210º to ~150º, with most oriented ~170º (**Figure 2.7b**).

Figure 2.8 shows esker clast fabric poles, the V1 of the poles, and density contours that demonstrate a pronounced cluster of orientations. Esker clast fabric results indicate a unidirectional subglacial paleocurrent towards 116º at this location. Typically, this analysis done on esker clast fabric is used for till fabric data, and it would have been more useful to collect several sets of data along a vertical profile of the esker to investigate potential paleocurrent shifting. Still, these results have been included to demonstrate a general paleocurrent orientation. **Figure 2.9** presents all results in their spatial context within the study area.

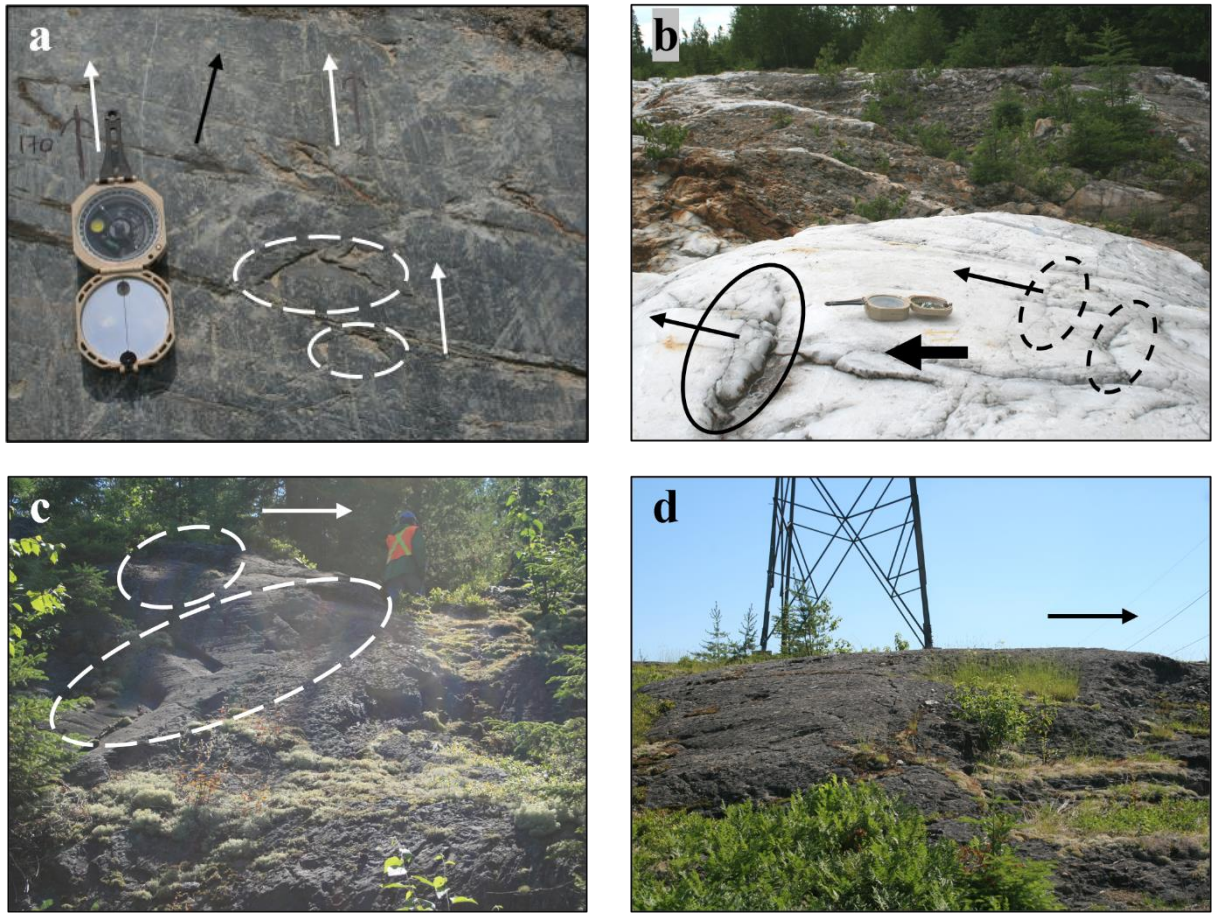

Figure 2.5 Various ice flow indicators throughout the Malartic study area. (a) Site CT-014 shows evidence of two ice flow phases. Younger striations and chatter marks (black marker in the field; white arrows), and crescentic gouges (within white dashed ovals), with a direction of 170º, dominate the meta-sedimentary bedrock surface and crosscut older chatter marks (~190º, black arrow). (b) Site CT-024 shows evidence of two ice flow phases. Younger striations (buff arrow in the field, emphasized by bold black arrow, 158º) occur on glacially shaped quartz that is marked with older (~166º, black arrows) crescentic gouges (within black dashed ovals) and a lunate fracture (within black oval). Note preferential erosion of dark host bedrock compared to light quartz veins in the background. (c) Site CT-030 shows large crescentic gouges (within white dashed ovals), plucking (down-ice) and the general direction of ice flow (171º, white arrow). (d) Site CT-032 showing a *roche moutonnée* landform. The position of the smooth, polished (up-ice) stoss side relative to the rough, plucked (down-ice) lee side indicates the ice flow direction from left to right (~172º, black arrow).

Table 2.2 Summary of ice flow indicator measurements. PCS: NAD 1983, UTM Zone 17N.

Station ID	X	Y	Indicators & Directional Criteria[ab]	Azimuth Measurements (º)[ac]
16-CT-014	708613	5342665	1. *Chatter marks* 2. Striations, *chatter marks, gouges*	1. 188, 190, 193 ($\bar{x}$ = 190) 2. 168, 173, 170, 180 ($\bar{x}$ = 173)
16-CT-016	708558	5342557	Cross-striations	1. 193, 188, 190 ($\bar{x}$ = 190) 2. 170, 180, 182 ($\bar{x}$ = 177)
16-CT-018	713190	5320062	Grooves	178, 179 ($\bar{x}$ = 179)
16-CT-020	713272	5321465	*Roche moutonnée*	188
16-CT-024	710846	5336635	1. *Chatter marks on quartz vein,lunate fracture, roche moutonnée* 2. Striations, friction cracks	1. 158, 163, 168, 161, 164, 173, 174 ($\bar{x}$ = 166) 2. 158, 158
16-CT-025	710759	5336643	*Roche moutonnée*	213
16-CT-026	712519	5334664	Groove on quartz vein	173
16-CT-027	712721	5331532	Striations	169, 170 ($\bar{x}$ = 170)
16-CT-028	713897	5336441	Friction cracks in quartz veins, grooves, *roche moutonnée*	163, 163, 163
16-CT-030	713486	5342724	Striations, grooves, *cresentic gouges*	171, 171, 171
16-CT-032	702535	5345030	*Roche moutonnée*	148, 168, 173, 170, 170, 175, 180, 190 ($\bar{x}$ = 172)

[a]Relative chronology: 1 – older, 2 – younger.
[b]Directional criteria in *italics*. Measurements for non-directional features represent the orientation of a trend line.
[c]Compass measurements are corrected using a magnetic declination of 12.4º W (Government of Canada, Natural Resources Canada, 2020).

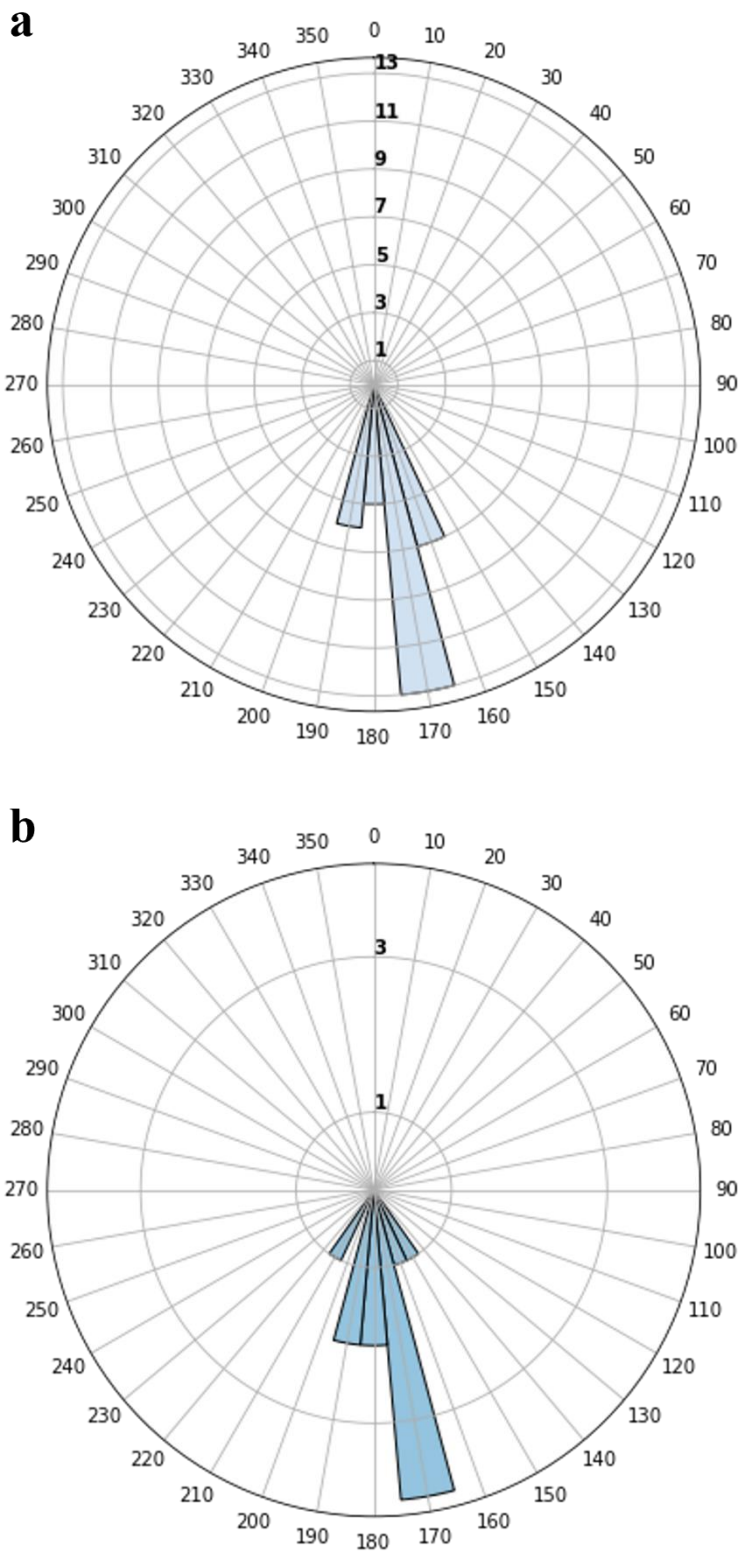

Figure 2.6 Rose diagrams showing the direction (10º bins) and frequency (numbered concentric circles) of mapped ice flow indicator measurements by feature category. (a) shows small-scale measurements such as striations, grooves, crescentic gouges, and friction cracks. (b) shows landform features, i.e., *roches moutonnées*.

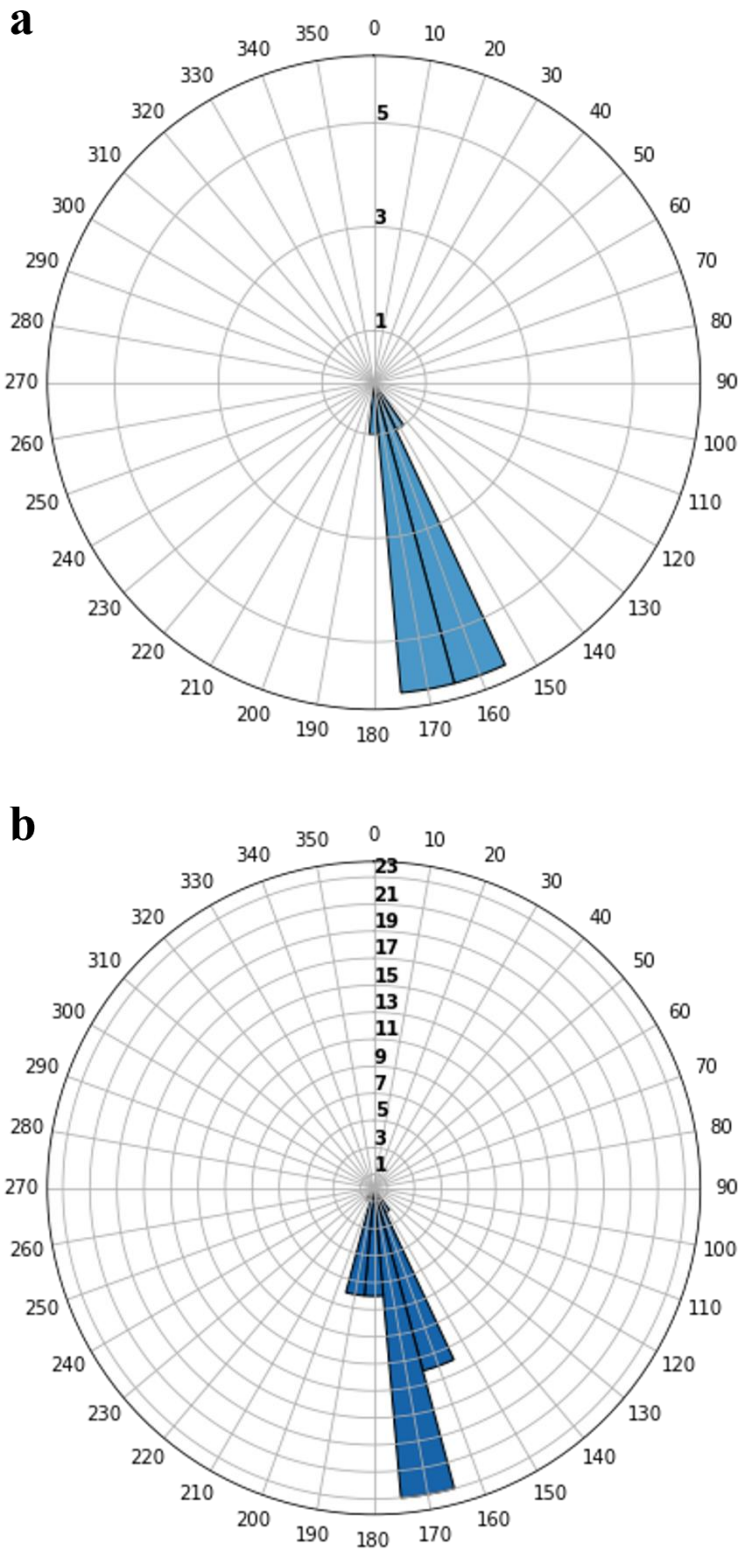

Figure 2.7 Rose diagrams showing the direction (10º bins) and frequency (numbered concentric circles) of mapped ice flow indicator measurements for (a) legacy data from SIGEOM (https://sigeom.mines.gouv.qc.ca/signet/classes/I1108_afchCarteIntr) and (b) all data within the study area.

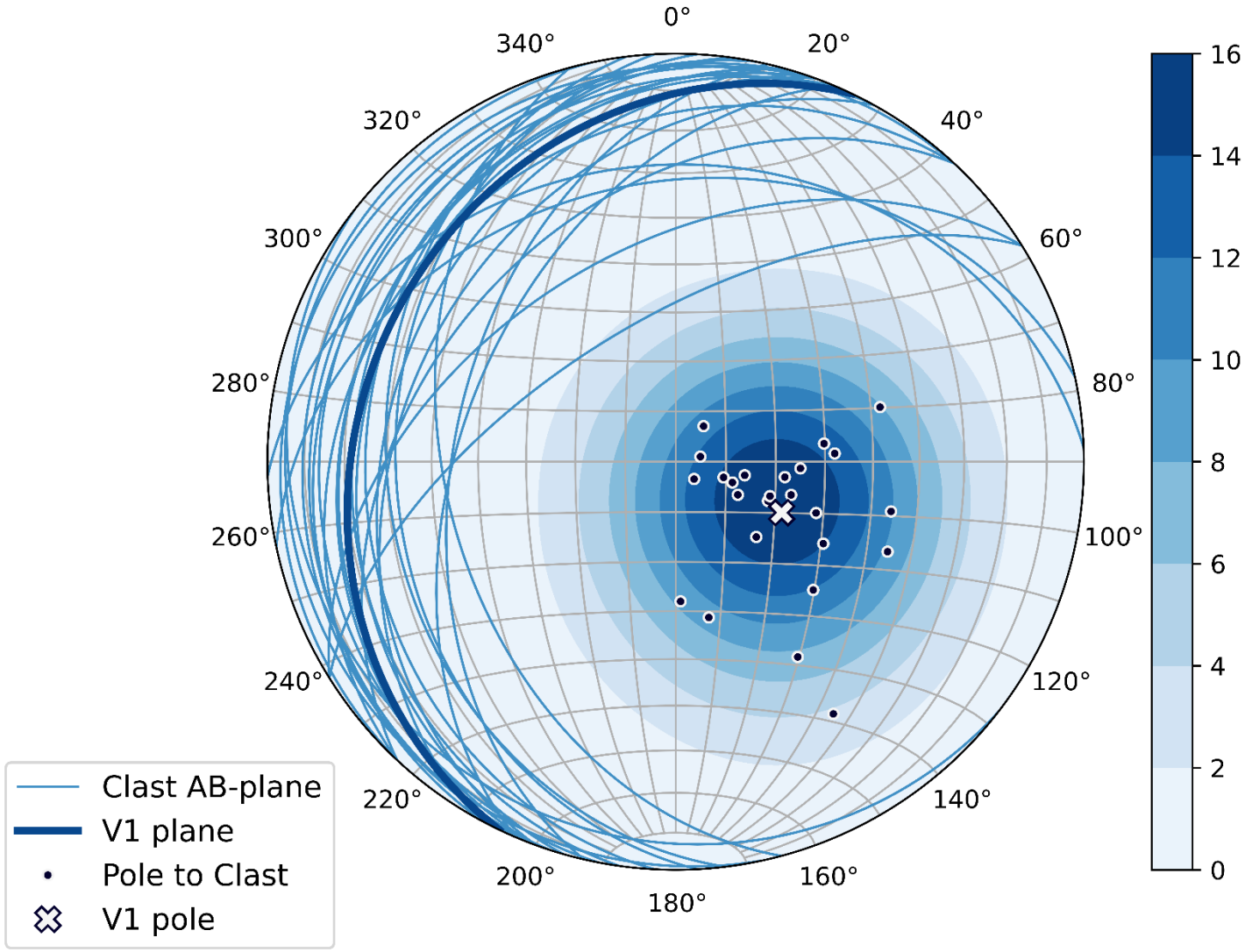

Figure 2.8 Stereonet showing esker clast fabric for site CT-013 with imbricated clast AB-planes (light blue great circles), the V1 plane (dark blue great circle), poles to clast A/B planes (dark blue circles), and the V1 of the poles (white 'x'). The V1 of the poles has a trend of 116°, which indicates a paleocurrent to the SE. Density contours around the poles indicate a pronounced cluster of orientation tensors in the fabric.

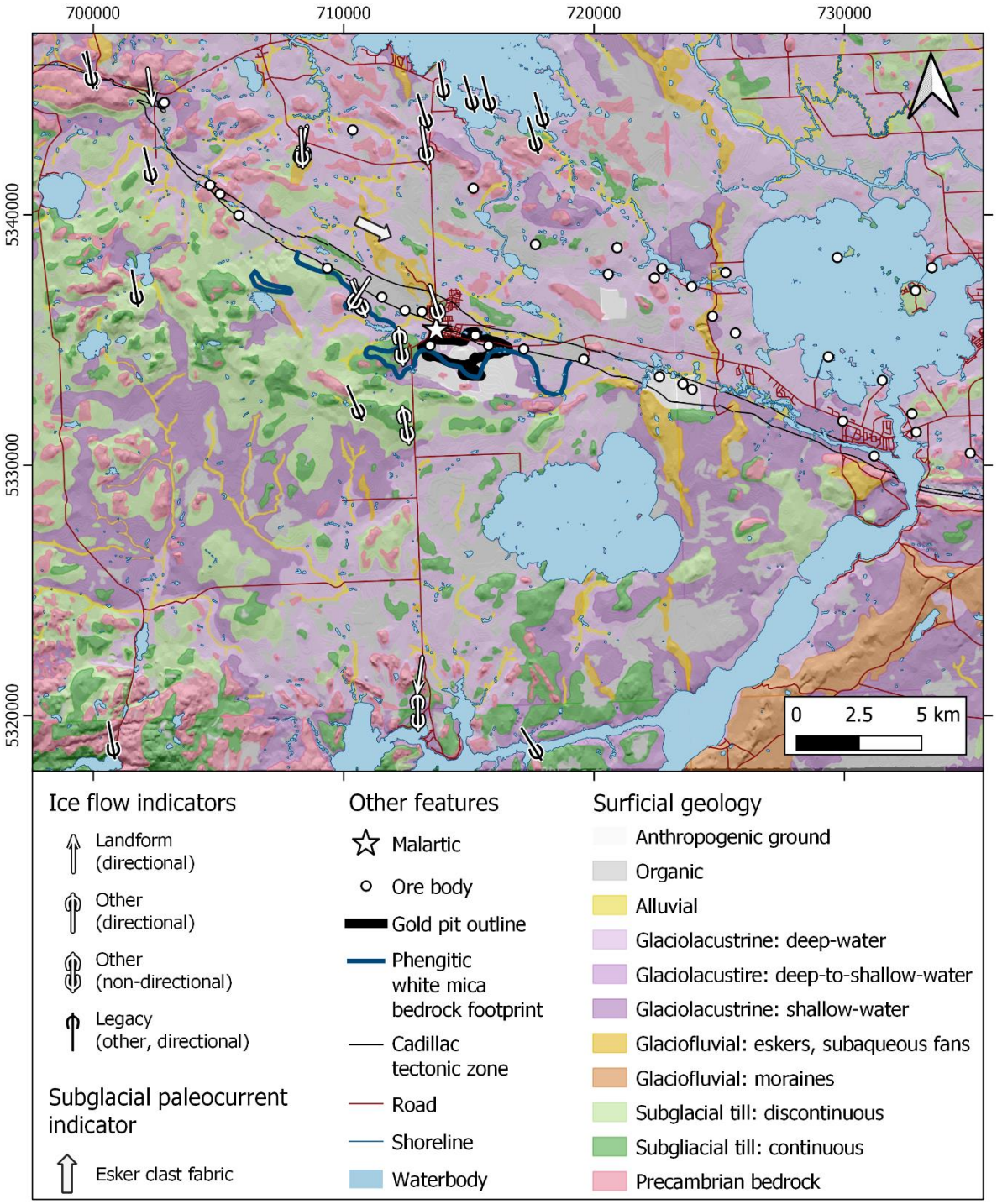

Figure 2.9 Distribution and orientation of measured and legacy ice flow indicators. Each indicator represents the mean flow direction at that observation station. At sites with cross-striations, the 1 and 2 represent older and younger ice flow directions, respectively. The subglacial paleocurrent indicator is for site CT-013. The simplified surficial geology map was generated using data from the GSC MITE project (Bonham-Carter, 2005). The gold pit outline and phengitic white mica bedrock footprint are after Lypaczewski et al. (2019). Waterbodies and hillshade are from Natural Resources Canada (https://maps.canada.ca/czs/index-en.html). Legacy ice flow indicators, ore bodies, Cadillac tectonic zone, roads, and shorelines are from SIGEOM (https://sigeom.mines.gouv.qc.ca/signet/classes/I1108_afchCarteIntr). Coordinate system: NAD 83, UTM zone 17N.

2.4.2. Field Sedimentology

In the field, till in hand-dug pits had a range of colours, from light grey (i.e., no apparent oxidation) to buff or orange colours (i.e., slightly or highly oxidized). The material was generally stiff, possibly overconsolidated, with low and sometimes moderate fissility. As seen in **Figure 2.1**, typical surficial till sample sites in the study area reveal a podzol soil profile, characteristic of soil in permeable material on Canadian shield rocks (Soil Classification Working Group, 1998; McMartin & Campbell, 2007).

Figure 2.10a and **b** show different sedimentary facies from within the core of an esker. **Figure 2.10a** shows a close-up of a lower flow regime, graded sand unit, including slightly deformed ripple cross-laminations, indicating partial post-depositional fluidization (pressurized water moving up) or liquefaction of the fine sand, probably due to rapid sediment loading from the coarse unit above. Soft deformation in the sandy unit produced load/flame structures from water escape and resedimentation. **Figure 2.10b** shows multiple boulder pavements, which decrease in size with successive layers, observed on an esker's flanks.

Taves (2015) observed laminated glaciolacustrine mud directly over bedrock at a site where till was reported in previous data from the Cadillac Project (LaSalle et al., 2005) (**Figure 2.10c** and **d**). Her data highlights 6 locations with no recovered drill till in areas where till samples are recorded in the Cadillac dataset.

Table 2.3 shows summary statistics of elevation (masl) data for surficial units, and **Table 2.4** shows the same for glaciolacustrine and till subunits. The maximum elevation for discontinuous till units occurs at 417 masl, and that for continuous till units occurs at 430 masl.

Figure 2.11 presents the distribution of surficial unit types by abundance and the relative frequency of area based on elevation (~4 m bins). The relative abundance of continuous till units supersedes that of discontinuous till units above the maximum elevation of glaciolacustrine units. The relative frequency of area decreases exponentially with increasing elevation throughout the study area.

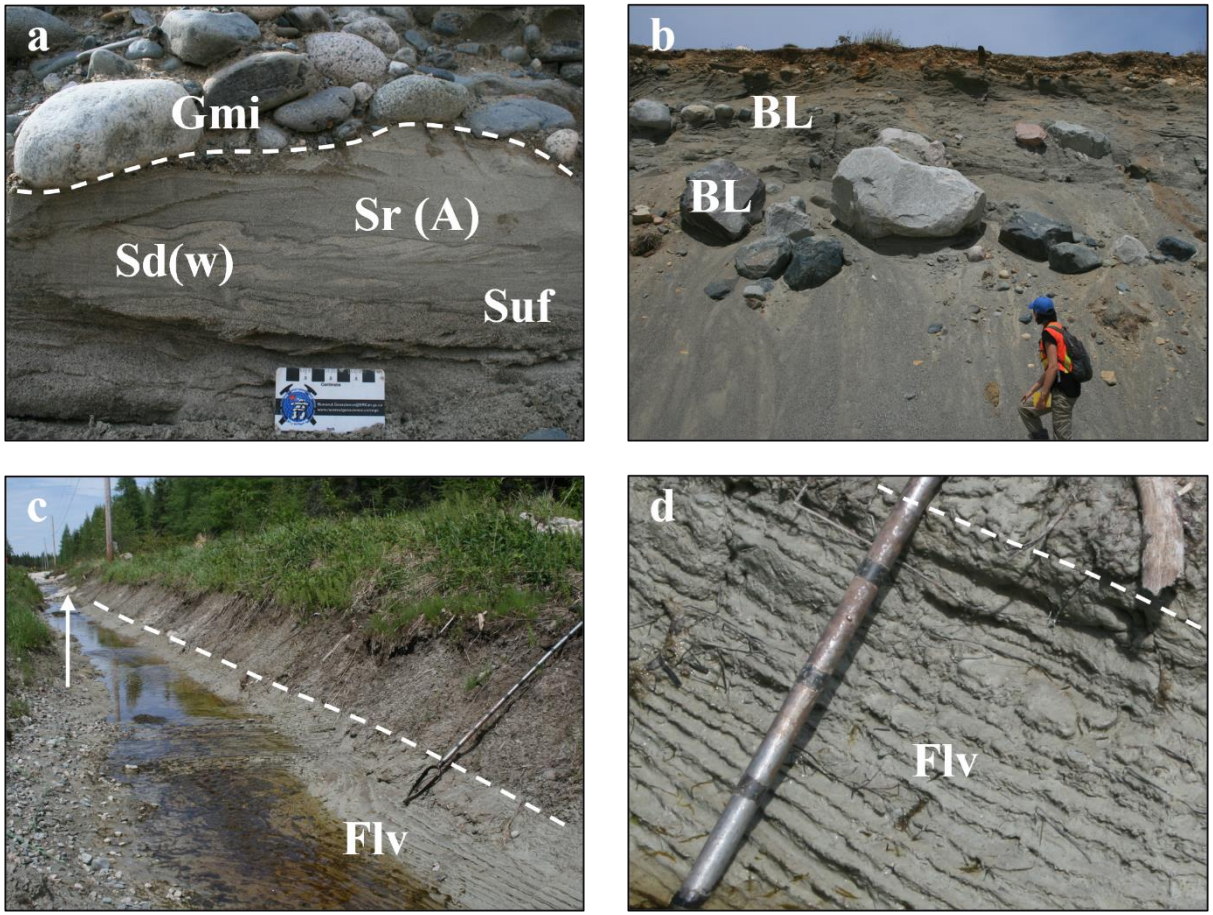

Figure 2.10. Glaciofluvial (esker) deposits in the Malartic study area. (a) is from site CT-013 and shows a close-up of a sand unit with preserved cross-bedding despite soft deformation and dewatering features (load-flame structures). Note the poorly-sorted, imbricated gravel unit on top of the upwards fining sand unit (a white dashed line traces the unit boundary). (b) is from site CT-015 and shows multiple boulder pavements within draping fan sediments. The boulders decrease in average size along a vertical profile, i.e., in subsequent layers. (c) Laminated mud overlying bedrock (white arrow) near the location of Pionjar drill sample DS 20. The presence of till was recorded near this location during the Cadillac Project (LaSalle et al., 2005). The white dashed line separates slumped and layered material. (d) A close-up of varves (i.e. seasonal laminations). The markings on the shaft of the hand auger represent 10 cm increments. Photos (c) and (d) are modified after Taves (2015).

Facies codes: BL – boulder lag or pavement; Flv – fine lamination with varves in silt and clay; Gmi – clast-supported, massive (imbricated) gravel; Sd(w) – deformed bedding with dewatering structures in sand; Sr (A) – ripple cross-laminated (type A) sand, Suf – upward fining sand.

Table 2.3 Summary statistics for elevation (masl) data of surficial units.

Surficial Unit	Glaciolacustrine	Till	Bedrock	Organic	Alluvial	Esker
Relative %	54	20	9	12	3	2
Minimum	286	290	294	291	285	290
Maximum	380	430	429	410	374	360
Range	94	140	135	119	89	70
Mean	310	341	340	314	310	317
Median	308	340	338	310	308	317
Mode	294	340	310	310	300	310
Variance	197	494	649	220	225	116
Standard deviation	14.0	22.2	25.5	14.8	15.0	10.8

Table 2.4 Summary statistics for elevation (masl) data of glaciolacustrine and till sediment subunits.

Surficial Subunit	Glaciolacustrine			Till	
	Deep water	*Deep-to-shallow (transitional) water*	*Shallow water*	*Continuous*	*Discontinuous*
% of main unit	67	2	31	30	70
Minimum	286	294	294	293	290
Maximum	368	326	380	430	417
Range	82	32	86	137	127
Mean	305	301	323	339	341
Median	303	299	322	330	340
Mode	294	296	330	330	340
Variance	91.5	31.3	203	821	351
Standard deviation	9.57	5.60	14.3	28.7	18.7

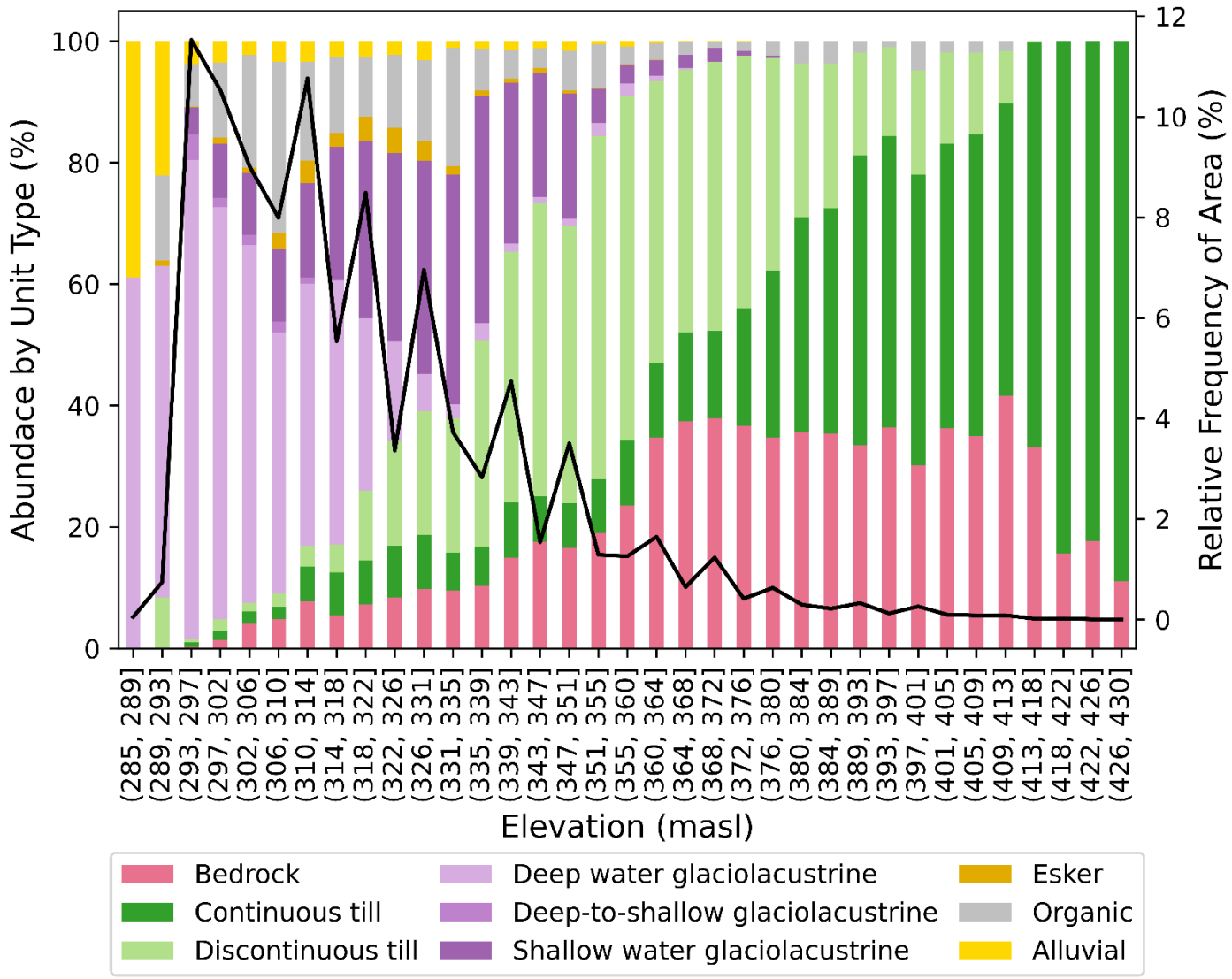

Figure 2.11 Distribution of the abundance of surficial unit types and the relative area frequency based on elevation (~4 m bins). The relative abundance of continuous till units is greater than that of discontinuous till units above the maximum elevation of glaciolacustrine units. Overall, the relative frequency of area decreases exponentially with increasing elevation.

2.4.3. Till Grain Size Distribution & Clay Content

Sieve and laser diffraction results and particle size distribution curves are presented in the **Appendix**. All samples are classified as "fine" (i.e. clast-poor and matrix-rich), "medium" (i.e. wide range), or "coarse" (i.e. clast-rich and matrix-poor) based on the relative cumulative weight percent (wt%) value of their >2 mm grain size fraction. The spatial distribution of the samples used in detailed grain size analysis is presented in **Figure 2.12**. "Coarse" and "medium" samples are usually located closer to glacial lake sediments, while more extensive areas of till generally surround "fine" samples. Exposed bedrock is commonly surrounded by or associated with continuous till, which is then surrounded by discontinuous till or glaciolacustrine sediments.

The till in the study area is variably clast-rich, with 11-50 cumulative wt. % particles >2 mm. It is also relatively sandy with sand wt. % ranging from 36-72. Results indicate all samples are polymodal and "very poorly sorted." **Figure 2.13** classifies samples used in detailed grain size analysis by textural group with a Gravel-Sand-Mud ternary diagram, highlighting relatively high sand and gravel content in all samples. Most samples plot within the "Gravelly Muddy Sand" textural group, and all other samples are proximal to that group; the till in the study area comprises gravelly sand to sandy gravel with smaller amounts of mud grains.

Table 2.5 shows summary statistics of clay (<2 μm) content variation for surficial till samples that were used in detailed grain size analysis as well as of silt-to-clay ratios for the same samples. Silt and clay weight percent values are in the **Appendix**. **Figure 2.14a** and **b** show a box and whiskers plot of clay content variation and that of silt-to-clay ratios, respectively, for surficial till samples that were used in detailed grain size analysis.

The following geochemical results are not normalized by clay content to avoid another level of complexity, which would introduce greater uncertainty to the results. Samples also show varying degrees of oxidation. This postglacial weathering may have a greater impact than clay content variation on the elements associated with labile minerals (e.g., sulfides); however, oxidation promotes the dissolution of labile minerals in the fine sand fraction, and the dissolved metals would then be adsorbed to clay particles. So, even a low clay content might still create anomalies, and no easy remedy exists for these circumstances. Even so, variations in silt-to-clay ratios and visual degree of oxidation may be useful when interpreting geochemical results.

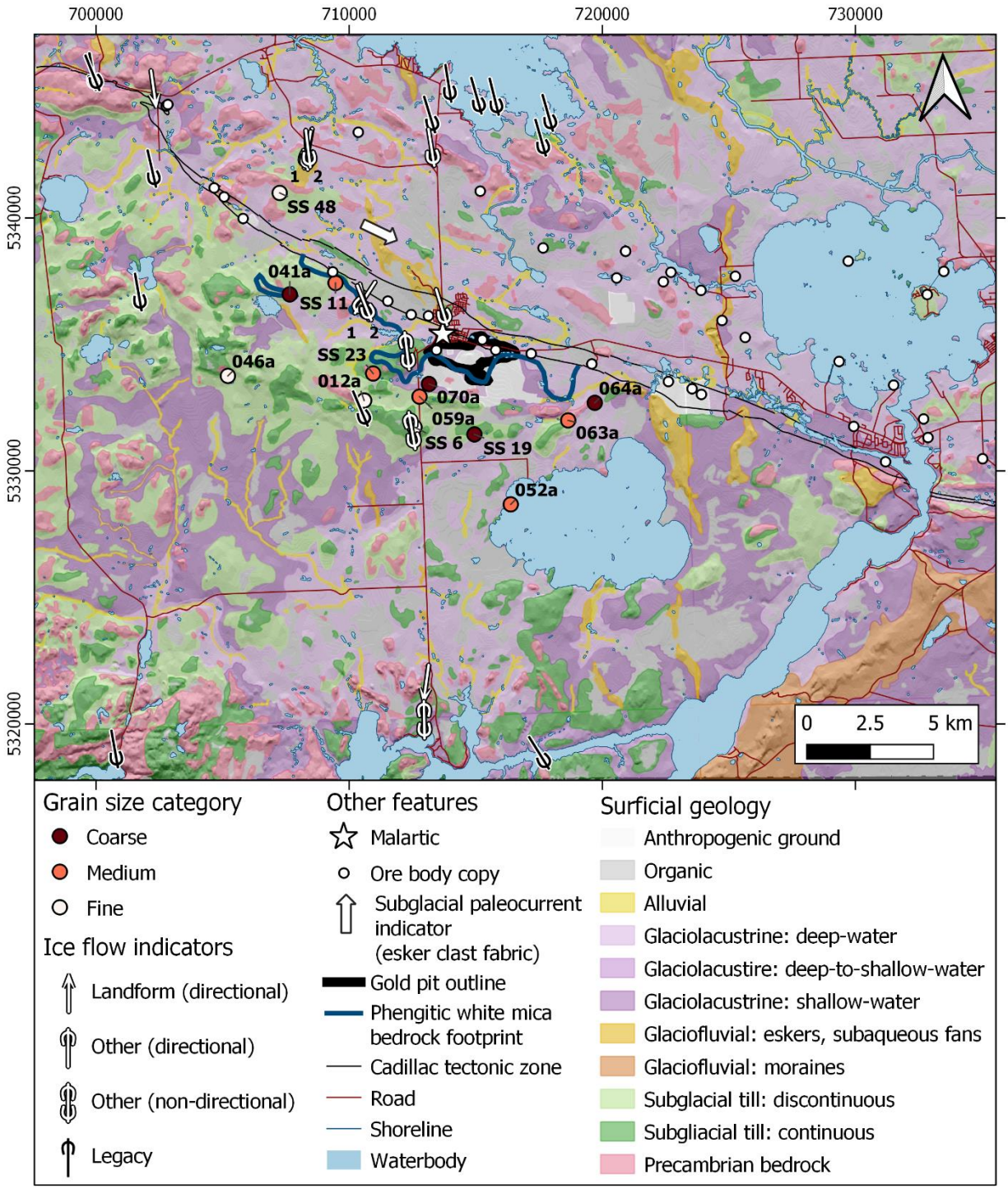

Figure 2.12 Distribution of surficial till samples used in detailed grain size analysis. At sites with cross-striations, the 1 and 2 represent older and younger ice flow directions, respectively. The simplified surficial geology map was generated using data from the GSC MITE project (Bonham-Carter, 2005). The gold pit outline and phengitic white mica bedrock footprint are after Lypaczewski et al. (2019). Waterbodies and hillshade are from Natural Resources Canada (https://maps.canada.ca/czs/index-en.html). Legacy ice flow indicators, ore bodies, Cadillac tectonic zone, roads, and shorelines are from SIGEOM (https://sigeom.mines.gouv.qc.ca/signet/classes/I1108_afchCarteIntr). Coordinate system: NAD 83, UTM zone 17N.

.

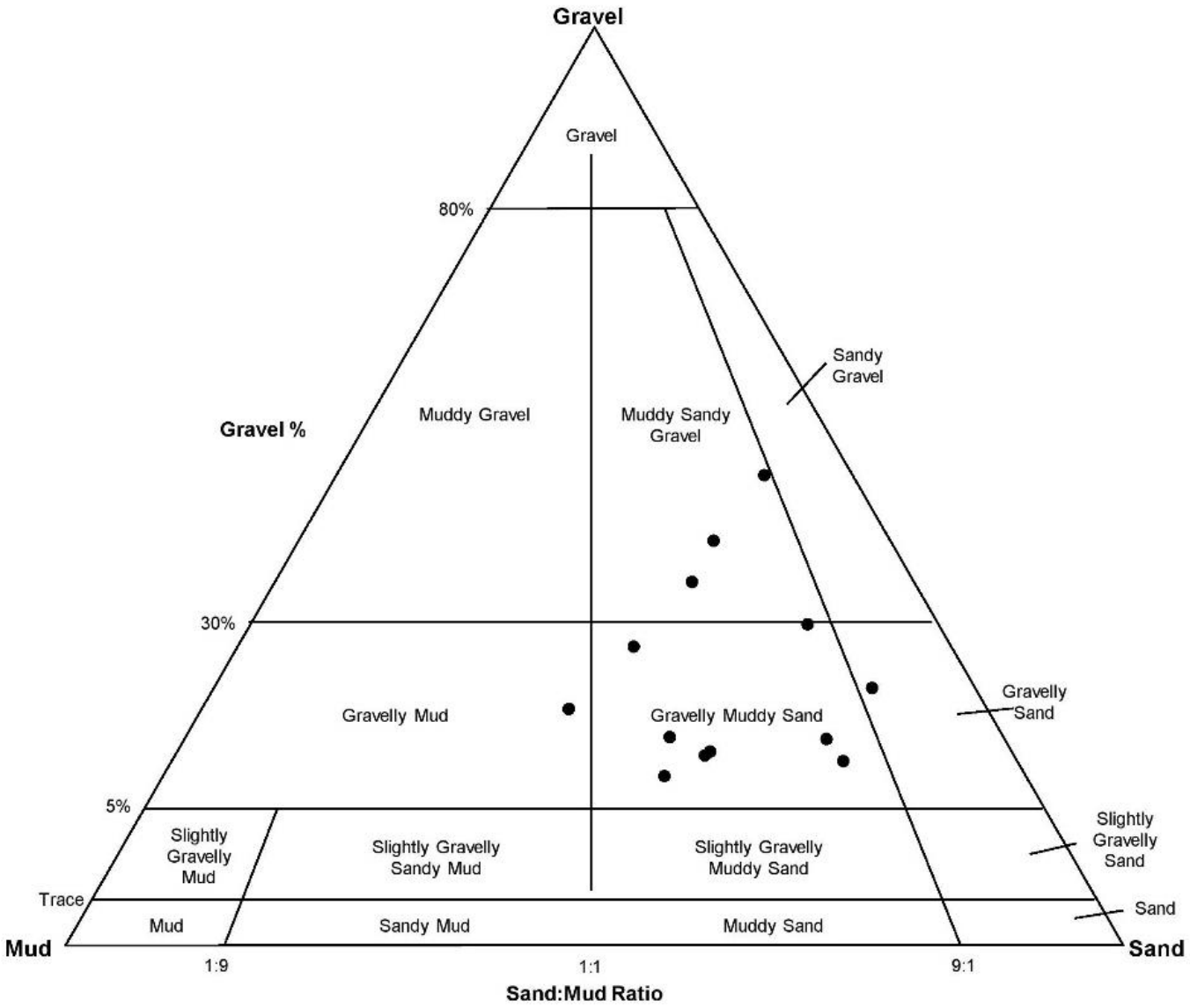

Figure 2.13 Classification of 13 surficial till samples on a Gravel-Sand-Mud ternary diagram, using Gradistat (Blott & Pye, 2001), based on detailed grain size dry sieve data. Most samples are classified as gravelly muddy sand; all other samples are close to this characterization.

Table 2.5 Summary statistics for clay (<2 μm) weight percent and silt-to-clay ratios for till samples that were used in detailed grain size analysis.

	Clay weight percent	**Silt-to-clay ratio**
Count	12	12
Minimum	0.3	10.2
Maximum	3	21.3
Range	2.7	11.1
Mean	1	17.0
Median	1	17.9
Mode	N/a	20.3
Variance	0.8	13.2
Standard deviation	0.9	3.64

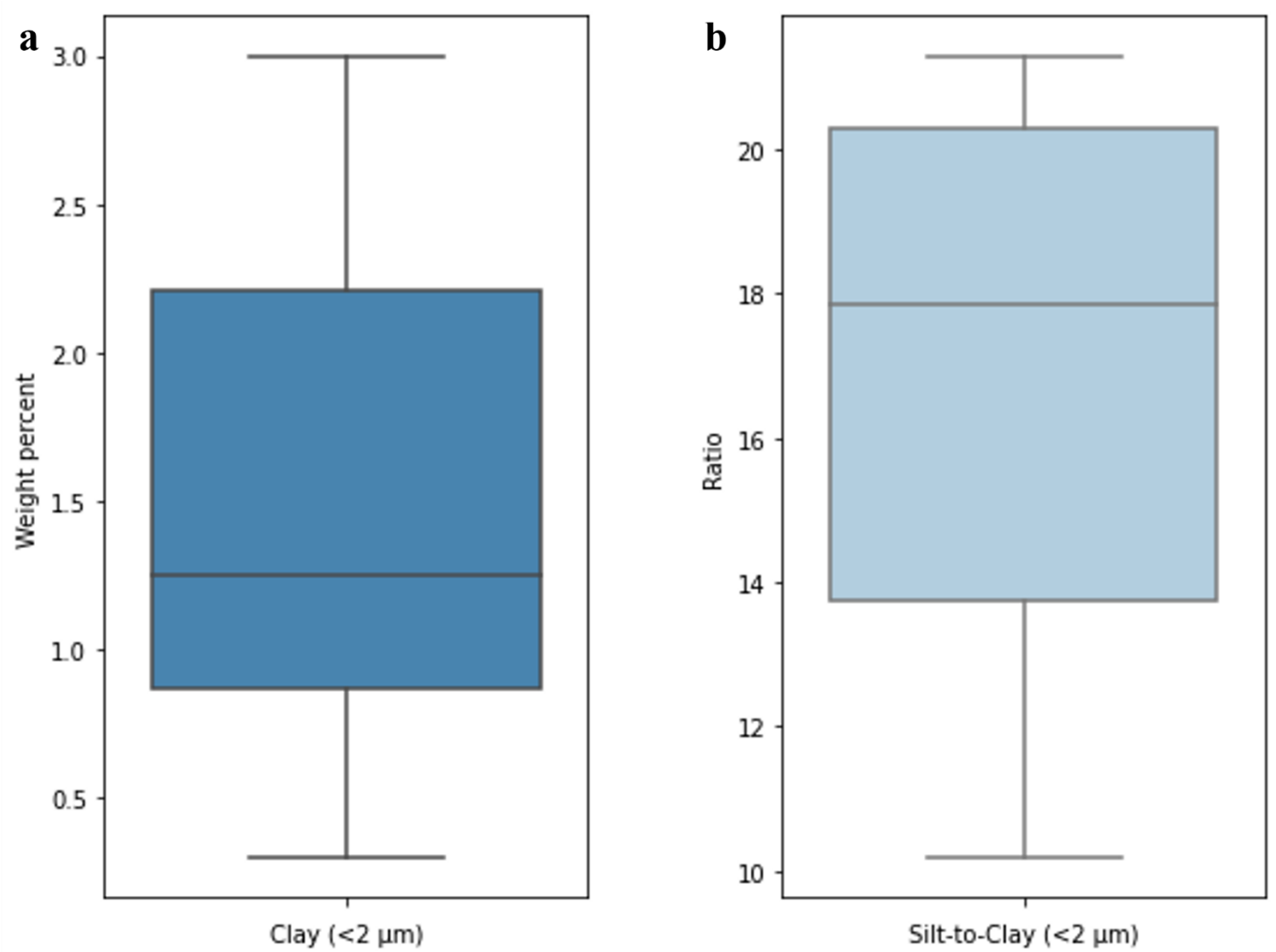

Figure 2.14 Box and whiskers plot showing (a) the range of clay weight percent and (b) the range of silt-to-clay ratios for the 41 till samples that underwent grain size analysis by laser diffractometry.

2.4.4. Till Matrix Major Oxide Geochemistry

Till matrix major oxide analysis was used to investigate the broad composition of till samples and get insights into the main bedrock sources. **Table 2.6** presents the summary statistics for till matrix major oxide geochemical analyses.

Major oxide measurements in surficial samples from both field seasons are consistent with similar medians and largely overlapping interquartile ranges, except for CaO values, which show the largest offset (**Figure 2.15**). Values of the 2016 survey show more spread, which was expected because these samples were collected over 340 km^2 instead of an area of 80 km^2 for the 2015 survey. Major oxide measurements in Pionjar samples are generally consistent with those from surficial samples, except for notable offsets such as relative enrichments in CaO, MgO, MnO, and P_2O_5.

Figure 2.16 presents the distribution of major oxide geochemical values based on the degree of visually apparent oxidation. Visually apparent oxidation is correlated with relative enrichments in Al_2O_3, Fe_2O_3, and depletions in CaO, K_2O, Na_2O, MnO, P_2O_5. MgO and TiO_2 values are the least affected.

Figure 2.17 presents the distribution of major oxide geochemical values based on the underlying bedrock type of the surficial sample. Samples from overtop meta-sedimentary and intrusive bedrock have similar values but contrast those from overtop mafic/ultramafic bedrock. Underlying mafic/ultramafic bedrock is correlated with a relative enrichment in TiO_2, and depletions in Al_2O_3, CaO, Fe_2O_3, MgO, MnO, Na_2O, and P_2O_5.

Figure 2.18 presents the distribution of till matrix major oxide geochemical values. It compares them to lithogeochemical values by bedrock type within the study area (see **Appendix** for summary statistics of lithogeochemical values). Lithogeochemical values represent varying degrees of alteration described as ‘unaltered,’ ‘altered,’ or ‘mineralized.’

The relative abundance of bedrock type in the study area is meta-sedimentary > intrusive > mafic. The relationship between till and bedrock is not straightforward; however, till values fall within bedrock values in each case. Median till values are closest to median meta-sedimentary bedrock values for MgO, Al_2O_3, Na_2O, TiO_2, P_2O_5 and MnO. Median till values are closest to median intrusive bedrock values for Fe_2O_3 and CaO. The median till value closest to the median mafic bedrock value is for K_2O.

Table 2.6 Summary statistics for till matrix major oxide geochemical weight percent values (ICP-OES analysis; n = 72).

	Al_2O_3	CaO	Fe_2O_3[a]	K_2O	MgO	MnO	Na_2O	P_2O_5	TiO_2
Detection limit	0.01	0.01	0.01	0.002	0.001	0.001	0.01	0.002	0.001
Standard Error	0.13	0.07	0.16	0.028	0.069	0.002	0.05	0.008	0.015
Minimum	11.2	1.36	1.45	0.608	0.67	0.026	1.4	0.051	0.448
Maximum	17	4.8	8.52	2.28	3.85	0.118	4.1	0.485	1.2
Range	5.8	3.44	7.07	1.672	3.18	0.092	2.7	0.434	0.752
Mean	14	3.3	4.3	1.31	2.1	0.054	3.5	0.15	0.65
Median	14	3.4	3.9	1.28	2.0	0.053	3.6	0.15	0.63
Mode	14	3.6	3.3	1.26	1.8	0.052	3.5	0.15	0.64
Variance	1.3	0.36	1.8	0.056	0.35	0.0002	0.19	0.005	0.015
Standard Deviation	1.1	0.6	1.4	0.236	0.59	0.014	0.43	0.070	0.12

[a]Fe (total) expressed as Fe_2O_3.

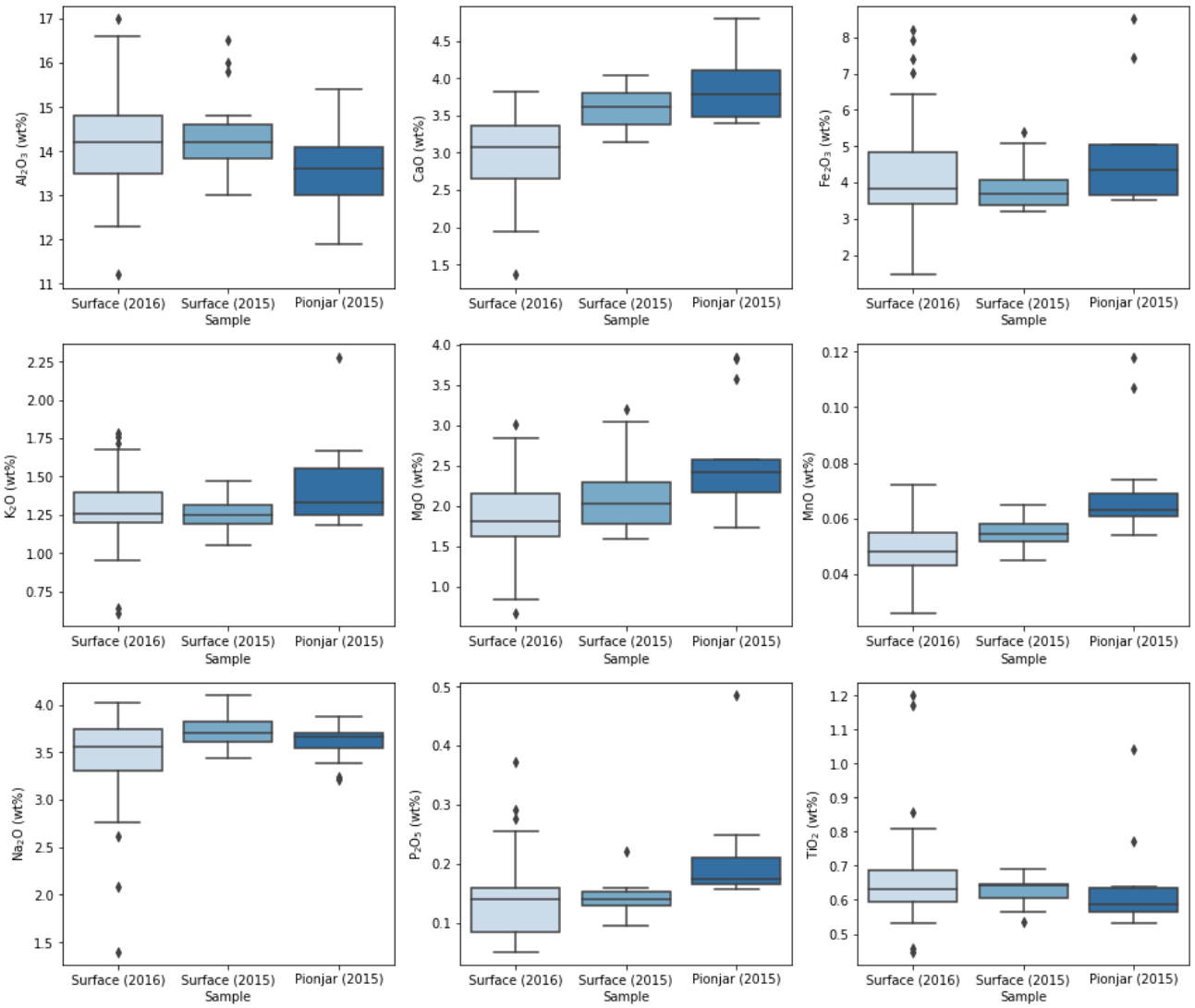

Figure 2.15 Boxplots showing sample year and type for till matrix major oxide weight percent values (ICP-OES analysis). n = 41, 18, and 13 for Surface (2016), Surface (2015), and Pionjar (2015) samples, respectively.

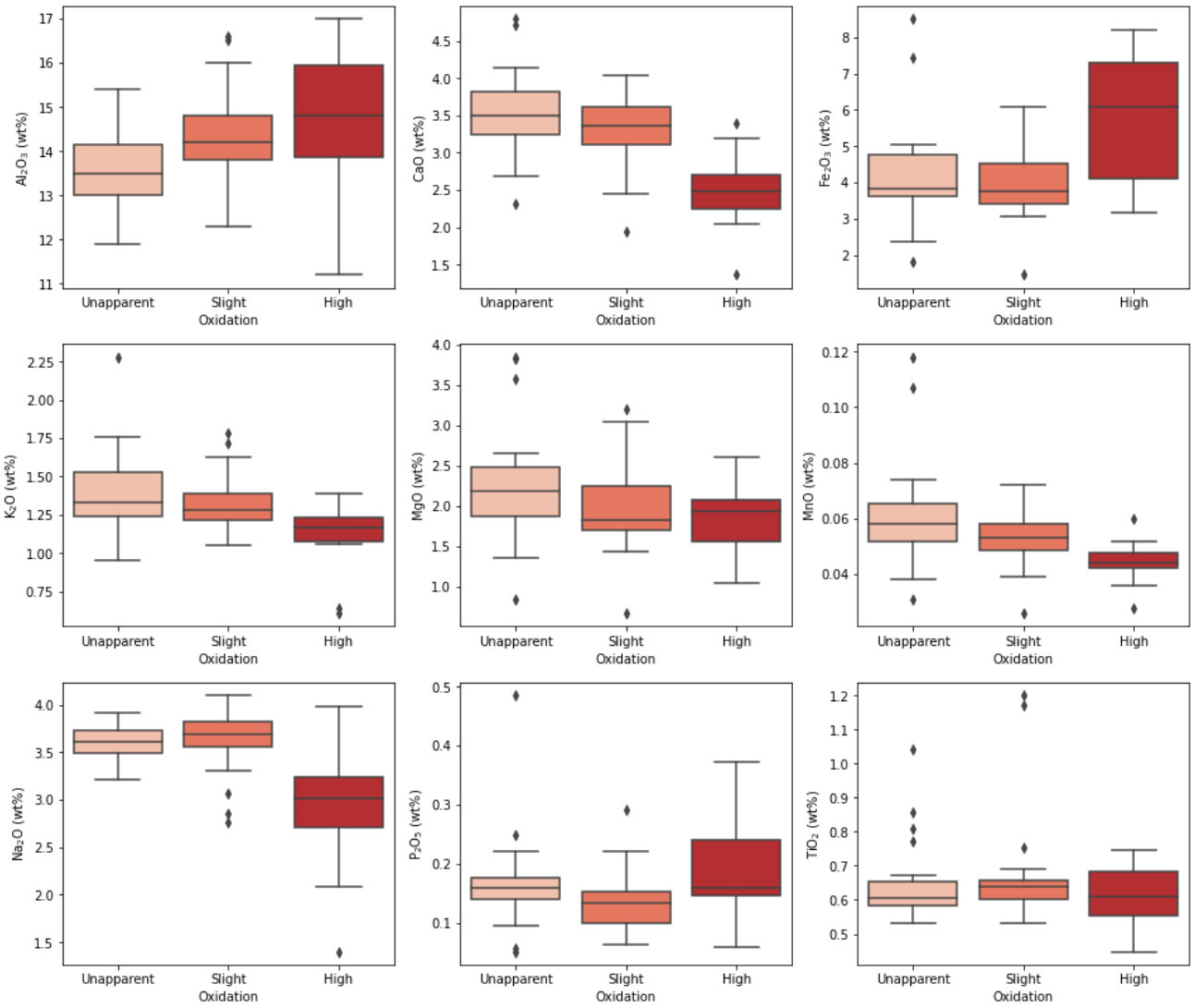

Figure 2.16 Boxplots showing the degree of oxidation for till matrix major oxide weight percent values (ICP-OES analysis). n = 39, 23, and 10 for 'Unapparent,' 'Slight,' and 'High' oxidation, respectively.

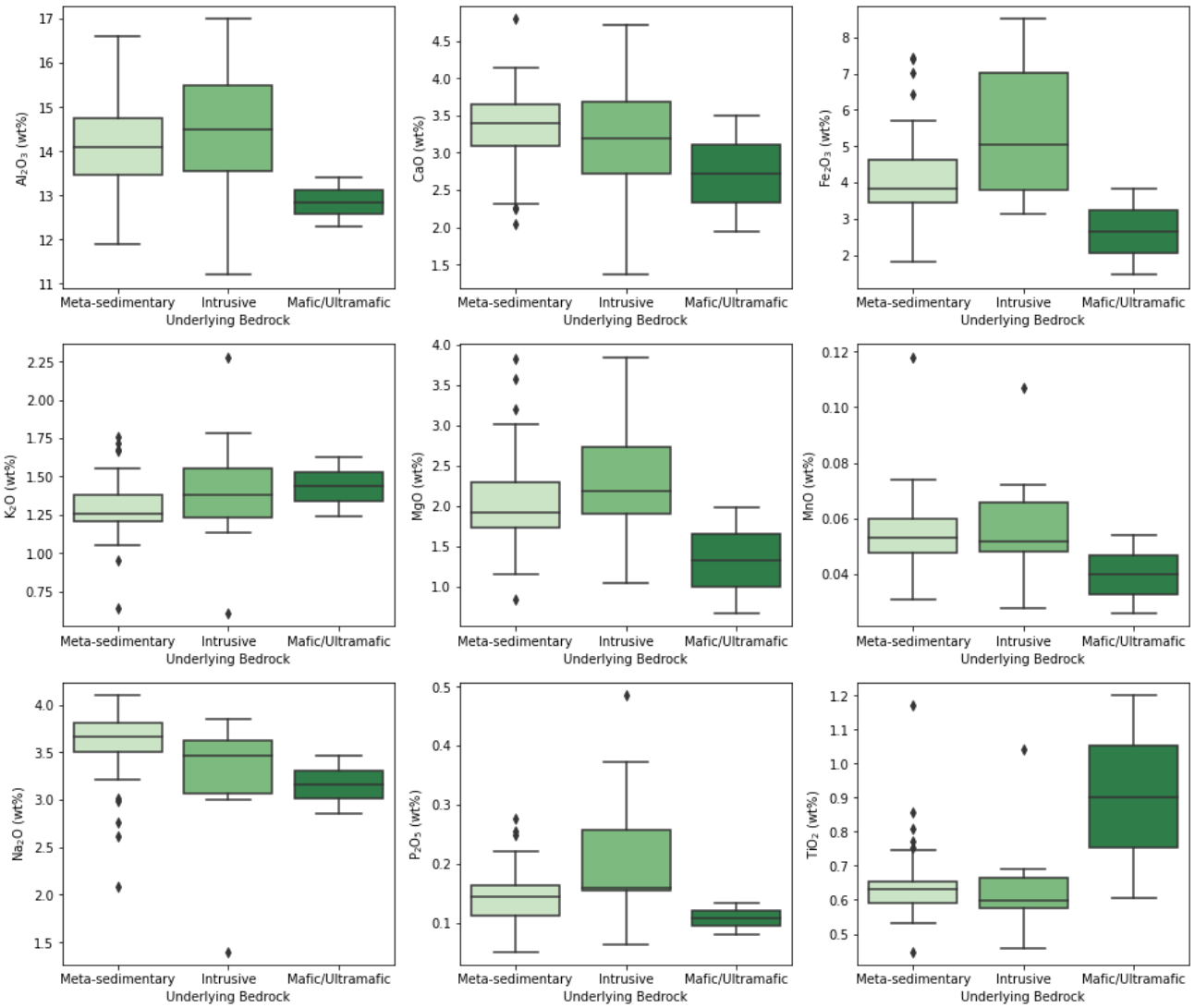

Figure 2.17 Boxplots showing till samples by underlying bedrock type for till matrix major oxide weight percent values (ICP-OES analysis). n = 59, 11, and 2 for meta-sedimentary, intrusive, and mafic/ultramafic types, respectively.

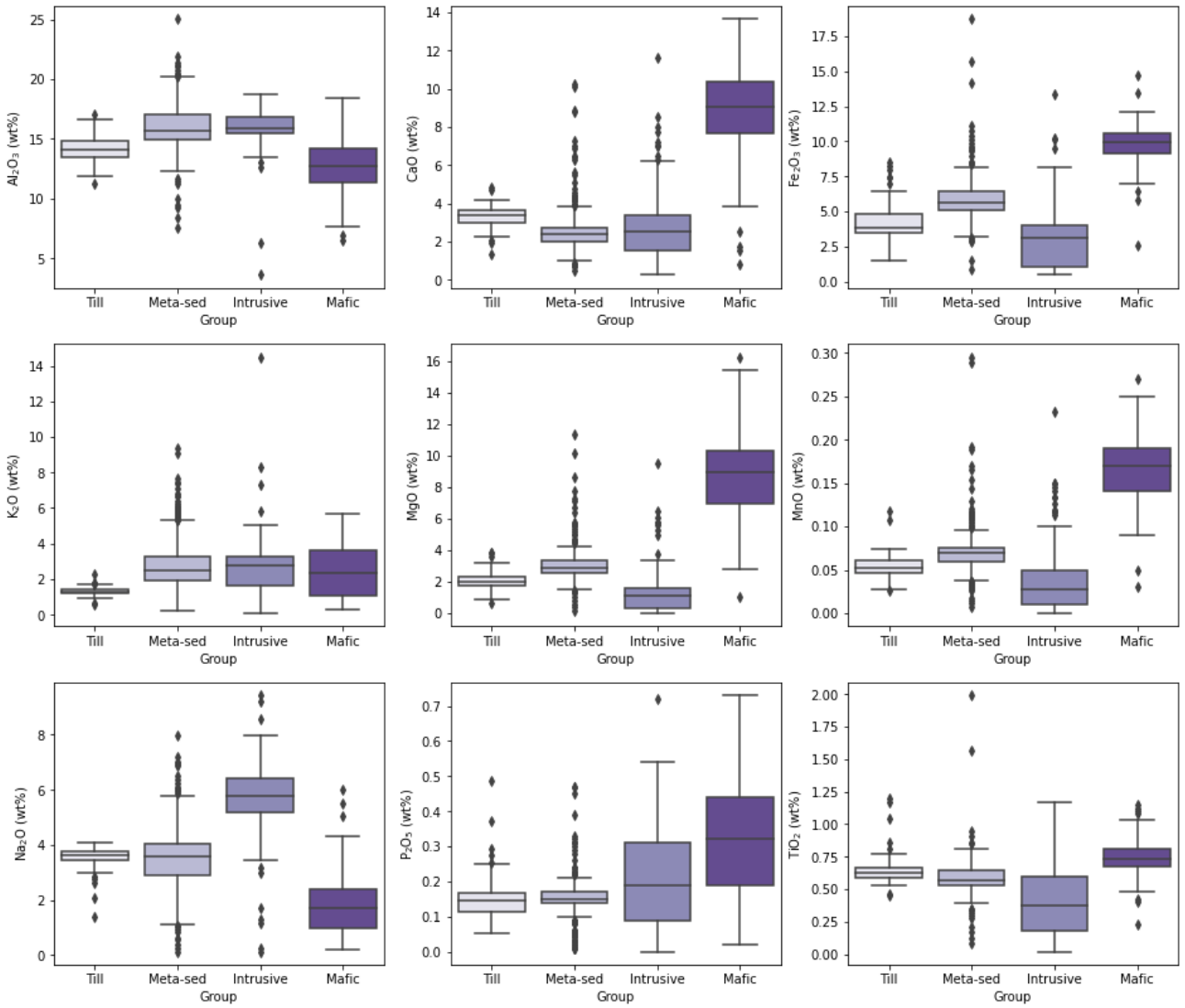

Figure 2.18 Boxplots showing matrix major oxide weight percent values for till matrix (ICP-OES) and bedrock (XRF) (Perrouty et al., 2019; Gaillard et al., 2020) analyses. n = 72, 605, 121, and 122 for till, meta-sedimentary, intrusive, and mafic samples, respectively.

2.4.5. Till Matrix Multivariate Analysis

Principal component and k-means clustering analyses were conducted using till matrix (<0.063 mm) major oxide geochemical values for 72 samples (see **Appendix** for Jupyter notebook).

Principal component analysis (PCA) shows that the total variance in the dataset is ~0.2187, and the variance for 95% of the data is ~0.2077. A scree plot shows the first four principal components explain ~95% of the variance (**Figure 2.19)**. The explained variance by the first, second, third, and fourth principal components is ~0.4946, ~0.2487, ~0.1052, and ~0.0914, respectively. **Figure 2.20** shows major oxide PC loadings for the first four principal components.

Based on the PCA results, k-means clustering analysis was completed using four principal components. Four clusters were chosen for k-means cluster analysis of this data because this number strikes a balance between a relatively low inertia (i.e. summing the squared distance of each point to its cluster's centroid) score (~5.491) and a low-enough number of clusters that can be used to make reasonable geological inferences (Grunsky, 2010; Wang, 2018). Biplots of PC1 vs PC2, PC1 vs PC3, and PC1 vs PC4 are shown in **Figure 2.21**, **Figure 2.22**, and **Figure 2.23,** respectively.

Table 2.7 summarizes till sample traits by k-means cluster, and **Figure 2.24** presents the spatial distribution of all four clusters throughout the study area superimposed on bedrock geology. Cluster 1 is the smallest (n = 7) and is dominated by samples with high oxidation levels (86%). All samples within this cluster are found in medium or coarse-grained particle size. Based on **Figure 2.24**, this cluster is spatially associated with felsic and intermediate intrusions, even though only 43% of samples lie on intrusive bedrock.

Cluster 2 is larger than all the other clusters combined (n = 43). This cluster is dominated by samples with slight oxidation levels (70%) and those in the medium particle size category (74%). Cluster 2 is strongly associated with underlying meta-sedimentary bedrock (91%). Although multiple samples are spatially associated with the phengitic mica footprint, most samples in this cluster are west of and beyond the down-ice direction from the Canadian Malartic deposit (**Figure 2.24**).

Cluster 3 is also relatively small (n = 8) and has samples exclusively from 2016. This cluster is characterized by samples with slight oxidation levels (63%) and those in the medium particle size category (63%). Based on **Figure 2.24**, this cluster is spatially associated with felsic and intermediate intrusions, even though only 13% of samples lie on intrusive bedrock and 75% lie on meta-sedimentary bedrock. Cluster 3 is generally distal to the phengitic mica footprint and has the greatest mean distance from the gold pit (6193 m) at the Canadian Malartic Mine.

Cluster 4 (n = 14) is dominated by samples with unapparent levels of oxidation (71%) and Pionjar (i.e., portable drill) samples. 71% of samples lie on meta-sedimentary bedrock. Based on **Figure 2.24**, Cluster 4 is spatially associated with the phengitic mica footprint and the down-ice direction from the

Canadian Malartic Mine; this cluster has the lowest mean distance from the gold pit (4525 m). This cluster may be most important for prospecting purposes.

Overall, these clusters represent distinct compositional spread and variation in till matrix major oxide geochemical values, which suggests limited blending/mixing over the study area (~340 km^2).

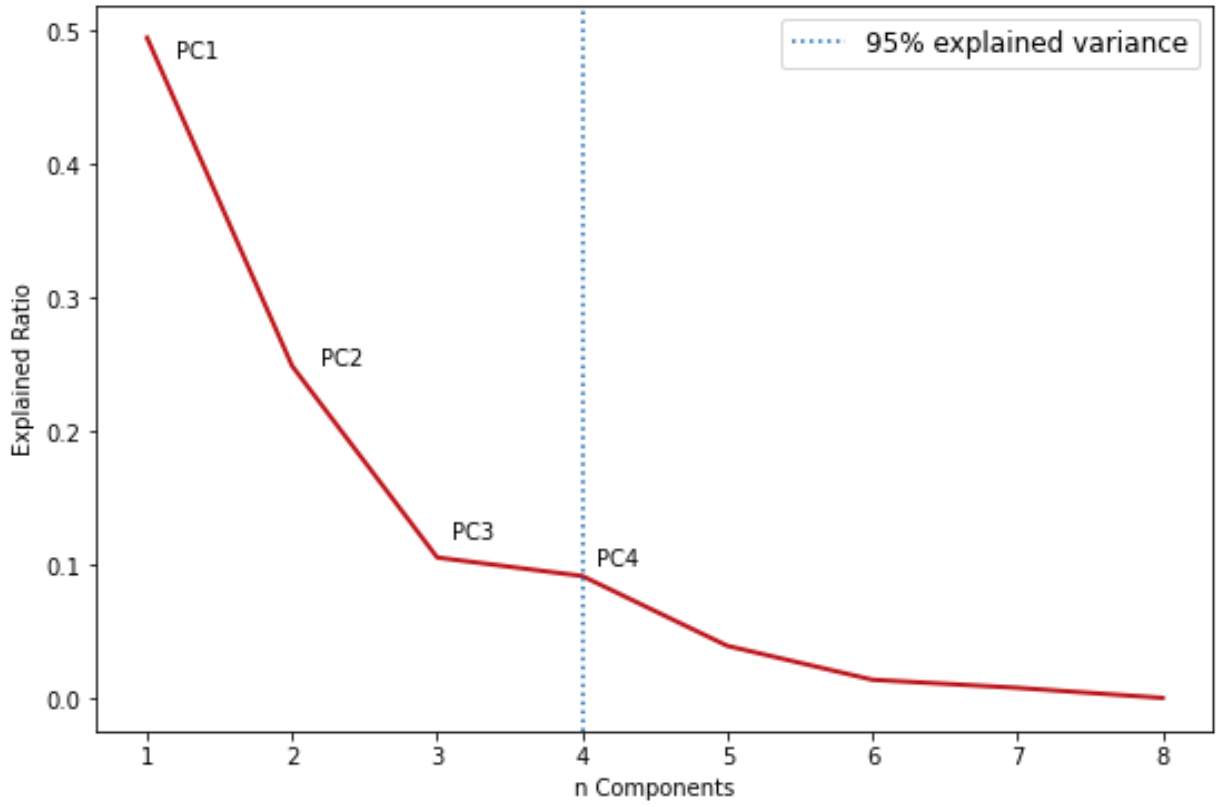

Figure 2.19 Scree plot showing the first 4 principal components explain 95% of the variance in the till matrix major oxide geochemistry dataset (excluding MnO). The explained variance by PC1, PC2, PC3, and PC4 is ~0.4946, ~0.2487, ~0.1052, and ~0.0914, respectively.

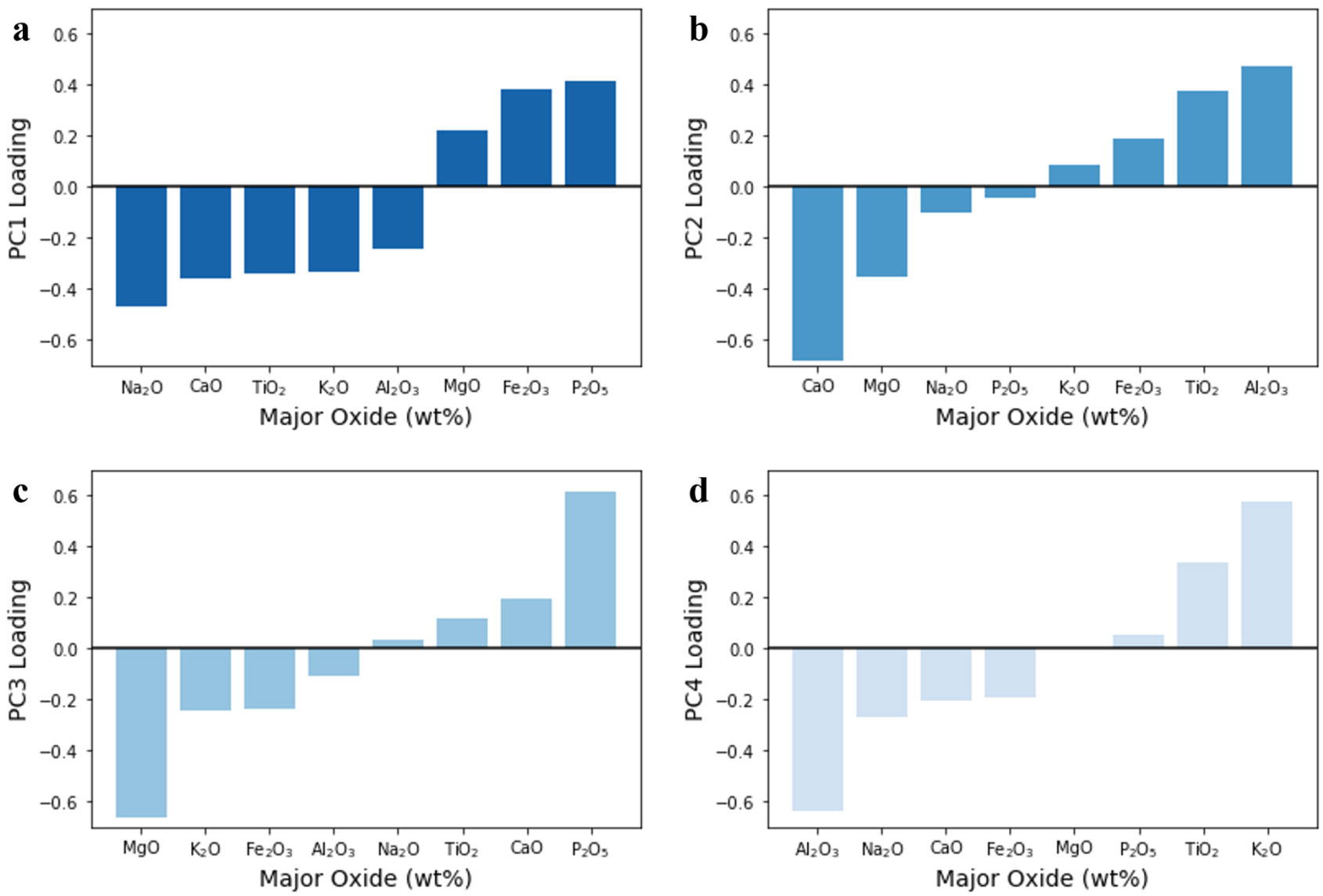

Figure 2.20 Major oxide (excluding MnO) principal component (PC) loadings for (a) PC1, (b) PC2, (c) PC3, and (d) PC4. PC loadings are sorted in ascending order in each subfigure.

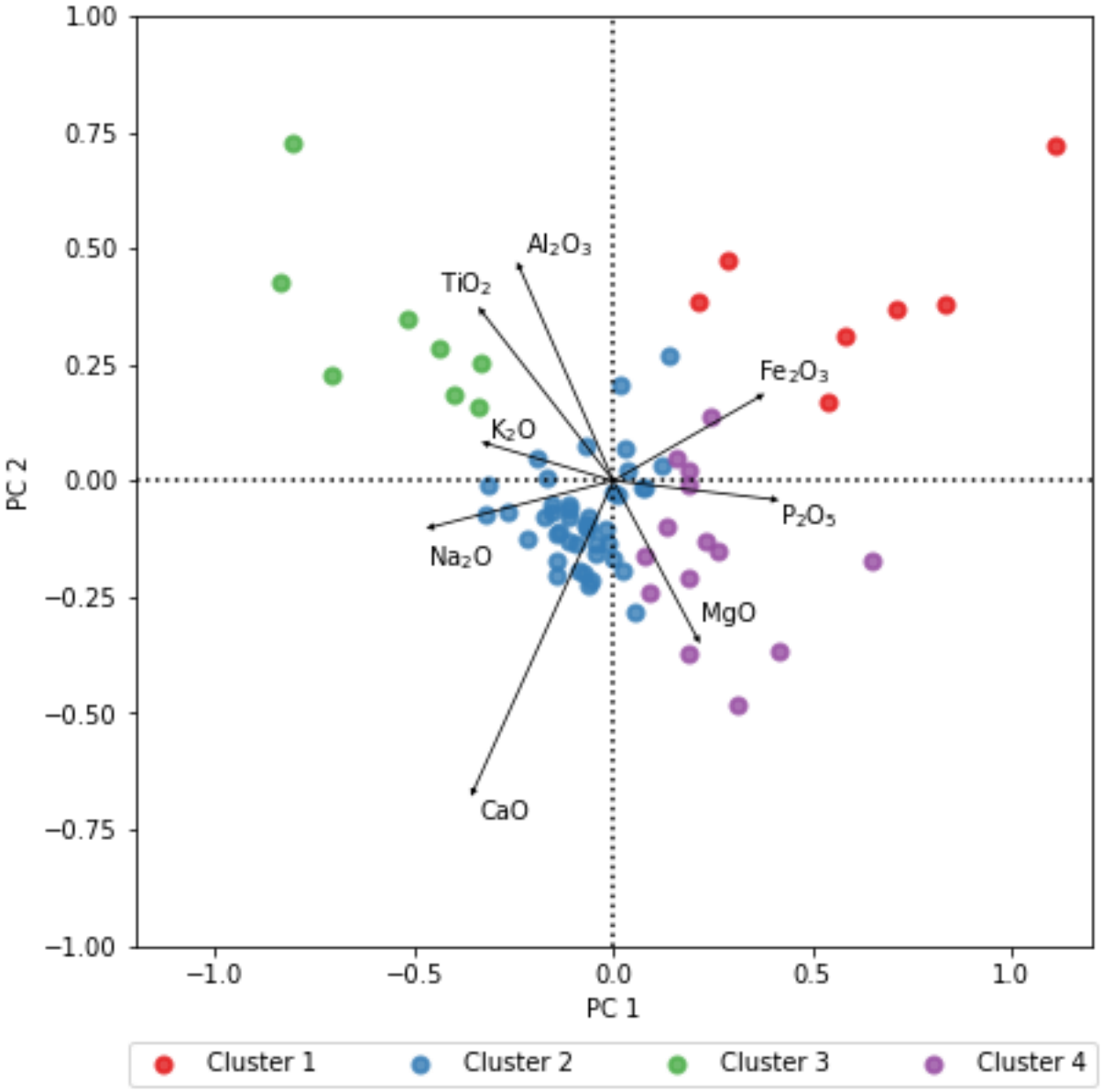

Figure 2.21 Till matrix major oxide (excluding MnO) geochemistry principal component (PC) biplot of PC1 vs PC2. Arrows indicate PC loadings and samples are classified according to k-means clustering analysis using 4 k-means clusters.

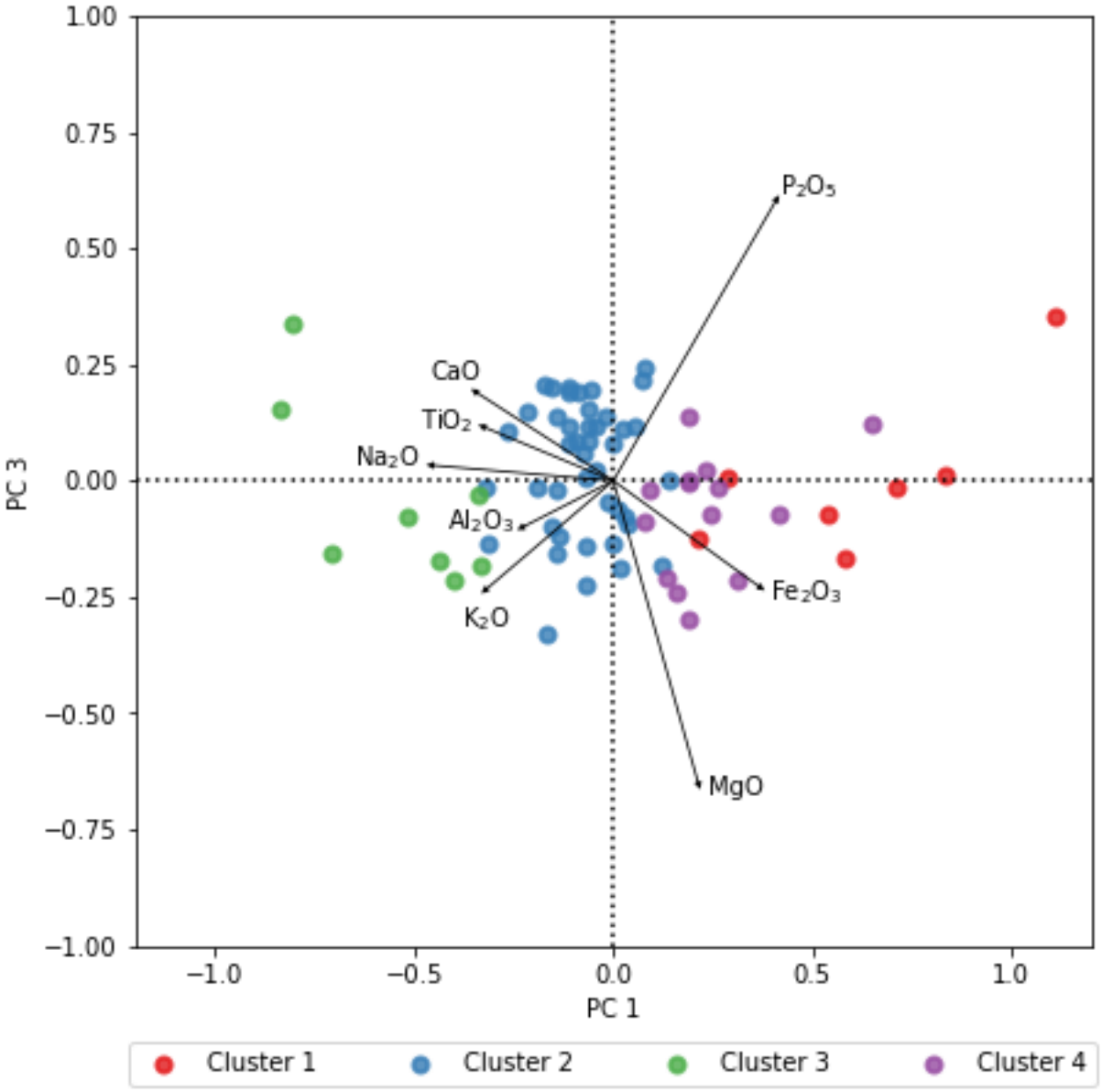

Figure 2.22 Till matrix major oxide (excluding MnO) geochemistry principal component (PC) biplot of PC1 vs PC3. Arrows indicate PC loadings and samples are classified according to k-means clustering analysis using 4 k-means clusters.

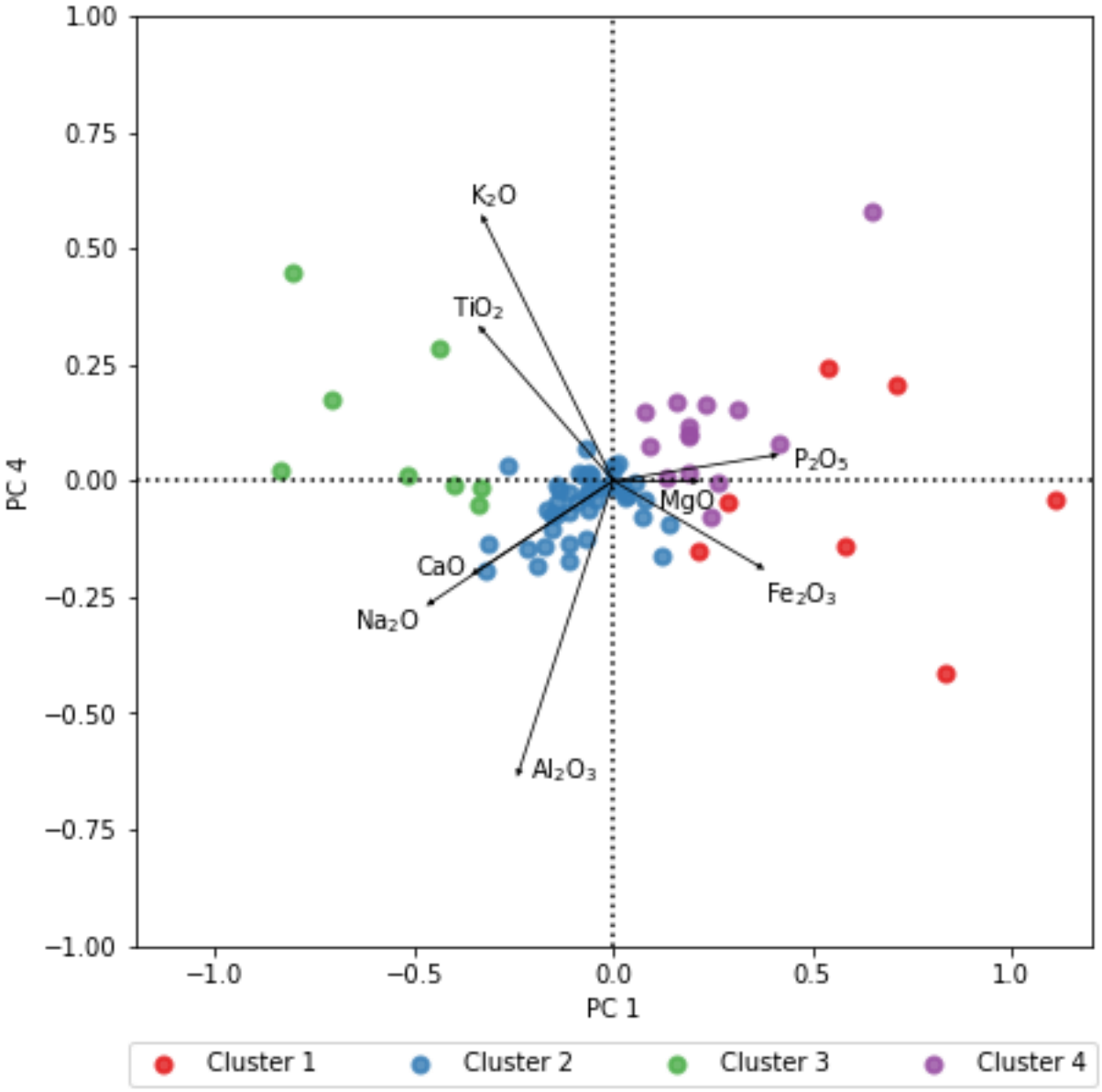

Figure 2.23 Till matrix major oxide (excluding MnO) geochemistry principal component (PC) biplot of PC1 vs PC4. Arrows indicate PC loadings and samples are classified according to k-means clustering analysis using 4 k-means clusters.

Table 2.7 Summary of till sample traits by major oxide k-means cluster. (Percentages may not total 100 due to rounding).

k-means Cluster	**1 (n = 7)**	**2 (n = 43)**	**3 (n = 8)**	**4 (n = 14)**
Degree of Oxidation (%)				
Unapparent	0	26	25	71
Slight	14	70	63	21
High	86	5	13	7
Underlying Bedrock (%)				
Meta-sedimentary	57	91	75	71
Intrusive	43	7	13	29
Mafic/Ultramafic	0	2	13	0
[a]*Grain Size Category (%)*				
Coarse	43	10	13	60
Medium	57	74	63	40
Fine	0	15	25	0
Averages				
Sample Depth (m)	0.4	0.8	0.3	3.4
Distance to Pit (m)	4606	4982	6193	4525

[a]Values exclude Pionjar samples, which were not categorized based on grain size.

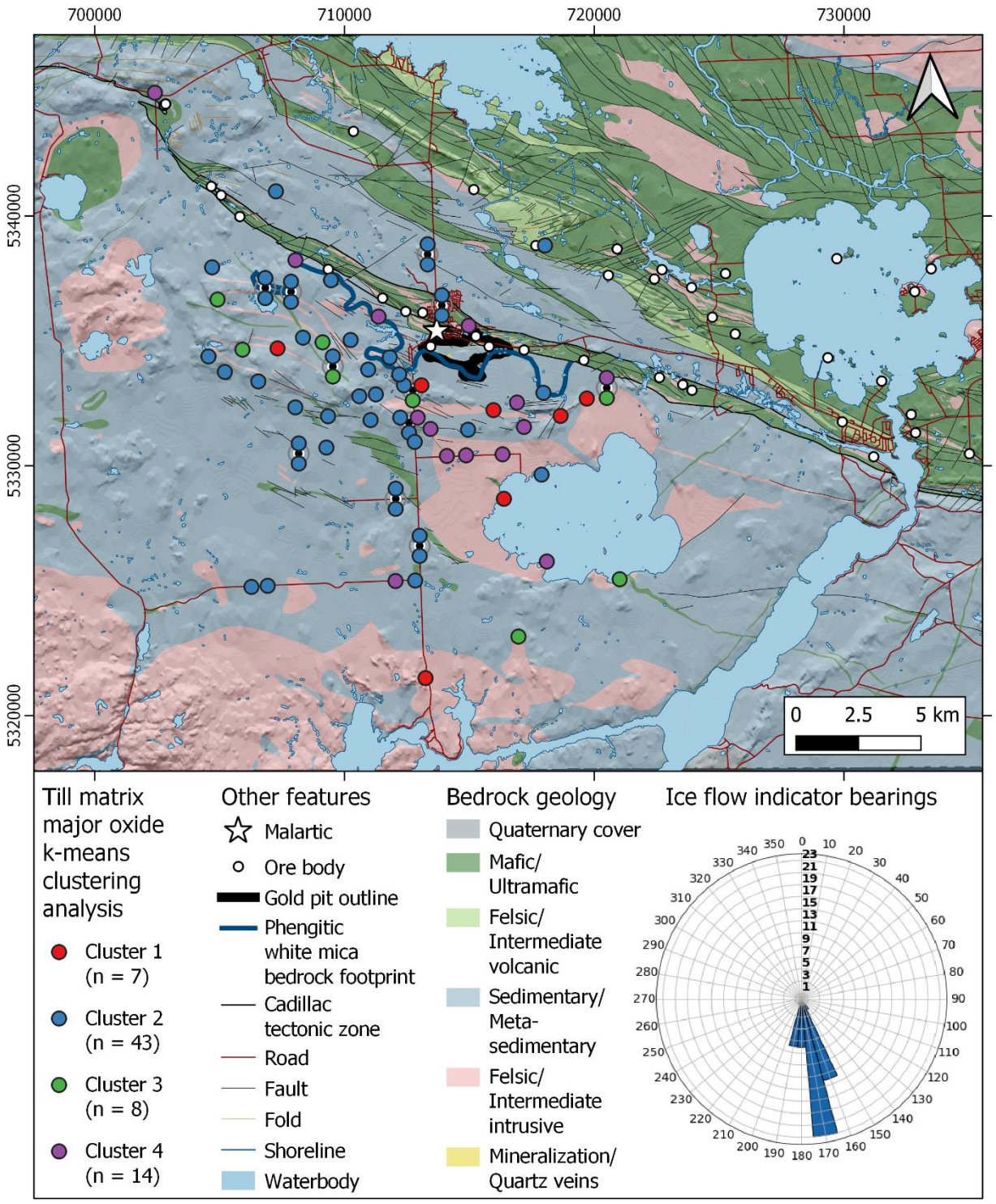

Figure 2.24 Spatial distribution of till matrix major oxide k-means clusters in the study area around the Canadian Malartic Mine on bedrock geology and a hillshade elevation model. The gold pit outline and phengitic white mica bedrock footprint are after Lypaczewski et al. (2019). Waterbodies and hillshade are from Natural Resources Canada (https://maps.canada.ca/czs/index-en.html). Bedrock geology, ore bodies, Cadillac tectonic zone, roads, faults, folds, and shorelines are from SIGEOM (https://sigeom.mines.gouv.qc.ca/signet/classes/I1108_afchCarteIntr). Coordinate system: NAD 83, UTM zone 17.

2.4.6. Glacial Clast Lithology

Generally, the order of abundance of pebble clast content in till samples is made of meta-sedimentary, intrusive, and quartz fragments, accurately reflecting the composition and relative abundance of the bedrock geology within the study area.

Figure 2.25, **Figure 2.26** and **Figure 2.27** show proportional dot maps for intrusive clast content, mafic clast content within the intrusive fraction, and meta-sedimentary clast content in till samples, respectively. Intrusive clast content increases overtop or down-ice of intrusive bedrock most clearly. Mafic clasts account for a larger proportion of intrusive clasts overtop or down-ice of mafic/ultramafic rocks and, in some cases, overtop of down-ice of intrusive rocks while decreasing in proportion in areas underlain by meta-sediments. A larger proportion of mafic clasts in till may be associated with a footprint at the Canadian Malartic deposit. Meta-sedimentary clast content also increases on or down-ice of meta-sedimentary bedrock in an apparent way.

Further, the >8 mm grain size fraction shows relatively more intrusive clasts than meta-sedimentary clasts, whereas the 4-8 mm grain size fraction shows relatively more meta-sedimentary clasts than intrusive clasts. Also, there are more mafic clasts (within the intrusive fraction) in the 4-8 mm grain size fraction relative to the >8 mm grain size fraction.

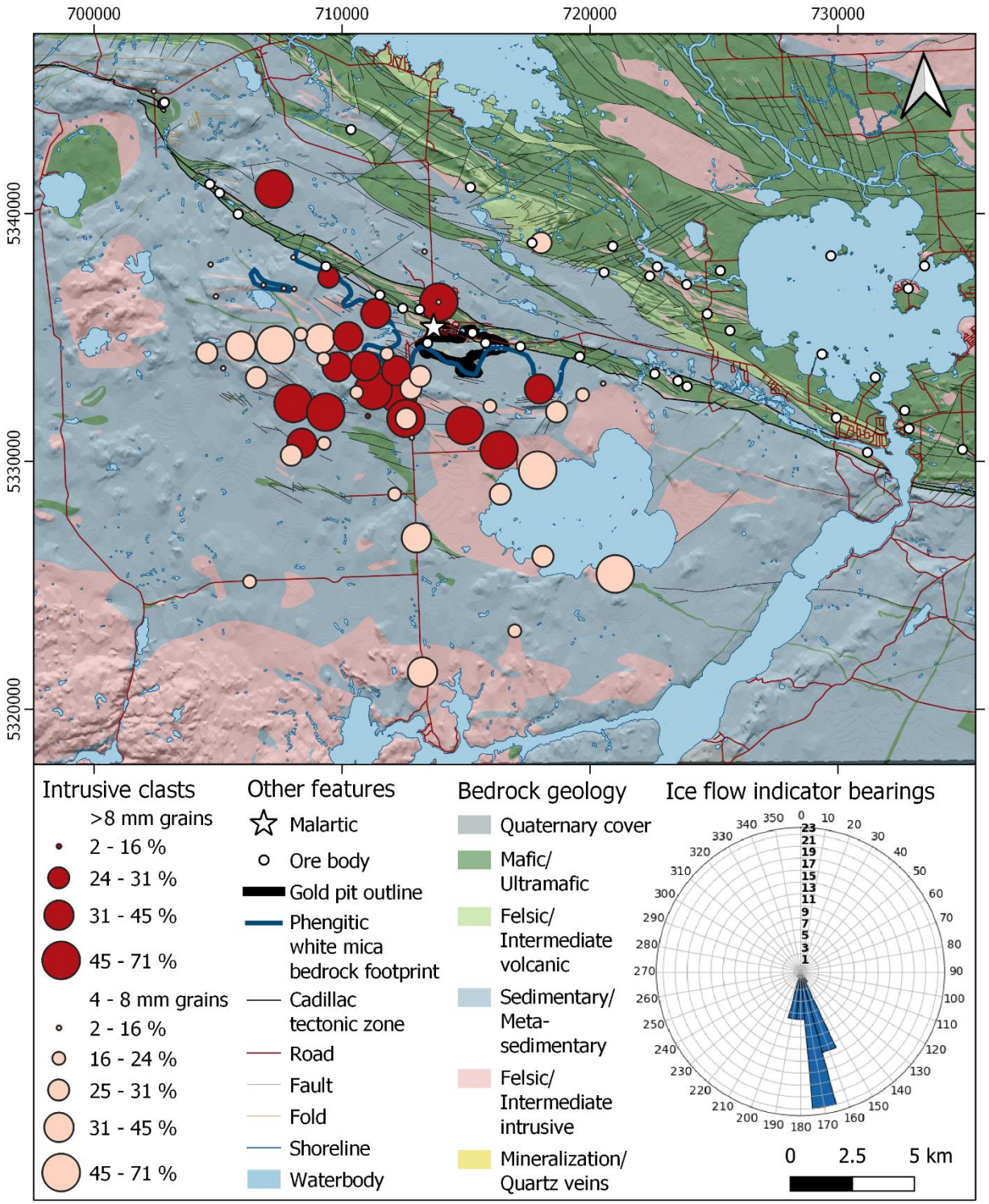

Figure 2.25 Intrusive clast content in glacial till. Smaller clast sizes (4-8 mm) show relatively lower abundances than larger clast sizes (>8 mm). The gold pit outline and phengitic white mica bedrock footprint are after Lypaczewski et al. (2019). Waterbodies and hillshade are from Natural Resources Canada (https://maps.canada.ca/czs/index-en.html). Bedrock geology, ore bodies, Cadillac tectonic zone, roads, faults, folds, and shorelines are from SIGEOM (https://sigeom.mines.gouv.qc.ca/signet/classes/I1108_afchCarteIntr). Coordinate system: NAD 83, UTM zone 17.

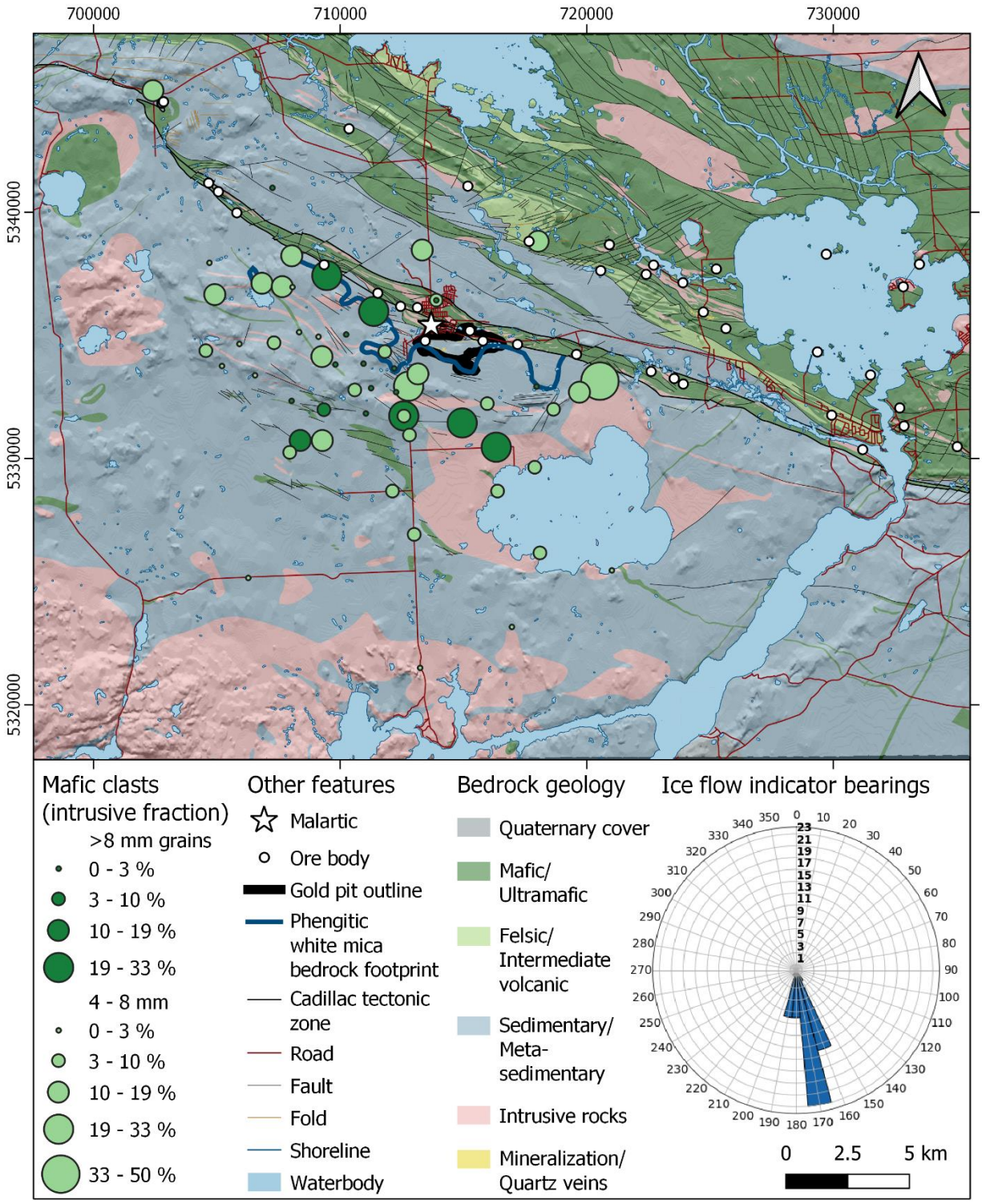

Figure 2.26 Mafic clast content as a percent of intrusive clast content in glacial till. The gold pit outline and phengitic white mica bedrock footprint are after Lypaczewski et al. (2019). Waterbodies and hillshade are from Natural Resources Canada (https://maps.canada.ca/czs/index-en.html). Bedrock geology, ore bodies, Cadillac tectonic zone, roads, faults, folds, and shorelines are from SIGEOM (https://sigeom.mines.gouv.qc.ca/signet/classes/I1108_afchCarteIntr). Coordinate system: NAD 83, UTM zone 17.

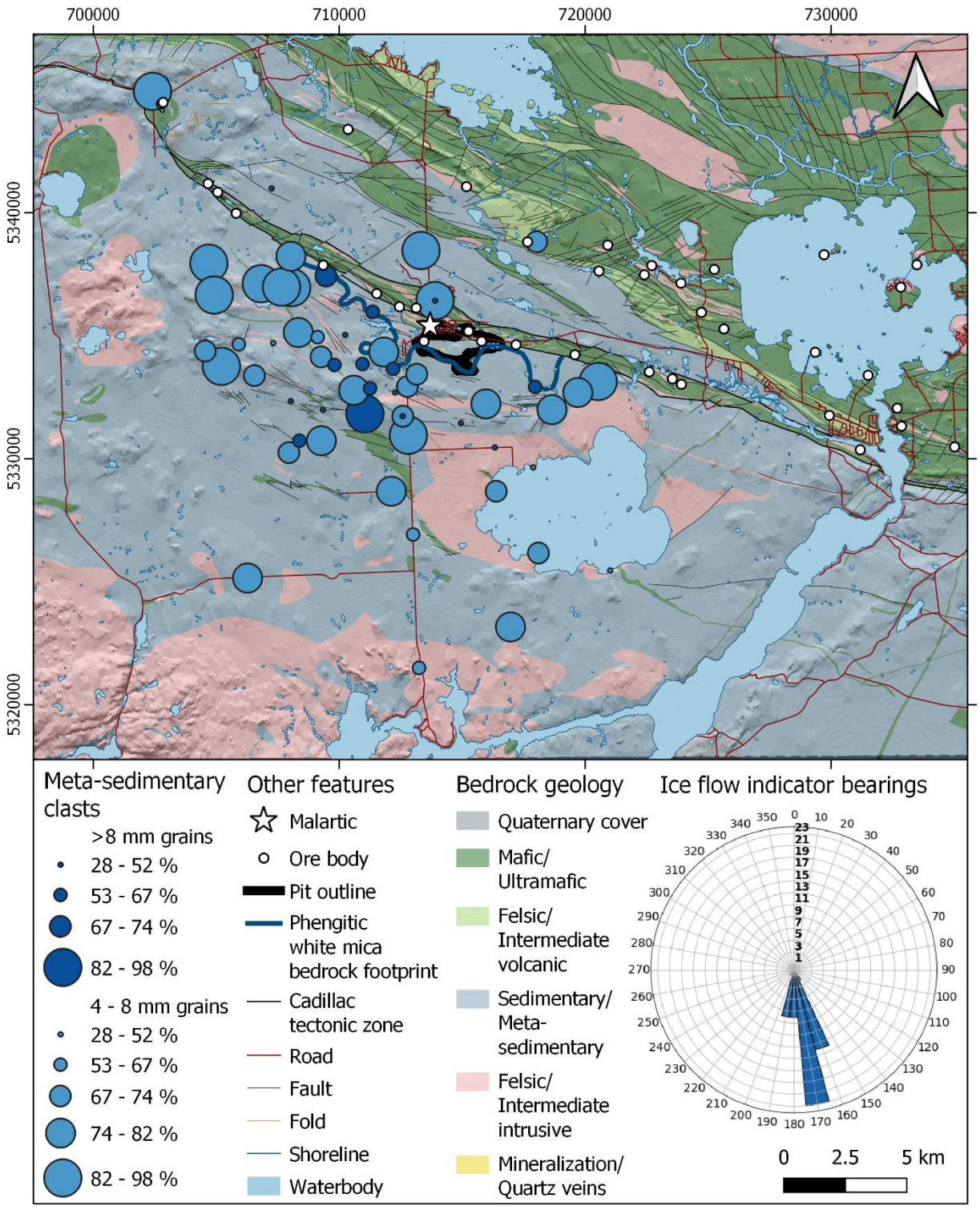

Figure 2.27 Meta-sedimentary clast content in glacial till. Smaller clast sizes (4-8 mm) show relatively higher abundances than larger clast sizes (>8 mm). The gold pit outline and phengitic white mica bedrock footprint are after Lypaczewski et al. (2019). Waterbodies and hillshade are from Natural Resources Canada (https://maps.canada.ca/czs/index-en.html Bedrock geology, ore bodies, Cadillac tectonic zone, roads, faults, folds, and shorelines are from SIGEOM (https://sigeom.mines.gouv.qc.ca/signet/classes/I1108_afchCarteIntr). Coordinate system: NAD 83, UTM zone 17.

2.5. Discussion

2.5.1. Till Coverage & Evolution

The Canadian Malartic deposit is surrounded by sporadic, mainly discontinuous till coverage. Particle size distribution, till matrix major oxide geochemistry and clast lithology analyses support the interpretation that this is a relatively homogeneous till sheet with a range in composition based on degree of oxidation, spatial relation to bedrock lithology, and proximity to the down-ice direction from the Canadian Malartic Mine. Differences between grain size profiles can be attributed to a combination of local factors such as ice-bed interface conditions (i.e., if quarrying or abrasion was the dominant erosive process in action) or the incorporation of fines in till during ice readvance over glacial lake sediments.

Till with relatively high clast content may have been partially reworked by late-stage Glacial Lake Ojibway fluctuations during deglaciation (Veillette et al., 2005), which may have washed away a component of the finer fraction in shallow areas and along littoral zones, and may be true with "coarse" and "medium" samples, which are generally located closer to glaciolacustrine sediments. In contrast, "fine" samples are generally surrounded by more extensive till areas (**Figure 2.12**). Another possibility is that clast-rich till may be from locations close to esker tunnels, where meltwater flow could have flushed some of the fine matrix out of the till in the vicinity of those conduits, such as with the coarsest sample, 064a (**Figure 2.12**). A lower amount of fine fraction matrix material is also to be expected in cases where ideal sample depths were not reached, and the till material was oxidized and possibly affected by surface runoff, as was the case with samples 052a, 064a, 070a (**Figure 2.12**).

The multivariate analysis produces four reasonable subcategories of till within the study area (**Figure 2.19**, **Figure 2.20**, **Figure 2.21**, **Figure 2.22**, and **Figure 2.23**). Based on four k-means clusters (**Figure 2.24** and **Table 2.7**), cluster 1 represents highly oxidized samples; cluster 2 represents till composition associated with high input from meta-sedimentary bedrock; cluster 3 represents till composition associated with high input from felsic and intermediate intrusions; and cluster 4 represents the deepest, least-oxidized samples that appear to be spatially associated with the phengitic mica footprint as well as with the down-ice dispersal region from the Canadian Malartic footprint. Most of the region is dominated by meta-sedimentary rocks. Still, the greater variation in bedrock types around the deposit may explain the increase in the 'mafic' signal in cluster 4.

In terms of clast lithology, larger clasts (>8 mm) show relatively more igneous clasts (**Figure 2.25**), whereas smaller clasts (4-8 mm) show relatively more meta-sedimentary clasts (**Figure 2.27**); therefore, intrusive rocks are more competent than meta-sedimentary rocks because the meta-sedimentary rocks break more readily under erosive glacial ice forces. These results align with the work done by Bukhari et al. (2021). However, the study area poses challenges for clast lithological analysis. Mafic clasts are repeatedly related spatially to underlying intrusive felsic/intermediate bedrock (**Figure 2.26**),

which may suggest they are mafic mineral concentrations or bands within that bedrock as opposed to coming from an overall mafic/ultramafic bedrock source. Further, there is uncertainty in differentiating between local meta-sedimentary and mafic clasts because of their similar fine-grained, dark appearance. Even so, clast lithology results suggest till samples are from local bedrock because clast counts mirror bedrock abundance by lithology type; meta-sedimentary rocks are the most abundant, followed by intrusive rocks (noticeably more felsic than mafic), and the relative abundance of these rock types as clasts in till is spatially correlated to underlying bedrock type (**Figure 2.25**, **Figure 2.26**, and **Figure 2.27**).

2.5.2. Implications for Glacial Dispersal from the Canadian Malartic Gold Deposit

Field observations and the ice flow reconstruction presented herein thus allow some predictions to be made about till dispersal and dispersion patterns. The modern glacial landscape of the study area records an overall ice flow shift from ~210º to ~150º. Small-scale feature orientations (**Figure 2.6a**) are recorded between ~190º to ~160º and landform-scale feature orientations (**Figure 2.6b**) are recorded between ~210º to ~150º; however, both small-scale features and landform-scale features record the same dominant ice flow direction of ~170º. The till in the area is likely to have been produced and re-entrained from extensive local sources during the deglacial ice flow shift, which suggests that the dispersal of Canadian Malartic tracers should match the observed local ice flow history, i.e., potentially forming fan-shaped dispersal patterns from ~210º to ~150º that are particularly elongated ~170º of the deposit. The subglacial paleocurrent 116° is likely linked to the formation of the Harricana Moraine.

Surficial till samples were collected from shallower depths than ideal (Hirvas & Nenonen, 1990; McMartin & Campbell, 2007) because the water table was high and deeper holes would get flooded, which prevented till retrieval (Taves, 2015). Also, till samples collected in 2016 were lower in weight than the recommended 8 – 10 kg bulk for gold grain and heavy mineral counts (McMartin & Campbell, 2007). This sample size is the standard for investigating sand-sized grains (0.25 – 2.00 mm); however, at the Canadian Malartic deposit, disseminated native gold grains are <30 µm in diameter (Helt et al., 2014), so investigating sand-sized grains is not expected to be an effective prospecting strategy. Moreover, the 2016 samples are ample in size for fine fraction (<63 µm) trace element geochemical analyses, which require approximately 1 kg of bulk (McMartin & Campbell, 2007), and for hyperspectral imaging analysis on glacial clasts (2 – 8 mm) (**Chapter 3**), which requires smaller sample sizes with increasing clast-content. Sample depths and sizes in this study are sufficient for delineating dispersal trains and for drift prospecting purposes under similar conditions.

Integrating ice flow results with sediment characterization results reveals till samples with a relative increase in mafic clast content and those within k-means cluster 4 may represent a footprint at the Canadian Malartic deposit.

2.6. Summary

This chapter refines previously reported regional ice flow dynamics (Veillette & McClenaghan, 1996; Veillette et al., 2005) by mapping ice flow indicators on a North-to-South running transect and at additional lateral sites. Overall, ice flow phases (~210º to ~150º) are constrained by oriented striations, and glacially streamlined erosional landforms and paleocurrent (116º) are constrained by glaciofluvial sediment fabric. Previous work did not include older, southwesterly ice flow indicators in this vicinity, and this study identifies three sites with such cross-striations.

Particle size distribution analysis reveals till samples generally comprise gravelly, muddy sand grains. Till matrix major oxides and clast lithology counts suggest that compositional differences across the study area appear to reflect local changes in bedrock (or slightly up-ice) and postglacial processes (e.g., oxidation of the till matrix). They are reasonably defined by four principal components and four k-means clusters. Till clast analysis reveals the same relative proportion of clast lithologies as the underlying bedrock type. Overall, integrating ice flow and sediment record results and interpretations suggests the till in the study area is a single, locally derived sheet with local compositional variations. Despite the till having mixed provenance, its dominant input is local (underlying bedrock and slightly up-ice).

This work lays the foundation for the next chapter, which presents the application of traditional drift prospecting techniques as well as a novel interdisciplinary approach to delineate footprints at the Canadian Malartic gold deposit and results that can be extended to drift prospecting for other Canadian Malartic-type gold deposits.

CHAPTER 3: Geochemical & Gold Grain Dispersal Trains & a Novel Application of Hyperspectral Imaging Analysis Supported by Glacial Clast Petrography at the World-Class Canadian Malartic Gold Mine

3.1. Introduction

This chapter applies the principles of drift prospecting to the Canadian Malartic gold deposit in Malartic, Quebec, within the Abitibi greenstone belt, by using previously established knowledge of bedrock and alterations from the Footprints project (Lesher et al., 2017) and connecting them to the glacial dispersion in the area. Fieldwork techniques, local ice flow dynamics, surficial sediment characteristics and bulk composition results are presented in **Chapter 2**.

The chapter presents an analysis of till matrix minor and trace element geochemistry, sand-sized heavy mineral counts from till, and petrography of glacial clasts to define glacial dispersal patterns down-ice of the Malartic bedrock footprint area (see **Figure 1.9**, which shows previously established footprints). In addition, a new exploration technique is presented and applied. Specifically, it uses hyperspectral imaging analysis of glacial clasts to map the glacial dispersal from the most extensive alteration assemblage in bedrock at the Canadian Malartic gold deposit. Petrographic analyses of clasts strengthen the interpretation of results.

3.2. Applied Drift Prospecting: Well-Established & Novel Techniques

Chapter 1 describes the applicability of well-established drift prospecting techniques to different glacial sediment components (based on grain size), including sampling strategy and unique strengths and weaknesses of each technique. This section presents concrete examples of geochemical, mineralogical, and lithological pathfinders and well-established indicators as effective drift exploration tools and evaluates their applicability to the Canadian Malartic gold deposit. This section also presents background information regarding the novel approach of applying hyperspectral imaging analysis to glacial clasts and its utility concerning the Canadian Malartic deposit.

3.2.1. Geochemical Anomalies in Till Matrix

One established form of drift prospecting is the use of geochemical indicator and pathfinder elements in till matrix, i.e. the <63µm (silt and clay) fraction, for various deposit types (McMartin & McClenaghan, 2001; McClenaghan et al., 2013a). For instance, Au, Pb, Cu, and As are a subsample of elements that can be used for volcanogenic massive sulfide (VMS) deposits and have been found in dispersal trains more than 8 km from the source (Lett, 2001; McClenaghan & Peter, 2016). Unconformity-associated uranium deposits can be traced using U, Ni, Co, Cu, As, and Mo (Jefferson et al. 2007). However, these deposits often do not intersect the bedrock surface. In the case of deeper deposits, the pathfinders associated with their surrounding alteration, such as B and Ni, and major oxides, will be used instead to determine the relative proportion of clay minerals associated with the alteration halo (Earle 2001). Magmatic Ni-Cu-PGE deposits are another example, and they are associated with many elements such as Ni, Cu, Pt, Cr, Co, S, etc. (McMartin & McClenaghan, 2001; McClenaghan et al., 2013a). Similarly, the use of geochemical pathfinders such as Ni, Cr, Ba, Co, Sr, Rb, and many more is well-established in prospecting for diamondiferous kimberlites (e.g. McClenaghan & Kjarsgaard, 2001; McClenaghan, 2005; Thorleifson, 2007). A final, but not exhaustive, example is the use of elements such as As, Bi, and Te, among others, as pathfinders for gold, along with Au itself, within the Abitibi region and elsewhere (McClenaghan, 2001; Taivalkoski et al., 2015).

One possible diagnostic indicator for the Canadian Malartic deposit is W-enriched rutile (TiO_2), associated with alteration in ore genesis at the deposit (Clark & William-Jones, 2004; Helt, 2012; Helt et al., 2014). Rutile is a compelling candidate indicator mineral because (1) it is resistant to weathering and glacial transport (hardness of 6-6.5), (2) it is more abundant than gold, and (3) it shows anomalous compositions from specific substitutions that occur in particular deposit types. However, W-enriched rutile grains, like gold grains, are typically fine (silt-sized) at Malartic (Clark, J., personal communication, 2016). The two associated trace elements, i.e. W and Au, could thus produce a geochemical signal in the fine fraction of till, making them useful as geochemical tracer elements in the till matrix.

3.2.2. Sand-Sized Exotic Heavy Mineral Counts

Another established form of drift prospecting uses sand-sized indicator minerals from till (usually 0.5-2 mm grains), particularly heavy minerals (Peuraniemi, 1990). Indicator minerals are used extensively to prospect for many deposit types, traditionally in exploration for diamonds and gold, with increasing use in exploration for base metals (McClenaghan et al., 2000; Averill, 2001; Thorleifson, 2010). For instance, minerals such as Cr-pyrope, Mg-ilmenite, Cr-diopside, Cr-spinel, and others are standard indicators for assessing the potential of diamondiferous kimberlites in an area (McClenaghan & Kjarsgaard, 2001;

McClenaghan, 2005). W-bearing indicators such as scheelite and wolframite are effective for W-Mo deposits (McClenaghan et al., 2013b). Magmatic massive sulfide minerals tend to be enriched in Mg, Mn, Al or Cr. They can act as indicators for various magmatic deposit types such as volcanogenic massive sulfides (VMS), sedimentary exhalative (SEDEX), skarn, greisen, and Ni-Cu sulfide deposits, among others (Averill, 2001). Galena and sphalerite have recently been used as indicator minerals for Mississippi Valley-type Pb-Zn deposits (Oviatt et al., 2015). Grains of gold, sulfides (e.g., cinnabar, arsenopyrite, chalcopyrite, galena), tellurides, scheelite, cassiterite, barite, and rutile, among others, have all been used as indicators for gold deposits (Plouffe, 2001; McClenaghan, 2005; McClenaghan & Cabri, 2011; Taivalkoski et al., 2015). When using gold grains as indicators, their quantity, mass, morphology, and composition can be used to vector toward their source deposit (Dilabio, 1991).

Standard practice in the industry is to extract sand-sized gold grains from heavy mineral concentrates (HMC) (Peuraniemi, 1990; Averill, 2001), but most of the gold grains from the Canadian Malartic deposit rarely exceed 30 µm in diameter (Helt et al., 2014). Moreover, the deposit is within a region that hosts several gold deposits, and disseminated-to-coarse gold from nearby deposits and a relatively high regional background may mask a finer signal from the Canadian Malartic deposit. Further, dispersal trains from gold grain counts tend to be short, on the order of <1 km (Peuraniemi, 1990; Averill, 2001). As such, it has not been established whether there is sufficient coarser gold at the Canadian Malartic deposit to produce a detectable dispersal train that could be separated from other sources in its proximity. Since grains large enough for visual identification are in the minority, geochemical analysis on the silt and clay fraction or other methods might be more effective alternatives to gold grain counts.

3.2.3. Glacial Clast Lithology & Boulder Tracing

Analyzing glacial pebbles based on their lithology is a standard technique that is a common part of investigating till provenance, which is reviewed and applied to the study area (**Chapter 2**). This analysis is based on indicator lithologies and conducted routinely by subjective inspection, which is prone to human error. Petrographic analyses may also be used to describe clasts. Imaging analysis to sort clasts based on mineralogy is still largely developmental and not widespread.

Boulder tracing has been used successfully to locate deposits for numerous commodities, including uranium (Earle, 2001) and lode gold (Prest W.H. 1911 Prospecting in Nova Scotia (first account of dispersal plume, gold dispersal train, in Stea Finck 2001)). Still, it is most effective on a reconnaissance scale and requires a boulder field, which is not always present. The glacial landscape in the study area does not represent a melt-out environment; therefore, there is no boulder field. Additionally, the Canadian Malartic deposit does not exhibit a compelling geophysical signal in bedrock

for exploration purposes (Wares & Burzynski, 2011). Other techniques are thus needed for uncovering the Canadian Malartic and similar-type deposits.

3.2.4. Novel Application of Hyperspectral Imaging Analysis to Glacial Clasts

This work presents an innovative technique that integrates hyperspectral imaging with drift prospecting. Hyperspectral imaging analysis (HIA) is a technique that collects and processes data across the electromagnetic spectrum by using continuous spectral bands (Hagen & Kudenov, 2013) to identify absorption features of hydrated minerals. Hyperspectral imaging is reflectance spectroscopy, i.e., it measures the spectrum of light reflected from a sample and generates an image containing the spectrum for every pixel. This technique is gaining prominence and has seen a wide range of successful applications in recent years, such as airborne mapping of Ni-Cu-PGE ultramafic rocks (Rogge et al., 2014), airborne mapping of mine tailing pH and mineralogy (Zabcic et al., 2014), scanning of core samples to determine bitumen content in oil sands (Speta et al., 2015), and mapping rocks and minerals at various scales both in the field and the laboratory (e.g., Salisbury et al., 1991; Resmini et al., 1997; Clark, 1999). Diagnostic alteration minerals have been mapped on outcrops, sections, and drill cores (e.g., Kruse, 1996; Laakso et al., 2015; Mathieu et al., 2017).

This research builds on the work that establishes hydrothermal mica alteration minerals, i.e. phengitic white mica and Mg-rich biotite, as exploration vectors towards the Canadian Malartic deposit (Gaillard et al., 2018), by investigating their occurrence in glacial clasts. Phengitic white mica (Mg-rich, Al-poor muscovite) can be identified and mapped using spectral imagery (e.g., van Ruitenbeek et al., 2006; Tappert et al., 2013). The mica end-member muscovite is associated with zones distal to the ore at Malartic, whereas the phengitic white mica is associated with ore (Lypaczewski et al., 2015, 2019). Pure muscovite has an absorption feature at 2195-2200 nm, whereas phengitic white mica has one at a longer wavelength, >2210 nm (Clark et al., 1990). Similarly, biotite with moderate Mg content (Mg# 50-55) is associated with zones distal to the Malartic ore. In contrast, biotite with high Mg content (Mg# >65) is associated with ore and shows an absorption feature at 2250 nm (Lypaczewski et al., 2015). HIA (using shortwave infrared (SWIR) light, i.e., 1000-2500 nm wavelengths) identifies these hydrothermal mica alteration minerals based on their absorption features. Applying hyperspectral imaging analysis to map phengitic white mica and Mg-rich biotite in glacial clasts represents a new way of tracing transported rocks of interest back to their source in mineral exploration.

Hyperspectral imaging analysis of glacial clasts allows identifying the full mineral assemblage of altered rocks, which can be associated with known sources, as opposed to powdered, grain-mounted XRD samples; however, it is necessary to know enough about an alteration system to know what to look for.

Moreover, HIA is a non-destructive and fast technique that maps the minerals in the rock, whereas XRD reveals bulk mineralogy. The technique is an automated process that is faster and more accurate than subjective visual inspection and requires minimal sample preparation. One challenge is that SWIR does not penetrate deeply; therefore, clasts need to be thoroughly cleaned (because glacial clasts tend to be coated with fine matrix), and this type of HIA is not effective on highly oxidized clasts.

3.3. Methods

Surficial till and esker samples were collected throughout the study area and then underwent preliminary laboratory processing (drying, splitting, archiving, and dry sieving to sort based on grain size) and characterization, detailed in the **Methods** section in **Chapter 2**. First, traditional prospecting methods such as till matrix minor, trace element geochemistry, and sand-sized Au grain counts were applied. Next, hyperspectral imaging analysis (using SWIR light) was applied in two ways. First, it was used to analyze 2-4 mm and 4-8 mm grain size fractions for their indicator clast content, and results were mapped to establish the glacial dispersal of those clasts down-ice of Malartic. Then, it was used to select potential indicator clasts to create thin sections for petrographic analyses. The following sub-sections describe this methodology in greater detail.

3.3.1. Till Matrix Minor & Trace Element Geochemistry

Till matrix (<0.63μm) was analyzed at the Saskatchewan Research Council Geoanalytical Laboratory on the 2015 and 2016 samples in separate batches, which was done using the 'ICPMS1 Sandstone Exploration Package' and 'AU1 Gold by Fire Assay' techniques (SRC Geoanalytical Laboratories, 2016). The ICPMS1 package was chosen for multi-element analysis because 'sandstone' better approximates the metamorphosed Pontiac greywackes and associated till than the alternative 'basement' package suited for mafic or felsic igneous rocks. The AU1 package was chosen for gold because it is designed to measure low-grade gold, corresponding to the gold at Malartic (Wares & Burzynski, 2011). The ICPMS1 package included inductively-coupled plasma mass spectrometry (ICP-MS) measurements for trace elements following total digestion and inductively coupled plasma optical emission spectrometry (ICP-OES) measurements for minor elements following total digestion. Total digestion was achieved by heating the pulp in ultrapure $HF/HNO_3/HClO_4$ until dry and then dissolving the residue in dilute ultrapure HNO_3 (SRC Geoanalytical Laboratories, 2016). The AU1 package comprised atomic absorption spectrometry (AAS) measurements for gold values, following lead (Pb) fire assay pre-concentration. Quality assurance and quality control (QA/QC) were conducted following Piercey (2014) (see **Appendix**).

Select minor and trace element data from till samples were described with summary statistics, and their spatial distribution was mapped using QGIS (QGIS Development Team, 2020). 8 minor and trace elements (i.e., Au, Ag, Ba, Cs, Mo, Pb, Rb, Sr, and W) were selected from previously identified footprints presented in **Figure 1.9** and the corresponding schematic map in Lesher et al. (2017). Au and W were chosen to expand on the previous surficial work by Taves (2015), which is part of this collaboration. The other elements were chosen randomly to perform a preliminary assessment, and additional elements (such as K, Ti, Bi, Be, etc.) remain to be explored. Principal component analysis and k-means clustering (Grunsky, 2010) were done to investigate till matrix minor and trace element variations (to explore 8 minor and trace element variables with 72 samples). The data was prepared using centered-log-ratio transformation and standardization by using SciPy (Virtanen et al., 2020) and scikit-learn (Pedregosa et al., 2011) (see **Appendix** for QA/QC and Jupyter notebooks). The spatial distribution of k-means clusters was mapped using QGIS (QGIS Development Team, 2020).

3.3.2. Heavy Mineral Separation & Gold Grain Counts

Heavy mineral concentrates (HMC) were prepared from sand-sized till fractions at Overburden Drilling Management for 2015 and 2016 samples in separate batches using heavy liquid separation, ferromagnetic and paramagnetic separation. Gold grains were hand-picked from the 125-250 μm and 250-500 μm non-magnetic HMC fractions using a binocular microscope and were classified based on their morphology as "reshaped," "modified," or "pristine" to infer relative transport distance, which is shortest for "pristine" grains and longest for "reshaped" grains (Dilabio, 1990). The grain counts per HMC fraction were normalized to counts per 100 g HMC, and their spatial distribution was mapped using QGIS (QGIS Development Team, 2020).

3.3.3. SWIR Imaging of Glacial Clasts

Multiple clast size fractions were considered for hyperspectral imaging analysis. The goal was to find the optimal balance of clast abundance, preserved source bedrock characteristics, and amenability to creating thin sections. There was an element of trial-and-error in this stage, and the optimal size fraction for this technique may vary based on sediment clast characteristics within each unique study area. Generally, a minimum number of clasts is necessary for the results to be considered meaningful, which has not been constrained for this application. Still, the recommended approach of using 250-300 clasts for lithological analysis (Bridgland, 1986) was a reasonable guideline.

In our study, the 4-8 mm clast fraction was selected for hyperspectral imaging analysis because it was considered large enough to preserve mineral assemblages and alteration signatures of the source

bedrock while also being large enough to be made into thin sections. The 2-4 mm clast fraction was also selected because it represented a greater abundance of clasts, but clasts from this fraction were considered too small to be made into thin sections. The >8 mm clast fraction was also considered for this analysis and may be a useful fraction in principle, but the collected samples had too few clasts in this size range to include these results as part of this research.

First, clasts were washed in water by hand with scrub brushes (with plastic bristles) to remove surface clay until the water they were in remained clear with further scrubbing. Most samples required multiple rounds of scrubbing, and some required as much as three rounds of 10-20-minute sessions. Alternative methods for cleaning the clasts were considered, such as placing them in an ultrasonic bath, but washing by hand (with a brush in each hand) proved to be the most effective and efficient approach. **Figure 3.1** shows washed clasts that are ready for hyperspectral imaging analysis.

Hyperspectral imaging analysis was performed at the Core-Net Spectral Laboratory at the University of Alberta (Core-Net Spectral Laboratory, 2020) on 4-8 mm and 2-4 mm surface till and esker clasts. Spectral imaging data was collected per the method set out by Lypaczewski et al. (2019) to measure phengitic white mica (indicator values >2205 nm; measurement range 2190-2215 nm) and Mg-rich biotite content (indicator values 2241-2252 nm; measurement range 2240-2255 nm) based on imaged pixel counts with 25 nm smoothing. Measured values for both indicators were combined per pixel and then normalized by the total white mica content (2190-2220 nm) to increase the strength of the signal. The dispersion of this signal, not including esker values, was analyzed by interpolation using the minimum curvature method described by Briggs (1974). The extent of dispersion was calculated in QGIS (QGIS Development Team, 2020) as the area within contours at 3% and 5% tracer mica signature content, in granules and pebbles, and was compared to the area of the phengitic white mica bedrock footprint.

Additionally, a selection of 4-8 mm clasts (i.e., “pebbles”) was hand-picked from samples based on highly phengitic colours (>2205 nm) and no apparent textural variations (**Figure 3.2a**). Clasts were discarded from this initial selection if they were composed of tourmaline or if they showed deep 2100 nm, indicating thick white mica, which is distinct from the footprint alteration signature (Philip Lypaczewski, personal communication, Dec. 13, 2017; **Figure 3.2b**). 42 pebbles from 11 samples were made into thin sections.

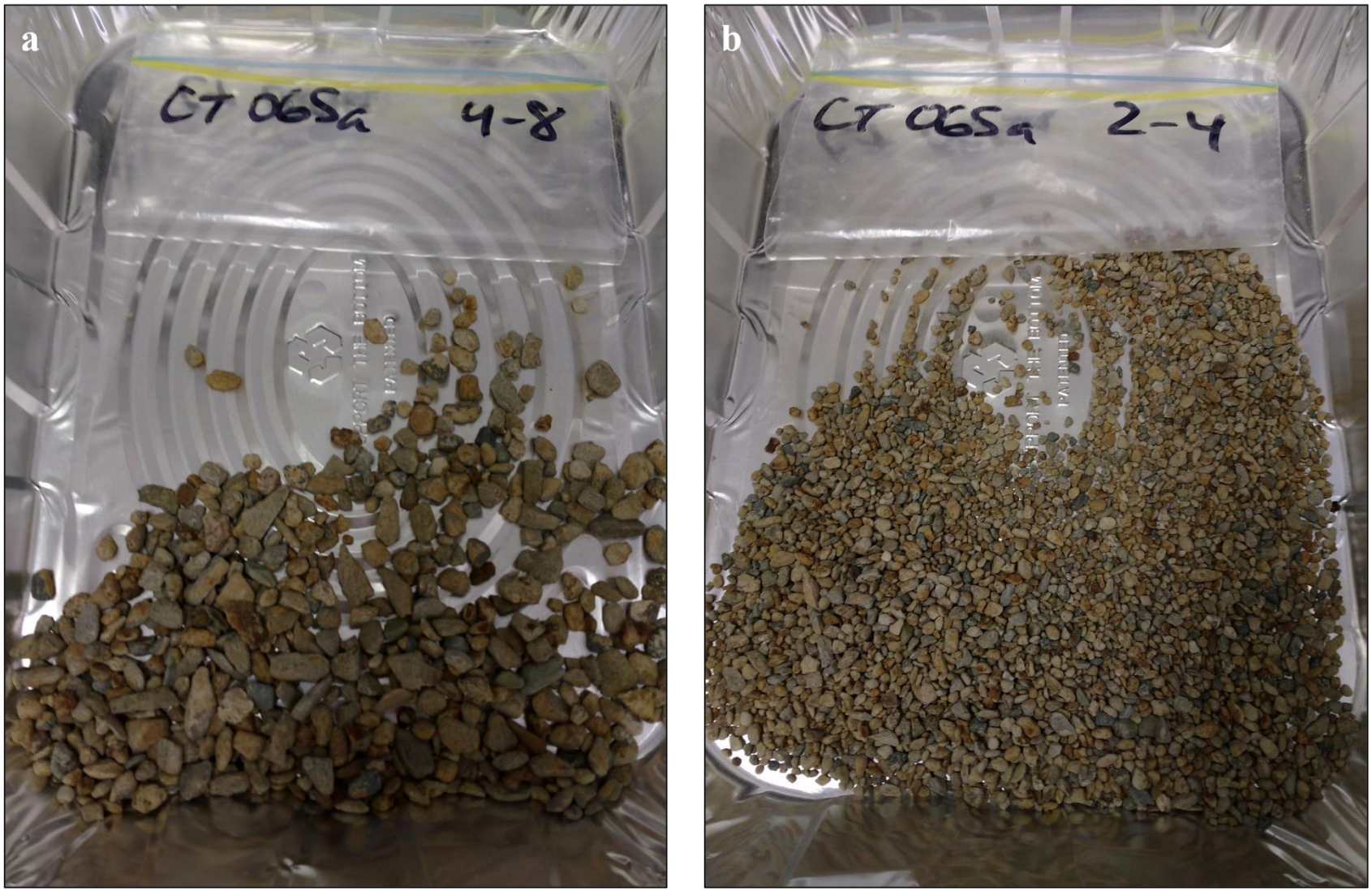

Figure 3.1 Sample CT-065a washed glacial clasts in preparation for hyperspectral imaging analysis. (a) shows 4-8 mm clasts, and (b) shows 2-4 mm clasts.

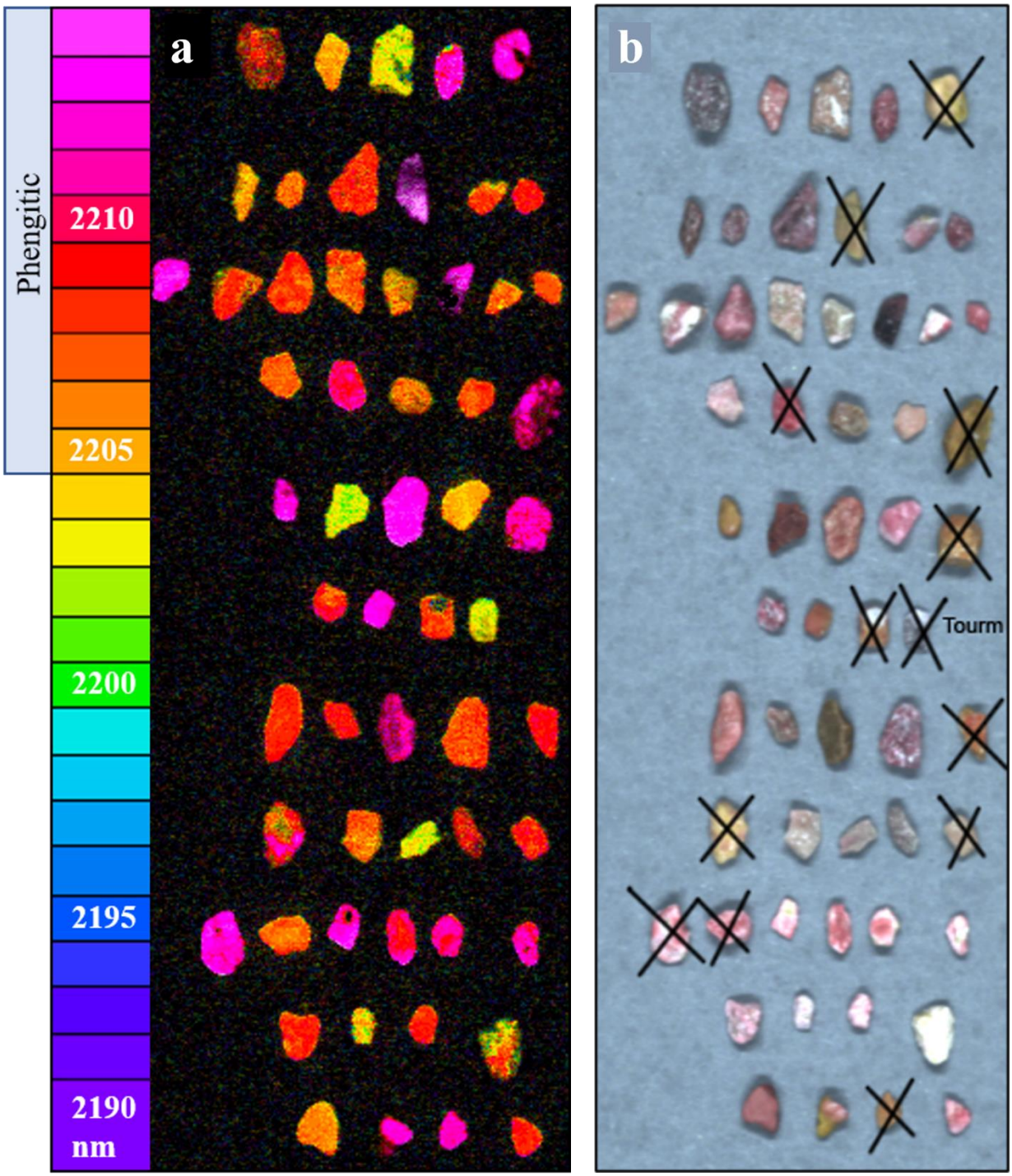

Figure 3.2 Selected 4-8 mm clasts from multiple subglacial till samples made into thin sections for petrographic analyses. (a) shows phengitic white mica (>2205 nm) content. (b) shows a false colour image (R:2160 nm, G:2205 nm, B:2350 nm). Black X's mark discarded clasts because they were either made of tourmaline or thick white mica, neither of which is part of the targeted bedrock footprint at the Canadian Malartic deposit (Philip Lypaczewski, personal communication, Dec. 13, 2017).

3.3.4. Glacial Clast Petrography

Once potential indicator clasts were selected using hyperspectral imaging analysis and made into thin sections, then optical microscopy and scanning electron microscopy with electron probe microanalysis (SEM-EPMA) were conducted to identify and characterize mineral occurrence and associations, alteration, rock textures, and to look for gold grains within these selected clasts. Optical microscope work was performed with binocular optical microscopes at the University of Waterloo and again, after SEM-EPMA work, at Queen's University. Notes were made to describe alteration, mineral associations, deformation, potential protolith and bedrock source.

SEM-EPMA was performed at the Surface Science Western University Laboratory (https://epma.uwo.ca/about/Electron%20Microprobe.html Western Science Centre, 2020) on the selected phengitic mica-bearing glacial clasts. Thin sections were carbon-coated for SEM-EPMA work. Major, minor, and trace minerals were identified. Mineral associations and textural descriptions were also noted. Once the data collection was complete, each clast was then categorized by referencing published descriptions of the regional bedrock geology as either being similar to intrusive or meta-sedimentary bedrock associated with the Canadian Malartic gold deposit or dissimilar to these rocks (Gervais et al., 2014; De Souza et al., 2015; Perrouty et al., 2019; Lypaczewski et al., 2019).

3.4. Results & Interpretation

3.4.1. Till Matrix Minor & Trace Element Geochemistry

The till matrix minor and trace element analysis investigated potential gold or alteration-related geochemical anomalies. **Table 3.1**Error! Reference source not found. presents the summary statistics for s elected till matrix minor and trace element geochemical analyses.

Figure 3.3 shows the spatial distribution of Au (ppb). A glacial dispersion train of moderate to highly elevated Au values is present down-ice from the Canadian Malartic deposit and from the eastern portion of the phengitic white mica bedrock footprint. The single highest Au value of 267 ppb (sample RT-DS 30) is 5.7 times greater than the second highest value (47 ppb), occurs directly 3.2 km down-ice from the nearest point of the gold pit. The train is characterized by moderate Au values (17-28 ppb) and is relatively short and dwindles to low Au values (<6 ppb) 4.6 km down-ice from the deposit. The western half of the study area is dominated by low to moderately low Au values (<15 ppb).

Figure 3.4 presents the spatial distribution of Ag (ppm). A glacial dispersion train of elevated Ag values is present down-ice from the Canadian Malartic deposit. The study area is interspersed with a relatively uniform distribution of low (0.10-0.13 ppm) to moderately high (0.24-0.31 ppm) Ag values, but all instances of high Ag values (0.37-0.47 ppm) occur down-ice from the Canadian Malartic deposit and the eastern portion of the phengitic white mica bedrock footprint. This train is relatively long, and the furthest high Ag value (sample CT-007a) occurs directly 10.5 km down-ice from the nearest point of the gold pit.

Figure 3.5 depicts the spatial distribution of Rb (ppm). A glacial dispersion train of elevated Rb values is present down-ice from the Canadian Malartic deposit. The train is distinguished by moderately high (49.7-62.8 ppm) to high (80.8-81.4 ppm) Rb values, which occur down-ice from the Canadian Malartic deposit and the eastern portion of the phengitic white mica bedrock footprint. The western side of the study area does not contain any moderately high to high Rb values, except for one associated with the Lapa Cadillac Mine in the northwest corner. This train is relatively long, and the furthest high Rb value (sample CT-019a) occurs 13.2 km directly south of the western edge of the gold pit.

Figure 3.6 displays the spatial distribution of W (ppm). A glacial dispersion train of elevated W values may be present down-ice from the Canadian Malartic deposit. The entire phengitic white mica bedrock footprint is distinguished by moderate (1.3-1.7 ppm) to moderately high (1.9-3.2 ppm) W values, and in contrast, the Canadian Malartic deposit is distinguished by high (4.5-5.6 ppm) W values that are only present in the study area directly down-ice from the deposit. This train is relatively short, and the furthest high W value (sample RT-DS 30) occurs directly 3.2 km down-ice from the nearest point of the

gold pit. Low (0.4-0.7 ppm) to moderately low (0.8-1.2 ppm) W values dominate the study area beyond ~3 km down-ice from the phengitic white mica bedrock footprint and the Canadian Malartic deposit.

Similar figures illustrating the spatial distribution of Ba, Cs, Mo, Pb, and Sr are in the **Appendix**. A glacial dispersion train of Ba may be associated with the phengitic white mica bedrock footprint and down-ice from the Canadian Malartic deposit. Glacial dispersion trains of Cs, Mo, Pb, and Sr are unclear and may or may not be present down-ice from the Canadian Malartic deposit.

Table 3.1 Summary statistics for till matrix minor and trace element geochemical values (analysis; n = 72).

	Au[a]	**Ag**	**Ba**	**Cs**	**Mo**	**Pb**	**Rb**	**Sr**	**W**
Method	AAS	ICP-MS	ICP-OES	ICP-MS	ICP-MS	ICP-MS	ICP-MS	ICP-OES	ICP-MS
Unit	ppb	ppm	ppm	ppm	ppm	ppm	ppm	ppm	ppm
Detection Limit	2	0.02	1	0.1	0.02	0.02	0.1	1	0.1
Standard Error	3.83	0.0086	8.77	0.13	0.182	0.507	1.19	7.82	0.099
Minimum	0	0.1	213	1.3	0.35	8.03	20.9	182	0.4
Maximum	267	0.47	727	7.9	9.57	29.3	81.4	582	5.6
Range	267	0.37	514	6.6	9.22	21.3	60.5	400	5.2
Mean	11.5	0.19	419	2.4	1.60	13.3	41.5	433	1.2
Median	2.5	0.18	414	2.1	1.2	11.9	39.5	443	1
Mode	0	0.15	452	2.3	0.42	10.2	39.5	483	0.8
Variance	$1.05*10^3$	0.0053	$5.54*10^3$	1.1	2.39	18.5	102	$4.41*10^3$	0.71
Standard Deviation	32.5	0.073	74.4	1.1	1.55	4.30	10.1	66.4	0.842

[a]Non-detect values were input as '0'.

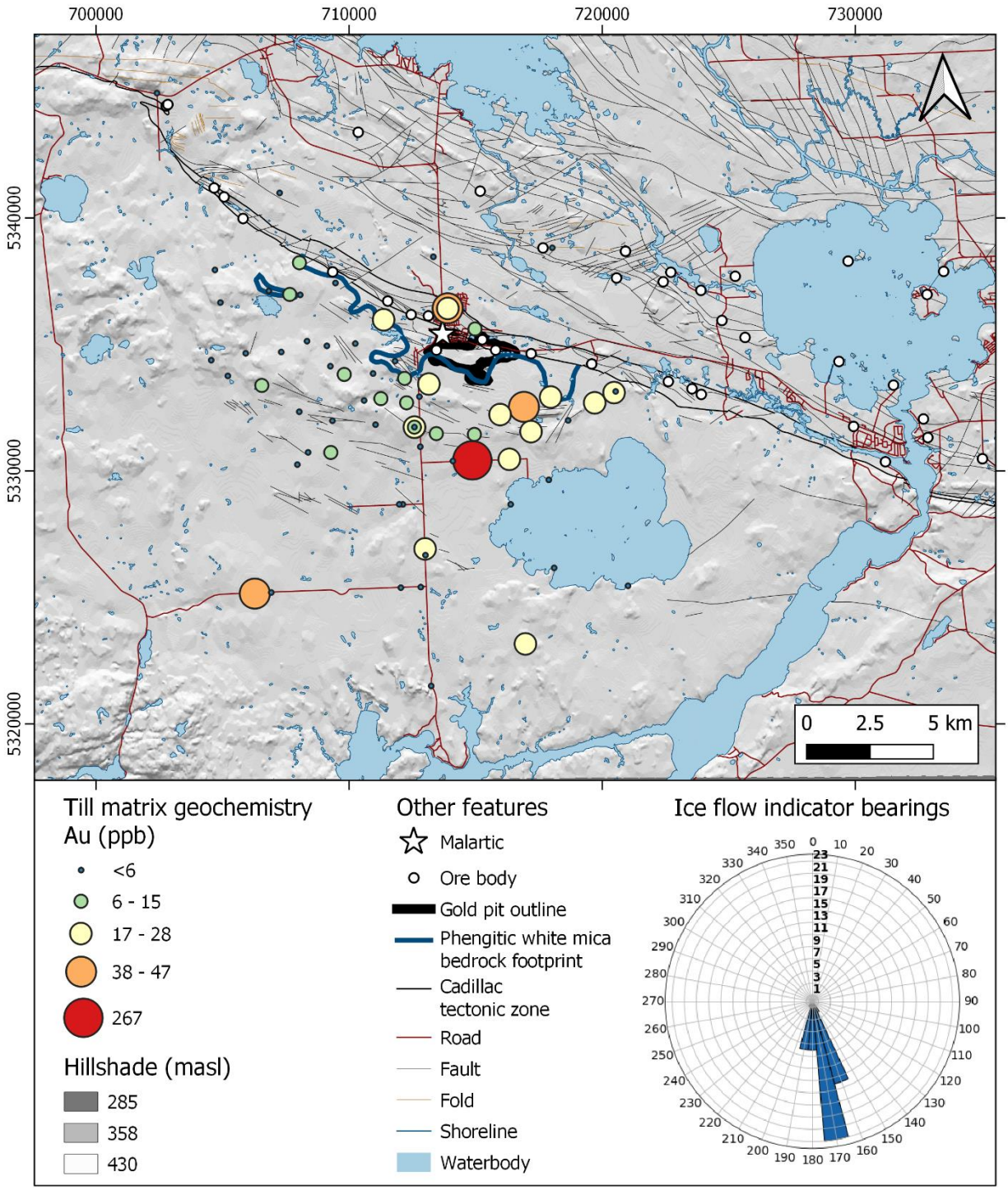

Figure 3.3 Spatial distribution of Au (ppb) based on till matrix geochemistry (AAS). The gold pit outline and phengitic white mica bedrock footprint are after Lypaczewski et al. (2019). Waterbodies and hillshade are from Natural Resources Canada (https://maps.canada.ca/czs/index-en.html). Ore bodies, Cadillac tectonic zone, roads, faults, folds, and shorelines are from SIGEOM (https://sigeom.mines.gouv.qc.ca/signet/classes/I1108_afchCarteIntr). Coordinate system: NAD 83, UTM zone 17.

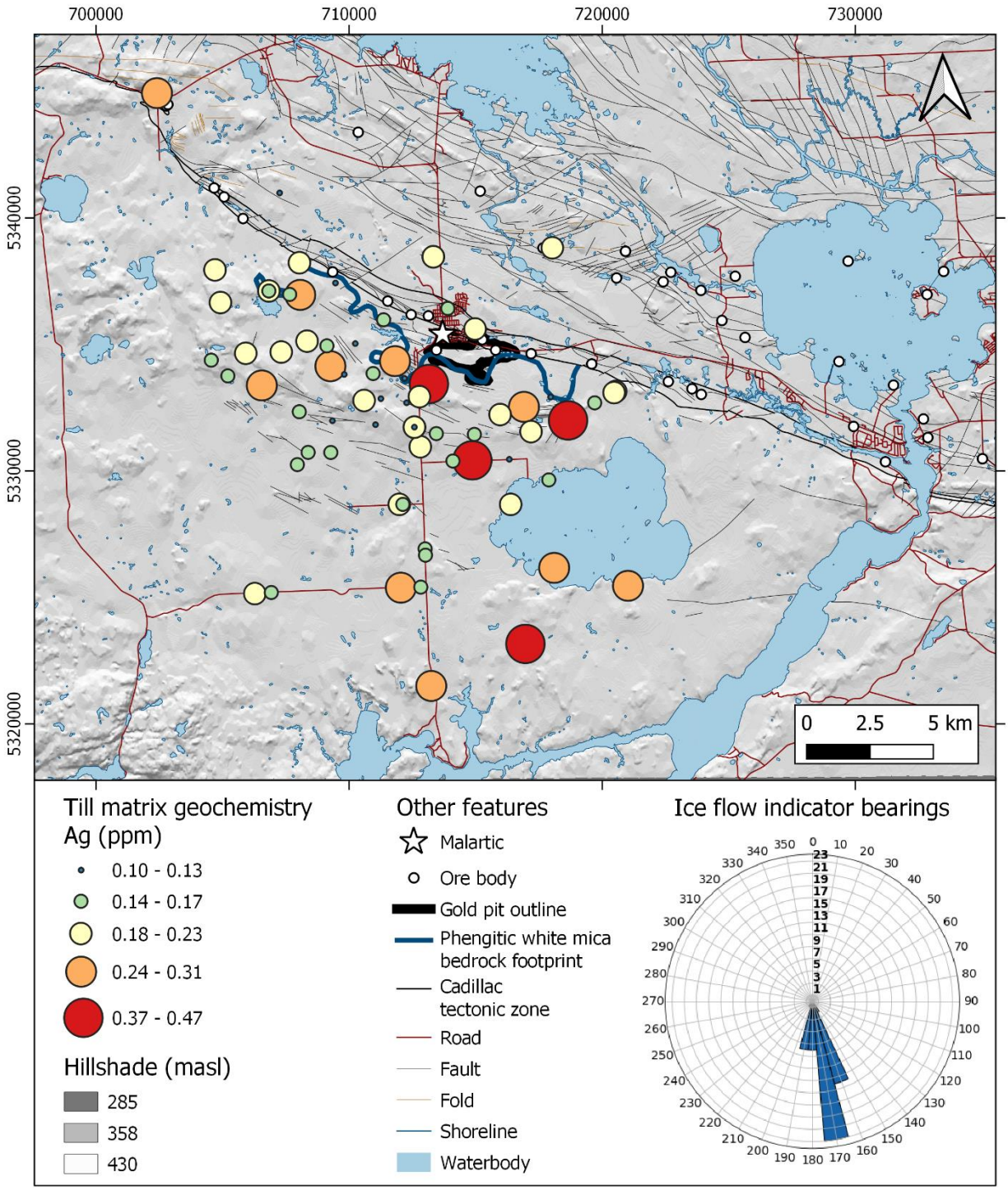

Figure 3.4 Spatial distribution of Ag (ppm) based on till matrix geochemistry (ICP-MS). The gold pit outline and phengitic white mica bedrock footprint are after Lypaczewski et al. (2019). Waterbodies and hillshade are from Natural Resources Canada (https://maps.canada.ca/czs/index-en.html). Ore bodies, Cadillac tectonic zone, roads, faults, folds, and shorelines are from SIGEOM (https://sigeom.mines.gouv.qc.ca/signet/classes/I1108_afchCarteIntr). Coordinate system: NAD 83, UTM zone 17.

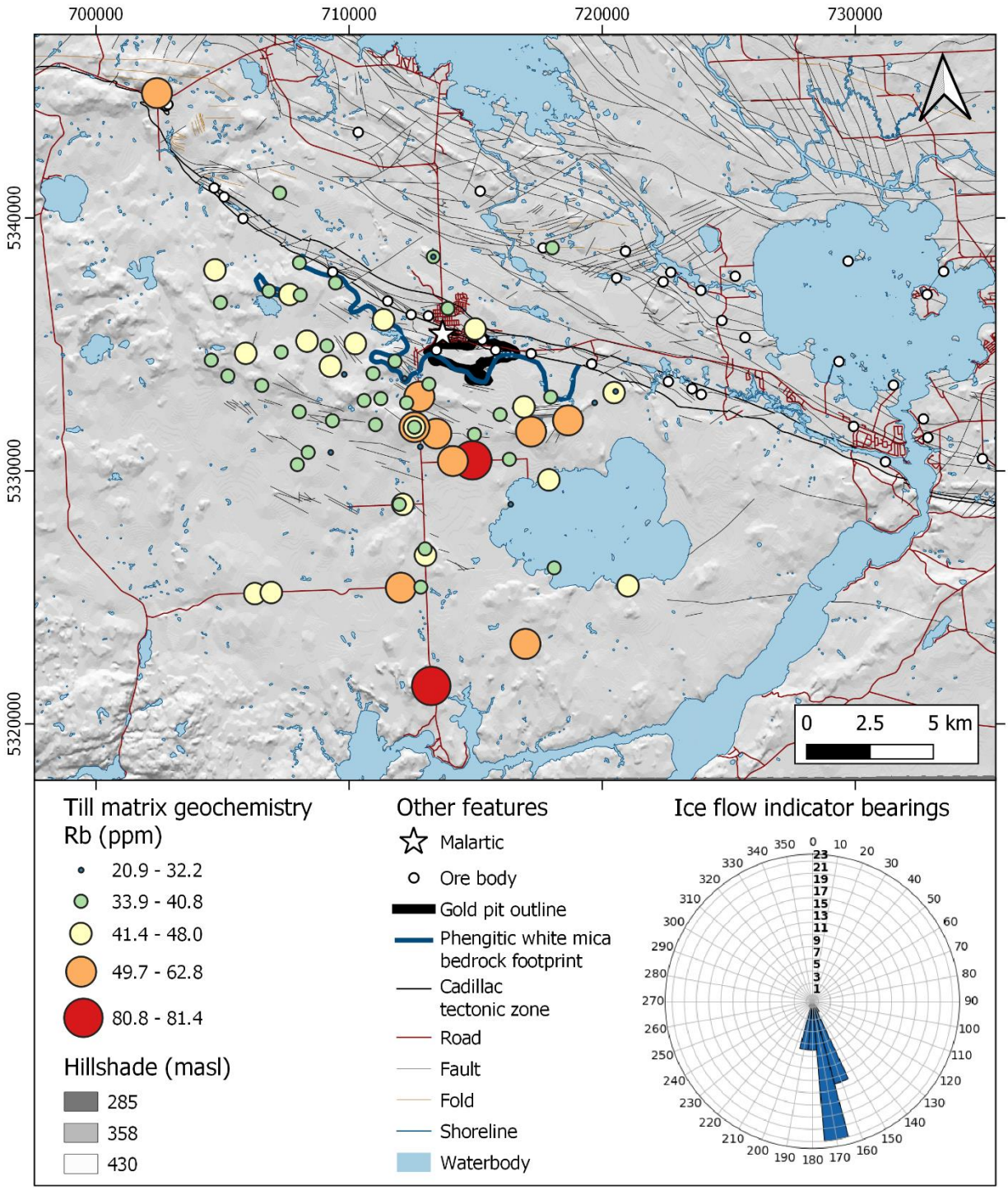

Figure 3.5 Spatial distribution of Rb (ppm) based on till matrix geochemistry (ICP-MS). The gold pit outline and phengitic white mica bedrock footprint are after Lypaczewski et al. (2019). Waterbodies and hillshade are from Natural Resources Canada (https://maps.canada.ca/czs/index-en.html). Ore bodies, Cadillac tectonic zone, roads, faults, folds, and shorelines are from SIGEOM (https://sigeom.mines.gouv.qc.ca/signet/classes/I1108_afchCarteIntr). Coordinate system: NAD 83, UTM zone 17.

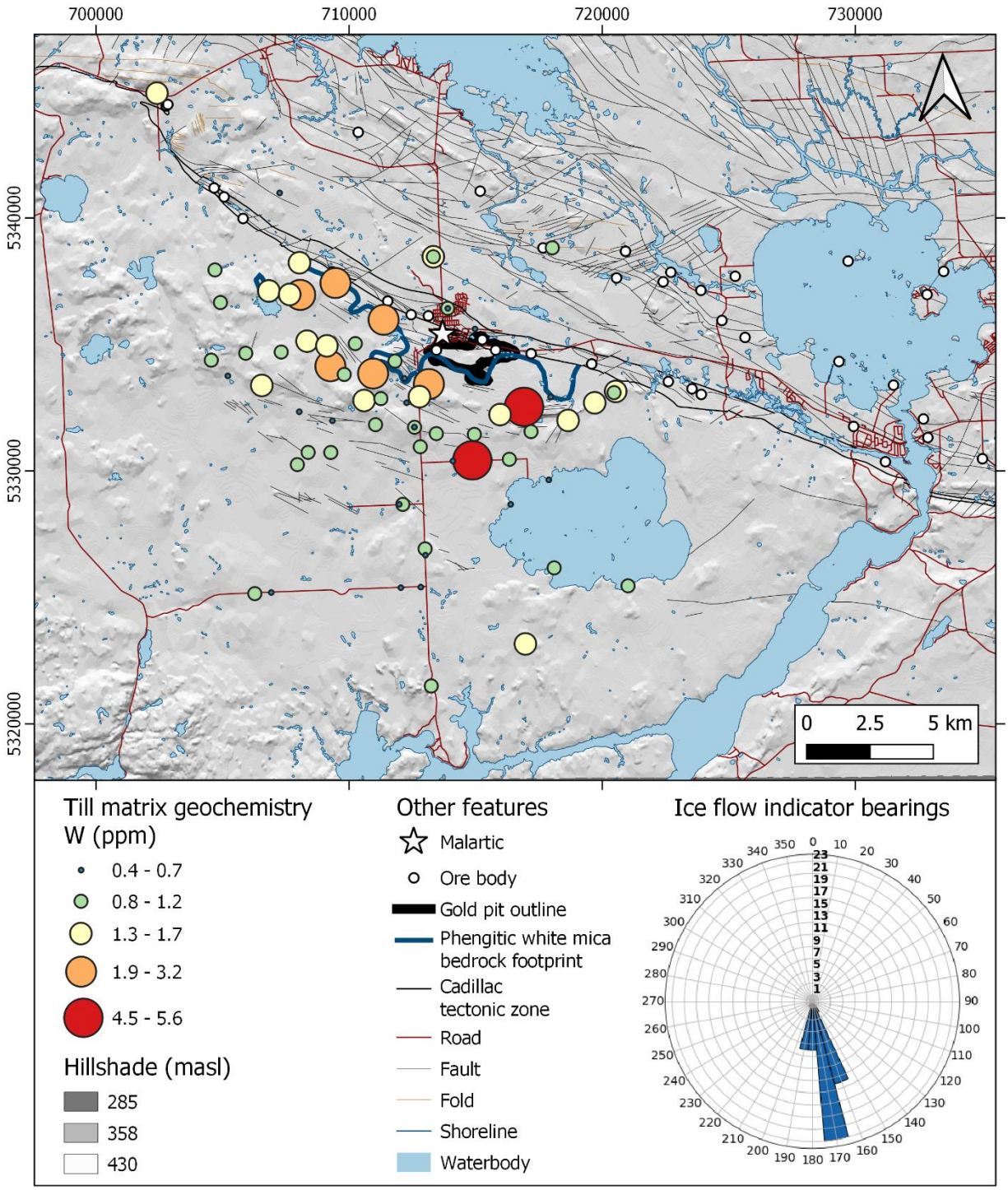

Figure 3.6 Spatial W distribution (ppm) based on till matrix geochemistry (ICP-MS). The gold pit outline and phengitic white mica bedrock footprint are after Lypaczewski et al. (2019). Waterbodies and hillshade are from Natural Resources Canada (https://maps.canada.ca/czs/index-en.html). Ore bodies, Cadillac tectonic zone, roads, faults, folds, and shorelines are from SIGEOM (https://sigeom.mines.gouv.qc.ca/signet/classes/I1108_afchCarteIntr). Coordinate system: NAD 83, UTM zone 17.

3.4.2. Till Matrix Minor & Trace Element Multivariate Analysis

Principal component and k-means clustering analyses were conducted using till matrix (<0.063 mm) minor and trace element geochemical values (elements Ag, Ba, Cs, Mo, Pb, Rb, Sr, and W) for 72 samples. PCA shows that the total variance in the dataset is ~0.3589, and the variance for 90% of the data is ~0.3230. A scree plot shows the first four principal components explain ~90% of the variance (**Figure 3.7)**. The explained variance by the first, second, third, and fourth principal components is ~0.4886, ~0.1822, ~0.1439, and ~0.0753, respectively. **Figure 3.8** shows the minor and trace element PC loadings of the first four principal components. K-means clustering was applied to the PC scores using four principal components. Four clusters were chosen for k-means cluster analysis of this data because this number strikes a balance between a relatively low inertia (i.e. summing the squared distance of each point to its cluster's centroid) score (~9.615) and a low-enough number of clusters that can be used to make reasonable geological inferences (Grunsky, 2010; Wang, 2018). Biplots of PC1 vs PC2, PC1 vs PC3, and PC1 vs PC4 are shown in **Figure 3.9**, **Figure 3.10**, and **Figure 3.11**, respectively.

Table 2.7 summarizes till sample traits by k-means cluster, and **Figure 3.12** presents the spatial distribution of all four clusters throughout the study area superimposed on bedrock geology. Cluster 1 (n = 19) is characterized by the greatest average distance to the pit (7063 m), does not occur on mafic/ultramafic bedrock, and more than half of the samples show "slight" oxidation. This cluster may represent background values with slightly oxidized samples.

Cluster 2 (n = 11) is the smallest and has the second-greatest average distance to the pit (6234 m). Like Cluster 1, it does not occur on mafic/ultramafic bedrock. Cluster 2 has the highest concentration of samples with "unapparent" oxidation and has the greatest average sample depth (8 out of 13 Pionjar drill samples are in this cluster). This cluster may represent background values with unoxidized samples. Cluster 3 (n = 17) is dominated by slightly oxidized samples and has the greatest proportion of samples on top of mafic/ultramafic bedrock.

Cluster 3 is spatially associated with the phengitic white mica bedrock footprint and the deposit (**Figure 3.12**). Cluster 3 samples are all in positive PC1 space (**Figure 3.9–3.11**). Mo has the highest PC1 positive loading (**Figure 3.8**); therefore, Mo is a significant component in this signature. Cluster 4 (n = 25) is the largest and has the shortest average distance to the pit (3901 m) and occurs partly on top of mafic/ultramafic bedrock (**Figure 3.12**).

Overall, these clusters represent distinct compositional spread and variation in till matrix minor and trace element geochemical values, which suggests limited blending/mixing over the study area (~340 km^2), and the distinct signature of Cluster 3 links surficial till to the alteration halo at the Canadian Malartic deposit.

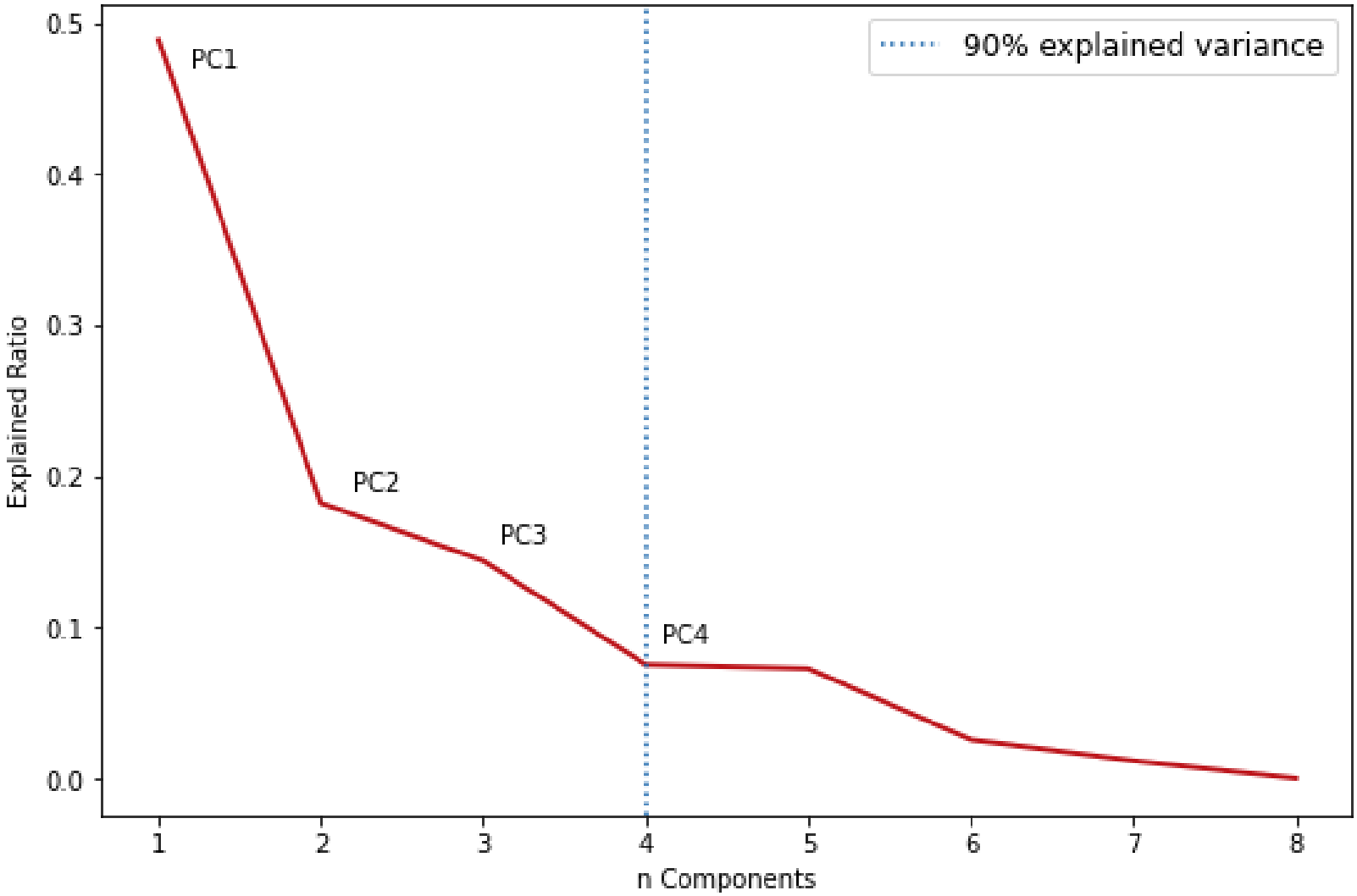

Figure 3.7 Scree plot showing the first 4 principal components explain 90% of the variance in the selected till matrix minor and trace element geochemistry dataset. The explained variance by PC1, PC2, PC3, and PC4 is ~0.4886, ~0.1822, ~0.1439, and ~0.0753, respectively.

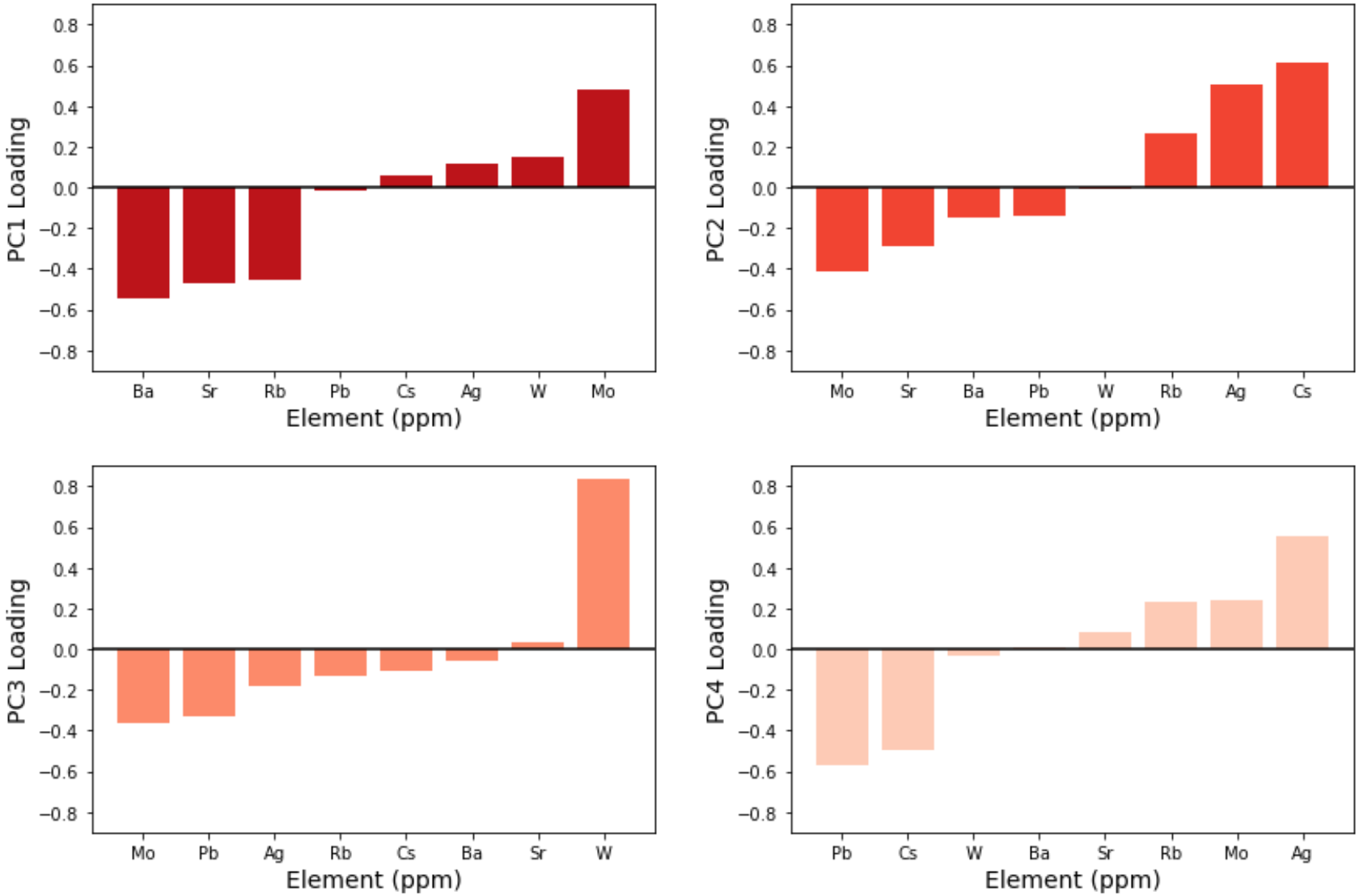

Figure 3.8 Selected minor and trace element principal component (PC) loadings for (a) PC1, (b) PC2, (c) PC3, and (d) PC4. PC loadings are sorted in ascending order in each subfigure.

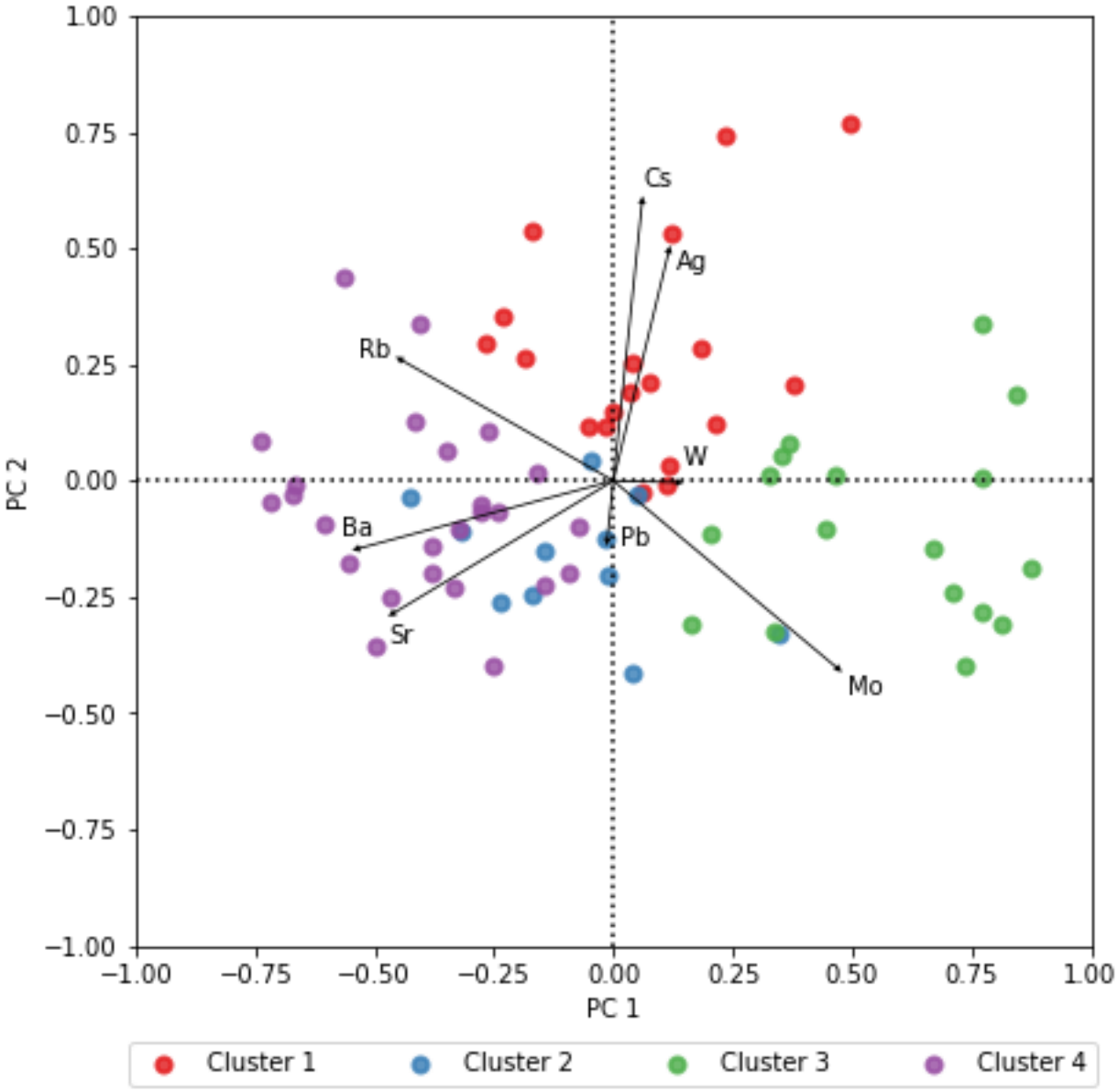

Figure 3.9 Selected till matrix minor and trace element geochemistry principal component (PC) biplot of PC1 vs PC2. Arrows indicate PC loadings and samples are classified according to k-means clustering analysis using 4 k-means clusters.

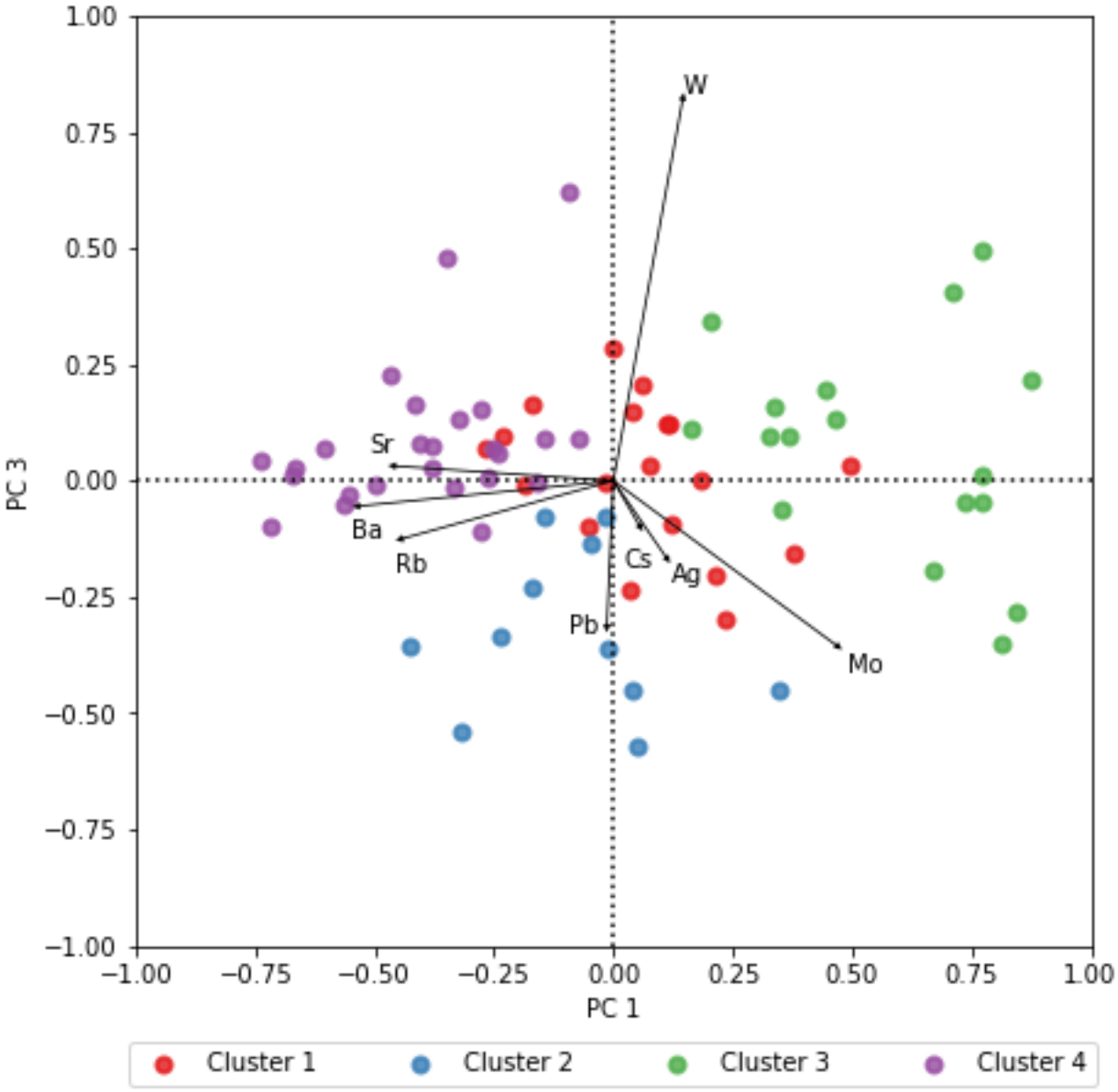

Figure 3.10 Selected till matrix minor and trace element geochemistry principal component (PC) biplot of PC1 vs PC3. Arrows indicate PC loadings and samples are classified according to k-means clustering analysis using 4 k-means clusters.

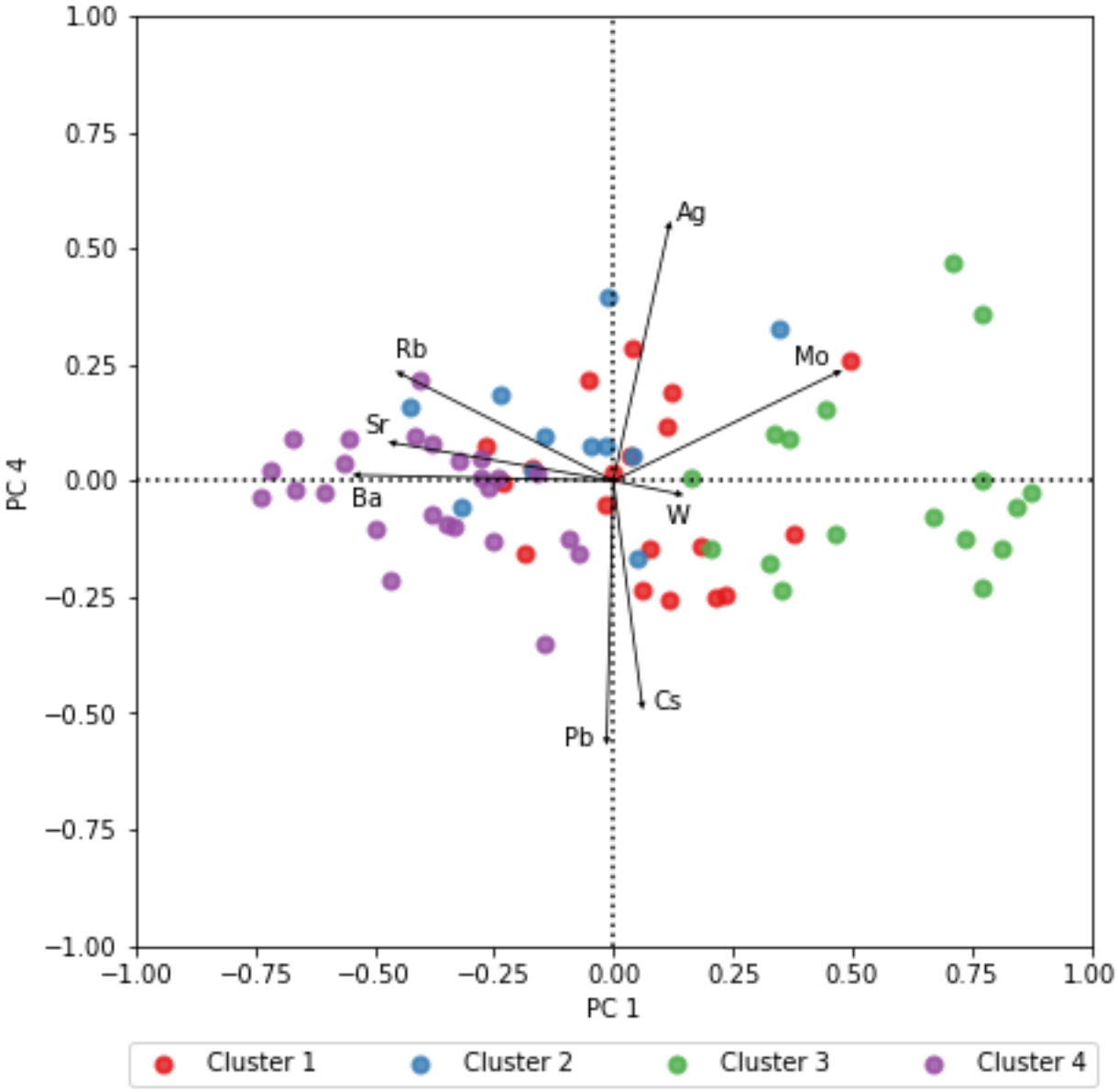

Figure 3.11 Selected till matrix minor and trace element geochemistry principal component (PC) biplot of PC1 vs PC4. Arrows indicate PC loadings and samples are classified according to k-means clustering analysis using 4 k-means clusters.

Table 3.2 Summary of till sample traits by minor and trace element k-means cluster. (Percentages may not total 100 due to rounding).

k-means Cluster	**1 (n = 19)**	**2 (n = 11)**	**3 (n = 17)**	**4 (n = 25)**
Degree of Oxidation (%)				
Unapparent	21	82	24	24
Slight	63	9	41	76
High	16	9	35	0
Underlying Bedrock (%)				
Meta-sedimentary	84	91	76	80
Intrusive	16	9	18	16
Mafic/Ultramafic	0	0	6	4
[a]*Grain Size Category (%)*				
Coarse	24	33	27	8
Medium	59	67	67	75
Fine	18	0	7	17
Averages				
Sample Depth (m)	1.6	2.7	0.7	0.7
Distance to Pit (m)	7063	6234	4115	3901

[a]Values exclude Pionjar samples, which were not categorized based on grain size.

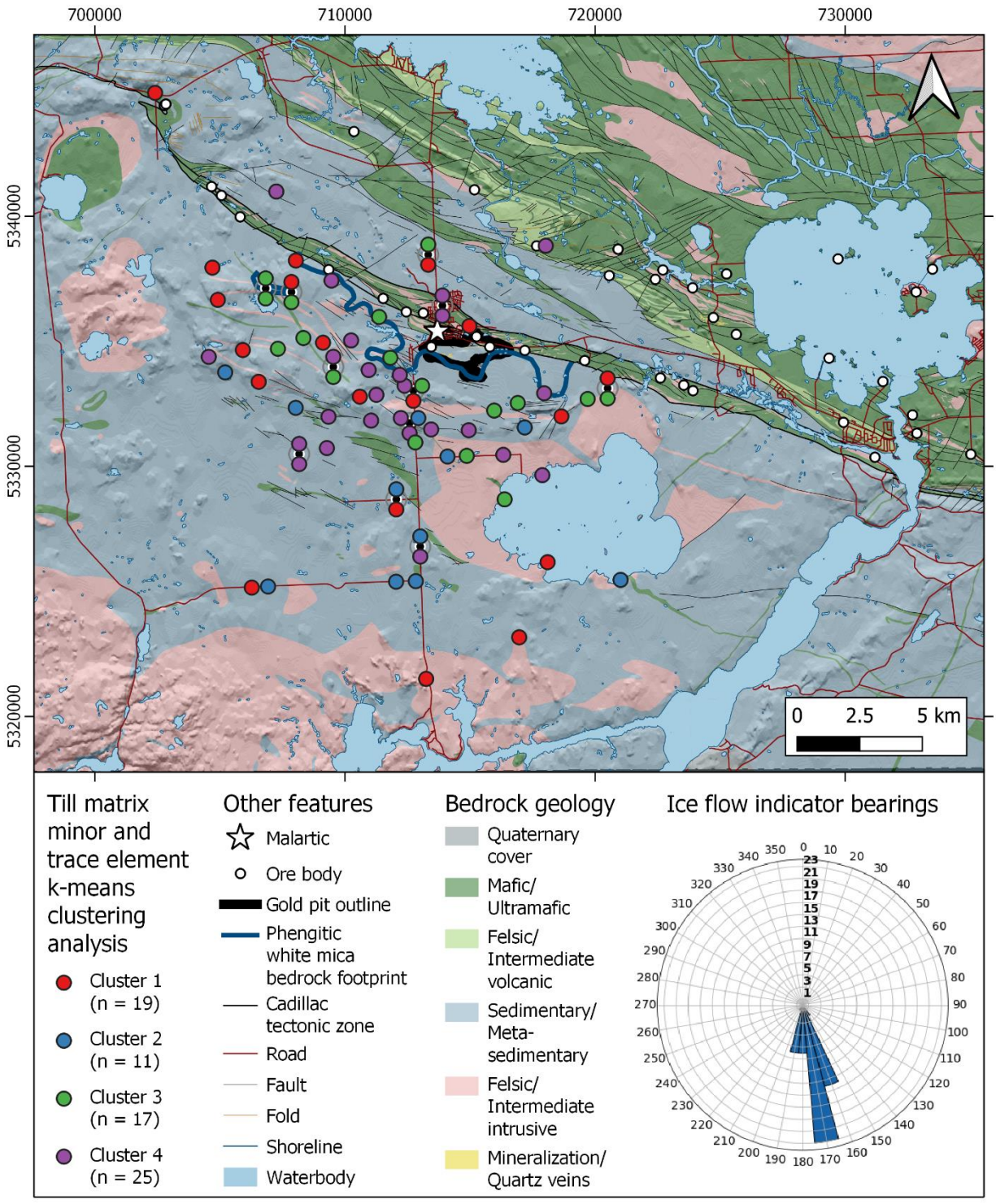

Figure 3.12 Spatial distribution of till matrix minor and trace element k-means clusters in the study area around the Canadian Malartic Mine on bedrock geology and a hillshade elevation model. The gold pit outline and phengitic white mica bedrock footprint are after Lypaczewski et al. (2019). Waterbodies and hillshade are from Natural Resources Canada (https://maps.canada.ca/czs/index-en.html). Bedrock geology, ore bodies, Cadillac tectonic zone, roads, faults, folds, and shorelines are from SIGEOM (https://sigeom.mines.gouv.qc.ca/signet/classes/I1108_afchCarteIntr). Coordinate system: NAD 83, UTM zone 17.

3.4.3. Sand-sized Gold Grain Counts & Morphology

Grain counts of visible gold in till were mapped based on total count and according to grain morphology.

Figure 3.13 shows the spatial distribution of total gold grain counts per 100 g non-magnetic heavy mineral concentrate (HMC). Moderately high (306-326) and high (478) gold grain counts are associated exclusively with the phengitic white mica bedrock footprint on either side of the Canadian Malartic pit at high proximity to the Cadillac tectonic zone.

Figure 3.14 presents the spatial distribution of reshaped gold grain counts per 100 g non-magnetic HMC. Moderate (36-59), moderately high (77-191) and high (326) gold grain counts are associated with the entire length of the phengitic white mica bedrock footprint on either side of the Canadian Malartic pit at high proximity to the Cadillac tectonic zone.

Figure 3.15 depicts the spatial distribution of modified gold grain counts per 100 g non-magnetic HMC. Moderately high (26-77) and high (96) gold grain counts are associated with the phengitic white mica bedrock footprint west of the Canadian Malartic pit at high proximity to the Cadillac tectonic zone.

Figure 3.16 displays the spatial distribution of pristine gold grain counts per 100 g non-magnetic HMC. Moderate (22-35) and high (153-191) gold grain counts are associated with the phengitic white mica bedrock footprint west of the Canadian Malartic pit at high proximity to the Cadillac tectonic zone, and moderately high (50-111) counts occur down-ice of the bedrock footprint on either side of the pit.

Overall, total gold grain counts and counts based on grain morphology are spatially associated with ore bodies related to the Cadillac tectonic zone; however, they do not reveal a dispersion pattern from the Canadian Malartic deposit itself.

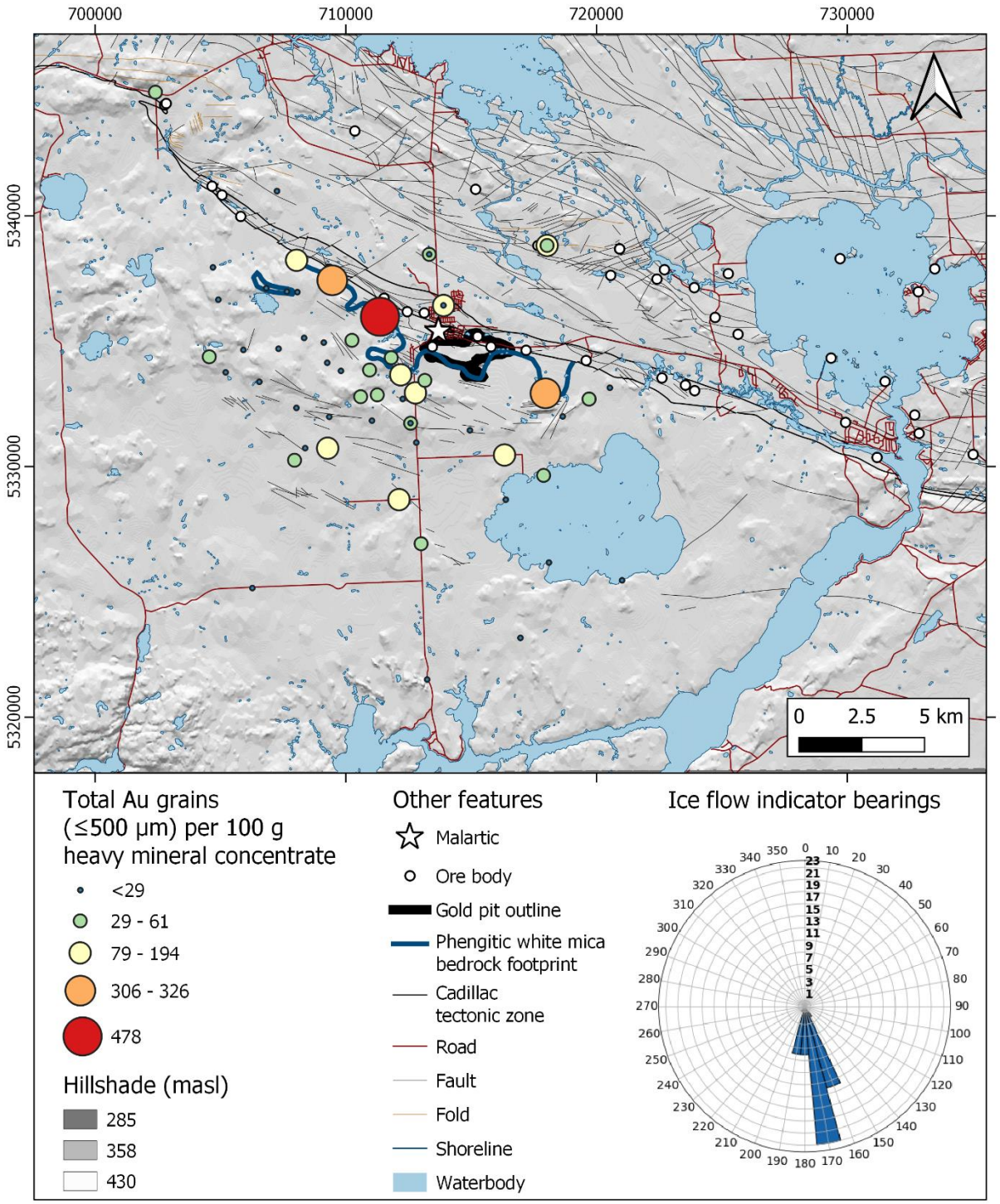

Figure 3.13 Spatial distribution of total gold grain counts in till from non-magnetic heavy mineral concentrate. The gold pit outline and phengitic white mica bedrock footprint are after Lypaczewski et al. (2019). Waterbodies and hillshade are from Natural Resources Canada (https://maps.canada.ca/czs/index-en.html). Ore bodies, Cadillac tectonic zone, roads, faults, folds, and shorelines are from SIGEOM (https://sigeom.mines.gouv.qc.ca/signet/classes/I1108_afchCarteIntr). Coordinate system: NAD 83, UTM zone 17.

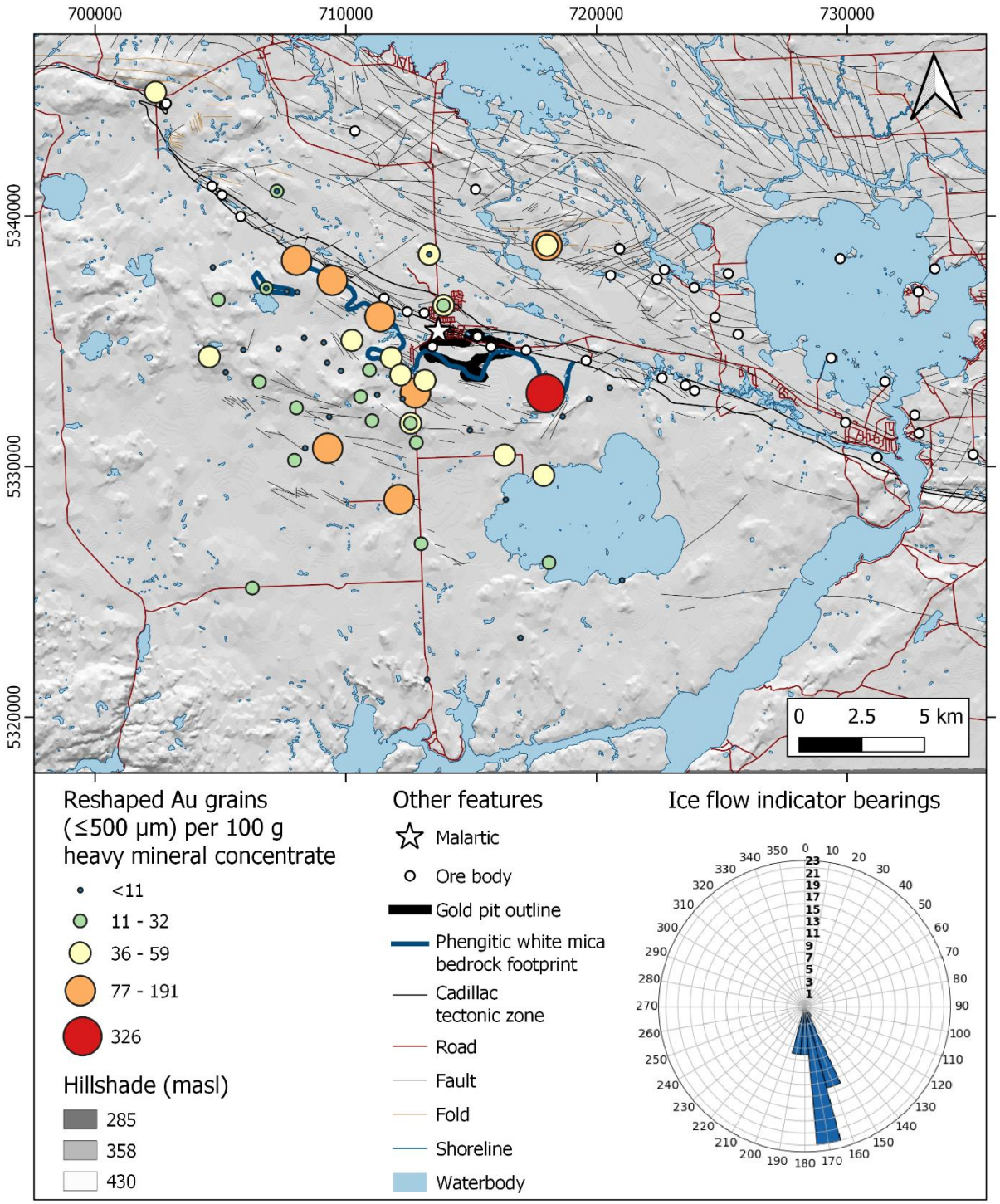

Figure 3.14 Spatial distribution of reshaped gold grain counts in till from non-magnetic heavy mineral concentrate. The gold pit outline and phengitic white mica bedrock footprint are after Lypaczewski et al. (2019). Waterbodies and hillshade are from Natural Resources Canada (https://maps.canada.ca/czs/index-en.html). Ore bodies, Cadillac tectonic zone, roads, faults, folds, and shorelines are from SIGEOM (https://sigeom.mines.gouv.qc.ca/signet/classes/I1108_afchCarteIntr). Coordinate system: NAD 83, UTM zone 17.

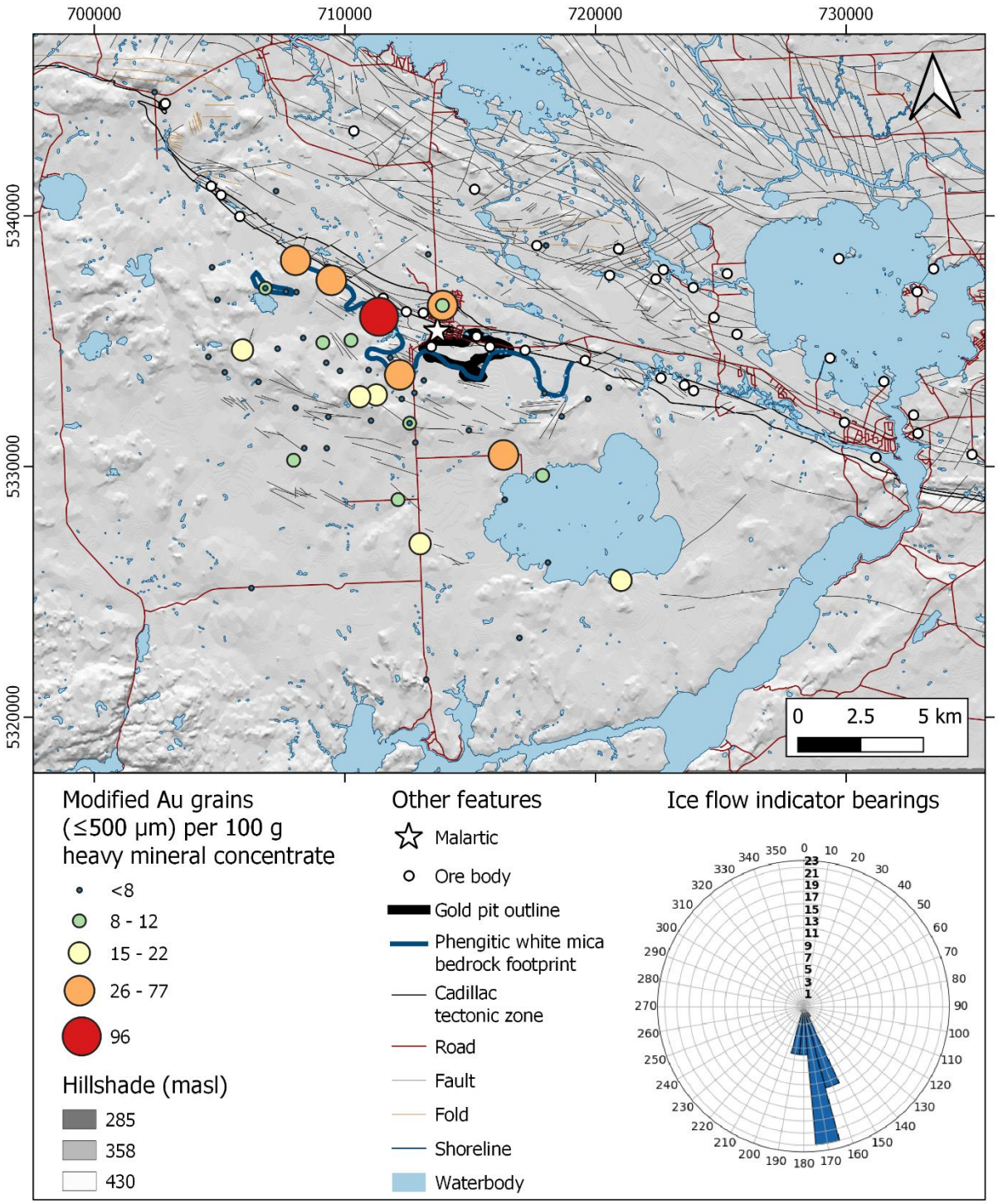

Figure 3.15 Spatial distribution of modified gold grain counts in till from non-magnetic heavy mineral concentrate. The gold pit outline and phengitic white mica bedrock footprint are after Lypaczewski et al. (2019). Waterbodies and hillshade are from Natural Resources Canada (https://maps.canada.ca/czs/index-en.html). Ore bodies, Cadillac tectonic zone, roads, faults, folds, and shorelines are from SIGEOM (https://sigeom.mines.gouv.qc.ca/signet/classes/I1108_afchCarteIntr). Coordinate system: NAD 83, UTM zone 17.

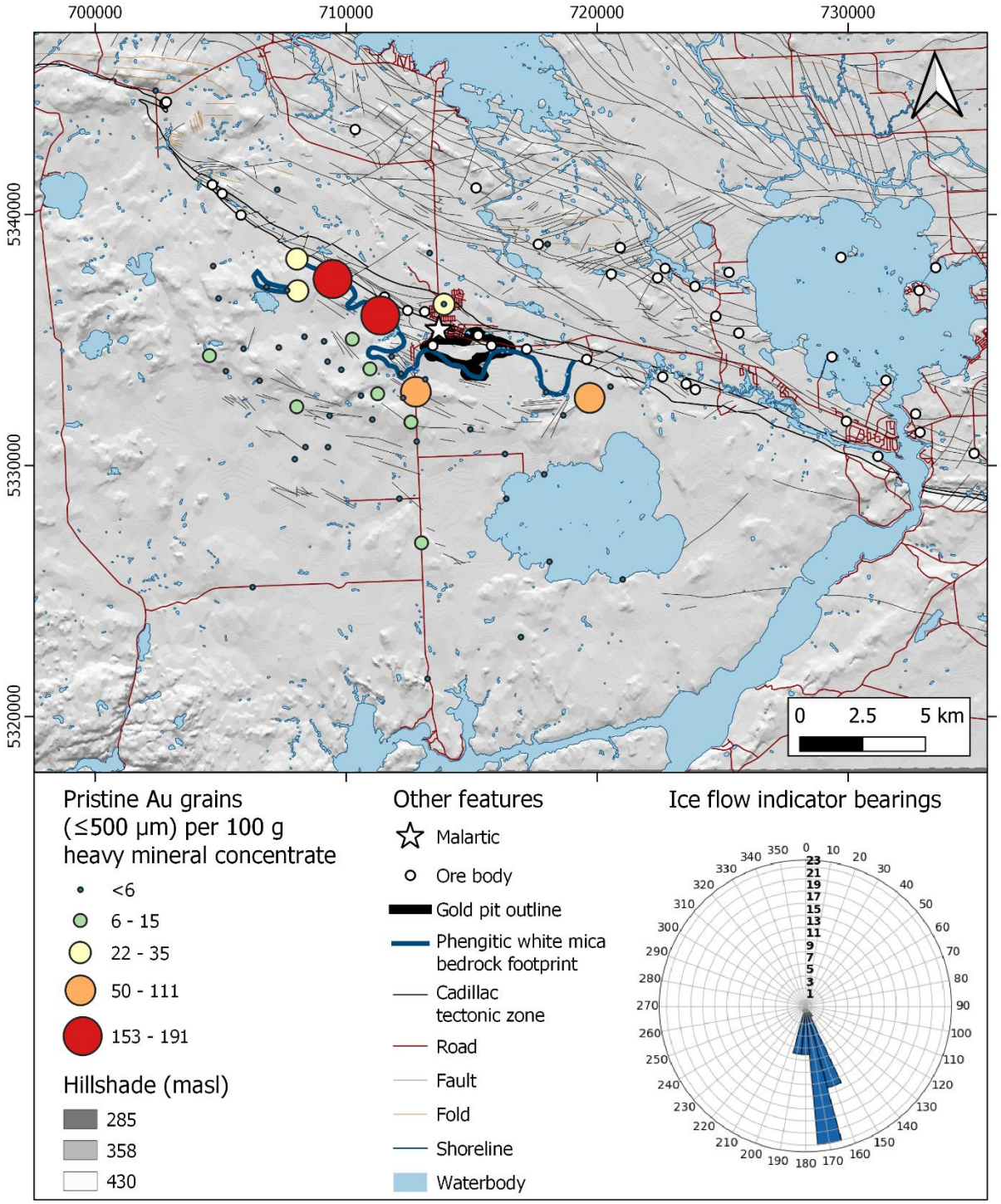

Figure 3.16 Spatial distribution of pristine gold grain counts in till from non-magnetic heavy mineral concentrate. The gold pit outline and phengitic white mica bedrock footprint are after Lypaczewski et al. (2019). Waterbodies and hillshade are from Natural Resources Canada (https://maps.canada.ca/czs/index-en.html). Ore bodies, Cadillac tectonic zone, roads, faults, folds, and shorelines are from SIGEOM (https://sigeom.mines.gouv.qc.ca/signet/classes/I1108_afchCarteIntr). Coordinate system: NAD 83, UTM zone 17.

3.4.4. Dispersion of Glacial Tracer Clasts Using Hyperspectral Imaging Analysis

The dispersion of tracer till clasts containing phengitic white mica and Mg-enriched biotite is significantly more extensive than the phengitic white mica footprint in bedrock, the largest previously identified footprint in bedrock.

Figure 3.17 shows hyperspectral imaging analysis of glacial clasts from till sample SS1. 4-8 mm pebbles and 2-4 mm granules are shown, respectively, with the imaged phengitic white mica (indicator values >2205 nm; measurement range 2190-2215 nm; **Figure 3.17 a** and **b**), Mg-rich biotite (indicator values 2241-2252 nm; measurement range 2240-2255 nm; **Figure 3.17 c** and **d**), and measured values for both indicators were combined per pixel (**Figure 3.17 e** and **f**) and then normalized by the total white mica content (2190-2220 nm) to increase the strength of the signal.

Figure 3.18 depicts the distribution of 2-4 mm glacial (till and esker) tracer clasts and interpolated contours for tracer till clasts. A dispersion train of tracer till clasts is present down-ice from the Canadian Malartic deposit. The train is distinguished by moderate (3-5%) to moderately high (5-7%) indicator mica signature content, which occurs directly down-ice from the Canadian Malartic deposit. This train is relatively long, and the furthest moderate indicator mica signature content (sample CT-054a) occurs 7.8 km down-ice of the gold pit. There is also proximal glacial dispersion from the phengitic white mica bedrock footprint, which is distinguished by moderate (3-5%) to very high (>9%) indicator mica signature content; the highest values are concentrated along its western portion. The minimum curvature interpolated glacial dispersion for the till clasts reveals glacial dispersion covering an area of 58 km^2 at 5% indicator mineral signature content and 111 km^2 at 3% indicator mineral signature content. The phengitic white mica footprint in bedrock is 13 km^2; therefore, the dispersion of 2-4 mm tracer till clasts is 4.5 to 8.4 times larger than the largest previously identified footprint in bedrock. An approximately northwest to southeast transect of tracer esker clast values shows a lateral profile that peaks nearest to the gold pit, excluding the easternmost value at the edge of the study area; however, this is based on a low number of esker clast samples.

Figure 3.19 displays the distribution of 4-8 mm glacial (till and esker) tracer clasts and interpolated contours for tracer till clasts. A dispersion train of tracer till clasts is present down-ice from the Canadian Malartic deposit. The train is distinguished by moderate (3-5%) to high (7-10%) indicator mica signature content, which occurs directly down-ice from the Canadian Malartic deposit. This train is relatively long, and the furthest moderate indicator mica signature content (sample CT-054a) occurs 7.8 km down-ice of the gold pit. There is also glacial dispersion from the phengitic white mica bedrock footprint, which is distinguished by moderately high (5-7%) to very high (>10%) indicator mica signature content; the highest values are concentrated along its western portion. The dispersion of 4-8 mm tracer till clasts from the phengitic white mica bedrock footprint has higher indicator mica signature content while

being larger in extent to that from 2-4 mm tracer till clasts. The minimum curvature interpolated glacial dispersion for the till clasts reveals glacial dispersion covering an area of 77 km^2 at 5% indicator mineral signature content and 148 km^2 at 3% indicator mineral signature content. The phengitic white mica footprint in bedrock is 13 km^2; therefore, the dispersion of 4-8 mm tracer till clasts is 7.0 to 13.5 times larger than the largest previously identified footprint in bedrock. An approximately northwest to southeast transect of tracer esker clast values shows a lateral profile that peaks nearest the gold pit, excluding the easternmost value at the edge of the study area. Once again, this is based on a low number of esker clast samples.

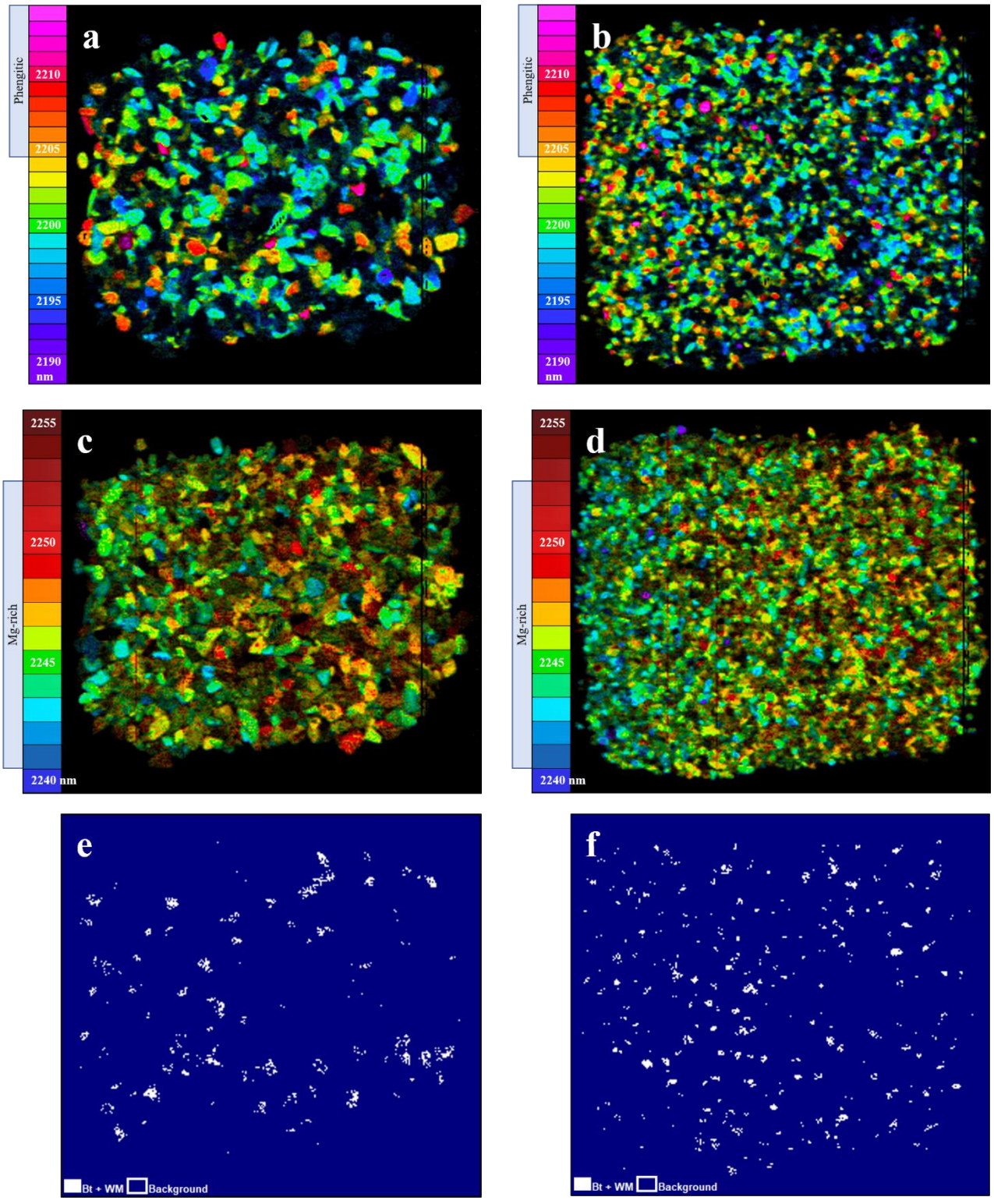

Figure 3.17 Hyperspectral imaging analysis of glacial clasts from till sample SS1. 4-8 mm pebbles and 2-4 mm granules are shown, respectively, with the imaged phengitic white mica (a & b), Mg-rich biotite (c & d), and pixels that contain both indicator micas (e & f). Multiple dashed vertical black and brown lines shown (a to d) are artifacts of the instrument and do not affect indicator content calculations. Abbr: Bt – Mg-rich biotite, WM – phengitic white mica.

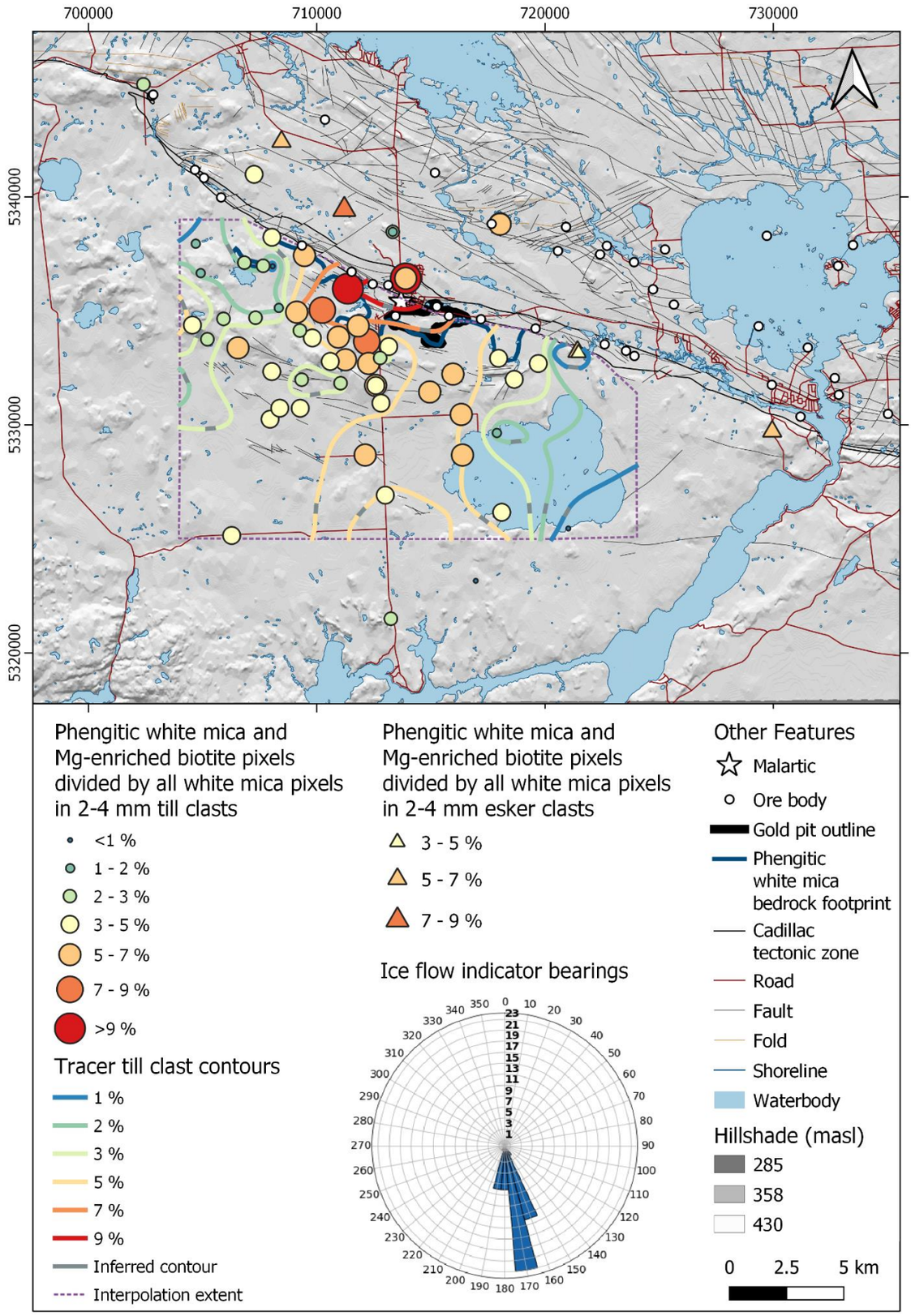

Figure 3.18 Glacial dispersion of tracer till clasts (2-4 mm) with hyperspectral imaging analysis (HIA) indicator signature (pixels with phengitic white mica (2205-2215 nm) and Mg-enriched biotite (2241-2252 nm), divided by all white mica-bearing pixels (2190-2220 nm)) with minimum curvature interpolation (and minimum point pair reconstruction for inferred contour segments). Tracer esker clasts (2-4 mm) with the same HIA indicator signature are shown (excluded from the interpolation). Bedrock footprint shows phengitic white mica (>2205 nm) boundary. The gold pit outline and phengitic white mica bedrock footprint are after Lypaczewski et al. (2019). Waterbodies and hillshade are from Natural Resources Canada (https://maps.canada.ca/czs/index-en.html). Ore bodies, Cadillac tectonic zone, roads, faults, folds, and shorelines are from SIGEOM (https://sigeom.mines.gouv.qc.ca/signet/classes/I1108_afchCarteIntr). Coordinate system: NAD 83, UTM zone 17.

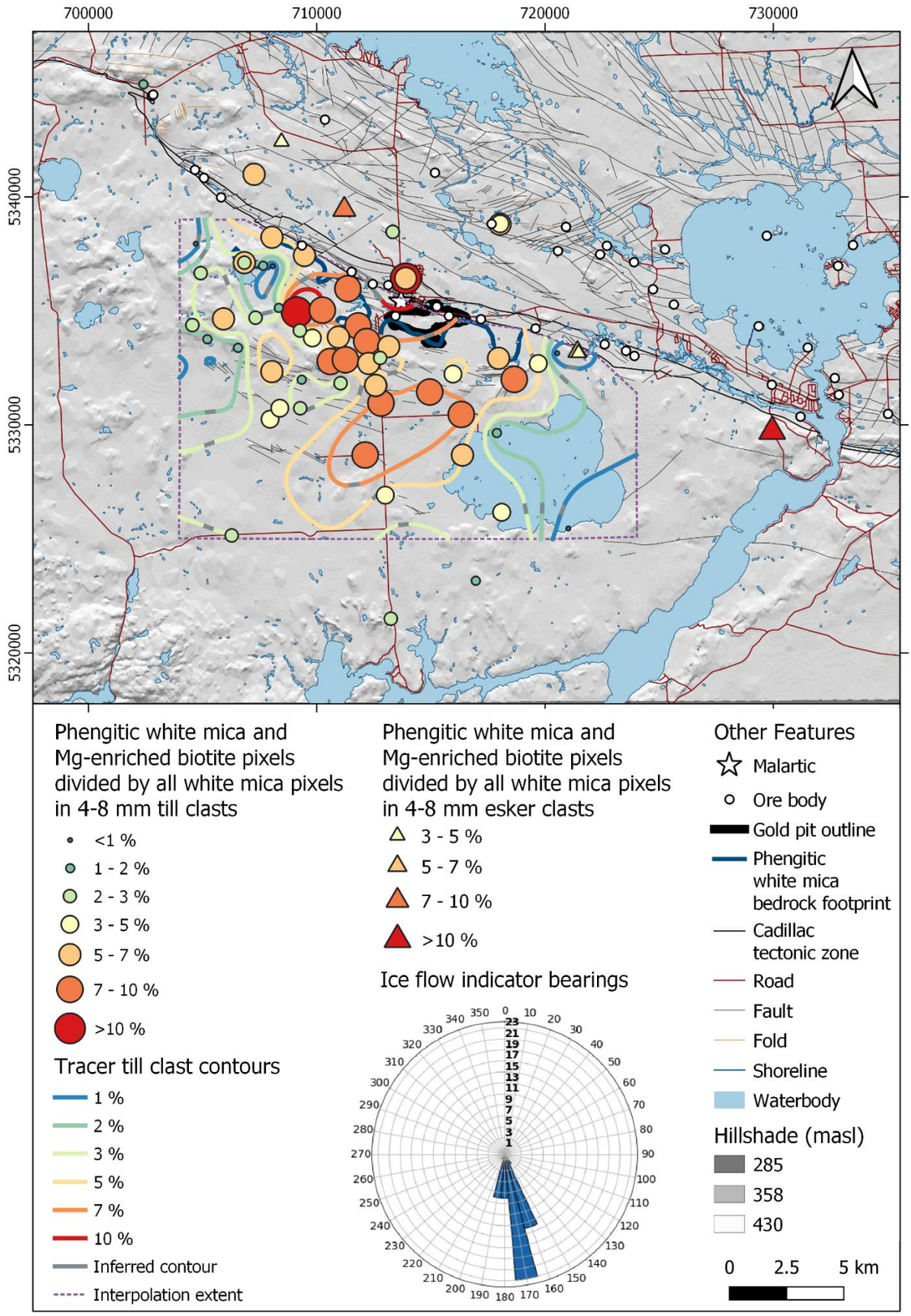

Figure 3.19 Glacial dispersion of tracer till clasts (4-8 mm) with hyperspectral imaging analysis (HIA) indicator signature (pixels with phengitic white mica (2205-2215 nm) and Mg-enriched biotite (2241-2252 nm), divided by all white mica-bearing pixels (2190-2220 nm)) with minimum curvature interpolation (and minimum point pair reconstruction for inferred contour segments). Tracer esker clasts (4-8 mm) with the same HIA indicator signature are shown (excluded from the interpolation). Bedrock footprint shows phengitic white mica (>2205 nm) boundary. The gold pit outline and phengitic white mica bedrock footprint are after Lypaczewski et al. (2019). Waterbodies and hillshade are from Natural Resources Canada (https://maps.canada.ca/czs/index-en.html). Ore bodies, Cadillac tectonic zone, roads, faults, folds, and shorelines are from SIGEOM (https://sigeom.mines.gouv.qc.ca/signet/classes/I1108_afchCarteIntr). Coordinate system: NAD 83, UTM zone 17.

3.4.5. Optical Microscopy of Till Clasts

Optical microscopy results determine that 14 clasts are similar to intrusive and meta-sedimentary host rocks at the Canadian Malartic deposit. They are likely sourced from there due to their proximity to the gold pit. Clasts were classified as similar to host rocks if they contained hydrothermal micas and displayed quartz-monzodioritic, granodioritic textures and mineralogy, or meta-sedimentary textures and mineralogy (Gervais et al., 2014; De Souza et al., 2015; Perrouty et al., 2019; Lypaczewski et al., 2019).

Additionally, one clast in this category was mineralized, i.e. it contained an Au-Te-bearing pyrite grain (identified with SEM-EPMA). This type of mineralization is similar to the ore found at the deposit (Gervais et al., 2014). To my knowledge, this is the first instance of Au identified within a glacial clast using HIA combined with petrography.

Optical microscopy results also determine that 28 clasts are dissimilar to intrusive and meta-sedimentary host rocks at the Canadian Malartic deposit and are likely sourced from elsewhere. Petrographic photos and detailed analysis of all clasts are in the **Appendix**.

Figure 3.20 shows a photo (cross-polarized light) of SS1-5, a mineralized and altered felsic intrusive clast. The clast is characterized by an Au-Te-bearing pyrite grain, fine-grained alteration, possibly albite, K-feldspar, or quartz. It has magmatic plagioclase with corroded margins, and hydrothermal white mica is replacing plagioclase, aligned with twinning. Primary Ti-bearing biotite is altered to produce phlogopite, rutile, and opaques.

Figure 3.21 presents a photo (cross-polarized light) of 36A-3, an altered meta-sedimentary clast. The clast is characterized by a relatively large amount of foliated biotite and a low amount of chlorite, which aligns with the thermal regime at the northern part of the Canadian Malartic deposit. Also, fine white mica is throughout, and pressure shadow quartz is associated with larger biotite grains. This clast may have originated from a siltstone protolith.

Figure 3.22 depicts a photo (plane-polarized light) of SS19-5, a chlorite-rich clast. The abundance of chlorite does not align with the thermal regime found at the deposit. The clast is characterized by phenocrysts that have been replaced by chlorite and have quartz margins, and iron-staining.

Figure 3.23 displays a photo (cross-polarized light) of 63A-4, a tourmaline-rich clast. The clast is characterized by acicular tourmaline, elongated biotite from altered mafic minerals, fine sericite, hematite, and chlorite. This clast appears completely altered, which does not allow for the determination of a protolith.

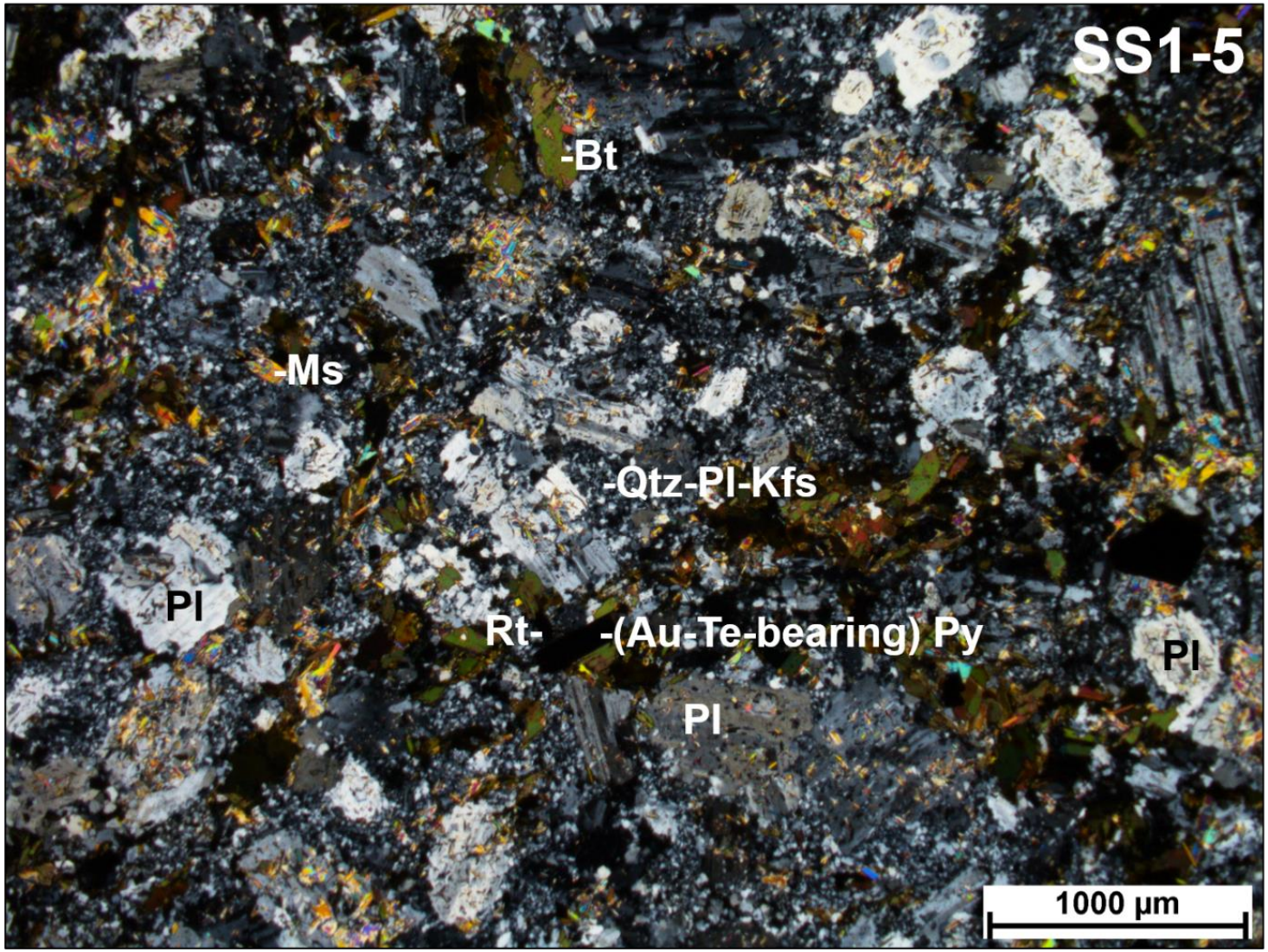

Figure 3.20 Optical microscope photo (cross-polarized light) of clast SS1-5, which is representative of the general texture of an altered felsic-intrusive clast that is like the Canadian Malartic deposit's host quartz-monzodioritic and granodioritic rocks (Gervais et al., 2014; De Souza et al., 2015; Perrouty et al., 2019; Lypaczewski et al., 2019). This clast also contains an Au-Te-bearing pyrite grain (identified with SEM-EPMA). Abbr: Au-Te – gold-telluride, Bt – biotite, Kfs – K-feldspar, Ms – muscovite, Pl – plagioclase, Qtz – quartz, Rt – rutile.

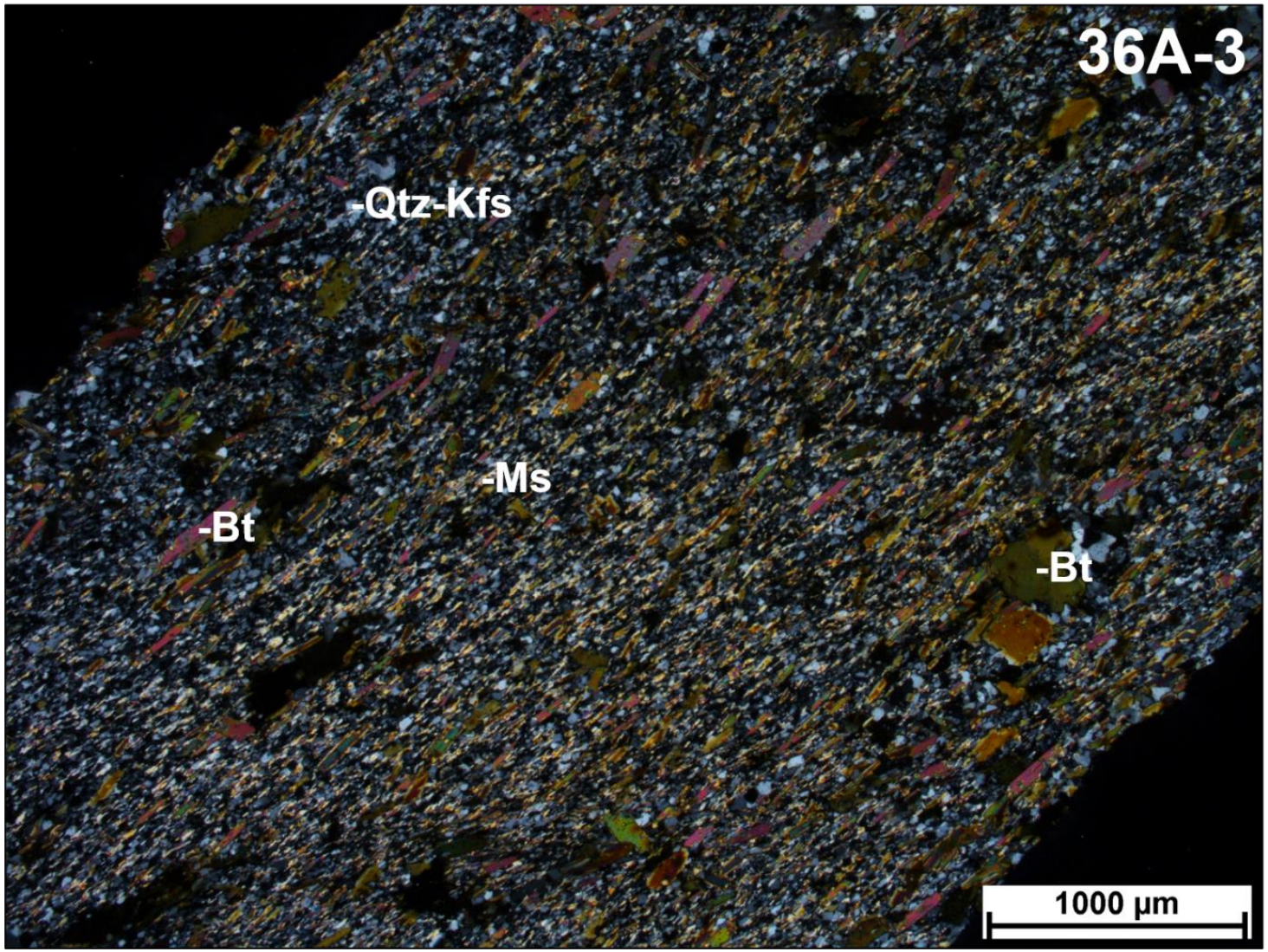

Figure 3.21 Optical microscope photo (cross-polarized light) of clast 36A-3, which is representative of the general texture of an altered meta-sedimentary clast that is like the Canadian Malartic deposit's host meta-sedimentary rocks (Gervais et al., 2014; De Souza et al., 2015; Perrouty et al., 2019; Lypaczewski et al., 2019). Biotite foliation is present, i.e., elongated biotite grains are aligned approximately on a diagonal from the bottom-left to the top-right of the image. Abbr: Bt – biotite, Kfs – K-feldspar, Ms – muscovite, Qtz – quartz, Rt – rutile.

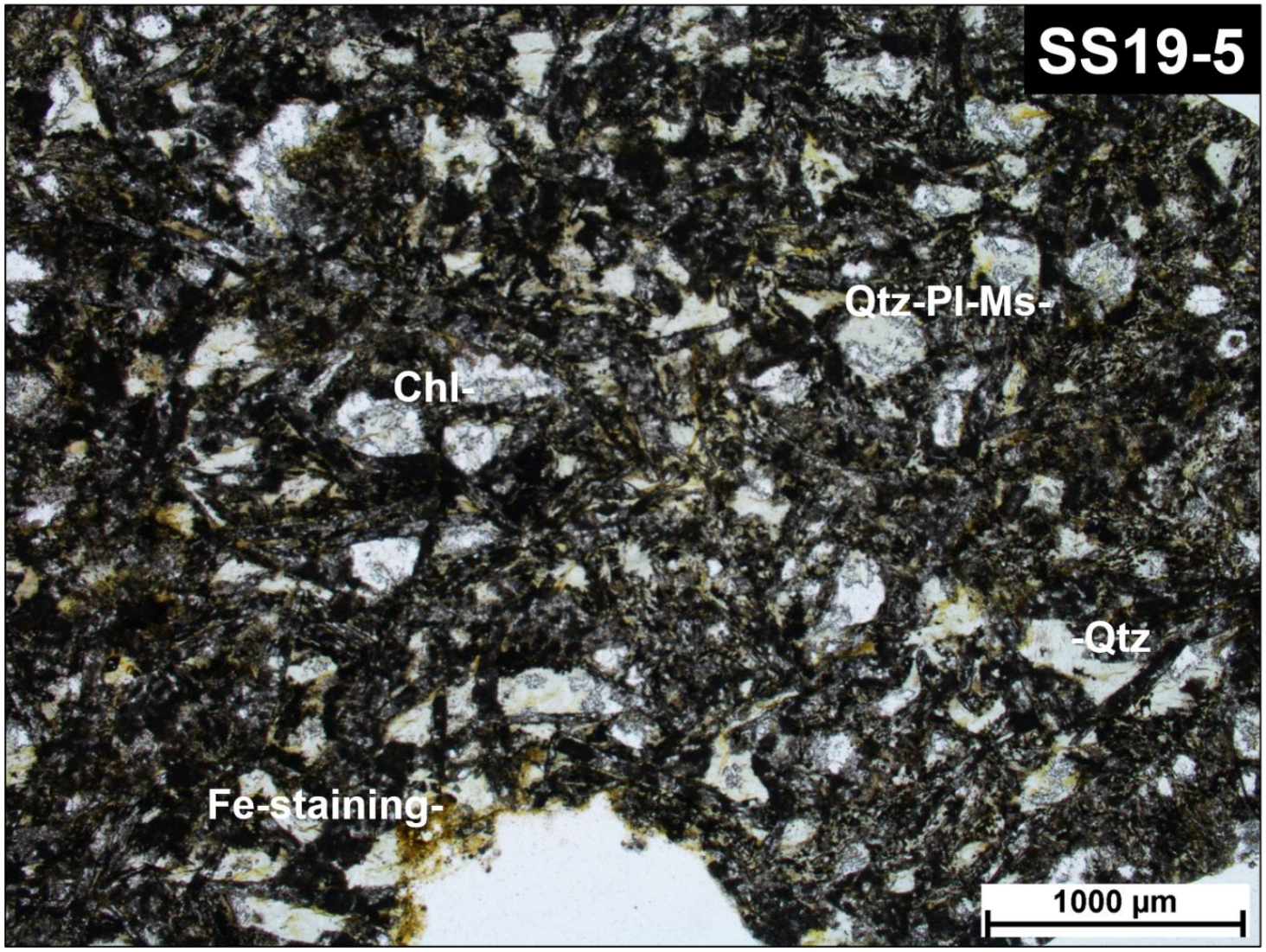

Figure 3.22 Optical microscope photo (plane-polarized light) of clast SS19-5, which shows mineralogy and texture that is chlorite-rich (i.e., dissimilar) relative to the Canadian Malartic deposit's host intrusive and meta-sedimentary rocks (Gervais et al., 2014; De Souza et al., 2015; Perrouty et al., 2019; Lypaczewski et al., 2019). Abbr: Chl – chlorite, Fe – iron, Ms – muscovite, Pl – plagioclase, Qtz – quartz.

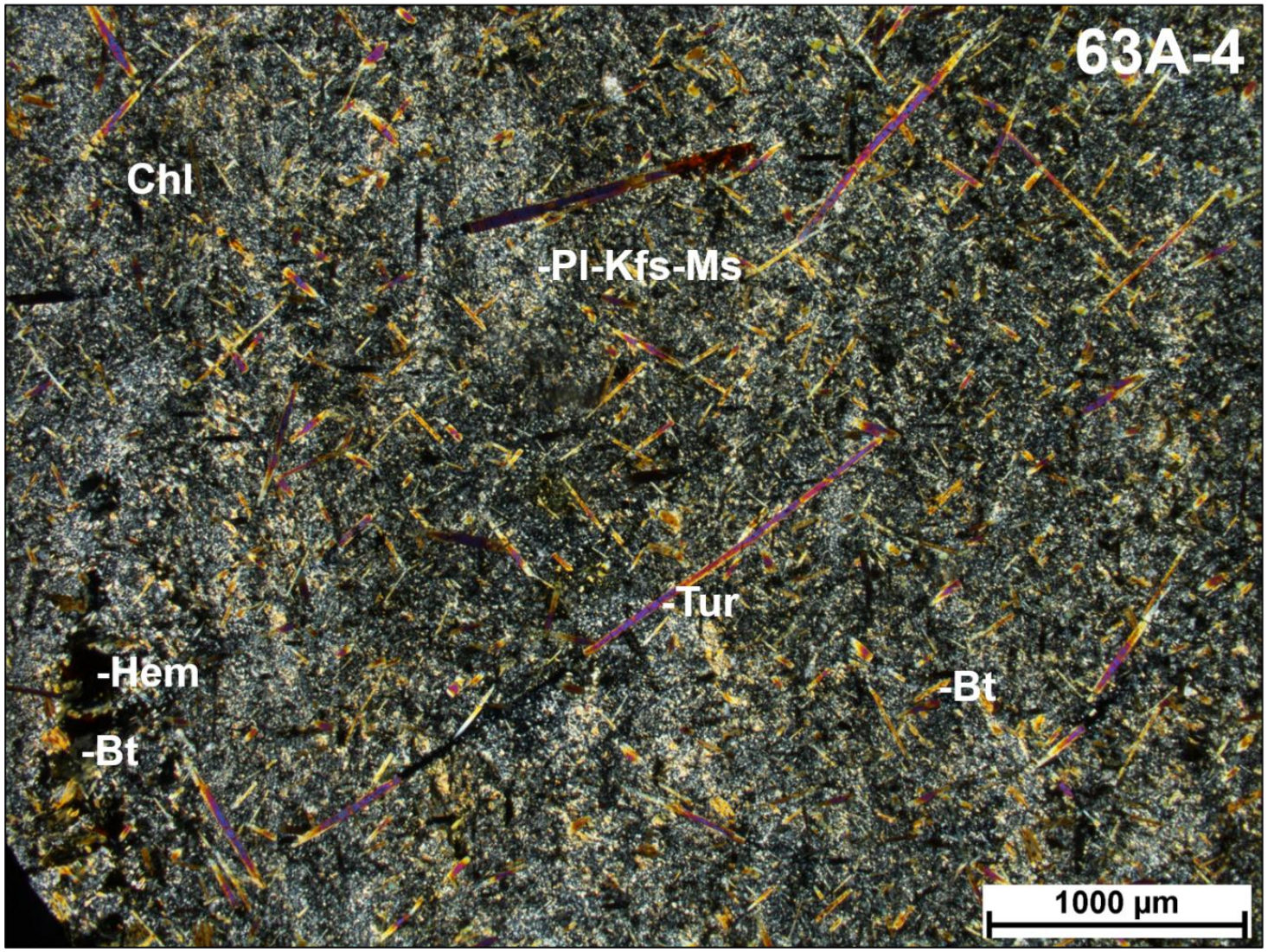

Figure 3.23 Optical microscope photo (cross-polarized light) of clast 63A-4, which shows mineralogy and texture that is tourmaline-rich (i.e., dissimilar) relative to the Canadian Malartic deposit's host intrusive and meta-sedimentary rocks (Gervais et al., 2014; De Souza et al., 2015; Perrouty et al., 2019; Lypaczewski et al., 2019). Abbr: Bt – biotite, Chl – chlorite, Hem- hematite, Kfs – K-feldspar, Ms – muscovite, Pl – plagioclase, Tur – tourmaline.

3.4.6. Scanning Electron Microscopy of Till Clasts

SEM analysis of till clasts that HIA selected revealed a gold-bearing intrusive clast, which has mineralization characteristics of the Canadian Malartic gold deposit. To my knowledge, this is the first documented instance of using HIA, which targeted mineralization-related minerals, followed by petrography, to identify a mineralized till clast. Petrographic photos and detailed analysis of all clasts are in the **Appendix**.

Figure 3.24 shows an SEM image of the highly phengitic intrusive glacial clast SS1-5, highlighting Au-Te mineralization within pyrite. The pyrite grain also contains a speck of monazite, and its margins and fractures are corroded with iron oxide. Further, ilmenite is being replaced by rutile and iron oxide minerals ($FeTiO_3 \rightarrow TiO_2 + Fe_XO_Y$), which is spatially associated with pyrite and is consistent with the mineralization at the Canadian Malartic gold deposit (De Souza et al., 2015). Biotite and muscovite are also spatially associated with pyrite.

Figure 3.25 presents SEM photos of highly phengitic glacial clasts from till with similar characteristics to host quartz-monzodioritic and granodioritic rocks at the Canadian Malartic deposit (Gervais et al., 2014; De Souza et al., 2015; Perrouty et al., 2019; Lypaczewski et al., 2019). (a) captures the mineralogy and texture of intrusive glacial clast SS1-5. This clast contains gold mineralization within pyrite, and rutile and iron oxide mineral replacement of ilmenite, which is spatially associated with pyrite. Apatite was identified in this clast but not captured in this image. Black voids, i.e., 'holes,' in the texture may represent dissolved carbonates in host rocks at the deposit. (b) shows intrusive clast SS9-3 with W-enrichment in a rutile grain and titanite characteristic of intrusive host rocks at the Canadian Malartic gold deposit.

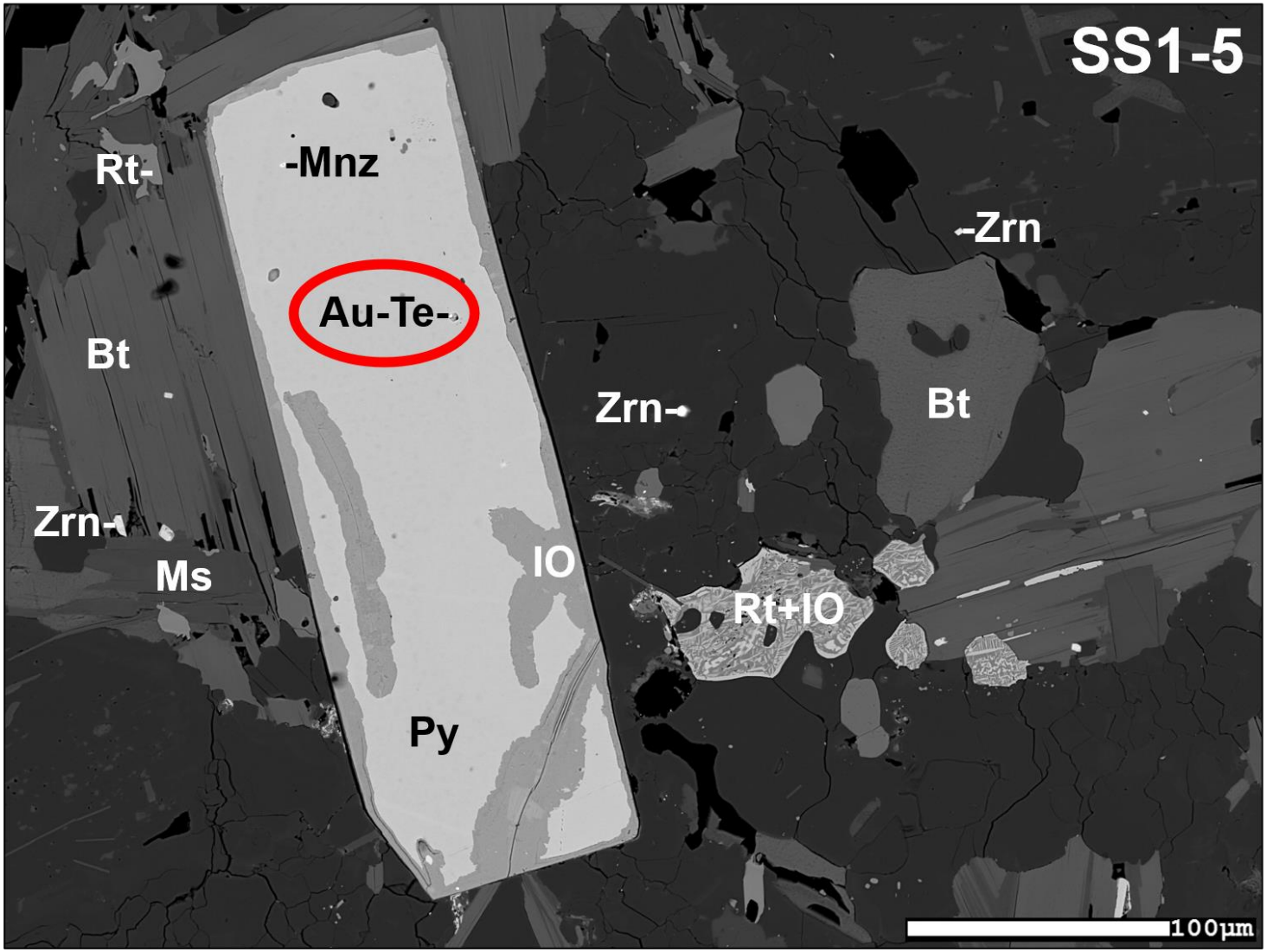

Figure 3.24 SEM image of glacial clast SS1-5 that contains gold mineralization (red oval) within pyrite, which is like the mineralization at the Canadian Malartic deposit (Gervais et al., 2014; De Souza et al., 2015; Perrouty et al., 2019; Lypaczewski et al., 2019). Also, the characteristic replacement of ilmenite with rutile and iron oxide minerals (Rt + IO) is present and spatially associated with pyrite. Abbr: Au-Te – gold-telluride, Bt – biotite, IO – iron oxide, Mnz – monazite, Ms – muscovite, Py – pyrite, Rt – rutile, Zrn – zircon.

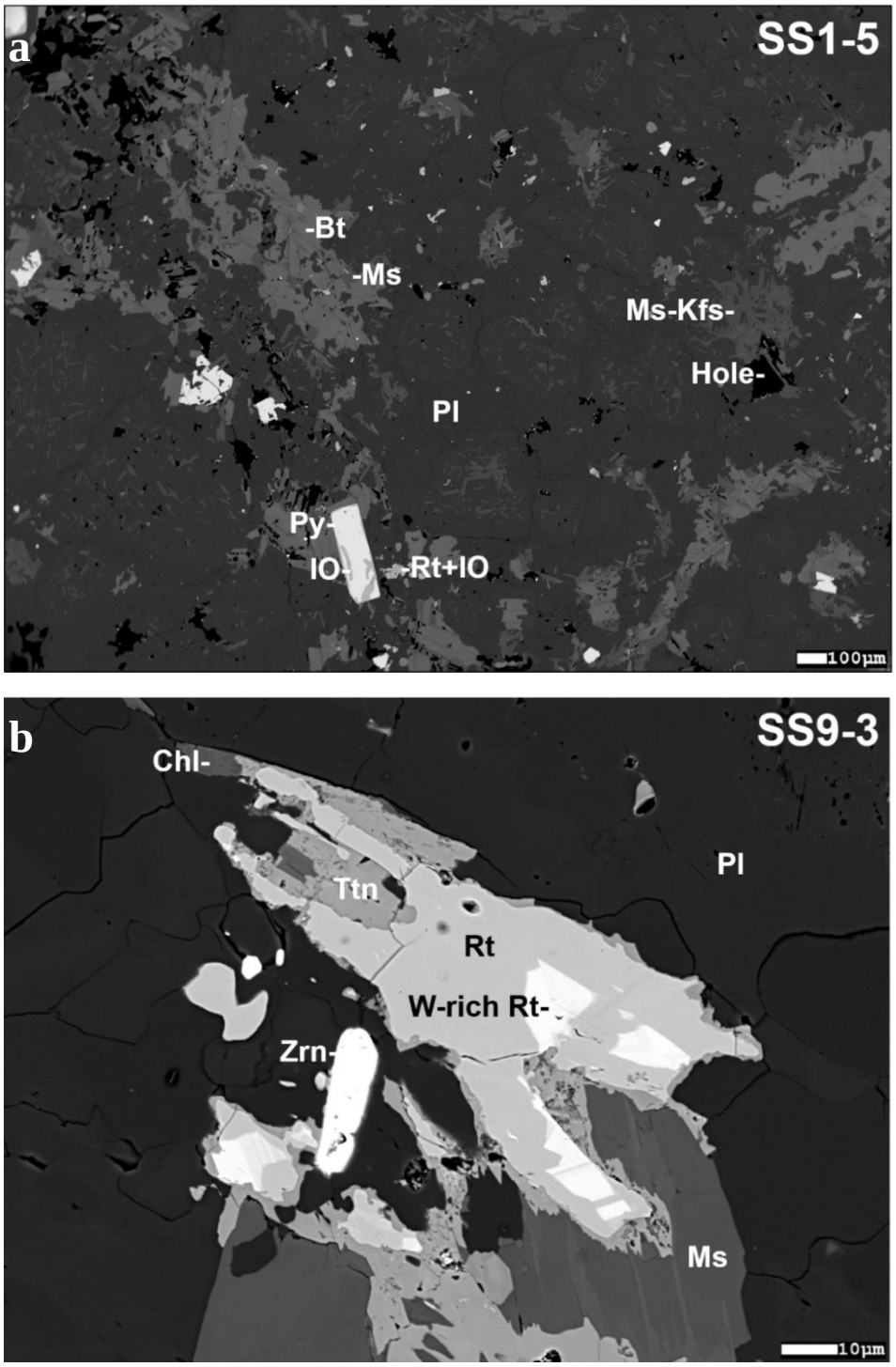

Figure 3.25 SEM photos of highly phengitic glacial clasts from till with characteristics that are associated with host quartz-monzodioritic and granodioritic rocks at the Canadian Malartic deposit (Gervais et al., 2014; De Souza et al., 2015; Perrouty et al., 2019; Lypaczewski et al., 2019). (a) shows the mineralogy and texture of glacial clast SS1-5. This clast contains gold mineralization within pyrite, and rutile and iron oxide mineral replacement that is spatially associated with pyrite. Apatite is present but not shown. 'Holes' in the texture may represent dissolved carbonates. (b) shows clast SS9-3 bearing W-enrichment in a rutile grain. Note that the contrast is slightly different between these images. Abbr: Bt – biotite, Chl – chlorite, IO – iron oxide, Kfs – K-feldspar, Ms – muscovite, Pl – plagioclase, Py – pyrite, Rt – rutile, Ttn – titanite, W – tungsten, Zrn – zircon.

3.5. Discussion

3.5.1. Extending Footprints in Bedrock with a Novel HIA & Drift Prospecting Approach

Hyperspectral imaging analysis of glacial clasts, particularly 4-8 mm pebbles, identifies footprint components in dispersal trains nearing 15 km distance (**Figure 3.19**), which is a meaningful extension to the previously established footprints that occur in bedrock (**Figure 1.9**). **Figure 3.26** presents a schematic emphasizing the significant Quaternary dispersion relative to the previously established footprints at the Canadian Malartic gold deposit.

The AGB has a remarkable concentration of base and precious metal deposits, notably volcanogenic massive sulfide (VMS), magmatic Ni-Cu-PGE, orogenic and porphyry Au deposits (Hufford (2015) and references therein), and diamondiferous kimberlite pipes (Veillette et al., 2005a; McClenaghan et al., 2017). However, prospecting within the AGB is challenging because of widespread surficial sediment cover and the extensive mining history throughout the region. Nonetheless, the Canadian Malartic gold deposit example demonstrates that it may be possible to find even a world-class deposit within a longstanding brownfield with the right innovation.

The results of this chapter are of practical value to interdisciplinary prospectors, and they warrant consideration during the planning and execution of prospecting/exploration campaigns in previously glaciated landscapes. These results may assist in prospecting new high-tonnage, low-grade, disseminated gold deposits within the Abitibi greenstone belt.

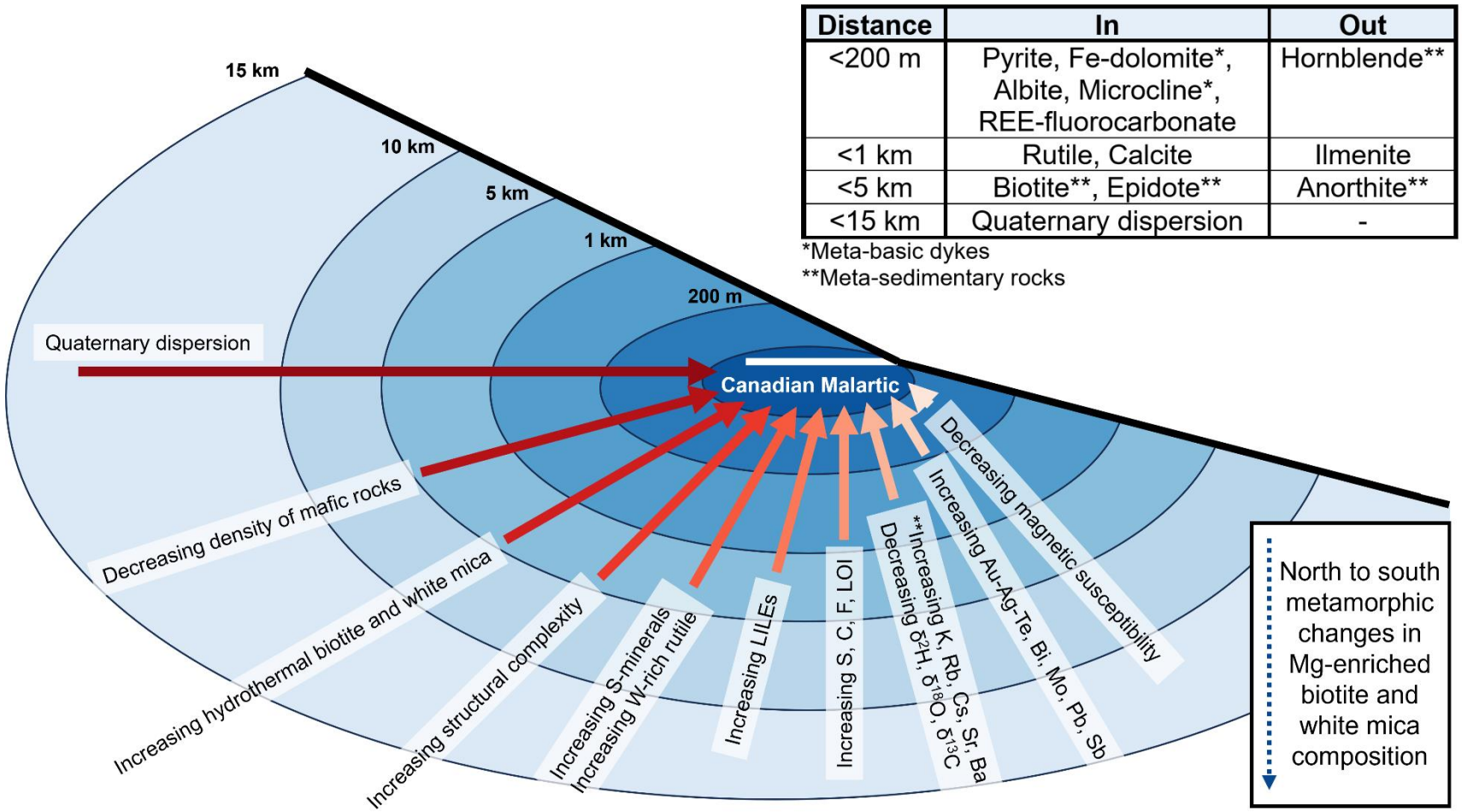

Distance	In	Out
<200 m	Pyrite, Fe-dolomite*, Albite, Microcline*, REE-fluorocarbonate	Hornblende**
<1 km	Rutile, Calcite	Ilmenite
<5 km	Biotite**, Epidote**	Anorthite**
<15 km	Quaternary dispersion	-

*Meta-basic dykes
**Meta-sedimentary rocks

Figure 3.26 Schematic showing the significant Quaternary dispersion relative to the previously established footprints at the Canadian Malartic gold deposit (**Figure 1.9**). Quaternary dispersion nears a distance of 15 km from the deposit, whereas no previously established footprint surpasses a distance of 5 km. Previously established footprints are modified after Lesher et al. (2017).

3.5.2. Opportunities for Future Work Using Hyperspectral Imaging Analysis

Hyperspectral imaging analysis will continue to develop and improve our ability to prospect with its versatility. For example, HIA has the potential to aid in classifying clast lithology, which is part of an in-depth provenance analysis. There are deposit types where the altered rocks are relatively hard and not friable (like kimberlites), meaning they are likely to survive glacial transport and may be used for prospecting. The bulk geochemistry might not be distinguishable, but HIA can be used to pick out these unique characteristics, which are not visible to the naked eye.

The granule and pebble fractions in till do not have an established use in drift prospecting other than in provenance analyses (Broster, 1986; Dilabio, 1990; Trommelen et al., 2013), but the research presented in this chapter demonstrates their utility as exploration vectors, particularly when they preserve mineralization-related alteration haloes from the source bedrock as opposed to direct mineralization.

The best size fraction for analysis would depend on the friability of the rock and might be larger than the pebbles analyzed at Canadian Malartic. Clast screening could be completed in the field, i.e. within a 5 m radius of a sample site. For example, the most significant uranium deposits in the world are found in the Athabasca Basin in Saskatchewan, Canada. There are multiple deeply buried unconformity-type uranium deposits in this basin, which are housed in the basal sandstone Proterozoic Manitou Falls Formation that overlies older basement rocks (Earle, 2001). This region is covered by significant glacial sediments with drift thickness (>5 m) and multiple till sheets. Uranium deposits occur where the sandstone layer tends to be approximately 500 m thick. The minerals associated with alteration are clay minerals such as illite, chlorite, and dravite. These hydrothermal minerals have OH bonds, which can be imaged with hyperspectral imaging analysis. This signature is already established as being effectively preserved in the clast fraction of till in cobbles and boulders, and their composite geochemistry is strongly correlated to that of the Manitou Falls Formation (Earle et al., 1990 in Earle, 2001). Boulder tracing has been used extensively in this region. Pebbles would occur at a higher frequency in the till and may be used to map the dispersion of bedrock alteration haloes to a higher precision. Thin sections of clasts could be investigated to understand mineral assemblages and rock textures. It may also work to do composite geochemical analyses on smaller clasts as they have been done on boulders, but this would be more labour-intensive than HIA.

HIA has separated proximal versus distal pebbles at the Highland Valley Copper Mine in British Columbia, Canada (Reman, 2020). The HIA approach may also apply to other deposit types in resistant bedrock. HIA may also be applicable for in-situ measurements and invaluable feedback during an active exploration campaign. Concerning drift prospecting, this approach could also be used to do far more in-depth esker analyses, but HIA is applicable in other sedimentary environments as well.

3.6. Summary

This chapter reports the application of traditional and novel drift prospecting techniques to the Canadian Malartic gold deposit and its surrounding area.

Results show that applying traditional drift prospecting techniques in the study area effectively uses select (not all) minor and trace elements in the till matrix and is ineffective with sand-sized heavy mineral grains. Till matrix minor and trace element geochemistry reveal glacial dispersal trains for Au, Ag, Rb, W, and potentially Ba, and Mo. Multivariate analysis of these elements suggests trends that are reasonably defined by four principal components and four k-means clusters. Cluster 3 is associated with the phengitic white mica bedrock footprint, and cluster 3 samples are all in positive PC1 space. Mo has the highest PC1 positive loading; therefore, Mo is important in this signature.

The distribution of sand-sized gold grain counts from till and their morphology are associated with the phengitic white mica bedrock footprint; however, there are no apparent glacial dispersal trains down-ice from the Canadian Malartic deposit.

The novel combination of petrography with HIA is an effective drift prospecting technique within the study area. The distribution of till clasts with an indicator mica signature, measurable through HIA, reveals extensive glacial dispersion from the deposit. Dispersal trains of 2-4 mm and 4-8 mm tracer till clasts down-ice from the gold pit are 4.5-8.4 times larger and 7.0-13.5 times larger, respectively, than the phengitic white mica footprint in bedrock, which is the largest previously identified footprint in bedrock. There is also clear glacial dispersion of the phengitic white mica footprint in bedrock, which comes from the deposit. Optical microscopy and SEM of phengitic till clasts (selected through HIA) identified 14 clasts that are similar to host quartz-monzodioritic, granodioritic, and meta-sedimentary rocks at the deposit and 28 clasts that are dissimilar to the target lithologies. One altered felsic intrusive clast is mineralized and contains Au-Te within a pyrite grain, characteristic of the disseminated Au mineralization at the Canadian Malartic deposit, and this is the first reported instance of using HIA to identify an Au-mineralized till clast in glacial sediments.

The concluding chapter will explore research opportunities for future work, such as the applicability of HIA in prospecting for similar Canadian Malartic-type deposits and other deposit types in postglacial and other sedimentary environments.

CHAPTER 4: Conclusions & Opportunities for Future Work

4.1. Research Summary & Contributions

Drift prospecting is a collection of effective exploration techniques that focus on using information about past ice flow and glacial history in an area, as well as using geologic tracers in glacial sediments, which are generally of Quaternary age (2.6 Ma and younger), to vector back to a mineralized bedrock source. Traditional tracers in drift prospecting can be subdivided into anomalous geochemical elements, exotic minerals, and mineralized boulders and cobbles. Using Quaternary sediments for exploration is highly applicable in many parts of Canada because of the country's recent and extensive glacial history (Prest, 1983), as well as in numerous other parts of the world that were covered by ice during the most recent glaciation (Ehlers & Gibbard, 2007).

The most recent glaciation produced extensive surficial sediments, which cover most of Canada's landmass (e.g., Fulton, 1995), including globally important mineral resource-rich areas such as the Abitibi Gold Belt in the AGB. Traditionally, mineral prospectors have been impeded by glacial regolith, but drift prospectors seek to take advantage of surficial sediments when finding new mineral deposits. Drift prospectors sift through glacial sediments and trace anomalous signals from deposits to their bedrock sources (Shilts, 1996). They rely on signs of mineralization through geochemical and mineral indicator analyses and assist their efforts with mineralization-related associations, such as geochemical pathfinder elements specific to deposit types (Rose, Hawkes, & Webb, 1979). Current drift prospecting techniques focus on silt and clay till matrix geochemistry, on sand-sized heavy minerals from till sediments, and on mineralized boulder (and cobble) tracing, as summarized by Thorleifson (Thorleifson, 2017, and references therein) to locate evidence of one or more dispersion trains in glacial sediments and then trace them back to the bedrock source (Dilabio, 1990). Careful analyses are done on all other fractions to extract valuable data, and each fraction is unique in what it preserves, which is no less true of the pebble and cobble fractions.

Successful innovation builds upon a solid foundation of a comprehensive understanding of the region of interest, including but not limited to a synthesized view of the various components of the region's geologic framework and glacial history. Understanding how these various components interact and evolve is necessary to refine existing exploration techniques with practical implications and to develop innovations.

This study applies a much-needed drift prospecting strategy to a resource-rich yet glacially covered Abitibi Gold Belt. We develop an innovative drift prospecting technique by extending concepts from the well-established method of boulder tracing and tailoring it to smaller glacial clast fractions,

specifically cobbles within the 2-4 mm range and pebbles within the 4-8 mm range, which can potentially preserve mineralization-related alteration signatures in competent rock. We then integrate an interdisciplinary approach to measure their dispersal, which occurs commonly on a regional scale. We evaluate the applicability of our new technique by using the Canadian Malartic gold deposit as a case study. We expand on previous project results by using glacially dispersed pathfinder pebbles to search for the most easily identifiable and largest bedrock footprint, which is the hydrothermal mica alteration halo that is measurable with SWIR hyperspectral imaging analysis (Lypaczewski et al., 2019). We compare our new technique to traditional glacial sediment analyses on silt and clay matrix geochemistry, sand-sized detrital gold grains, and pebble lithology. Finally, we discuss our technique's potential applicability to other alteration haloes for other mineral deposit types likely to produce pebbles by sedimentary erosion and transport processes while being responsive to a range of hyperspectral imaging analysis techniques.

Such a shift in strategy makes the exploration target much larger by expanding the search to include the outer envelope of the alteration halo, which is also more likely to intersect the bedrock surface and is thus more accessible to secondary erosional processes than the core of the mineralized system. It is challenging, however, to identify mineralization-related alteration as opposed to working with direct deposit indicators. Alteration in bedrock may not be visible to the naked eye, may be present as anomalies with subtle or indiscernible signals, may be part of overlapping or unclear dispersal patterns in areas with multiple deposits, and may have indicator grains in surficial sediments that are smaller than the conventional sand-sized grain fraction.

Despite these challenges and potential limitations, tracing alteration assemblages in pebbles may have several advantages over traditional techniques. It may thus represent a new and important component of the exploration toolkit in sediment-covered terrains. One important advantage is that pathfinder pebbles represent a rock fragment of the targeted system, as opposed to an admixture of particles such as sediment matrix (silt and clay), whose indicator minerals and geochemical pathfinders may represent a complex signal from multiple sources, especially in a mining district like Abitibi. Another advantage is that new techniques like HIA may apply to pebbles without extensive sample processing, providing a rapid, cost-effective and reliable exploration technique provided some knowledge exists about the alteration system of interest. This new strategy thus can potentially discriminate more readily unique sources with specific alteration signatures within a region of relatively high gold grain background from multiple sources and unclear gold signature or particularly challenging fine gold grain sizes.

4.2. Ongoing Research Questions

There is always an opportunity for progress, and the development of interdisciplinary prospecting techniques is ongoing. As with any project, there remain unanswered research questions.

The spatial distribution of Au (ppb) based on till matrix geochemistry (**Figure 3.3**) shows an elevated value in the southwest corner of the study area. There does not appear to be a reported ore deposit in the up-ice vicinity of that sample location, so one recommendation stemming from this work would be to investigate this anomaly as a potential indicator of an ore deposit.

Sparse and discontinuous till coverage, like at the Canadian Malartic Mine, is an ongoing issue to contend with in some regions with extensive glacial sediments. Till is the material of choice for drift prospecting; therefore, understanding an area's evolving erosional and depositional environment, which produced its modern sediments, is fundamental to any sediment dispersion study.

Other potential research areas concerning the Canadian Malartic deposit include investigating the mass of gold in the sand-sized grain fraction instead of grain counts and morphology. Further, multiple geochemical minor or trace elements remain to be investigated to explore their expression in Quaternary sediments. HIA has many applications, from capitalizing on "pre-washed" clasts within esker deposits to in-situ feedback during fieldwork. Another common problem is prospecting for uranium in areas with thick drift, like in the Athabasca Basin; however, HIA on sedimentary clasts, combined with petrography, may offer valuable information even under these conditions.

The key to ongoing discoveries in the AGB lies in innovative drift prospecting techniques that utilize the extensive surficial cover instead of mistaking it for a limitation. The Canadian Malartic deposit is one example of a recently "re-discovered" high-tonnage, disseminated gold deposit, and other deposits of this type and calibre are likely waiting to be discovered.

References

Agnico Eagle. (2021). Odyssey project

Allmendinger, R. W., Cardozo, N. C., & Fisher, D. (2012). Structural geology algorithms: Vectors & tensors. Cambridge, England: Cambridge University Press.

Anand, R. R., Cornelius, M., & Phang, C. (2007). Use of vegetation and soil in mineral exploration in areas of transported overburden, yilgarn craton, western australia: A contribution towards understanding metal transportation processes. Geochemistry: Exploration, Environment, Analysis, 7(3), 267-288. doi:10.1144/1467-7873/07-142

Antevs, E. (1925). Retreat of the last ice-sheet in eastern canada. Geological Survey of Canada, Memoir, 146, 1-142. doi:10.4095/100850

Averill, S. A. (2001). The application of heavy indicator mineralogy in mineral exploration with emphasis on base metal indicators in glaciated metamorphic and plutonic terrains. Geological Society, London, Special Publications, 185(1), 69-81. doi:10.1144/GSL.SP.2001.185.01.04

Barber, D. C., Dyke, A., Hillaire-Marcel, C., Jennings, A. E., Andrews, J. T., Kerwin, M. W., . . . Gagnon, J. -. (1999). Forcing of the cold event of 8,200 years ago by catastrophic drainage of laurentide lakes. Nature, 400, 344.

Bedeaux, P., Pilote, P., Daigneault, R., & Rafini, S. (2017). Synthesis of the structural evolution and associated gold mineralization of the cadillac fault, abitibi, canada. Ore Geology Reviews, 82(Complete), 49-69. doi:10.1016/j.oregeorev.2016.11.029

Benn, D. (1995). Fabric signature of subglacial till deformation, breidamerkurjökull, iceland. Sedimentology, 42(5), 735-747. doi:10.1111/j.1365-3091.1995.tb00406.x

Benn, D. I., & Evans, D. J. A. (2010). Glaciers and glaciation (2nd ed.). London: Hodder Education.

Bhushan, S., Syed, T. H., Kulkarni, A. V., Gantayat, P., & Agarwal, V. (2017). Quantifying changes in the gangotri glacier of central himalaya: Evidence for increasing mass loss and decreasing velocity doi:10.1109/JSTARS.2017.2771215

Blott, S. J., & Pye, K. (2001). GRADISTAT: A grain size distribution and statistics package for the analysis of unconsolidated sediments. Earth Surface Processes and Landforms, 26(11), 1237-1248. doi:https://doi.org/10.1002/esp.261

Bonham-Carter, G. (2005). Metals in the environment around smelters at rouyn-noranda, quebec, and belledune, new brunswick: Results and conclusions of the GSC MITE point sources project. Geological Survey of Canada, Bulletin, 584, 1-265. doi:10.4095/221047

Boulton, G. S. (1978). Boulder shapes and grain-size distributions of debris as indicators of transport paths through a glacier and till genesis. Sedimentology, 25(6), 773-799. doi:10.1111/j.1365-3091.1978.tb00329.x
Boulton, G. S. (1996). Theory of glacial erosion, transport and deposition as a consequence of subglacial sediment deformation. Journal of Glaciology, 42(140), 43-62. doi:10.3189/S0022143000030525

Brennand, T. A., Shaw, J., & Sharpe, D. R. (1996). Regional-scale meltwater erosion and deposition patterns, northern quebec, canada. Annals of Glaciology, 22, 85-92. doi:10.3189/1996AoG22-1-85-92

Bridgland, D. R. (1986). Clast lithological analysis. Great Britain: Quaternary Research Association. Retrieved from https://books.google.ca/books?id=gWHwAAAAMAAJ

Briggs, I. C. (1974). Machine contouring using minimum curvature. Geophysics, 39(1), 39-48. doi:https://doi.org/10.1190/1.1440410

Broster, B. E., Munn, M. D., & Pronk, A. G. (1997). Inferences on glacial flow from till clast dispersal, waterford area, new brunswick. Géographie Physique Et Quaternaire., 51(1), 29-39. doi:10.7202/004773ar

Broster, B. E. (1986). Till variability and compositional stratification: Examples from the port huron lobe. Canadian Journal of Earth Sciences, 23(11), 1823-1841. doi:10.1139/e86-167

Budd, W. F., & Radok, U. (1971). Glaciers and other large ice masses. Reports on Progress in Physics, 34(1), 1-70. doi:10.1088/0034-4885/34/1/301

Bukhari, S., Eyles, N., Sookhan, S., Mulligan, R., Paulen, R., Krabbendam, M., & Putkinen, N. (2021). Regional subglacial quarrying and abrasion below hard-bedded palaeo-ice streams crossing the Shield–Palaeozoic boundary of central canada: The importance of substrate control. Boreas, 50(3), 781-805. doi:https://doi-org.proxy.lib.uwaterloo.ca/10.1111/bor.12522

Caracciolo, L., Tolosana-Delgado, R., Le Pera, E., von Eynatten, H., Arribas, J., & Tarquini, S. (2012). Influence of granitoid textural parameters on sediment composition: Implications for sediment generation. Sedimentary Geology, 280, 93-107. doi:https://doi-org.proxy.lib.uwaterloo.ca/10.1016/j.sedgeo.2012.07.005

Clark, C. D., Hughes, A. L. C., Greenwood, S. L., Spagnolo, M., & Ng, F. S. L. (2009). Size and shape characteristics of drumlins, derived from a large sample, and associated scaling laws doi:https://doi-org.proxy.lib.uwaterloo.ca/10.1016/j.quascirev.2008.08.035

Clark, P. U. (1987). Subglacial sediment dispersal and till composition. The Journal of Geology, 95(4), 527-541. Retrieved from http://www.jstor.org.proxy.lib.uwaterloo.ca/stable/30081084

Core-Net Spectral Laboratory. (2020). Core-net spectral laboratory. Retrieved from http://coresensing.net/

Cummings, D. I., Kjarsgaard, B. A., Russell, H. A. J., & Sharpe, D. R. (2011). Eskers as mineral exploration tools doi:https://doi-org.proxy.lib.uwaterloo.ca/10.1016/j.earscirev.2011.08.001

De Souza, S., Dubé, B., McNicoll, V. J., Dupuis, C., Mercier-Langevin, P., Creaser, R. A., & Kjarsgaard, I. M. (2015). Geology, hydrothermal alteration, and genesis of the world-class canadian malartic stockwork-disseminated archean gold deposit, abitibi, quebec. (No. 7852).Natural Resources Canada. doi:10.4095/296633 Retrieved from https://geoscan.nrcan.gc.ca/starweb/geoscan/servlet.starweb?path=geoscan/fulle.web&search1=R=296633

Delaney, C. (2001). Esker formation and the nature of deglaciation: The ballymahon esker, central ireland. Northwest Geography, 1, 23-33.

Derry, D. R. (1939). The geology of the canadian malartic gold mine, N. quebec. Economic Geology, 34(5), 495-523. doi:10.2113/gsecongeo.34.5.495

Dilabio, R. N. W. (1990). Glacial dispersal trains. In R. Kujansuu, & M. Saarnisto (Eds.), Glacial indicator tracing (pp. 109-122). Rotterdam: A.A. Balkema.

Dilabio, R. N. W. (1991). Classification and interpretations of the shapes and surface textures of gold grains from till. In G. Herail, & M. Fornari (Eds.), Actes du symposium international sur les gisements alluviaux D'or (pp. 297-313) Retrieved from https://geoscan.nrcan.gc.ca/starweb/geoscan/servlet.starweb?path=geoscan/fulle.web&search1=R=133094

Drake, L. D. (1972). Mechanisms of clast attrition in basal till. GSA Bulletin, 83(7), 2159-2166. doi:10.1130/0016-7606(1972)83[2159:MOCAIB]2.0.CO;2

Dreimanis, A. (1989). Tills: Their genetic terminology and classification. In R. P. Goldthwait, & C. L. Matsch (Eds.), Genetic classification of of glacigenic deposits (pp. 17-84). Rotterdam: Balkema.

Dreimanis, A., & Vagners, U. J. (1971). Bimodal distribution of rock and mineral fragments in basal till. In R. P. Goldthwait (Ed.), Till - A symposium (pp. 237-250). Columbus: Ohio State University Press.

Dreimanis, A. (1990). Formation, deposition, and identification of subglacial and supraglacial tills. In R. Kujansuu, & M. Saarnisto (Eds.), Glacial indicator tracing (pp. 35-59). Rotterdam, Netherlands: A.A. Balkema.

Dyke, A. S., Andrews, J. T., Clark, P. U., England, J. H., Miller, G. H., Shaw, J., & Veillette, J. J. (2002). The laurentide and innuitian ice sheets during the last glacial maximum. Quaternary Science Reviews, 21(1), 9-31. doi:https://doi-org.proxy.lib.uwaterloo.ca/10.1016/S0277-3791(01)00095-6

Ehlers, J., & Gibbard, P. L. (2007). The extent and chronology of cenozoic global glaciation. Quaternary International, 164-165, 6-20. doi:https://doi-org.proxy.lib.uwaterloo.ca/10.1016/j.quaint.2006.10.008

Esri. (2014). ESRI ocean Esri.

Evans, D. J. A. (2018). Till: A glacial process sedimentology (1st ed.) John Wiley & Sons Ltd.

Evans, D. J. A., & Benn, D. I. (2004). A practical guide to the study of glacial sediments. London: Edward Arnold.

Flint, R. F., Sanders, J. E., & Rodgers, J. (1960). Damictite, a substitute term for symmictite. GSA Bulletin, 71(12), 1809-1810. doi:10.1130/0016-7606(1960)71[1809:DASTFS]2.0.CO;2

Fulton, R. J. (1995). Surficial materials of canada ("A" Series Map 1880A ed.) Natural Resources Canada. doi:10.4095/205040

Gaillard, N., Williams-Jones, A. E., Clark, J. R., Lypaczewski, P., Salvi, S., Perrouty, S., . . . Linnen, R. L. (2018). Mica composition as a vector to gold mineralization: Deciphering hydrothermal and metamorphic effects in the malartic district, quebec. Ore Geology Reviews, 95, 789-820. doi:10.1016/j.oregeorev.2018.02.009

Gaillard, N., Williams-Jones, A. E., Clark, J. R., Salvi, S., Perrouty, S., Linnen, R. L., & Olivo, G. R. (2020). The use of lithogeochemistry in delineating hydrothermal fluid pathways and vectoring towards gold mineralization in the malartic district, québec. Ore Geology Reviews, 120, 103351. doi:https://doi.org/10.1016/j.oregeorev.2020.103351

Garrett, R., & Grunsky, E. (2003). S and R functions for the display of thompson-howarth plots. Computers & Geosciences, 29, 239-242. doi:10.1016/S0098-3004(02)00080-8

Gauthier, M. S., Hodder, T. J., Ross, M., Kelley, S. E., Rochester, A., & McCausland, P. (2019). The subglacial mosaic of the laurentide ice sheet; a study of the interior region of southwestern hudson bay. Quaternary Science Reviews, 214, 1-27. doi:https://doi-org.proxy.lib.uwaterloo.ca/10.1016/j.quascirev.2019.04.015

Geikie, A. (1863). On the phenomena of the glacial drift of scotland. Glasgow: Transactions of the Geological Society of Glasgow.

Girard, R., Tremblay, J., Néron, A., Longuépée, H., & Makvandi, S. (2021). Automated gold grain counting. part 2: What a gold grain size and shape can tell! Minerals, 11(4) Retrieved from https://doi.org/10.3390/min11040379

Glasser, N. F., & Bennett, M. R. (2004). Glacial erosional landforms: Origins and significance for palaeoglaciology. Progress in Physical Geography: Earth and Environment, 28(1), 43-75. doi:10.1191/0309133304pp401ra

Google. (2015). Map data ©2015 google

Grunsky, E. (2010). The interpretation of geochemical survey data. Geochemistry-Exploration Environment Analysis - GEOCHEM-EXPLOR ENVIRON ANAL, 10, 27-74. doi:10.1144/1467-7873/09-210

Gunning, H. C., & Ambrose, J. W. (1940). Malartic area, quebec. Geological Survey of Canada, Memoir, 222, 1-142. doi:10.4095/101604

Haldorsen, S. (1978). Glacial comminution of mineral grains. Norsk Geologisk Tidsskri, 58, 241-243.

Haldorsen, S. (1981). Grain-size distribution of subglacial till and its realtion to glacial scrushing and abrasion. Boreas, 10(1), 91-105. doi:10.1111/j.1502-3885.1981.tb00472.x

Hardy, L. (1976). Contribution à l'étude géomorphologique de la portion québécoise des basses terres de la baie de james (Ph.D.). Retrieved from http://digitool.Library.McGill.CA:80/R/-?func=dbin-jump-full&object_id=69198&silo_library=GEN01

Harper, M., Weinstein, B., Tgwoodcock, Simon, C., chebee7i, Morgan, W., . . . Zuidhof, G. (2019). Python-ternary: Ternary plots in python [computer software] Zenodo.

Harris, C. R., Millman, K. J., van der Walt, S. J., Gommers, R., Virtanen, P., Cournapeau, D., . . . Oliphant, T. E. (2020). Array programming with NumPy. Nature, 585(7825), 357-362. doi:10.1038/s41586-020-2649-2

Harris, J. R., Wilkinson, L., & Bernier, M. (2001). Analysis of geochemical data for mineral exploration using a GIS — A case study from the swayze greenstone belt, northern ontario, canada. Geological Society, London, Special Publications, 185(1), 165-200. doi:10.1144/GSL.SP.2001.185.01.08

Helt, K. M., Williams-Jones, A. E., Clark, J. R., Wing, B. A., & Wares, R. P. (2014). Constraints on the genesis of the archean oxidized, intrusion-related canadian malartic gold deposit, quebec, canada. Economic Geology, 109(3), 713-735. doi:10.2113/econgeo.109.3.713

Hildes, D. H. D., Clarke, G. K. C., Flowers, G. E., & Marshall, S. J. (2004). Subglacial erosion and englacial sediment transport modelled for north american ice sheets. Quaternary Science Reviews, 23(3), 409-430. doi:https://doi-org.proxy.lib.uwaterloo.ca/10.1016/j.quascirev.2003.06.005

Hirvas, H., & Nenonen, K. (1990). Field methods for glacial indicator tracing. In R. Kujansuu, & M. Saarnisto (Eds.), Glacial indicator tracing (pp. 217-246). Rotterdam: A. A. Balkema.

Hodder, T. J., Ross, M., & Menzies, J. (2016). Sedimentary record of ice divide migration and ice streams in the keewatin core region of the laurentide ice sheet. Sedimentary Geology, 338, 97-114. doi:https://doi-org.proxy.lib.uwaterloo.ca/10.1016/j.sedgeo.2016.01.001

Holt, J. W., Safaeinili, A., Plaut, J. J., Head, J. W., Phillips, R. J., Seu, R., . . . Gim, Y. (2008). Radar sounding evidence for buried glaciers in the southern mid-latitudes of mars. Science, 322(5905), 1235-1238. doi:10.1126/science.1164246

Hufford, G. (2015). Tectono-hydrothermal evolution of the neoarchean abitibi greenstone belt, canada Retrieved from http://hdl.handle.net/11124/170007

Huintjes, E., Neckel, N., Hochschild, V., & Schneider, C. (2015). Surface energy and mass balance at purogangri ice cap, central tibetan plateau, 2001–2011. Journal of Glaciology, 61(230), 1048-1060. doi:10.3189/2015JoG15J056

Irvine-Fynn, T., Hodson, A. J., Moorman, B. J., Vatne, G., & Hubbard, A. L. (2011). Polythermal glacier hydrology: A review. Reviews of Geophysics, 49(4) doi:10.1029/2010RG000350

Iverson, N. R. (2012). A theory of glacial quarrying for landscape evolution models. Boulder, CO] : Geological Society of America. doi:10.1130/G33079.1

J. D. Hunter. (2007). Matplotlib: A 2D graphics environment doi:10.1109/MCSE.2007.55

Jackson, S. L., & Cruden, A. R. (1995). Formation of the abitibi greenstone belt by arc-trench migration. Geology, 23(5), 471-474. doi:https://doi.org/10.1130/0091-7613(1995)023<0471:FOTAGB>2.3.CO;2

Jari, M. (1995). Effects of grinding and chemical factors on the generation and composition of the till fine fraction: An experimental study doi:https://doi-org.proxy.lib.uwaterloo.ca/10.1016/0375-6742(95)00008-D

Jenner, G. A. (1996). Trace element geochemistry of igneous rocks: Geochemical nomenclature and analytical geochemistry. In D. A. Wyman (Ed.), Trace element geochemistry of volcanic rocks: Applications for massive sulfide exploration (pp. 51-77) Geological Association of Canada.

Kelley, S. E., Ross, M., Elliott, B., & Normandeau, P. X. (2019). Effect of shifting ice flow and basal topography in shaping three-dimensional dispersal patterns, lac de gras region, northwest territories, canada. Journal of Geochemical Exploration, 199, 105-127. doi:10.1016/j.gexplo.2019.01.012

Kington, J. (2020). Mplstereonet [computer software]

Klassen, R. A., & Bolduc, A. (1984). Ice flow directions and drift composition, churchill falls, labrador. Geological Survey of Canada, Paper, 84-1A, 255-258. doi:10.4095/119673

Klassen, R. A. (2001). A quaternary geological perpective on geochemical exploration in glaciated terrain. Geological Society, London, Special Publications, 185(1), 1-17. doi:10.1144/GSL.SP.2001.185.01.01

Kleman, J., & Borgstrom, I. (1996). Reconstruction of palaeo-ice sheets: The use of geomorphological data. Earth Surface Processes and Landforms, 21(10), 893-909. doi:10.1002/(SICI)1096-9837(199610)21:10<893::AID-ESP620>3.0.CO;2-U

Larson, P. C., & Mooers, H. D. (2004). Glacial indicator dispersal processes: A conceptual model. Boreas, 33(3), 238-249. doi:10.1111/j.1502-3885.2004.tb01144.x

LaSalle, P., Warren, B., Jacob, H. L., & Gilbert, P. (1975). Échantillonnage du till en profondeur en abitibi, québec. ().Ministère des Richesses naturelles.

LaSalle, Y., LaSalle, P., & Beaumier, M. (2005). Fractions lithiques et minéralogiques du till de base de la partie sud de l'abitibi (données numériques du MB 85-29). ().Ministère des Ressources naturelles et de la Faune.

Lavallab. (2020). Nanometric particle size analyzer analysette 22 NanoTec. Retrieved from https://lavallab.com/products/particle-size-analyzers/nano-particle-sizer/

Lee, S., Wolberg, G., & Shin, S. Y. (1997). Scattered data interpolation with multilevel B-splines doi:10.1109/2945.620490

Lepper, K., Gorz, K. L., Fisher, T. G., & Lowell, T. V. (2011). Age determinations for glacial lake agassiz shorelines west of fargo, north dakota, USA. Canadian Journal of Earth Sciences, 48(7), 1199-1207. doi:10.1139/e11-025

Lesher, M., El Goumi, N., Layton-Matthews, D., Piette-Lauzière, N., & William-Jones, A. (2017). Integrated multi-parameter Footprints of the canadian malartic disseminated au , McArthur river-millennium unconformity U , and highland valley porphyry cu deposits : Preliminary results from the NSERC-CMIC mineral Footprints research network. Paper presented at the Exploration 17: Sixth Decennial International Conference on Mineral Exploration, 325-347.

Lintern, M., Anand, R., Ryan, C., & Paterson, D. (2013). Natural gold particles in eucalyptus leaves and their relevance to exploration for buried gold deposits. Nature Communications, 4(1), 2614. doi:10.1038/ncomms3614

Lowell, T. V., Kite, J. S., Calkin, P. E., & Halter, E. F. (1990). Analysis of small-scale erosional data and a sequence of late pleistocene flow reversal, northern new england. GSA Bulletin, 102(1), 74-85. doi:10.1130/0016-7606(1990)102<0074:AOSSED>2.3.CO;2

Lundqvist, J. (1990). Glacial morphology as an indicator of the direction of glacial transport. In R. Kujansuu, & M. Saarnisto (Eds.), Glacial indicator tracing (pp. 61-70). Rotterdam, Netherlands: A.A. Balkema.

Lypaczewski, P., Rivard, B., Gaillard, N., Perrouty, S., Piette-Lauzière, N., Bérubé, C. L., & Linnen, R. L. (2019). Using hyperspectral imaging to vector towards mineralization at the canadian malartic gold deposit, québec, canada. Ore Geology Reviews, 111, 102945. doi:10.1016/j.oregeorev.2019.102945

MacGregor, K. R., Anderson, R. S., Anderson, S. P., & Waddington, E. D. (2000). Numerical simulations of glacial-valley longitudinal profile evolution. Geology, 28(11), 1031-1034. doi:10.1130/0091-7613(2000)28<1031:NSOGLP>2.0.CO;2

McClenaghan, M. B. (2001). Regional and local-scale gold grain and till geochemical signatures of lode au deposits in the western abitibi greenstone belt, central canada. Geological Society, Special Publication, 185, 201-224. doi:10.1144/gsl.sp.2001.185.01.09

McClenaghan, M. B. (2005). Indicator mineral methods in mineral exploration. Geochemistry Exploration Environment Analysis, 5, 233-245. doi:10.1144/1467-7873/03-066

McClenaghan, M. B., & Cabri, L. (2011). Review of gold and platinum group element (PGE) indicator minerals methods for surficial sediment sampling. Geochemistry Exploration Environment Analysis, 11, 251-263. doi:10.1144/1467-7873/10-IM-026

McClenaghan, M. B., Kjarsgaard, I. M., & Kjarsgaard, B. A. (2017). Reconnaissance-scale till survey in the new liskeard-temagami region, ontario: Kimberlite indicator minerals and geochemistry. (No. 4086). Ottawa, Canada: Natural Resources Canada. doi:10.4095/306189 Retrieved from https://geoscan.nrcan.gc.ca/starweb/geoscan/servlet.starweb?path=geoscan/fulle.web&search1=R=306189

McClenaghan, M. B., Kjarsgaard, I. M., Kjarsgaard, B. A., & Heaman, L. M. (2002). Mineralogy of kimberlite boulders from eskers in the lake timiskaming and kirkland lake areas, northeastern ontario. (No. 4361).Natural Resources Canada. doi:10.4095/213614 Retrieved from https://geoscan.nrcan.gc.ca/starweb/geoscan/servlet.starweb?path=geoscan/fulle.web&search1=R=213614

McClenaghan, M. B., & Paulen, R. C. (2018). In Menzies J., van der Meer J. J. M.(Eds.), Chapter 20 - application of till mineralogy and geochemistry to mineral exploration Elsevier. doi:https://doi-org.proxy.lib.uwaterloo.ca/10.1016/B978-0-08-100524-8.00022-1

McClenaghan, M. B., Paulen, R. C., Smith, I. R., Rice, J. M., Plouffe, A., McMartin, I., . . . Beckett-Brown, C. E. (2023). Review of till geochemistry and indicator mineral methods for mineral exploration in glaciated terrain. Geochemistry: Exploration, Environment, Analysis, 23(4), geochem2023-013. doi:10.1144/geochem2023-013

McClenaghan, M. B., Plouffe, A., McMartin, I., Campbell, J. E., Spirito, W. A., Paulen, R. C., . . . Hall, G. E. M. (2013). Till sampling and geochemical analytical protocols used by the geological survey of canada. Geochemistry: Exploration, Environment, Analysis, 13(4), 285-301. doi:10.1144/geochem2011-083

McKinney, W. (2010). Data structures for statistical computing in python. Paper presented at the P}Roceedings of the 9th {P}Ython in {S}Cience {C}Onference, 56. doi:10.25080/Majora-92bf1922-00a

McMartin, I., & Campbell, J. E. (2007). Near-surface till sampling protocols in shield terrain, with examples from western and northern canada. In R. C. Paulen, & I. McMartin (Eds.), Application of till and stream sediment heavy mineral and geochemical methods to mineral exploration in western and northern canada (pp. 75-95) Geological Association of Canada.

McMartin, I., & Paulen, R. C. (2009). Ice-flow indicators and the importance of ice-flow mapping for drift prospecting. In R. C. Paulen, & I. McMartin (Eds.), Application of till and stream sediment heavy mineral and geochemical methods to mineral exploration in western and northern canada (pp. 15-34) Geological Association of Canada.

McMartin, I., Campbell, J. E., & Dredge, L. A. (2019). Middle wisconsinan marine shells near repulse bay, nunavut, canada: Implications for marine isotope stage 3 ice-free conditions and laurentide ice sheet dynamics in north-west hudson bay. Journal of Quaternary Science, 34(1), 64-75. doi:10.1002/jqs.3081

Melanson, A., Bell, T., & Tarasov, L. (2013). Numerical modelling of subglacial erosion and sediment transport and its application to the north american ice sheets over the last glacial cycle. Quaternary Science Reviews, 68, 154-174. Retrieved from http://www.sciencedirect.com.proxy.lib.uwaterloo.ca/science/article/pii/S0277379113000711

Menzies, J. (2023). Glacial microsedimentology—a new lens to investigate glacial sediments—a review. Ottawa : National Research Council Canada. doi:10.1139/cjes-2022-0048

Menzies, J., & Ross, M. (2022). 4.10 - glacial processes and Landforms—Transport and deposition. In J. (. F. Shroder (Ed.), Treatise on geomorphology (second edition) (pp. 182-202). Oxford: Academic Press. doi:10.1016/B978-0-12-818234-5.00027-4 Retrieved from https://www.sciencedirect.com/science/article/pii/B9780128182345000274

Menzies, J., van der Meer, J. J. M., & Rose, J. (2006). Till—as a glacial “tectomict”, its internal architecture, and the development of a “typing” method for till differentiation. Geomorphology, 75(1), 172-200. doi:https://doi-org.proxy.lib.uwaterloo.ca/10.1016/j.geomorph.2004.02.017

Natural Resources Canada. (2019). Métadonnées de levé: Levé d'échantillonnage de till de fond, région d'abitibi-témiscamingue, québec, 1971-1973. Retrieved from https://geochem.nrcan.gc.ca/cdogs/content/svy/svy200180_f.htm

Nye, J. F. (2015). The mechanics of a glacier snout. Journal of Glaciology, 61(230), 1118-1120. doi:10.3189/2015JoG15J164

OpenStreetMap contributors. (2019). Topographic map malartic Retrieved from http://en-ca.topographic-map.com/places/Malartic-378672/

Parent, M., Paradis, S. J., & Boisvert, É. (1995). Ice-flow patterns and glacial transport in the eastern hudson bay region: Implications for the late quaternary dynamics of the laurentide ice sheet. Canadian Journal of Earth Sciences, 32(12), 2057-2070. doi:10.1139/e95-159
Parent, M., Paradis, S. J., & Doiron, A. (1996). Palimpsest glacial dispersal trains and their significance for drift prospecting. Journal of Geochemical Exploration, 56(2), 123-140. doi:https://doi-org.proxy.lib.uwaterloo.ca/10.1016/0375-6742(96)00011-8

Paulen, R. C. (2017). A revised look at canada's landscape: Glacial processes and dynamics. (No. 7374).Natural Resources Canada. doi:10.4095/300286 Retrieved from https://geoscan.nrcan.gc.ca/starweb/geoscan/servlet.starweb?path=geoscan/fulle.web&search1=R=300286

Paulen, R. C., McClenaghan, M. B., & Hicken, A. K. (2013). Regional and local ice-flow history in the vicinity of the izok lake Zn–Cu–Pb–Ag deposit, nunavut. Canadian Journal of Earth Sciences, 50(12), 1209-1222. doi:10.1139/cjes-2013-0064

Pedregosa, F., Varoquaux, G., Gramfort, A., Michel, V., Thirion, B., Grisel, O., . . . Duchesnay, E. (2011). Scikit-learn: Machine learning in python. Journal of Machine Learning Research, 12, 2825-2830.

Perrouty, S., Gaillard, N., Piette-Lauzière, N., Mir, R., Bardoux, M., Olivo, G. R., . . . Morris, W. A. (2017). Structural setting for canadian malartic style of gold mineralization in the pontiac subprovince, south of the cadillac larder lake deformation zone, québec, canada. Ore Geology Reviews, 84(Complete), 185-201. doi:10.1016/j.oregeorev.2017.01.009

Perrouty, S., Linnen, R. L., Lesher, C. M., Olivo, G. R., Piercey, S. J., Gaillard, N., . . . Enkin, R. J. (2019a). Expanding the size of multi-parameter metasomatic footprints in gold exploration: Utilization of mafic dykes in the canadian malartic district, québec, canada. Mineralium Deposita, 54(5), 761-786. doi:10.1007/s00126-018-0829-x

Perrouty, S., Linnen, R. L., Lesher, C. M., Olivo, G. R., Piercey, S. J., Gaillard, N., . . . Enkin, R. J. (2019b). Expanding the size of multi-parameter metasomatic footprints in gold exploration: Utilization of mafic dykes in the canadian malartic district, québec, canada. Mineralium Deposita, 54(5), 761-786. doi:10.1007/s00126-018-0829-x

Piercey, S. J. (2014). Modern analytical facilities 2: A review of quality assurance and quality control (QA/QC) procedures for lithogeochemical data. Journal of the Geological Association of Canada, 41(1), 75-88.

Plouffe, A. (2001). The glacial transport and physical partitioning of mercury and gold in till: Implications for mineral exploration with examples from central british columbia, canada. Geological Society, London, Special Publications, 185(1), 287-299. doi:10.1144/GSL.SP.2001.185.01.13

Prest, V. K. (1983). Canada's heritage of glacial features. ().Geological Survey of Canada.

Prest, W. H. (1915). The gold fields of nova scotia: A prospector's handbook. Halifax, Canada: Industrial Publishing Co., Limited.

QGIS Development Team. (2020). QGIS geographic information system [computer software]

Rea, B. R. (2007). GLACIAL LANDFORMS, EROSIONAL FEATURES | micro- to macroscale forms. In S. Elias (Ed.), Encyclopedia of quaternary science (pp. 853-864) doi:10.1016/B0-44-452747-8/00097-1

Rea, B. R., Evans, D. J. A., Dixon, T. S., & Brian Whalley, W. (2000). Contemporaneous, localized, basal ice-flow variations: Implications for bedrock erosion and the origin of p-forms. Journal of Glaciology, 46(154), 470-476. doi:10.3189/172756500781833197

Reman, A. (2020). Assessing stratigraphic controls on the secondary detrital footprint from buried mineralization and alteration at the highland valley copper mine, british columbia (M.Sc.). Retrieved from http://hdl.handle.net/10012/15571

Rice, J. (2020). Laurentide ice sheet dynamics evolution in the inner-ice sheet region of northeastern quebec, canada Retrieved from http://hdl.handle.net/10012/15826

Rice, J. M., Ross, M., Paulen, R. C., Kelley, S. E., Briner, J. P., Neudorf, C. M., & Lian, O. B. (2019). Refining the ice flow chronology and subglacial dynamics across the migrating labrador divide of the laurentide ice sheet with age constraints on deglaciation. Journal of Quaternary Science, 34(7), 519-535. doi:https://doi-org.proxy.lib.uwaterloo.ca/10.1002/jqs.3138

Richard, P. J. H., & Larouche, A. C. (1989). La vgtation postglaciaire du tmiscamingue, qubec, durant l'pisode glaciolacustre barlow. Canadian Journal of Botany, 67(2), 544-558. doi:10.1139/b89-076

Richard, P. J. H., Veillette, J. J., & Larouche, A. C. (1989). Palynostratigraphie et chronologie du retrait glaciaire au tmiscamingue: Valuation des ges 14C et implications paloenvironnementales. Canadian Journal of Earth Sciences, 26(4), 627-641. doi:10.1139/e89-054

Robert, F., & Poulsen, K. H. (1997). World-class archaean gold deposits in canada: An overview. Null, 44(3), 329-351. doi:10.1080/08120099708728316

Roman, M. (2019). Ice-flow directions of the last scandinavian ice sheet in central poland. Quaternary International, 501, 4-20. doi:https://doi-org.proxy.lib.uwaterloo.ca/10.1016/j.quaint.2017.11.035

Rose, A. W., Hawkes, H. E., & Webb, J. S. (1979). Geochemistry in mineral exploration (2nd ed.). New York: Academic Press Inc.

Ross, M., Campbell, J. E., Parent, M., & Adams, R. S. (2009). Palaeo-ice streams and the subglacial landscape mosaic of the north american mid-continental prairies. Boreas, 38(3), 421-439. doi:10.1111/j.1502-3885.2009.00082.x

Roy, M. (2013). Piézométrie régionale: Abitibi-témiscamingue Groupe de recherche sur l'eau souterraine - Université du Québec en Abitibi-Témiscamingue.
Roy, M., Veillette, J. J., Daubois, V., & Ménard, M. (2015). Late-stage phases of glacial lake ojibway in the central abitibi region, eastern canada. Geomorphology, 248(Complete), 14-23. doi:10.1016/j.geomorph.2015.07.026

Saarnisto, M. (1990). An outline of glacial indicator tracing. In R. R. Kujansuu, & M. Saarnisto (Eds.), Glacial indicator tracing (pp. 1-13) CRC Press.

Salminen, R., & Tarvainen, T. (1995). Geochemical mapping and databases in finland. Journal of Geochemical Exploration, 55, 321-327. doi:10.1016/0375-6742(94)00062-X

Sarala, P., & Nykanen, V. (2017). Spatial analysis and modelling of glaciogenic geochemical dispersion – implication for mineral exploration in finland. Journal of African Earth Sciences., 128, 61-71. doi:10.1016/j.jafrearsci.2016.12.002

Sarala, P., Pulkkinen, E., Ojala, V. J., & Peltoniemi-Taivalkoski, A. (2009). Gold exploration using till at petäjälehto, northern finland. Geochemistry: Exploration, Environment, Analysis, 9(3), 247-255. doi:10.1144/1467-7873/09-187

Shilts, W. W. (1971). Till studies and their application to regional drift prospecting. Canadian Mining Journal., 92(4), 45-50.

Shilts, W. W. (1976). Glacial till and mineral exploration. In R. F. Legget (Ed.), Glacial till - an inter-disciplinary study (pp. 205-224). Ottawa, Canada: The Royal Society of Canada.

Shilts, W. W. (1995). Geochemical partitioning in till. In P. T. Bobrowksy, S. J. Sibbick, J. M. Newell & P. F. Matysek (Eds.), Drift exploration in the canadian cordillera (pp. 149-164) British Columbia Ministry of Energy, Mines and Petroleum Resources.

Shilts, W. (1996). Drift exploration. In J. Menzies (Ed.), Past glacial environments, sediment forms, and techniques (pp. 411-439). Toronto, ON: Butterworth Heinemann.

Sibbick, S. J., & Fletcher, W. K. (1993). Distribution and behavior of gold in soils and tills at the nickel plate mine, southern british columbia, canada doi:https://doi-org.proxy.lib.uwaterloo.ca/10.1016/0375-6742(93)90065-T

Slatt, R. M. (1972). Texture and composition of till derived from parent rocks of contrasting textures: Southeastern newfoundland doi:https://doi-org.proxy.lib.uwaterloo.ca/10.1016/0037-0738(72)90026-7

Stanley, C. R. (2009). Geochemical, mineralogical, and lithological dispersal models in glacial till: Physical process constraints and application in mineral exploration. In R. C. Paulen, & I. McMartin

(Eds.), Application of till and stream sediment heavy mineral and geochemical methods to mineral exploration in western and northern canada (pp. 35-48) Geological Association of Canada.

Stea, R. R. (1994). Relict and palimpsest glacial landforms in nova scotia, canada. Formation and Deformation of Glacial Deposits, , 141-158.

Stea, R. R., & Finck, P. W. (2001). An evolutionary model of glacial dispersal and till genesis in maritime canada. Geological Society, London, Special Publications, 185(1), 237-265. doi:10.1144/GSL.SP.2001.185.01.11

Stone, P., & McMillan, A. A. (2013). Regional geochemical patterns in SE scotland: Source lithology, inheritance and glacial overprinting. Scottish Journal of Geology, 49(1), 33-40. doi:10.1144/sjg2013-002

Strahler, A. N. (1952). Dynamic basis of geomorphology. GSA Bulletin, 63(9), 923-938. doi:10.1130/0016-7606(1952)63[923:DBOG]2.0.CO;2

Strobel, M. L., & Faure, G. (1987). Transport of indicator clasts by ice sheets and the transport half-distance: A contribution to prospecting for ORE deposits. The Journal of Geology, 95(5), 687-697. Retrieved from http://www.jstor.org.proxy.lib.uwaterloo.ca/stable/30065728

Taivalkoski, A., Sarala, P., & Hulkki, H. (2015). Gold exploration using heavy minerals in till and weathered bedrock in petäjäselkä, northern finland. Geochemistry : Exploration, Environment, Analysis., 15(2-3), 205-221. doi:10.1144/geochem2014-288

Taves, R. (2015). Glacial dispersion of indicator minerals and geochemical pathfinders from the canadian malartic gold deposit val d'Or, quebec: Testing legacy data and new indicators

Thorleifson, L. H. (2017). History and status of till geochemical and indicator mineral methods in mineral exploration. (No. 7374).Natural Resources Canada. doi:10.4095/300285 Retrieved from https://geoscan.nrcan.gc.ca/starweb/geoscan/servlet.starweb?path=geoscan/fulle.web&search1=R=300285

Thorleifson, L.H., Wyatt, P.H., Warman, T.A. (1993). Quaternary stratigraphy of the severn and winisk drainage basins, northern ontario. Ottawa, Canada: Geological Survey of Canada. doi:nfo:doi/

Thurston, P. C., Ayer, J. A., Goutier, J., & Hamilton, M. A. (2008). Depositional gaps in abitibi greenstone belt stratigraphy: A key to exploration for syngenetic mineralization. Economic Geology, 103, 1097-1134.

Trommelen, M. S., Ross, M., & Campbell, J. E. (2013). Inherited clast dispersal patterns: Implications for palaeoglaciology of the SE keewatin sector of the laurentide ice sheet. Boreas, 42(3), 693-713. doi:10.1111/j.1502-3885.2012.00308.x

Trommelen, M. S., Ross, M., & Campbell, J. E. (2012). Glacial terrain zone analysis of a fragmented paleoglaciologic record, southeast keewatin sector of the laurentide ice sheet. Quaternary Science Reviews, 40, 1-20. doi:https://doi-org.proxy.lib.uwaterloo.ca/10.1016/j.quascirev.2012.02.015

Umurhan, O. M., Howard, A. D., Moore, J. M., Earle, A. M., White, O. L., Schenk, P. M., . . . Young, L. A. (2017). Modeling glacial flow on and onto pluto's sputnik planitia doi:https://doi-org.proxy.lib.uwaterloo.ca/10.1016/j.icarus.2017.01.017

Valkama, J. O. (2011). Dogs in exploration in finland. Tutkimusraportti - Geologian Tutkimuskeskus, , 1-22.

Van Rossum, G., & Drake, F. L. (2009). Python 3 reference manual. Scotts Valley, CA: CreateSpace.

Veillette, J. J. (1986). Former southwesterly ice flows in the abitibi-timiskaming region: Implications for the configuration of the late wisconsinan ice sheet. Canadian Journal of Earth Sciences, 23(11), 1724-1741. doi:10.1139/e86-159

Veillette, J. J. (1989). Ice movements, till sheets and glacial transport in abitibi-timiskaming, quebec and ontario. Geological Survey of Canada, Paper, 89-20, 139-154. doi:10.4095/127369

Veillette, J. J. (1994). Evolution and paleohydrology of glacial lakes barlow and ojibway. Quaternary Science Reviews, 13(9-10), 945-971. doi:10.1016/0277-3791(94)90010-8

Veillette, J. J. (2004a). Géologie des formations en surface et histoire glaciaire, cadillac, québec Natural Resources Canada. doi:10.4095/215047

Veillette, J. J. (2004b). Ice-flow chronology and palimpsest, long-distance dispersal of indicator clasts, north of the st. lawrence river valley, quebec. Géographie Physique Et Quaternaire., 58(2-3), 187-216. doi:10.7202/013138ar

Veillette, J. J., Dyke, A. S., & Roy, M. (1999). Ice-flow evolution of the labrador sector of the laurentide ice sheet: A review, with new evidence from northern quebec. Quaternary Science Reviews, 18(8-9), 993-1019. doi:10.1016/S0277-3791(98)00076-6

Veillette, J. J., & McClenaghan, M. B. (1996). Sequence of glacial ice flows in abitibi-timiskaming; implications for mineral exploration and dispersal of calcareous rocks from the hudson bay basin, quebec and ontario doi:10.4095/205756

Veillette, J. J., Paradis, S. J., & Buckle, J. (2005). Bedrock and surficial geology of the general area around rouyn-noranda, quebec and ontario. Geological Survey of Canada, Bulletin, 584, 1-16. doi:10.4095/221131

Veillette, J. J., Paradis, S. J., & Thibaudeau, P. (2003). Les cartes de formations en surface de l'abitibi, québec. (No. 1523). doi:10.4095/213987 Retrieved from

https://geoscan.nrcan.gc.ca/starweb/geoscan/servlet.starweb?path=geoscan/fulle.web&search1=R=213987

Veillette, J. (1988). Déglaciation et évolution des lacs proglaciaires post-algonquin et barlow au témiscamingue, québec et ontario. Géographie Physique Et Quaternaire, 42(1), 7-31. doi:10.7202/032706ar

Virtanen, P., Gommers, R., Oliphant, T. E., Haberland, M., Reddy, T., Cournapeau, D., . . . SciPy 1.0 Contributors. (2020). SciPy 1.0: Fundamental algorithms for scientific computing in python. Nature Methods, 17, 261-272. doi:10.1038/s41592-019-0686-2

Vollmer, F. W. (1995). C program for automatic contouring of spherical orientation data using a modified kamb method. Computers & Geosciences, 21(1), 31-49. doi:https://doi-org.proxy.lib.uwaterloo.ca/10.1016/0098-3004(94)00058-3

Wang, Y. (2018). Statistical analysis of till geochemistry in the nelson river area, northeastern manitoba: Implications for quaternary glacial stratigraphy Retrieved from http://hdl.handle.net/10012/12948

Wang, Y. (2018). Statistical analysis of till geochemistry in the nelson river area, northeastern manitoba: Implications for quaternary glacial stratigraphy

Wares, R., & Burzynski, J. (2011). The canadian malartic mine, southern abitibi belt, quebec, canada: Discovery and development of an archean bulk-tonnage gold deposit. (). Montreal, Quebec: Osisko Mining Corporation.

Waskom, M., Botvinnik, O., Hobson, P., Cole, J. B., Halchenko, Y., Hoyer, S., . . . Allan, D. (2014). Seaborn: V0.5.0 (november 2014). doi:10.5281/zenodo.12710

Wentworth, C. K. (1922). A scale of grade and class terms for clastic sediments. The Journal of Geology, 30(5), 377-392. Retrieved from http://www.jstor.org/stable/30063207

Western Science Centre. (2020). Electron microprobe laboratory. Retrieved from https://epma.uwo.ca/about.html

Wickham, H. (2016). Ggplot2: Elegant graphics for data analysis. Retrieved from https://ggplot2.tidyverse.org

Wiken, E. B., Gauthier, D., Marshall, I., Lawton, K., & Hirvonen, H. (1996). A perspective on canada's ecosystems: An overview of the terrestrial and marine ecozones. (Occasional Paper 14). Ottawa, ON: Canadian Council on Ecological Areas.

Wilson, M. E. (1918). Timiskaming county, quebec. Geological Survey of Canada, Memoir, 103, 1-197. doi:10.4095/101670

APPENDICES

5.1. Research Methodology Flowchart

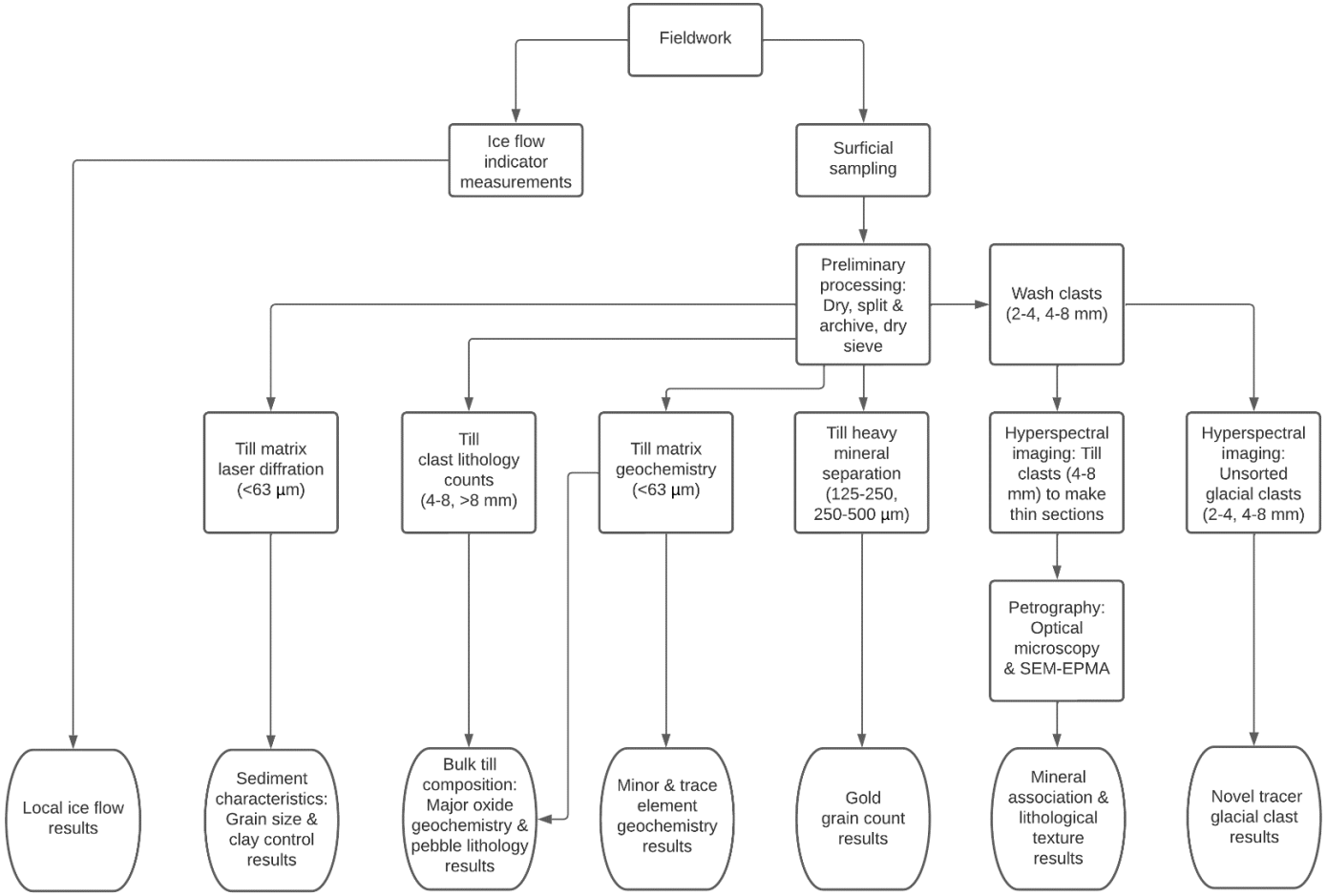

Supplementary Figure 5. 1 Research methodology summary flowchart showing processes (rectangles) and results (rounded rectangles) for till samples.

5.2. Field Sample Details

An unknown number of locations with "no surficial till" were not recorded during both years (approximately 20 unrecorded sites in 2016, many of which were in the area north of the Canadian Malartic Mine). Depth data were not recorded at surficial esker sample sites. Degree of oxidation was approximated by visual inspection of field photos (not recorded for several Pionjar drill till samples). Details for samples from 2015 are reproduced from field notes and photos by Taves (2015).

Supplementary Table 5. 1 Field sample details and coordinates (field duplicate details are in parentheses). Samples from 2015 were collected by Taves (2015). PCS: NAD 1983, UTM Zone 17N.

Sample ID	X	Y	Year	Sample	Oxidation	Depth where sampling began (m)
001a	712587	5331728	2016	Surficial till	Slight	0.35
002a	705100	5332339	2016	No surficial till	-	0.35
003a	705067	5330530	2016	No surficial till	-	0.35
004a	706551	5333381	2016	Surficial till	Slight	0.1
005a	706274	5325153	2016	Surficial till	Slight	0.3
006a	711934	5325324	2016	No surficial till	-	-
007a	716966	5323165	2016	Surficial till	Slight	0.4
008a	716344	5335577	2016	No surficial till	-	0.35
009a (009b)	718028 (718028)	5338822 (5338802)	2016	Surficial till	Slight (Slight)	0.2 (0.4)
010a	707955	5330252	2016	Surficial till	Slight	0.4
011a	709276	5330732	2016	Surficial till	Slight	0.35
012a	710592	5332786	2016	Surficial till	Slight	0.2
013a	711208	5339445	2016	Surficial esker (clasts)	Slight	-
013b	711208	5339445	2016	Surficial esker (fines)	Slight	-
015a	708456	5342422	2016	Surficial esker (fines)	Slight	-
015b	708456	5342485	2016	Surficial esker (clasts)	Slight	-
017a	729951	5329715	2016	Surficial esker	Slight	-
017b	729952	5329720	2016	Surficial esker	Slight	-
019a	713245	5321503	2016	Surficial till	Slight	0.4
021a	712121	5328681	2016	Surficial till	Fresh till	0.8
031a	702408	5344935	2016	Surficial till	Fresh till	0.2
035a	712210	5334658	2016	No surficial till	-	0.65
036a	711813	5334343	2016	Surficial till	High	0.3

Sample ID	X	Y	Year	Sample	Oxidation	Depth where sampling began (m)
038a	706829	5337116	2016	Surficial till	Slight	0.25
038b	706829	5337116	2016	Surficial till	Slight	0.35
039a	708037	5338231	2016	Surficial till	Slight	0.35
040a	708068	5336960	2016	Surficial till	Slight	0.75
041a	707652	5336979	2016	Surficial till	Slight	0.35
042a	704700	5337948	2016	Surficial till	Slight	0.8
043a	708338	5335132	2016	Surficial till	Slight	0.4
044a	707318	5334702	2016	Surficial till	High	0.4
045a	704553	5334380	2016	Surficial till	Slight	0.55
046a	705209	5333758	2016	Surficial till	High	0.6
047a	709122	5334946	2016	Surficial till	Slight	0.35
048a	704916	5336658	2016	Surficial till	Slight	0.2
049a	709260	5334141	2016	Surficial till	Slight	0.3
050a	705916	5334652	2016	Surficial till	High	0.35
052a	716383	5328680	2016	Surficial till	High	0.35
053a	715775	5327893	2016	No surficial till	-	0.5
054a	718102	5326170	2016	Surficial till	High	0.45
055a	721020	5325461	2016	Surficial till	Fresh till	0.5
056a	717890	5329648	2016	Surficial till	Fresh till	0.35
057a	712812	5330958	2016	Surficial till	Fresh till	0.4
058a	713002	5326921	2016	Surficial till	Fresh till	0.45
059a	712777	5332939	2016	Surficial till	Slight	0.4
060a	713895	5336431	2016	Surficial till	Fresh till	0.55
061a	720533	5333144	2016	Surficial till	Fresh till	0.2
062a	715966	5332231	2016	Surficial till	High	0.3
063a	718651	5331999	2016	Surficial till	High	0.3
064a	719703	5332694	2016	Surficial till	High	0.65
065a	713328	5338467	2016	Surficial till	Slight	0.6
065b	713328	5338467	2016	Surficial till	Slight	0.35
070a	713152	5333437	2016	Surficial till	High	0.45
071a	713328	5338467	2016	No surficial till	-	0.4
DS 14	716460	5330468	2015	No drill till	-	4.52
DS 15	711137	5328642	2015	No drill till	-	5.97
DS 16	712818	5328710	2015	No drill till	-	9.15
DS 20	717053	5330472	2015	No drill till	-	10.53
DS 24	709540	5325168	2015	No drill till	-	10.8
DS 25	706925	5325197	2015	Drill till	Fresh till	2.92
DS 26	708009	5325239	2015	No drill till	-	4.54
DS 27	710967	5325346	2015	No drill till	-	3.7
DS 29	712832	5325410	2015	Drill till	Fresh till	11.29
DS 30	714868	5330421	2015	Drill till	Fresh till	2.57

Sample ID	X	Y	Year	Sample	Oxidation	Depth where sampling began (m)
DS 31a	714101	5330394	2015	Drill till	Fresh till	1.73
DS 31b	714101	5330394	2015	No drill till	-	1.73
DS 32	712963	5330344	2015	No drill till	-	5.94
DS 33	712982	5327998	2015	No drill till	-	1.22
DS 34a	713018	5326673	2015	Drill till	Fresh till	1.52
DS 34b	713018	5326673	2015	No drill till	-	1.52
DS 35	711982	5328681	2015	Drill till	Fresh till	1.77
DS 36	712917	5329687	2015	No drill till	-	4.06
DS 37	713095	5336474	2015	No drill till	-	6.91
DS 38	715700	5335549	2015	No drill till	-	12.75
DS 39	714975	5335614	2015	Drill till	Fresh till	13.1
DS 40	712612	5336338	2015	No drill till	-	8.05
DS 41	712044	5325388	2015	Drill till	Fresh till	3.96
DS 42	716908	5332534	2015	Drill till	Fresh till	3.6
DS 43	718182	5333744	2015	No drill till	-	5.15
DS 44	720469	5333098	2015	Drill till	Fresh till	10.29
DS 45	717187	5331556	2015	Drill till	Fresh till	3.15
DS 46	713446	5331477	2015	Drill till	Fresh till	6.53
DS 6a	712580	5331733	2015	Drill till	Fresh till	1.34
DS 6b	712580	5331733	2015	Drill till	-	1.84
ES 18a	721422	5333212	2015	Surficial esker (clasts)	-	-
ES 18b	721422	5333212	2015	Surficial esker (fines)	-	-
ES 21a	721470	5333155	2015	Surficial esker (fines)	-	-
ES 21b	721470	5333155	2015	Surficial esker (clasts)	-	-
SS 1	711363	5335976	2015	Surficial till	Slight	0.4
SS 10	711044	5331831	2015	Surficial till	Slight	0.4
SS 11	709461	5337431	2015	Surficial till	Slight	0.28
SS 12	709341	5331985	2015	Surficial till	Slight	0.4
SS 13	716330	5330461	2015	Surficial till	Slight	0.3
SS 19	714949	5331446	2015	Surficial till	Slight	0.35
SS 2	712271	5332696	2015	Surficial till	Slight	0.95
SS 22	717965	5332923	2015	Surficial till	Fresh till	0.4
SS 23	710948	5333852	2015	Surficial till	Slight	0.35
SS 3	712191	5333659	2015	Surficial till	Slight	0.4
SS 4	708380	5330735	2015	Surficial till	Slight	0.46
SS 48	707255	5340990	2015	Surficial till	Slight	0.42
SS 49	713900	5336426	2015	Surficial till	Slight	0.7

Sample ID	X	Y	Year	Sample	Oxidation	Depth where sampling began (m)
SS 5	708031	5332341	2015	Surficial till	Slight	0.54
SS 6	712580	5331733	2015	Surficial till	Slight	0.36
SS 7	710245	5335036	2015	Surficial till	Slight	0.4
SS 8	709807	5333816	2015	Surficial till	Slight	0.3
SS 9	711255	5332859	2015	Surficial till	Fresh till	0.51

5.3. Grain Size

5.3.1. Dry Sieve

Supplementary Table 5. 2 Dry sieve mass fraction measurements (g).

Sample	8 mm	4 mm	2 mm	1 mm	0.5 mm	0.25 mm	0.125 mm	0.09 mm	0.063 mm	Pan	Total (g)
001a	497.96	190.19	188.78	-	-	-	-	-	2768.06	1157.98	4802.97
004a	161.61	43.68	49.31	-	-	-	-	-	1058.69	318.49	1631.78
005a	50.01	45.52	48.70	-	-	-	-	-	2093.71	377.74	2615.68
007a	199.20	199.97	232.25	-	-	-	-	-	1861.15	146.25	2638.82
009a	775.86	216.58	220.51	-	-	-	-	-	2765.03	434.17	4412.15
009b	563.48	174.56	186.74	-	-	-	-	-	3051.44	591.56	4567.78
010a	156.43	139.20	202.64	-	-	-	-	-	3158.90	232.40	3889.57
011a	202.92	108.49	131.21	-	-	-	-	-	2333.28	87.90	2863.80
012a	154.04	125.66	101.50	111.55	145.42	303.96	459.77	321.75	510.99	1338.23	3572.87
019a	793.40	316.50	232.32	-	-	-	-	-	1801.28	239.64	3383.14
021a	163.92	139.93	124.26	-	-	-	-	-	2311.06	144.31	2883.48
031a	933.57	263.31	225.30	-	-	-	-	-	2269.18	239.88	3931.24
036a	344.21	165.45	162.35	-	-	-	-	-	1209.60	578.99	2460.60
038a	310.87	168.86	188.53	-	-	-	-	-	2324.20	235.07	3227.53
038b	262.82	143.32	123.01	-	-	-	951.03	-	324.79	186.39	1991.36
039a	942.11	399.39	354.49	-	-	-	-	-	2862.47	539.29	5097.75
040a	589.52	335.99	258.94	-	-	-	-	-	976.22	607.07	2767.74
041a	1084.98	328.27	294.45	272.79	225.63	300.07	347.48	-	573.16	673.66	4100.49
042a	333.61	117.27	79.59	-	-	-	-	-	1239.21	1150.04	2919.72
043a	259.54	186.66	195.30	-	-	-	-	-	863.03	69.71	1574.24
044a	485.12	328.65	284.38	-	-	-	-	-	1457.69	200.97	2756.81
045a	245.38	120.99	131.33	-	-	-	-	-	1734.99	275.55	2508.24
046a	99.49	51.67	41.13	38.32	44.39	86.74	212.67	-	380.00	414.15	1368.56
047a	171.73	75.67	66.32	-	-	-	-	-	2174.06	727.16	3214.94
048a	448.16	156.84	128.81	-	-	-	-	-	1945.40	306.82	2986.03
049a	50.50	24.16	30.84	-	-	-	-	-	1886.87	611.37	2603.74

Sample	8 mm	4 mm	2 mm	1 mm	0.5 mm	0.25 mm	0.125 mm	0.09 mm	0.063 mm	Pan	Total (g)
050a	505.96	152.05	115.82	-	-	-	-	642.43	1049.86	360.84	2826.96
052a	90.93	82.88	93.18	165.94	219.89	328.99	264.25	-	185.65	260.32	1692.03
054a	651.47	364.76	334.10	-	-	-	-	-	1565.13	404.77	3320.23
055a	312.20	194.09	140.63	-	-	-	-	-	1126.54	102.80	1876.26
056a	300.51	193.71	219.07	-	-	-	743.15	-	337.59	381.53	2175.56
057a	207.09	81.65	109.60	-	-	-	-	-	1808.09	874.09	3080.52
058a	439.43	169.45	177.16	-	-	-	-	-	2469.75	445.37	3701.16
059a	631.31	92.65	77.55	86.02	111.50	241.35	254.89	182.01	224.39	909.12	2810.79
060a	244.28	171.72	195.89	-	-	-	-	-	2021.14	389.24	3022.27
061a	503.54	119.98	52.62	-	-	-	-	-	798.14	868.83	2343.11
062a	238.60	112.30	113.22	-	-	-	-	-	998.64	536.69	1999.45
063a	382.42	171.27	197.11	409.16	943.52	637.87	199.09	62.00	54.50	234.82	3291.76
064a	1180.51	466.45	430.04	417.48	394.33	414.16	342.74	143.72	114.86	275.06	4179.35
065a	264.63	162.38	160.51	-	-	-	-	-	1100.80	1030.08	2718.40
065b	365.14	136.52	122.53	-	-	-	-	-	1172.04	690.78	2487.01
070a	750.87	163.72	130.90	126.58	218.29	597.70	569.12	-	423.30	346.54	3327.02
SS 1	-	-	3245.02	-	-	-	-	-	5535.37	3252.83	12033.22
SS 2	-	-	2806.01	-	-	-	-	-	6841.02	3510.73	13157.76
SS 3	-	-	1676.62	-	-	-	-	-	4632.43	5263.53	11572.58
SS 4	-	-	2224.97	-	-	-	-	-	6370.95	4839.17	13435.09
SS 5	-	-	2227.68	-	-	-	-	-	7831.06	2956.27	13015.01
SS 6	871.22	485.72	502.82	625.27	873.42	1345.68	2096.00	-	2685.08	4296.39	13781.60
SS 7	-	-	1615.25	-	-	-	-	-	5494.74	8192.32	15302.31
SS 8	-	-	1214.91	-	-	-	-	-	6917.82	3973.81	12106.54
SS 9	-	-	2190.61	-	-	-	-	-	7312.70	4882.60	14385.91
SS 10	-	-	1727.61	-	-	-	-	-	6600.50	4244.13	12572.24
SS 11	1333.35	778.57	679.06	692.17	598.41	797.26	891.67	-	2020.72	6216.79	14008.00
SS 12	-	-	2636.08	-	-	-	-	-	7389.86	3963.42	13989.36
SS 13	-	-	3287.07	-	-	-	-	-	3382.43	2151.94	8821.44

Sample	8 mm	4 mm	2 mm	1 mm	0.5 mm	0.25 mm	0.125 mm	0.09 mm	0.063 mm	Pan	Total (g)
SS 19	1899.17	810.66	857.98	819.72	808.66	747.91	759.20	-	951.30	2091.62	9746.22
SS 22	-	-	561.66	-	-	-	-	-	3740.30	7035.62	11337.58
SS 23	842.72	547.07	585.39	660.03	680.58	1158.33	1618.23	-	2014.05	4207.29	12313.69
SS 48	946.23	453.95	571.33	816.41	1262.37	4157.83	3545.91	-	1448.62	2289.31	15491.96
SS 49	-	-	446.99	-	-	-	-	-	7026.31	2505.02	9978.32

Supplementary Table 5. 3 Cumulative weight percent values and relative sample texture based on quartiles for values at 2 mm ("Fine": Q1 < 14.67 cumulative wt%; "Coarse": Q3 > 28.69 cumulative wt%; field duplicate sample data omitted in calculations; empty cells represent no measurement at that boundary).

Sample	8 mm	4 mm	2 mm	1 mm	0.5 mm	0.25 mm	0.125 mm	0.09 mm	0.063 mm	Pan	Texture
049a	1.94	2.87	4.05	-	-	-	-	-	76.52	100	Fine
SS 49	-	-	4.48	-	-	-	-	-	74.90	100	Fine
SS 22	-	-	4.95	-	-	-	-	-	37.94	100	Fine
005a	1.91	3.65	5.51	-	-	-	-	-	85.56	100	Fine
047a	5.34	7.70	9.76	-	-	-	-	-	77.38	100	Fine
SS 8	-	-	10.04	-	-	-	-	-	67.18	100	Fine
SS 7	-	-	10.56	-	-	-	-	-	46.46	100	Fine
012a	4.31	7.83	10.67	13.79	17.86	26.37	39.24	48.24	62.54	100	Fine
SS 48	6.11	9.04	12.73	18.00	26.14	52.98	75.87	-	85.22	100	Fine
010a	4.02	7.60	12.81	-	-	-	-	-	94.03	100	Fine
057a	6.72	9.37	12.93	-	-	-	-	-	71.63	100	Fine
SS 6	6.32	9.85	13.49	18.03	24.37	34.13	49.34	-	68.83	100	Fine
SS 10	-	-	13.74	-	-	-	-	-	66.24	100	Fine
046a	7.27	11.05	14.05	16.85	20.09	26.43	41.97	-	69.74	100	Fine
SS 3	-	-	14.49	-	-	-	-	-	54.52	100	Fine
021a	5.68	10.54	14.85	-	-	-	-	-	95.00	100	Medium
SS 9	-	-	15.23	-	-	-	-	-	66.06	100	Medium
011a	7.09	10.87	15.46	-	-	-	-	-	96.93	100	Medium
004a	9.90	12.58	15.60	-	-	-	-	-	80.48	100	Medium
052a	5.37	10.27	15.78	25.59	38.58	58.03	73.64	-	84.61	100	Medium

Sample	8 mm	4 mm	2 mm	1 mm	0.5 mm	0.25 mm	0.125 mm	0.09 mm	0.063 mm	Pan	Texture
SS 23	6.84	11.29	16.04	21.40	26.93	36.33	49.48	-	65.83	100	Medium
SS 4	-	-	16.56	-	-	-	-	-	63.98	100	Medium
SS 5	-	-	17.12	-	-	-	-	-	77.29	100	Medium
042a	11.43	15.44	18.17	-	-	-	-	-	60.61	100	Medium
001a	10.37	14.33	18.26	-	-	-	-	-	75.89	100	Medium
SS 12	-	-	18.84	-	-	-	-	-	71.67	100	Medium
045a	9.78	14.61	19.84	-	-	-	-	-	89.01	100	Medium
SS 11	9.52	15.08	19.92	24.87	29.14	34.83	41.19	-	55.62	100	Medium
060a	8.08	13.76	20.25	-	-	-	-	-	87.12	100	Medium
038a	9.63	14.86	20.70	-	-	-	-	-	92.72	100	Medium
058a	11.87	16.45	21.24	-	-	-	-	-	87.97	100	Medium
SS 2	-	-	21.33	-	-	-	-	-	73.32	100	Medium
065a	9.73	15.71	21.61	-	-	-	-	-	62.11	100	Medium
063a	11.62	16.82	22.81	35.24	63.90	83.28	89.33	91.21	92.87	100	Medium
062a	11.93	17.55	23.21	-	-	-	-	-	73.16	100	Medium
007a	7.55	15.13	23.93	-	-	-	-	-	94.46	100	Medium
048a	15.01	20.26	24.57	-	-	-	-	-	89.72	100	Medium
065b	14.68	20.17	25.10	-	-	-	-	-	72.22	100	Medium
038b	13.20	20.40	26.57	-	-	-	74.33	-	90.64	100	Medium
SS 1	-	-	26.97	-	-	-	-	-	72.97	100	Medium
036a	13.99	20.71	27.31	-	-	-	-	-	76.47	100	Medium
050a	17.90	23.28	27.37	-	-	-	-	50.10	87.24	100	Medium
009a	17.58	22.49	27.49	-	-	-	-	-	90.16	100	Medium
059a	22.46	25.76	28.52	31.58	35.54	44.13	53.20	59.67	67.66	100	Medium
061a	21.49	26.61	28.86	-	-	-	-	-	62.92	100	Coarse
070a	22.57	27.49	31.42	35.23	41.79	59.75	76.86	-	89.58	100	Coarse
056a	13.81	22.72	32.79	-	-	-	66.95	-	82.46	100	Coarse
039a	18.48	26.32	33.27	-	-	-	-	-	89.42	100	Coarse
055a	16.64	26.98	34.48	-	-	-	-	-	94.52	100	Coarse
031a	23.75	30.45	36.18	-	-	-	-	-	93.90	100	Coarse

Sample	8 mm	4 mm	2 mm	1 mm	0.5 mm	0.25 mm	0.125 mm	0.09 mm	0.063 mm	Pan	Texture
SS 19	19.49	27.80	36.61	45.02	53.31	60.99	68.78	-	78.54	100	Coarse
SS 13	-	-	37.26	-	-	-	-	-	75.61	100	Coarse
019a	23.45	32.81	39.67	-	-	-	-	-	92.92	100	Coarse
044a	17.60	29.52	39.83	-	-	-	-	-	92.71	100	Coarse
054a	19.62	30.61	40.67	-	-	-	-	-	87.81	100	Coarse
043a	16.49	28.34	40.75	-	-	-	-	-	95.57	100	Coarse
041a	26.46	34.47	41.65	48.30	53.80	61.12	69.59	-	83.57	100	Coarse
040a	21.30	33.44	42.79	-	-	-	-	-	78.07	100	Coarse
064a	28.25	39.41	49.70	59.69	69.12	79.03	87.23	90.67	93.42	100	Coarse

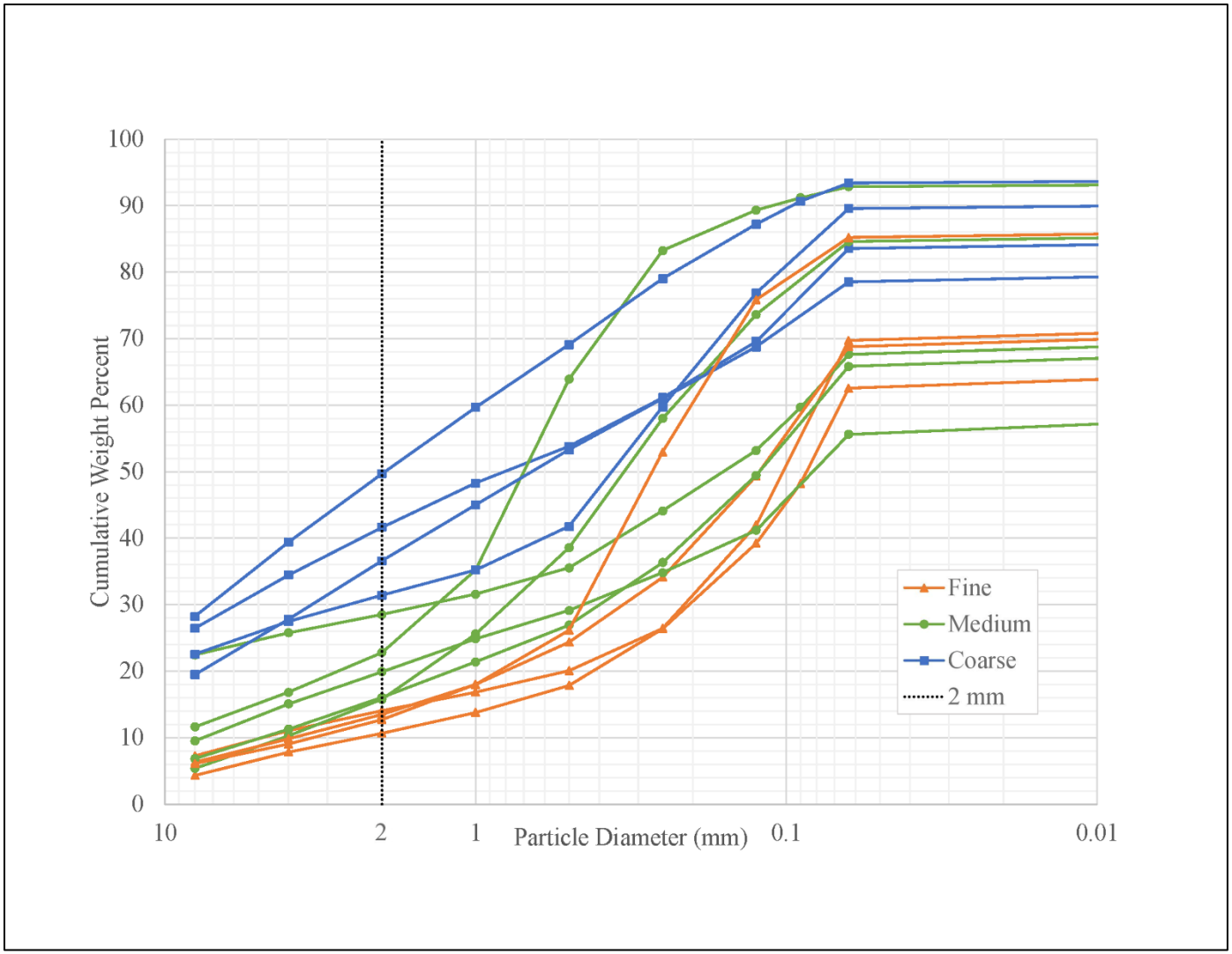

Supplementary Figure 5. 2 Cumulative weight percent curves showing dry sieve data for 13 selected surface till samples. All select samples are "very poorly sorted". Samples were sorted into "fine", "medium", and "coarse" textural groups using quartiles based on the >2 mm particle diameter cumulative weight percent for all samples.

5.3.2. Laser Diffraction Particle Sizing

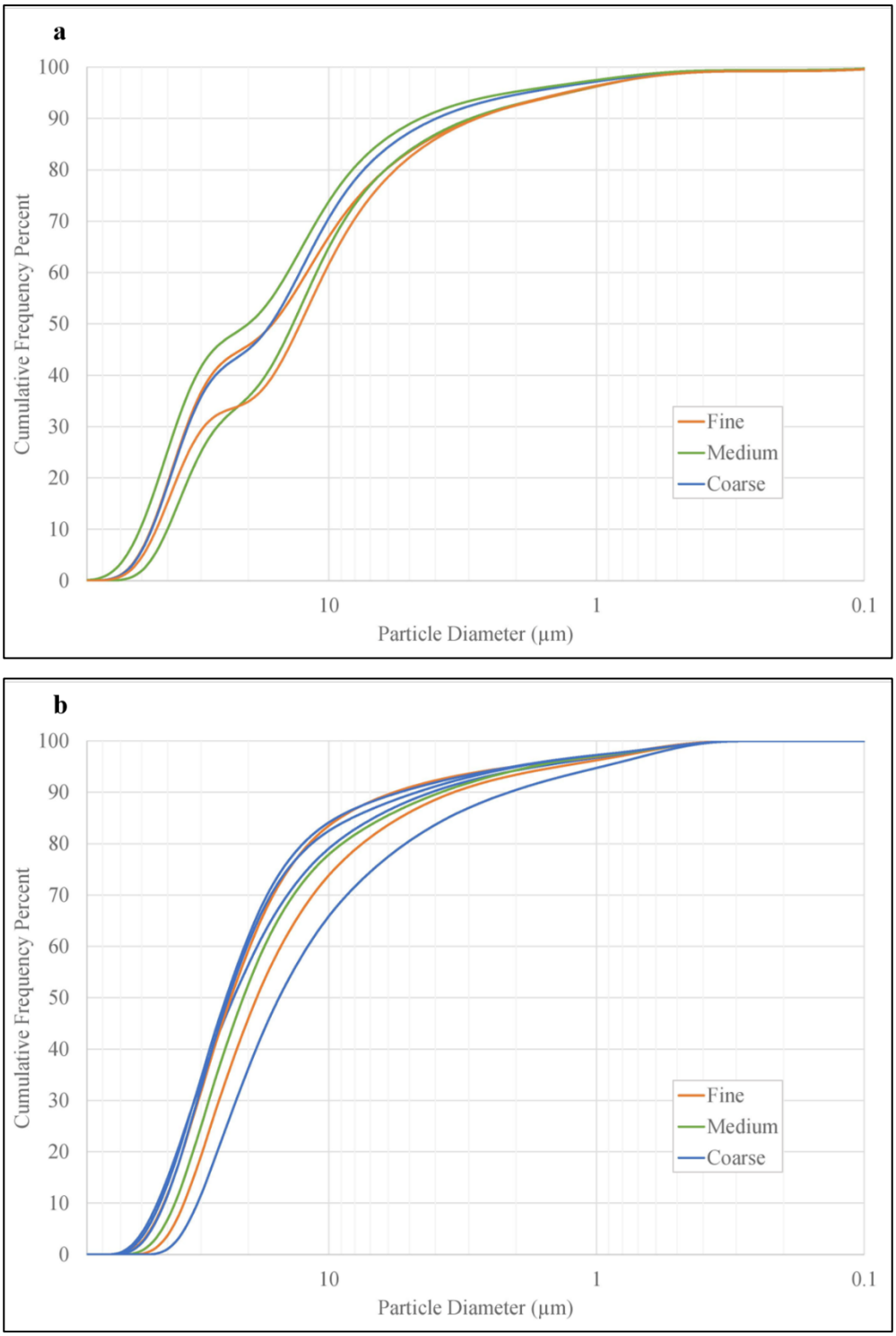

Supplementary Figure 5. 3 Cumulative frequency percent curves showing laser diffraction particle sizing data for select surface till samples from **(a)** 2015 (after Taves (2015)) and **(b)** 2016.

Supplementary Table 5. 4 Cumulative weight percent laser data for selected surficial till samples (Taves, 2015). Data is truncated to omit repeated values.

Size Mid (μm)	SS 6	SS 11	SS 19	SS 23	SS 48
0.0442	99.82	99.83	99.81	99.87	99.81
0.093	99.69	99.70	99.66	99.77	99.66
0.1027	99.57	99.58	99.54	99.68	99.53
0.1134	99.47	99.48	99.44	99.61	99.43
0.1252	99.40	99.40	99.36	99.55	99.36
0.1383	99.34	99.34	99.31	99.50	99.30
0.1528	99.30	99.29	99.27	99.47	99.26
0.1688	99.27	99.26	99.24	99.45	99.24
0.1864	99.25	99.24	99.23	99.43	99.22
0.2058	99.24	99.23	99.22	99.42	99.22
0.227	99.24	99.22	99.22	99.42	99.22
0.251	99.24	99.22	99.22	99.41	99.21
0.278	99.23	99.21	99.21	99.41	99.21
0.307	99.23	99.20	99.20	99.41	99.19
0.339	99.20	99.18	99.17	99.39	99.15
0.374	99.16	99.13	99.12	99.36	99.09
0.413	99.09	99.05	99.05	99.30	99.01
0.456	98.97	98.93	98.96	99.22	98.88
0.503	98.80	98.77	98.84	99.11	98.71
0.556	98.58	98.55	98.68	98.96	98.50
0.614	98.30	98.28	98.50	98.78	98.24
0.678	97.96	97.96	98.28	98.57	97.94
0.749	97.57	97.60	98.04	98.33	97.59
0.827	97.14	97.19	97.77	98.06	97.20
0.914	96.67	96.75	97.48	97.77	96.78
1.01	96.18	96.28	97.17	97.47	96.34
1.115	95.68	95.80	96.85	97.16	95.86
1.231	95.17	95.30	96.51	96.84	95.37
1.36	94.65	94.80	96.16	96.52	94.86
1.502	94.13	94.29	95.80	96.20	94.32
1.659	93.60	93.77	95.42	95.88	93.76
1.833	93.04	93.23	95.01	95.54	93.16
2.022	92.46	92.66	94.58	95.18	92.53
2.23	91.84	92.05	94.11	94.79	91.84
2.47	91.15	91.39	93.59	94.37	91.08
2.73	90.40	90.65	93.01	93.89	90.25
3.01	89.56	89.83	92.35	93.34	89.31
3.33	88.62	88.91	91.60	92.70	88.27
3.68	87.57	87.87	90.75	91.97	87.10
4.06	86.41	86.70	89.77	91.12	85.77

Size Mid (µm)	SS 6	SS 11	SS 19	SS 23	SS 48
4.48	85.12	85.39	88.66	90.15	84.27
4.95	83.69	83.92	87.40	89.03	82.58
5.47	82.10	82.26	85.96	87.74	80.66
6.04	80.32	80.37	84.30	86.25	78.47
6.67	78.31	78.19	82.38	84.51	75.97
7.36	76.03	75.65	80.13	82.48	73.11
8.13	73.43	72.67	77.49	80.09	69.83
8.98	70.48	69.18	74.40	77.30	66.10
9.92	67.19	65.16	70.84	74.07	61.92
10.96	63.61	60.65	66.85	70.44	57.35
12.1	59.88	55.79	62.54	66.51	52.55
13.36	56.18	50.83	58.14	62.47	47.77
14.76	52.76	46.09	53.94	58.57	43.33
16.31	49.84	41.89	50.25	55.09	39.57
18.01	47.56	38.47	47.29	52.24	36.75
19.85	45.87	35.85	45.10	50.09	34.92
21.9	44.50	33.77	43.45	48.47	33.86
24.2	42.98	31.75	41.85	46.98	33.08
26.8	40.71	29.19	39.67	45.04	31.88
29.6	37.19	25.63	36.32	42.08	29.63
32.7	32.20	20.96	31.51	37.74	25.97
36.1	25.97	15.55	25.42	32.03	21.03
39.8	19.14	10.16	18.70	25.38	15.40
44	12.60	5.62	12.26	18.52	9.96
48.6	7.19	2.50	6.95	12.24	5.52
53.7	3.41	0.83	3.26	7.16	2.51
59.3	1.26	0.18	1.18	3.58	0.88
65.5	0.33	0.02	0.30	1.45	0.22
72.4	0.06	-0.01	0.05	0.44	0.04
80	0.02	-0.01	0.01	0.09	0.01
88.3	0.02	-0.01	0.00	0.02	0.01
97.5	0.02	-0.01	0.00	0.01	0.01

Supplementary Table 5. 5 Cumulative weight percent laser data for selected surficial till samples (collected in 2016). Data is truncated to omit repeated values.

Size Mid (µm)	012a	041a	046a	052a	059a	064a	070a
0.2513	100.00	100.00	100.00	100.00	100.00	100.00	100.00
0.2775	100.00	100.00	100.00	99.99	99.99	99.98	99.99
0.3065	99.97	99.98	99.98	99.96	99.95	99.94	99.95
0.3385	99.91	99.92	99.93	99.88	99.86	99.86	99.88
0.3739	99.79	99.82	99.84	99.75	99.69	99.74	99.76

Size Mid (µm)	012a	041a	046a	052a	059a	064a	070a
0.4130	99.61	99.66	99.69	99.57	99.42	99.56	99.59
0.4561	99.35	99.44	99.49	99.33	99.06	99.33	99.37
0.5038	99.03	99.16	99.23	99.05	98.61	99.08	99.11
0.5564	98.66	98.83	98.93	98.75	98.10	98.80	98.83
0.6146	98.25	98.47	98.59	98.43	97.54	98.51	98.54
0.6788	97.83	98.10	98.24	98.13	96.95	98.24	98.25
0.7497	97.40	97.73	97.89	97.84	96.37	97.97	97.98
0.8280	96.98	97.37	97.55	97.56	95.80	97.72	97.73
0.9145	96.59	97.02	97.22	97.30	95.24	97.48	97.48
1.0101	96.20	96.69	96.92	97.03	94.69	97.24	97.23
1.1156	95.82	96.36	96.64	96.74	94.14	96.99	96.98
1.2321	95.45	96.04	96.37	96.42	93.58	96.73	96.70
1.3609	95.07	95.71	96.11	96.07	93.01	96.44	96.40
1.5031	94.68	95.37	95.85	95.67	92.40	96.13	96.07
1.6601	94.27	95.01	95.59	95.24	91.77	95.79	95.71
1.8335	93.84	94.62	95.31	94.76	91.09	95.43	95.31
2.0251	93.36	94.20	95.01	94.23	90.35	95.05	94.88
2.2367	92.85	93.76	94.70	93.68	89.58	94.65	94.43
2.4704	92.31	93.30	94.38	93.11	88.78	94.26	93.97
2.7285	91.68	92.77	94.01	92.47	87.88	93.82	93.45
3.0135	90.99	92.20	93.63	91.80	86.92	93.36	92.91
3.3284	90.23	91.60	93.21	91.09	85.89	92.89	92.34
3.6761	89.37	90.91	92.75	90.31	84.75	92.38	91.72
4.0602	88.41	90.16	92.23	89.46	83.49	91.83	91.05
4.4844	87.36	89.34	91.66	88.56	82.13	91.25	90.34
4.9529	86.21	88.45	91.04	87.60	80.67	90.64	89.60
5.4704	84.94	87.48	90.33	86.56	79.07	89.97	88.81
6.0420	83.55	86.41	89.54	85.44	77.34	89.25	87.97
6.6732	82.01	85.23	88.65	84.23	75.46	88.47	87.08
7.3704	80.32	83.95	87.64	82.92	73.42	87.61	86.12
8.1405	78.46	82.55	86.50	81.48	71.21	86.65	85.09
8.9910	76.36	80.97	85.17	79.86	68.77	85.53	83.92
9.9304	74.01	79.19	83.61	78.03	66.07	84.23	82.60
10.9679	71.32	77.14	81.73	75.88	63.03	82.63	81.01
12.1138	68.26	74.75	79.44	73.36	59.62	80.67	79.09
13.3794	64.79	71.99	76.68	70.39	55.82	78.25	76.73
14.7773	60.92	68.85	73.39	66.94	51.66	75.30	73.86
16.3212	56.57	65.25	69.47	62.92	47.06	71.69	70.33
18.0264	51.65	61.16	64.82	58.22	41.98	67.29	66.01
19.9098	46.13	56.56	59.39	52.77	36.41	62.04	60.80
21.9900	40.17	51.62	53.43	46.80	30.54	56.18	54.92

Size Mid (µm)	012a	041a	046a	052a	059a	064a	070a
24.2875	33.77	46.32	46.95	40.27	24.44	49.72	48.33
26.8250	27.08	40.66	40.09	33.36	18.31	42.83	41.23
29.6276	20.03	34.38	32.61	25.88	12.30	35.27	33.37
32.7231	13.58	27.97	25.34	18.82	7.23	27.88	25.73
36.1420	7.90	21.28	18.12	12.18	3.38	20.44	18.15
39.9180	3.80	15.03	11.87	6.92	1.11	13.86	11.67
44.0886	1.35	9.53	6.83	3.25	0.17	8.38	6.54
48.6950	0.25	5.10	3.18	1.09	0.00	4.21	2.93
53.7826	0.00	2.09	1.05	0.19	0.00	1.58	0.90
59.4017	0.00	0.49	0.15	0.00	0.00	0.32	0.11
65.6079	0.00	0.00	0.00	0.00	0.00	0.00	0.00

Supplementary Table 5. 6 Silt and clay weight percents as well as silt-to-clay ratios for till samples used in detailed grain size analysis.

Sample ID	<63 µm wt%	silt to 4 µm	silt to 2 µm	<4 µm wt%	<2 µm wt%	silt-clay (4 µm) ratio	silt-clay (2 µm) ratio
012a	37.46	33.48	35.15	3.98	2.31	8.4	15.2
041a	16.43	14.94	15.55	1.49	0.88	10	17.7
046a	30.26	28.07	28.84	2.19	1.42	12.8	20.3
052a	15.39	13.90	14.58	1.49	0.81	9.3	18
059a	32.34	27.41	29.46	4.93	2.88	5.6	10.2
064a	6.58	6.08	6.28	0.5	0.3	12.2	20.9
070a	10.42	9.56	9.93	0.86	0.49	11.1	20.3
SS 6	31.17	27.29	29.00	3.88	2.17	7	13.4
SS 11	44.38	39.00	41.38	5.38	3	7.2	13.8
SS 19	21.46	19.47	20.39	1.99	1.07	9.8	19.1
SS 23	34.17	31.42	32.64	2.75	1.53	11.4	21.3
SS 48	14.78	12.87	13.77	1.91	1.01	6.7	13.6

Supplementary Table 5. 7 Silt-to-clay ratios of samples that underwent laser diffraction particle sizing. Conditional formatting highlights variation from low (green) to high (red) silt-to-clay ratios. Data for samples from 2015 was collected by Taves. Approximate degree of oxidation not recorded for several Pionjar drill till samples.

Sample ID	Type	Silt cumulative weight percent	Silt-to-clay ratio	Oxidation
DS 14	Pionjar till 2015	90.12	9.12	-
DS 20	Pionjar till 2015	68.05	2.13	-
DS 24	Pionjar till 2015	91.78	11.16	-
DS 25	Pionjar till 2015	92.64	12.58	Fresh
DS 31a	Pionjar till 2015	85.72	6.00	Fresh
DS 32	Pionjar till 2015	69.01	2.23	-
DS 34a	Pionjar till 2015	93.10	13.49	Fresh

Sample ID	Type	Silt cumulative weight percent	Silt-to-clay ratio	Oxidation
DS 35	Pionjar till 2015	92.96	13.20	Fresh
DS 36	Pionjar till 2015	78.91	3.74	-
DS 37	Pionjar till 2015	92.24	11.89	-
DS 39	Pionjar till 2015	95.45	21.00	Fresh
DS 42	Pionjar till 2015	91.82	11.22	Fresh
DS 44	Pionjar till 2015	91.82	11.23	Fresh
DS 45	Pionjar till 2015	95.16	19.65	Fresh
DS 46	Pionjar till 2015	92.28	11.96	Fresh
DS 6a	Pionjar till 2015	92.26	11.93	Fresh
SS 1	Surficial till 2015	93.15	13.60	Slight
SS 10	Surficial till 2015	96.49	27.50	Slight
SS 11	Surficial till 2015	92.66	12.63	Slight
SS 12	Surficial till 2015	94.99	18.98	Slight
SS 13	Surficial till 2015	95.12	19.50	Slight
SS 19	Surficial till 2015	94.58	17.46	Slight
SS 2	Surficial till 2015	94.57	17.41	Slight
SS 22	Surficial till 2015	93.93	15.48	Fresh
SS 23	Surficial till 2015	95.18	19.75	Slight
SS 3	Surficial till 2015	96.81	30.33	Slight
SS 4	Surficial till 2015	93.15	13.60	Slight
SS 48	Surficial till 2015	92.53	12.38	Slight
SS 49	Surficial till 2015	94.21	16.28	Slight
SS 5	Surficial till 2015	93.80	15.13	Slight
SS 6	Surficial till 2015	92.46	12.27	Slight
SS 7	Surficial till 2015	92.14	11.72	Slight
SS 8	Surficial till 2015	96.13	24.81	Slight
SS 9	Surficial till 2015	95.68	22.16	Fresh
012a	Surficial till 2016	93.36	14.06	Slight
041a	Surficial till 2016	94.20	16.25	Slight
046a	Surficial till 2016	95.01	19.06	High
052a	Surficial till 2016	94.23	16.34	High
059a	Surficial till 2016	90.35	9.36	Slight
064a	Surficial till 2016	95.05	19.20	High
070a	Surficial till 2016	94.88	18.54	High

5.4. Bulk Composition Geochem QA/QC

5.4.1. Certified Standards

Total average percent relative standard deviation of reference materials is 2.8%, which indicates "excellent" precision (Jenner, 1996). Till 1 and Till 3 CANMET standard data available at https://www.nrcan.gc.ca/our-natural-resources/minerals-mining/mining-resources/till-1-till-2-till-3-and-till-4-certificate-analysis/8137.

Supplementary Table 5. 8 Percent relative standard deviation of CANMET till standard values (ICP-OES).

SRC Sample ID	Al_2O_3 wt%	CaO wt%	Fe_2O_3 wt%	K_2O wt%	MgO wt%	MnO wt%	Na_2O wt%	P_2O_5 wt%	TiO_2 wt%
Detection limit	0.01	0.01	0.01	0.002	0.001	0.001	0.01	0.002	0.001
2015 – Till 1									
27	14.6	2.84	7.34	2.16	2.26	0.185	2.86	0.239	0.996
68	13.8	2.65	6.81	2.23	2.18	0.174	2.76	0.221	0.915
Average	14.2	2.745	7.075	2.195	2.22	0.1795	2.81	0.23	0.9555
Standard deviation (SD)	0.566	0.134	0.375	0.049	0.057	0.008	0.071	0.013	0.057
%Relative SD	3.984	4.894	5.297	2.255	2.548	4.333	2.516	5.534	5.994
Ave %RSD	4.151								
2016 – Till 3									
CT-SRC-001	12.4	2.62	4.04	2.46	1.72	0.06	2.7	0.123	0.494
CT-SRC-027	12.2	2.66	3.97	2.44	1.74	0.061	2.69	0.124	0.505
CT-SRC-054	12.2	2.6	3.96	2.4	1.68	0.059	2.72	0.12	0.485
Average	12.267	2.627	3.990	2.433	1.713	0.060	2.703	0.122	0.495
Standard deviation (SD)	0.115	0.031	0.044	0.031	0.031	0.001	0.015	0.002	0.010
%Relative SD	0.941	1.163	1.092	1.256	1.783	1.667	0.565	1.702	2.025
Ave %RSD	1.355								
Total ave %RSD	**2.753**								

5.4.2. Duplicates

Supplementary Table 5. 9 ICP-OES values for original and duplicated samples.

Sample ID	Al_2O_3 wt% (original)	Al_2O_3 wt% (duplicate)	CaO wt% (original)	CaO wt% (duplicate)	Fe_2O_3 wt% (original)	Fe_2O_3 wt% (duplicate)	K_2O wt% (original)	K_2O wt% (duplicate)	MgO wt% (original)
009a	13.4	13.2	3.5	3.76	3.81	3.62	1.24	1.26	1.98
031a	14.8	14.6	3.03	3	5.01	4.97	1.76	1.73	2.65
038a	14.7	15.1	3.71	3.58	4.9	4.58	1.16	1.23	1.8
048a	14.3	14.5	2.88	2.91	3.26	3.29	1.37	1.38	1.44
059a	14.8	14.6	2.66	2.68	3.49	3.52	1.46	1.44	1.64
063a	14	13.1	2.24	2.11	7.4	6.93	1.24	1.15	2.35
070a	14.8	14.7	2.26	2.24	6.44	6.27	1.06	1.05	1.62
DS 36	14.6	14.1	3.33	3.29	5	4.95	2.09	2.06	3.03
DS 37	13.1	12.7	4.09	3.94	4.06	3.91	1.49	1.44	2.5
ES 18	13.4	13.3	3.95	3.92	10.2	10.1	1.31	1.3	5.32
SS 13	15.8	14.9	3.86	3.64	5.06	4.79	1.32	1.28	3.05
SS 3	13.4	14.4	3.33	3.54	3.35	3.64	1.05	1.15	1.75

Sample ID	MgO wt% (duplicate)	MnO wt% (original)	MnO wt% (duplicate)	Na_2O wt% (original)	Na_2O wt% (duplicate)	P_2O_5 wt% (original)	P_2O_5 wt% (duplicate)	TiO_2 wt% (original)	TiO_2 wt% (duplicate)
009a	2.14	0.054	0.056	3.46	3.62	0.133	0.153	0.606	0.631
031a	2.61	0.065	0.064	3.33	3.28	0.139	0.138	0.619	0.608
038a	1.8	0.071	0.066	3.94	4.02	0.204	0.208	0.754	0.656
048a	1.44	0.04	0.041	3.65	3.69	0.087	0.086	0.627	0.632
059a	1.65	0.043	0.042	3.63	3.61	0.073	0.071	0.674	0.677
063a	2.13	0.06	0.054	2.61	2.47	0.276	0.262	0.699	0.666
070a	1.65	0.044	0.044	3.02	3.01	0.15	0.148	0.726	0.699
DS 36	3.01	0.072	0.069	3.43	3.43	0.147	0.143	0.582	0.574
DS 37	2.43	0.066	0.064	3.63	3.56	0.144	0.136	0.588	0.568
ES 18	5.28	0.183	0.181	3.03	2.98	0.196	0.195	0.676	0.664

Sample ID	MgO wt% (duplicate)	MnO wt% (original)	MnO wt% (duplicate)	Na_2O wt% (original)	Na_2O wt% (duplicate)	P_2O_5 wt% (original)	P_2O_5 wt% (duplicate)	TiO_2 wt% (original)	TiO_2 wt% (duplicate)
SS 13	2.9	0.064	0.062	3.85	3.63	0.221	0.199	0.691	0.617
SS 3	1.91	0.047	0.05	3.7	3.99	0.128	0.142	0.535	0.581

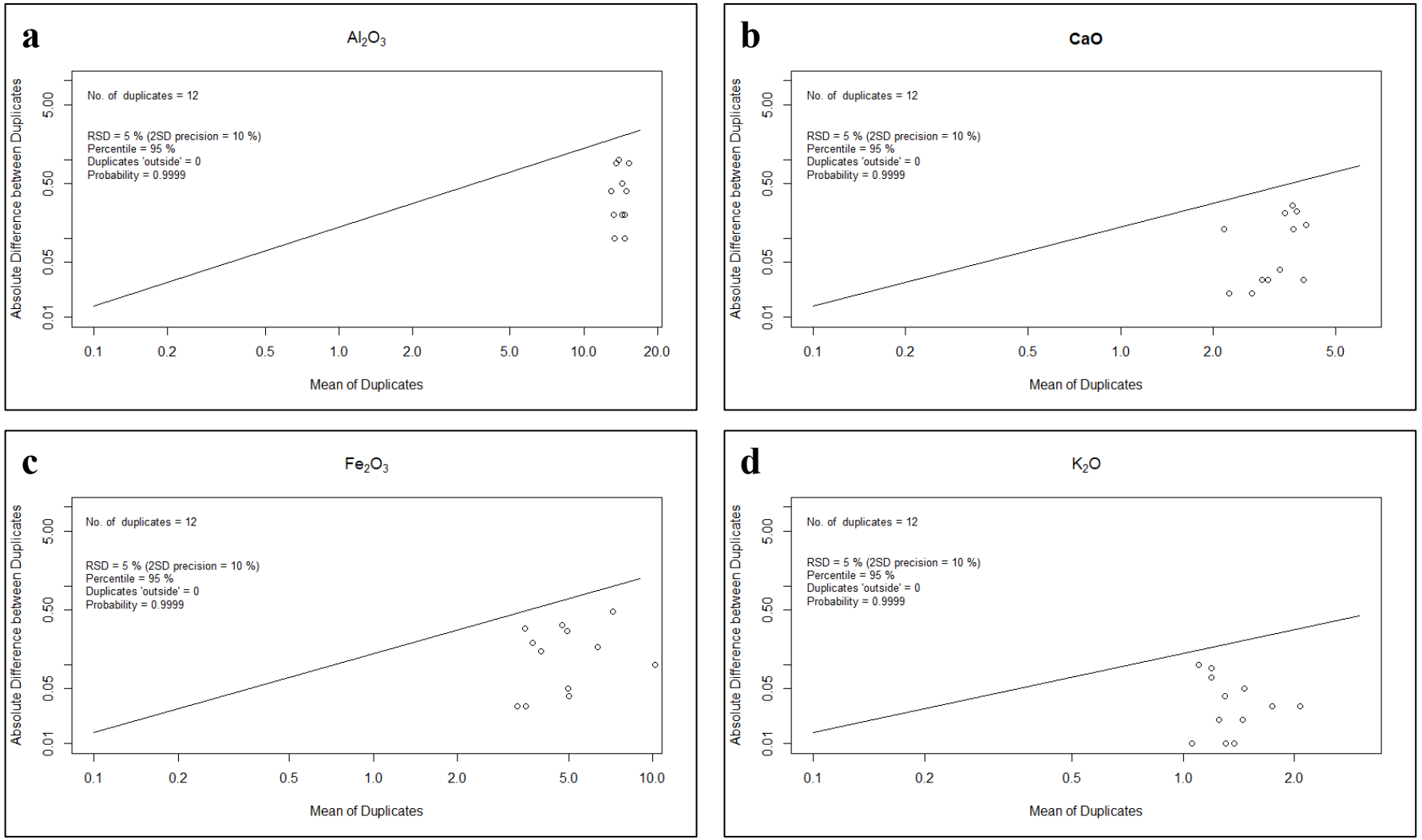

Supplementary Figure 5. 4 (a-d) Thompson-Howarth plots testing the precision of major oxide data as outlined by Piercey (2014). All major oxides measurements show greater than 95% precision to a 99% confidence level. Thompson-Howarth plots were generated using the R Statistical package (Garrett and Grunsky, 2003), including ggplot2 (Wickham, 2016).

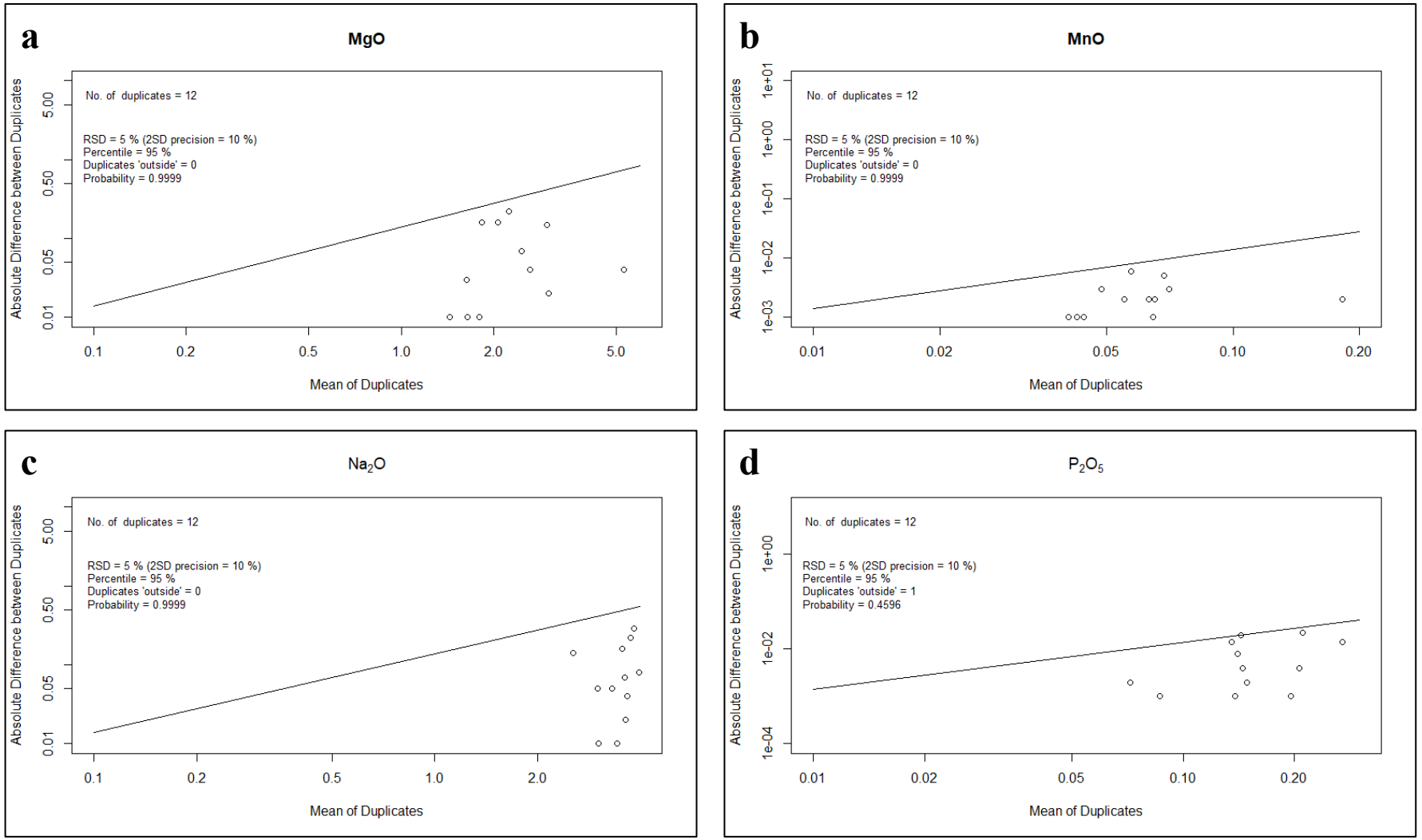

Supplementary Figure 5. 5 (a-d) Thompson-Howarth plots testing the precision of major oxide data as outlined by Piercey (2014). All major oxides measurements show greater than 95% precision to a 99% confidence level, excluding P_2O_5. Thompson-Howarth plots were generated using the R Statistical package (Garrett and Grunsky, 2003), including ggplot2 (Wickham, 2016).

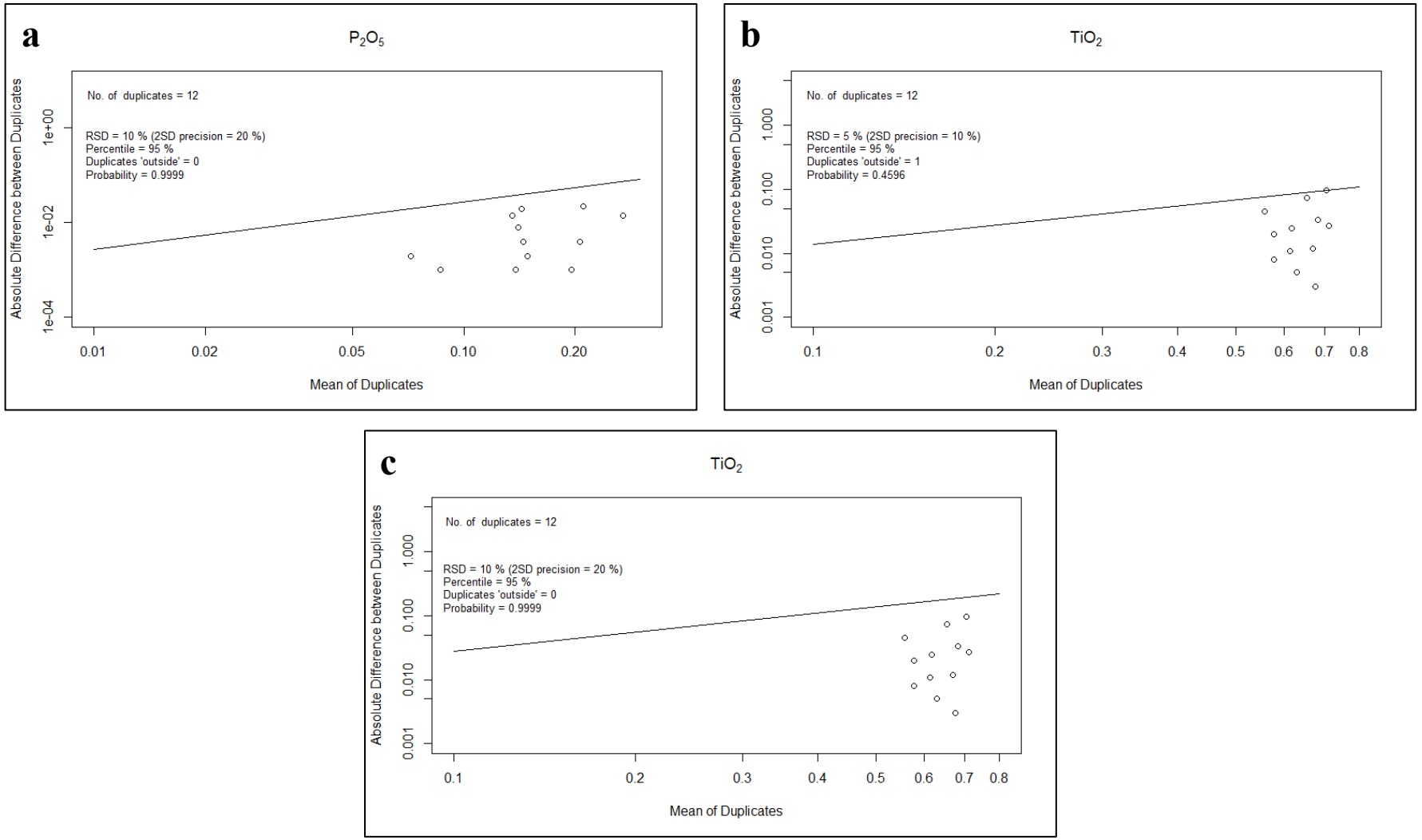

Supplementary Figure 5. 6 (a-c) Thompson-Howarth plots testing the precision of major oxide data as outlined by Piercey (2014). P_2O_5 and TiO_2 measurements, which show greater than 90% precision to a 99% confidence level. Thompson-Howarth plots were generated using the R Statistical package (Garrett and Grunsky, 2003), including ggplot2 (Wickham, 2016).

Supplementary Table 5. 10 Percent variance of major oxide values for duplicate samples. All major oxide measurements are precise to within 10% variance, excluding P_2O_5 and TiO_2 measurements, which are precise to within 15% variance. 'Field' duplicates represent samples that were collected twice within close proximity of one another during fieldwork, 'Sample' duplicates represent samples that were split and submitted twice for analysis, and 'Lab'duplicates represent individual samples that were analyzed twice.

Sample ID	Duplicate Type	Al_2O_3 % Variance	CaO % Variance	Fe_2O_3 % Variance	K_2O % Variance	MgO % Variance	MnO % Variance	Na_2O % Variance	P_2O_5 % Variance	TiO_2 % Variance
009a	Field	1.5	7.4	5.0	1.6	8.1	3.7	4.6	15.0	4.1
031a	Sample	1.4	1.0	0.8	1.7	1.5	1.5	1.5	0.7	1.8
038a	Field	2.7	3.5	6.5	6.0	0.0	7.0	2.0	2.0	13.0
048a	Lab	1.4	1.0	0.9	0.7	0.0	2.5	1.1	1.1	0.8
059a	Sample	1.4	0.8	0.9	1.4	0.6	2.3	0.6	2.7	0.4
063a	Sample	6.4	5.8	6.4	7.3	9.4	10.0	5.4	5.1	4.7
070a	Sample	0.7	0.9	2.6	0.9	1.9	0.0	0.3	1.3	3.7
DS 36	Lab	3.4	1.2	1.0	1.4	0.7	4.2	0.0	2.7	1.4
DS 37	Sample	3.1	3.7	3.7	3.4	2.8	3.0	1.9	5.6	3.4
ES 18	Lab	0.7	0.8	1.0	0.8	0.8	1.1	1.7	0.5	1.8
SS 13	Sample	5.7	5.7	5.3	3.0	4.9	3.1	5.7	10.0	10.7
SS 3	Sample	7.5	6.3	8.7	9.5	9.1	6.4	7.8	10.9	8.6

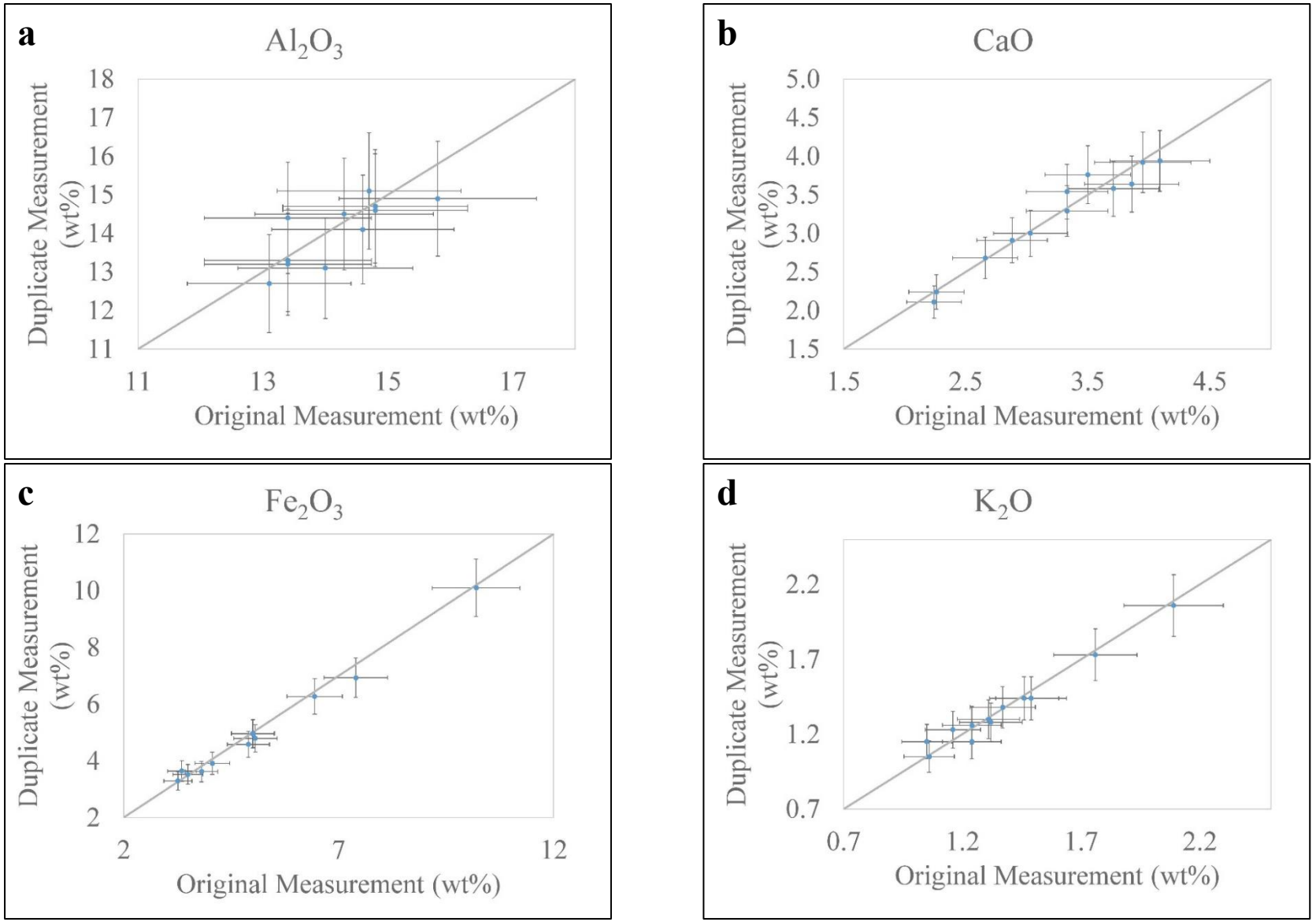

Supplementary Figure 5. 7 (a-d) Scatterplots with a 1:1 control line showing precision of major oxide duplicate measurements. All major oxide measurements are precise to within 10% variance.

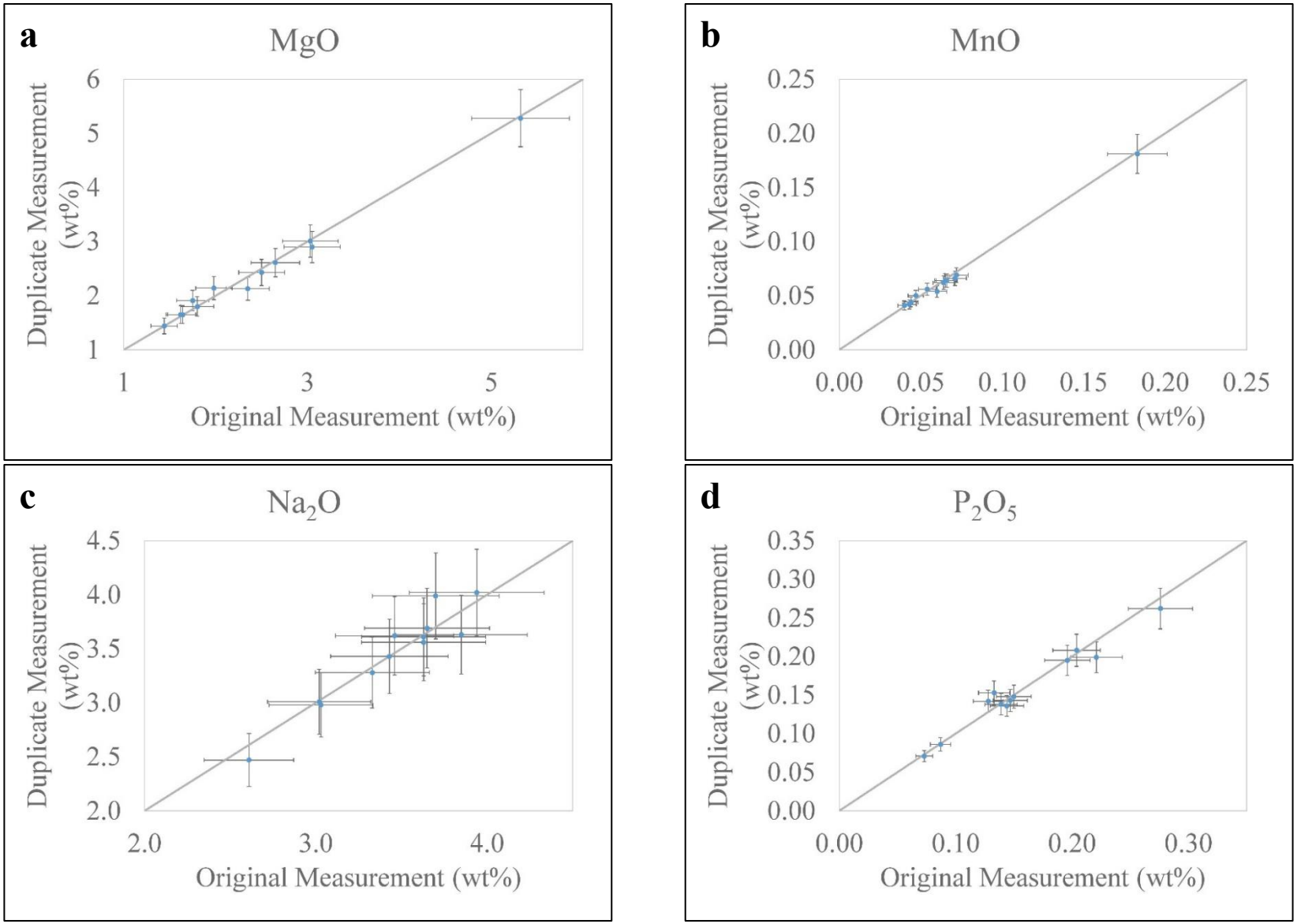

Supplementary Figure 5. 8 Scatterplots with a 1:1 control line showing precision of major oxide duplicate measurements. All major oxide measurements are precise to within 10% variance, excluding P_2O_5, which are precise to within 15% variance.

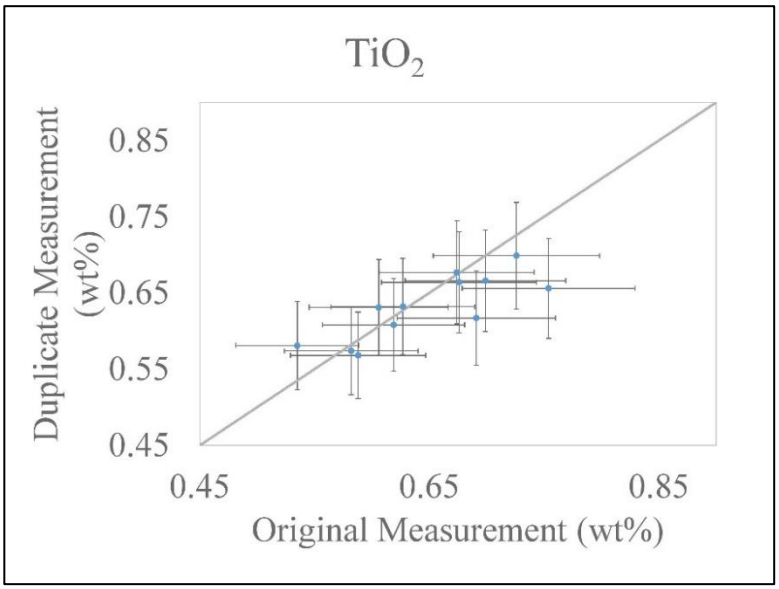

Supplementary Figure 5. 9 Scatterplot with a 1:1 control line showing precision of major oxide duplicate measurements. TiO_2 measurements, which are precise to within 15% variance.

5.4.3. Statistical Analyses

Non-detect values were replaced with "0".

Supplementary Table 5. 11 Major oxide summary statistics for meta-sedimentary bedrock lithogeochemical (XRF) analysis (Perrouty et al., 2019; Gaillard et al., 2020).

	Al_2O_3 wt%	CaO wt%	Fe_2O_3 wt%	K_2O wt%	MgO wt%	MnO wt%	Na_2O wt%	P_2O_5 wt%	TiO_2 wt%
Detection limit	0.01	0.01	0.01	0.01	0.01	0.01	0.01	0.01	0.01
Mean	15.997	2.495	5.841	2.801	3.024	0.068	3.515	0.153	0.588
Standard Error	0.073	0.040	0.055	0.051	0.037	0.001	0.046	0.002	0.005
Median	15.7	2.42	5.67	2.5	2.9	0.069	3.6	0.15	0.57
Mode	14.6	2.54	5.81	2.09	2.68	0.07	3.67	0.15	0.56
Standard Deviation	1.784	0.986	1.341	1.264	0.905	0.022	1.123	0.045	0.117
Sample Variance	3.184	0.972	1.798	1.598	0.818	0.000	1.260	0.002	0.014
Range	17.51	9.73	17.88	9.16	11.2	0.287	7.86	0.46	1.91
Minimum	7.55	0.48	0.89	0.19	0.14	0.008	0.13	0.01	0.08
Maximum	25.06	10.21	18.77	9.35	11.34	0.295	7.99	0.47	1.99
Count	605	605	605	605	605	605	605	605	605

Supplementary Table 5. 12 Major oxide summary statistics for felsic bedrock lithogeochemical (XRF) analysis (Perrouty et al., 2019; Gaillard et al., 2020).

	Al_2O_3 wt%	CaO wt%	Fe_2O_3 wt%	K_2O wt%	MgO wt%	MnO wt%	Na_2O wt%	P_2O_5 wt%	TiO_2 wt%
Detection limit	0.01	0.01	0.01	0.01	0.01	0.01	0.01	0.01	0.01
Mean	15.889	2.852	3.244	2.720	1.425	0.041	5.695	0.208	0.416
Standard Error	0.165	0.171	0.216	0.155	0.140	0.004	0.139	0.012	0.022
Median	15.9	2.51	3.11	2.75	1.11	0.027	5.76	0.19	0.37
Mode	15.8	1.5	0.95	2.97	0.3	0.01	6.77	0.09	0.18
Standard Deviation	1.811	1.876	2.372	1.707	1.543	0.042	1.534	0.128	0.246
Sample Variance	3.280	3.519	5.628	2.913	2.382	0.002	2.355	0.016	0.061
Range	15.09	11.34	12.87	14.42	9.51	0.232	9.3	0.72	1.15
Minimum	3.6	0.25	0.46	0.08	0	0	0.13	0	0.02
Maximum	18.69	11.59	13.33	14.5	9.51	0.232	9.43	0.72	1.17
Count	121	121	121	121	121	121	121	121	121

Supplementary Table 5. 13 Major oxide summary statistics for mafic dyke lithogeochemical (XRF) analysis (Perrouty et al., 2019; Gaillard et al., 2020).

	Al_2O_3 wt%	CaO wt%	Fe_2O_3 wt%	K_2O wt%	MgO wt%	MnO wt%	Na_2O wt%	P_2O_5 wt%	TiO_2 wt%
Detection limit	0.01	0.01	0.01	0.01	0.01	0.01	0.01	0.01	0.01
Mean	12.698	8.846	9.824	2.502	8.931	0.165	1.873	0.326	0.736
Standard Error	0.199	0.212	0.134	0.140	0.250	0.003	0.105	0.015	0.013
Median	12.755	9.08	9.99	2.34	8.965	0.17	1.705	0.32	0.73
Mode	11.09	11.66	10.39	0.77	7.99	0.15	0.92	0.14	0.77
Standard Deviation	2.193	2.347	1.477	1.550	2.763	0.038	1.160	0.162	0.142
Sample Variance	4.809	5.508	2.182	2.403	7.633	0.001	1.346	0.026	0.020
Range	11.96	12.87	12.17	5.42	15.24	0.24	5.78	0.71	0.92
Minimum	6.44	0.8	2.54	0.28	1.01	0.03	0.22	0.02	0.23
Maximum	18.4	13.67	14.71	5.7	16.25	0.27	6	0.73	1.15
Count	122	122	122	122	122	122	122	122	122

5.4.4. Pebble Lithology

Supplementary Table 5. 14 Clast lithology counts (normalized and rounded to the nearest percent). Counts in 2015 were completed by Taves.

Sample ID	Intrusive clasts (%)	Meta-sedimentary clasts (%)	Quartz fragments (%)	Total percent	Year
001a	27	68	6	100	2016
004a	26	72	2	100	2016
005a	19	79	2	100	2016
007a	19	74	8	100	2016
009a	26	73	2	100	2016
010a	27	70	3	100	2016
011a	22	76	2	100	2016
012a	18	80	2	100	2016
019a	34	63	3	100	2016
021a	23	75	3	100	2016
031a	15	85	1	100	2016
036a	20	77	4	100	2016
038a	14	84	3	100	2016
039a	16	81	4	100	2016
040a	4	90	6	100	2016
041a	11	84	6	100	2016
042a	6	94	1	100	2016
043a	19	77	5	100	2016
044a	53	46	2	100	2016
045a	26	69	5	100	2016
046a	11	86	4	100	2016
047a	35	60	5	100	2016
048a	16	84	1	100	2016
049a	20	69	12	100	2016
050a	36	62	3	100	2016
052a	25	73	2	100	2016
054a	30	69	2	100	2016
055a	69	28	4	100	2016
056a	62	37	2	100	2016
057a	15	82	4	100	2016
058a	33	66	2	100	2016
059a	28	70	3	100	2016
060a	15	85	1	100	2016
061a	2	98	1	100	2016
062a	24	74	3	100	2016
063a	25	76	0	100	2016
064a	21	77	3	100	2016

Sample ID	Intrusive clasts (%)	Meta-sedimentary clasts (%)	Quartz fragments (%)	Total percent	Year
065a	14	86	0	100	2016
070a	26	72	3	100	2016
SS 1	31	65	4	100	2015
SS 2	66	33	2	100	2015
SS 3	35	61	4	100	2015
SS 4	40	59	1	100	2015
SS 5	57	40	3	100	2015
SS 6	50	47	3	100	2015
SS 7	44	52	4	100	2015
SS 8	35	60	5	100	2015
SS 9	45	54	1	100	2015
SS 10	11	88	0	100	2015
SS 11	29	68	3	100	2015
SS 12	71	28	0	100	2015
SS 13	56	43	1	100	2015
SS 19	48	51	1	100	2015
SS 22	39	58	3	100	2015
SS 23	41	56	2	100	2015
SS 48	48	52	1	100	2015
SS 49	61	38	2	100	2015

Supplementary Table 5. 15 Pebble lithology counts used in the precision scatterplot for samples from 2016.

Sample ID	Intrusive	Meta-sed	Quartz	X	Y	Depth (m)
009a	26	73	2	718028	5338822	0.2
009b	28	71	2	718028	5338802	0.4
038a	14	84	3	706829	5337116	0.25
038b	20	78	3	706829	5337116	0.35
065a	14	86	0	713328	5338467	0.6
065b	11	86	3	713328	5338467	0.35

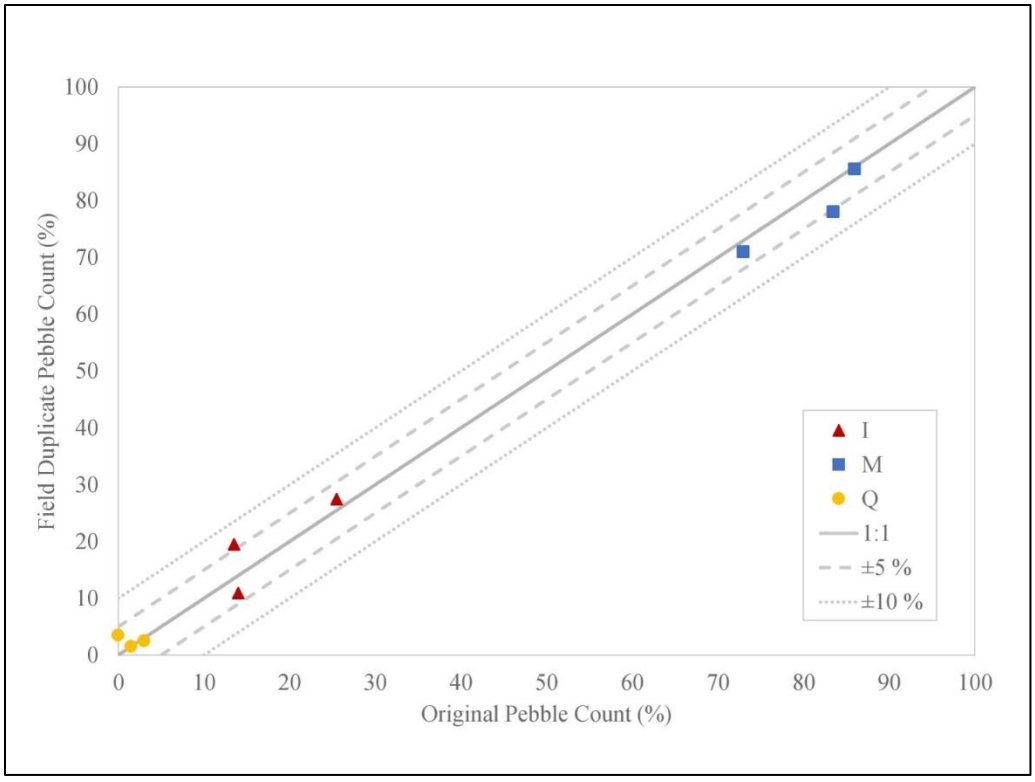

Supplementary Figure 5. 10 Precision scatterplot for pebble counts from 2016 showing 'original' and 'duplicated' counts. Results are precise to within 10%.
Abbr: I – igneous clasts, M – meta-sedimentary clasts, Q – quartz fragments.

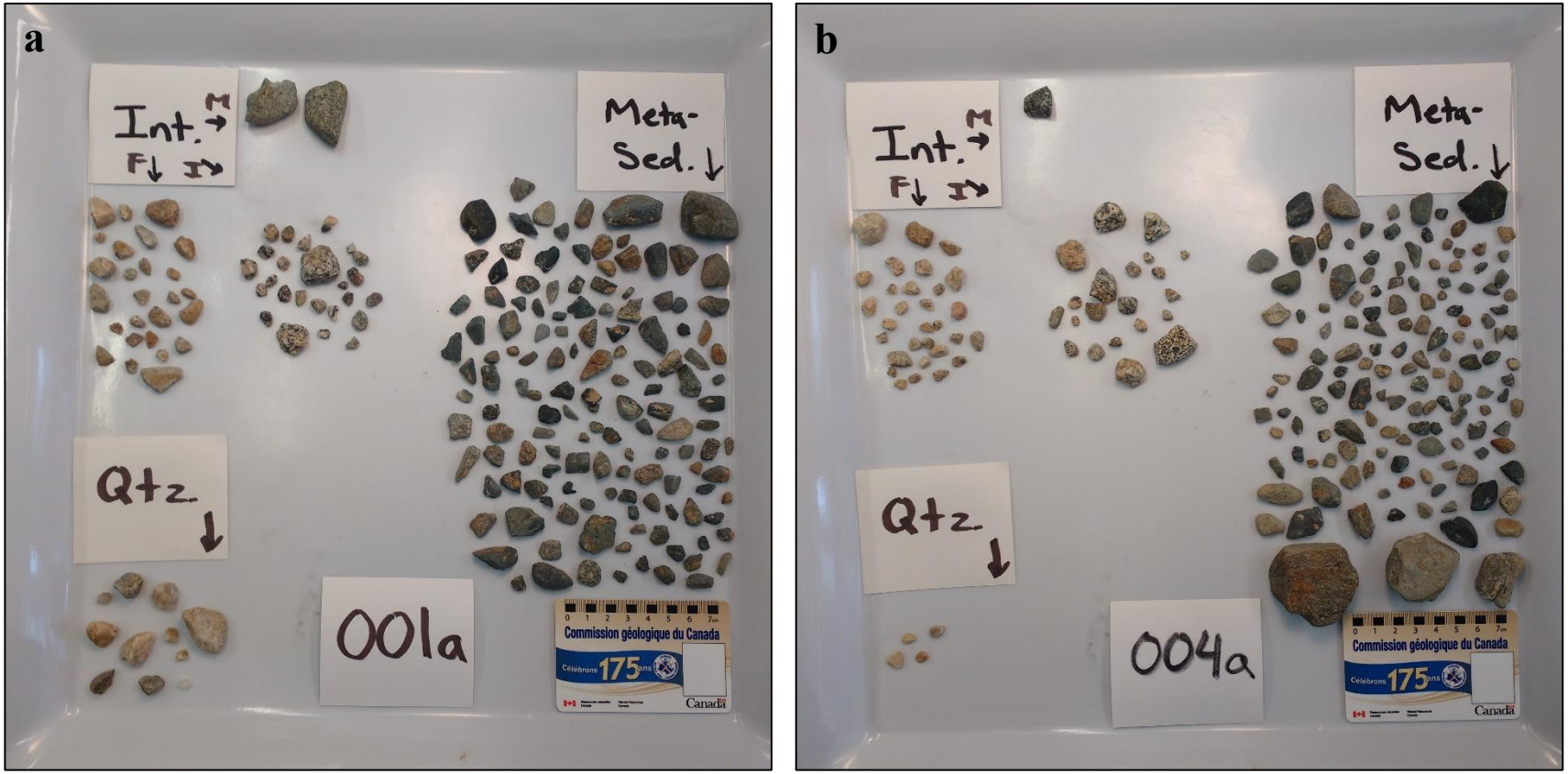

Supplementary Figure 5. 11 (a-b) Till clasts from 2016 sorted by lithology. Sample ID is listed (bottom-centre).
Abbr: F – felsic, I – intermediate, Int – intrusive, M – mafic, Meta-Sed – meta-sedimentary, Qtz – quartz.

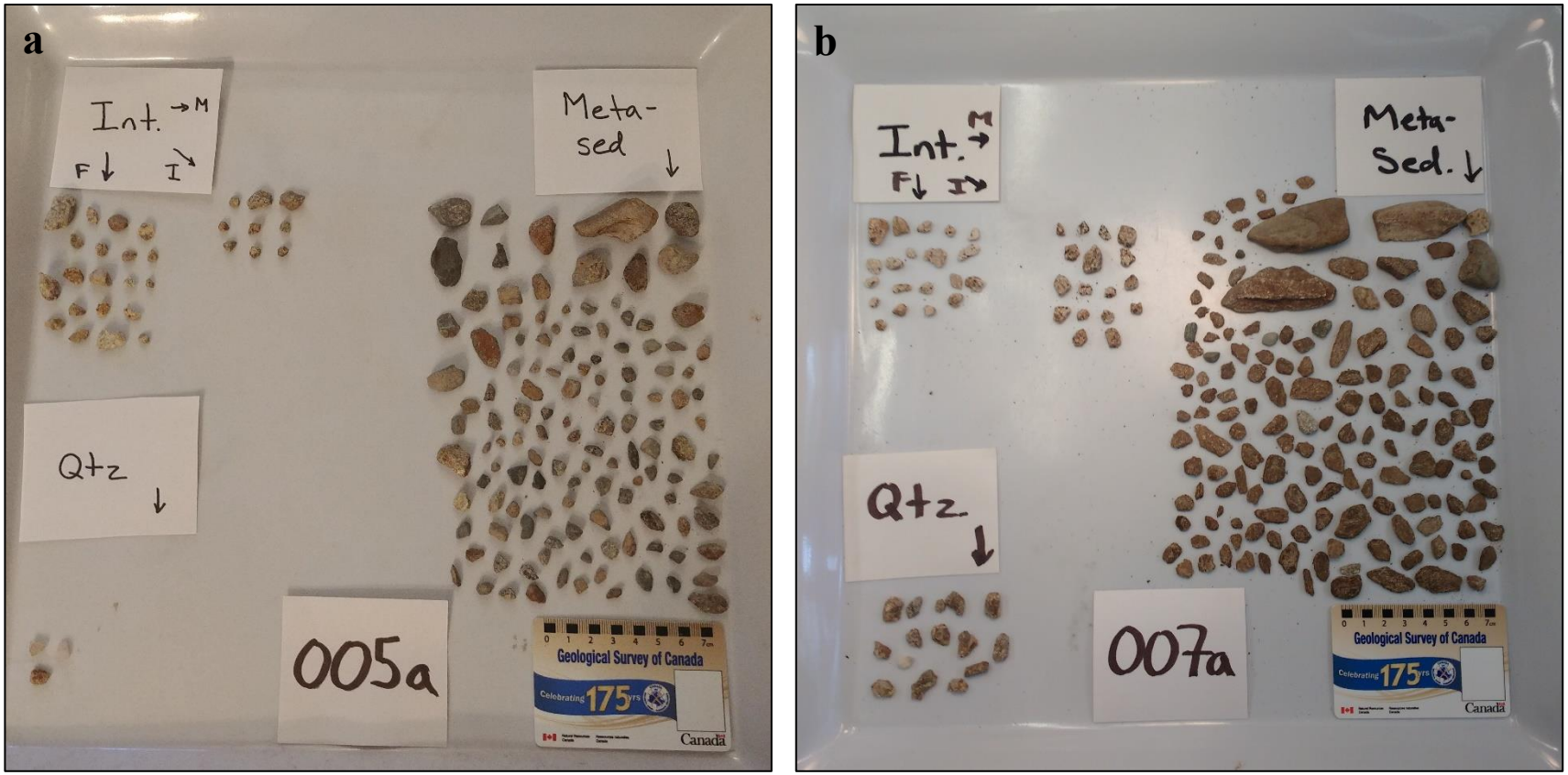

Supplementary Figure 5. 12 (a-b) Till clasts from 2016 sorted by lithology. Sample ID is listed (bottom-centre).
Abbr: F – felsic, I – intermediate, Int – intrusive, M – mafic, Meta-Sed – meta-sedimentary, Qtz – quartz.

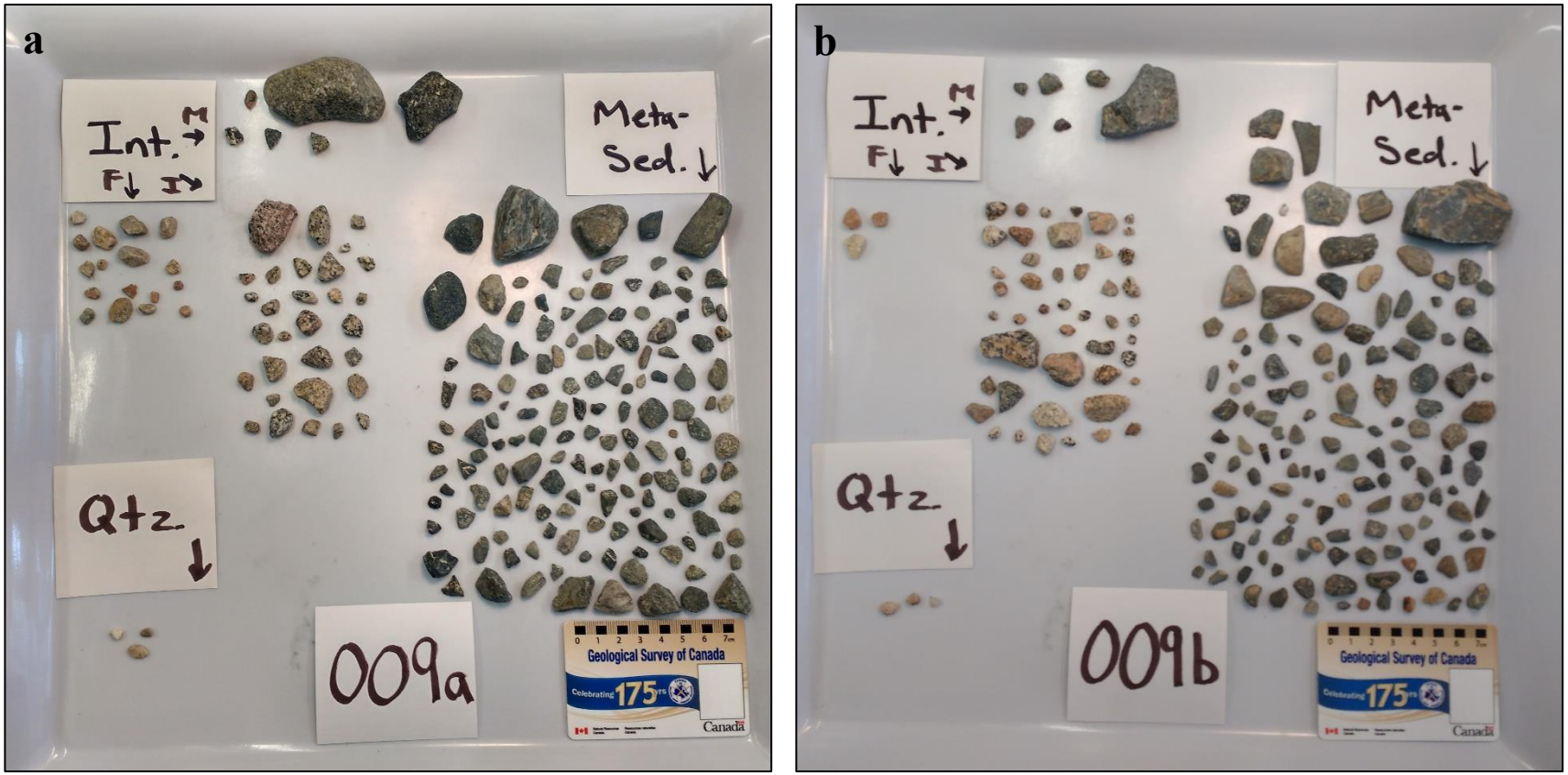

Supplementary Figure 5. 13 (a-b) Till clasts from 2016 sorted by lithology. Sample ID is listed (bottom-centre).
Abbr: F – felsic, I – intermediate, Int – intrusive, M – mafic, Meta-Sed – meta-sedimentary, Qtz – quartz.

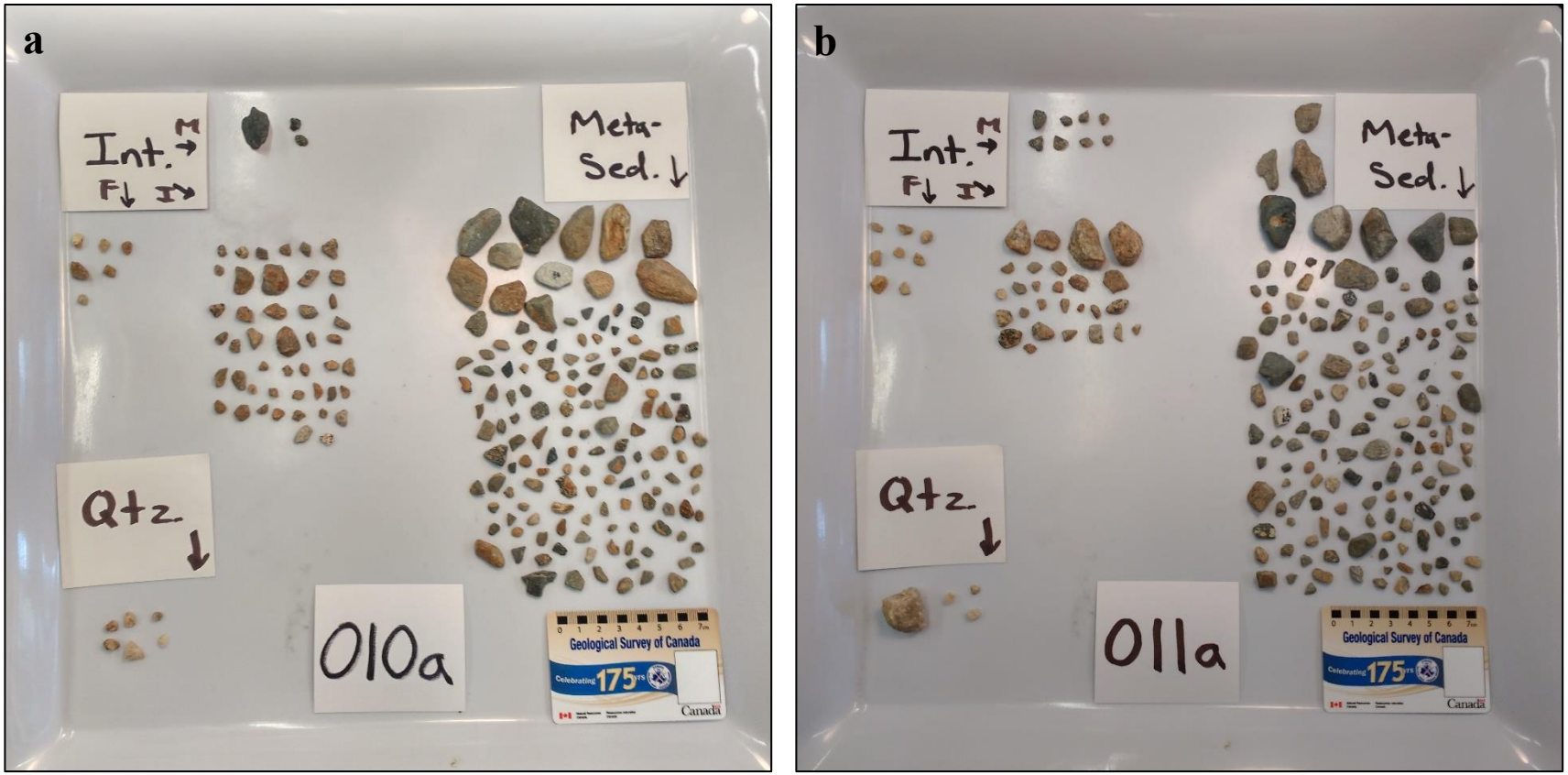

Supplementary Figure 5. 14 (a-b) Till clasts from 2016 sorted by lithology. Sample ID is listed (bottom-centre).
Abbr: F – felsic, I – intermediate, Int – intrusive, M – mafic, Meta-Sed – meta-sedimentary, Qtz – quartz.

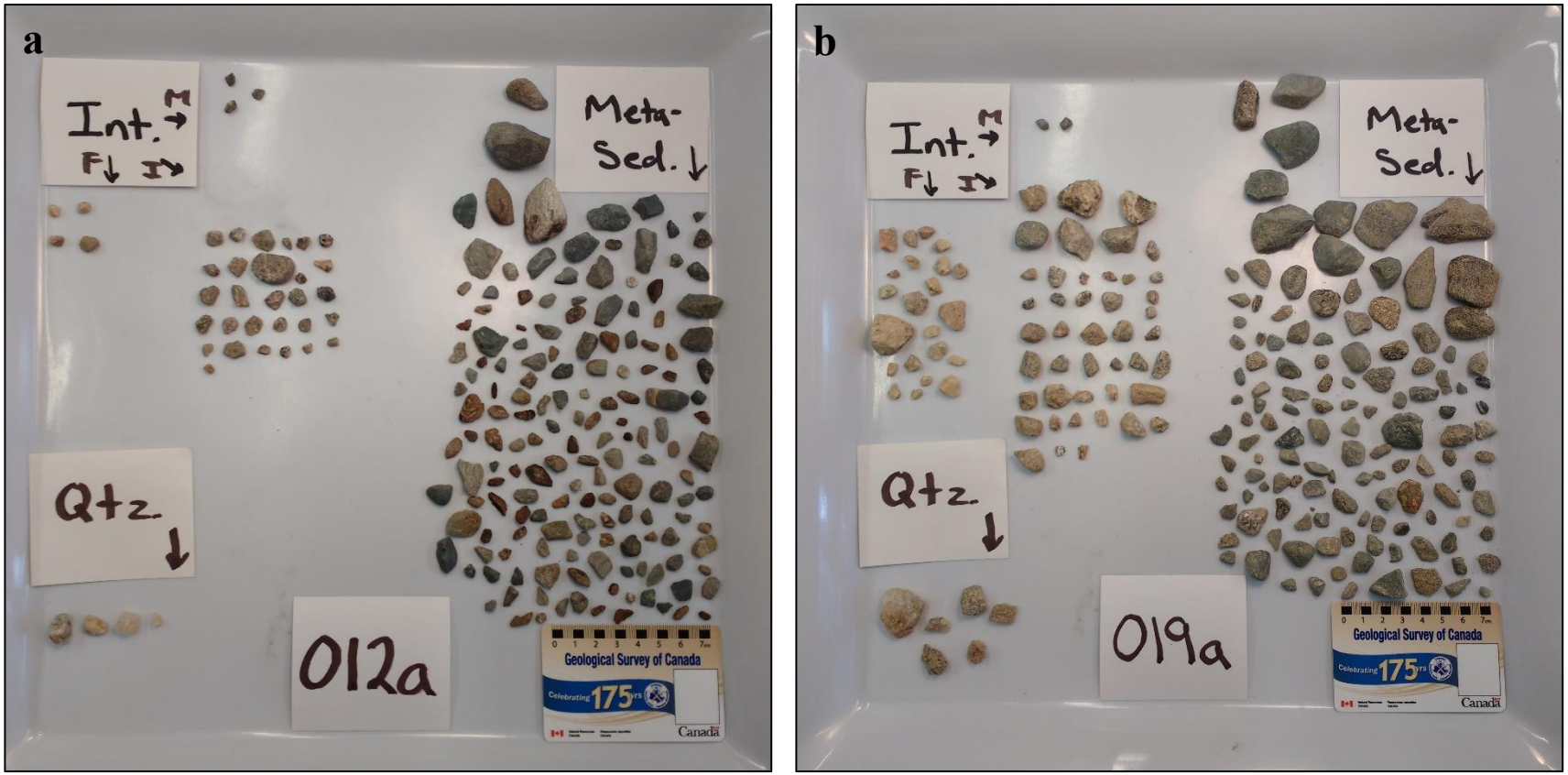

Supplementary Figure 5. 15 (a-b) Till clasts from 2016 sorted by lithology. Sample ID is listed (bottom-centre).
Abbr: F – felsic, I – intermediate, Int – intrusive, M – mafic, Meta-Sed – meta-sedimentary, Qtz – quartz.

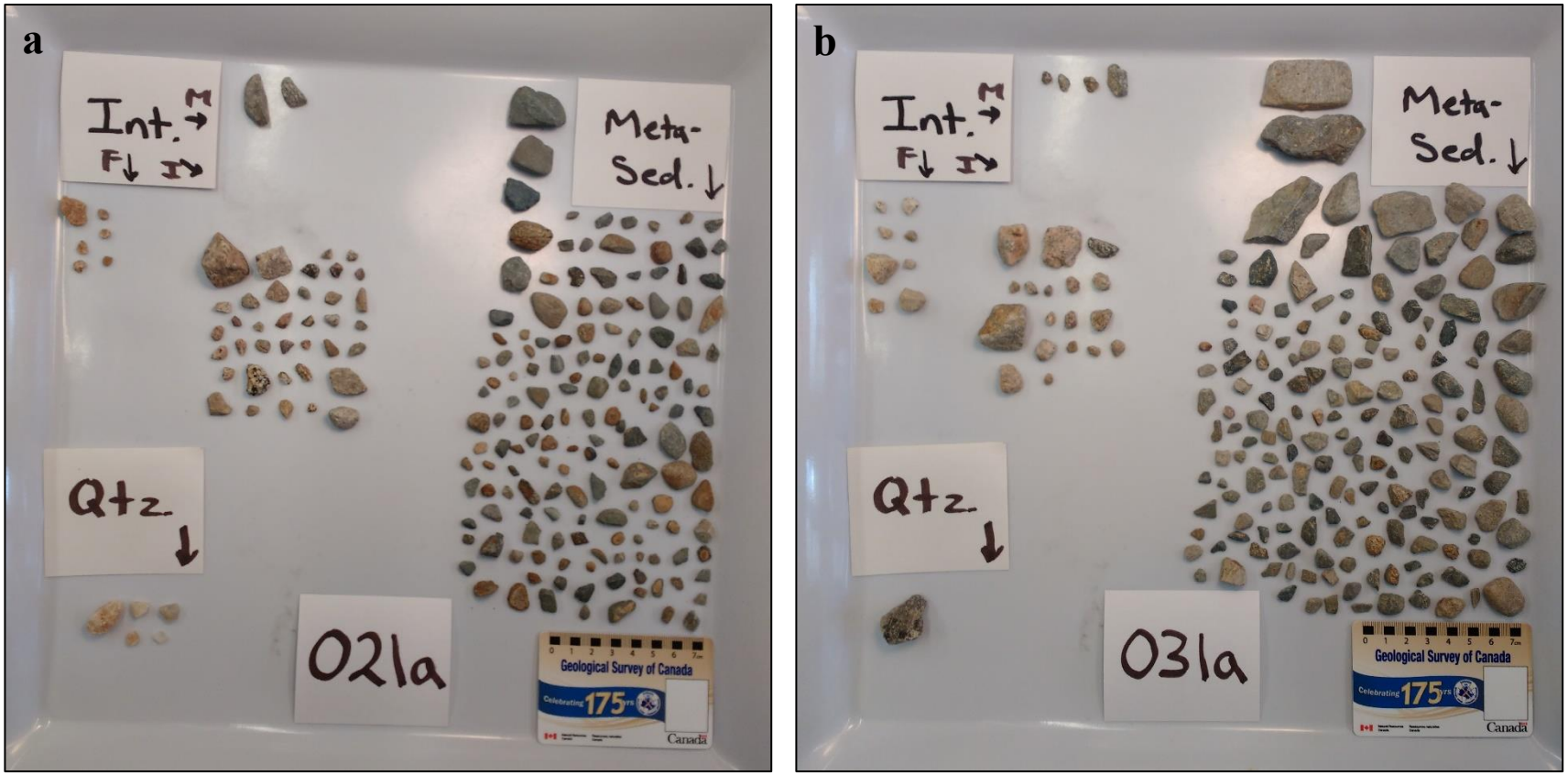

Supplementary Figure 5. 16 (a-b) Till clasts from 2016 sorted by lithology. Sample ID is listed (bottom-centre).
Abbr: F – felsic, I – intermediate, Int – intrusive, M – mafic, Meta-Sed – meta-sedimentary, Qtz – quartz.

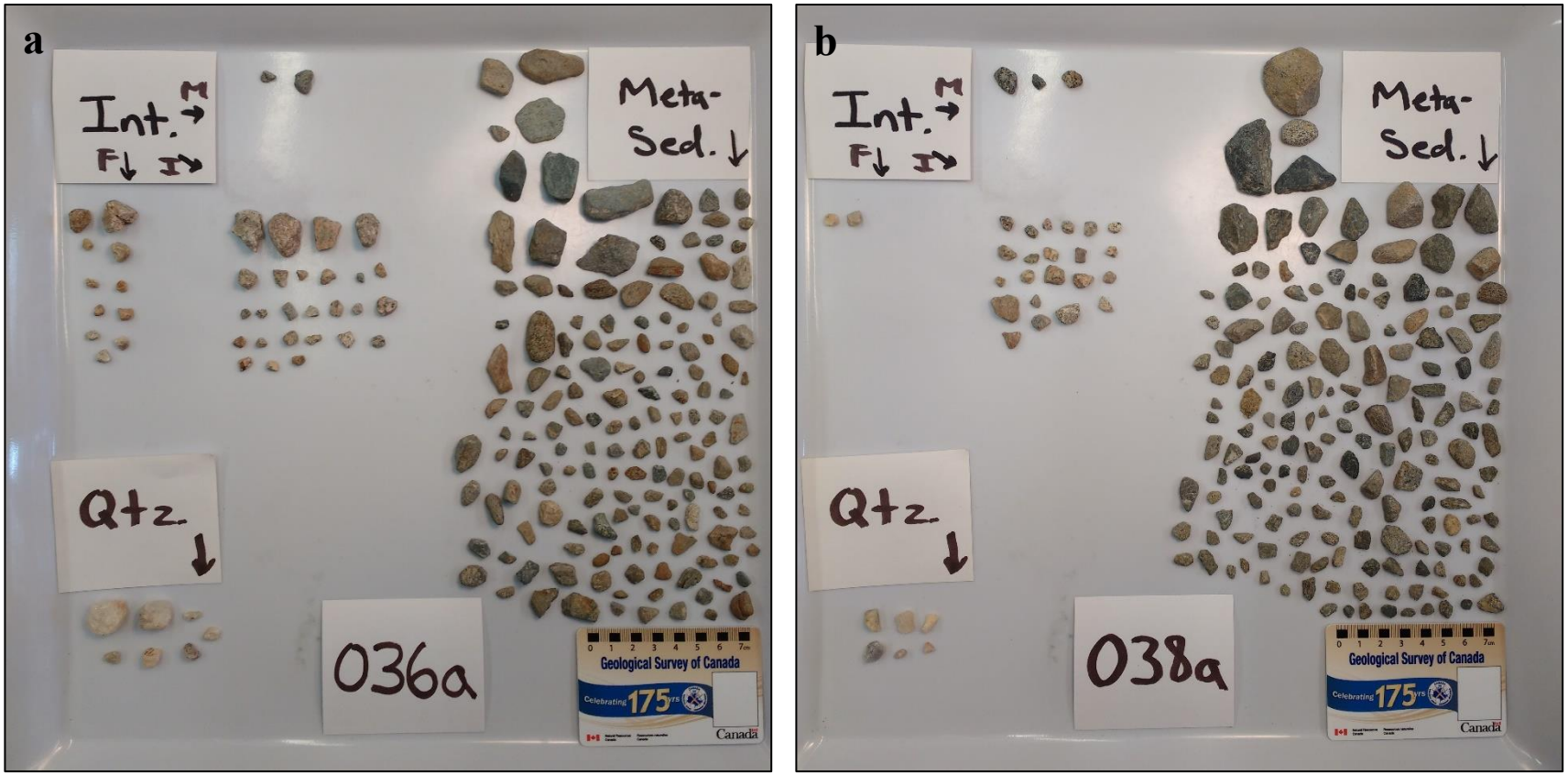

Supplementary Figure 5. 17 (a-b) Till clasts from 2016 sorted by lithology. Sample ID is listed (bottom-centre).
Abbr: F – felsic, I – intermediate, Int – intrusive, M – mafic, Meta-Sed – meta-sedimentary, Qtz – quartz.

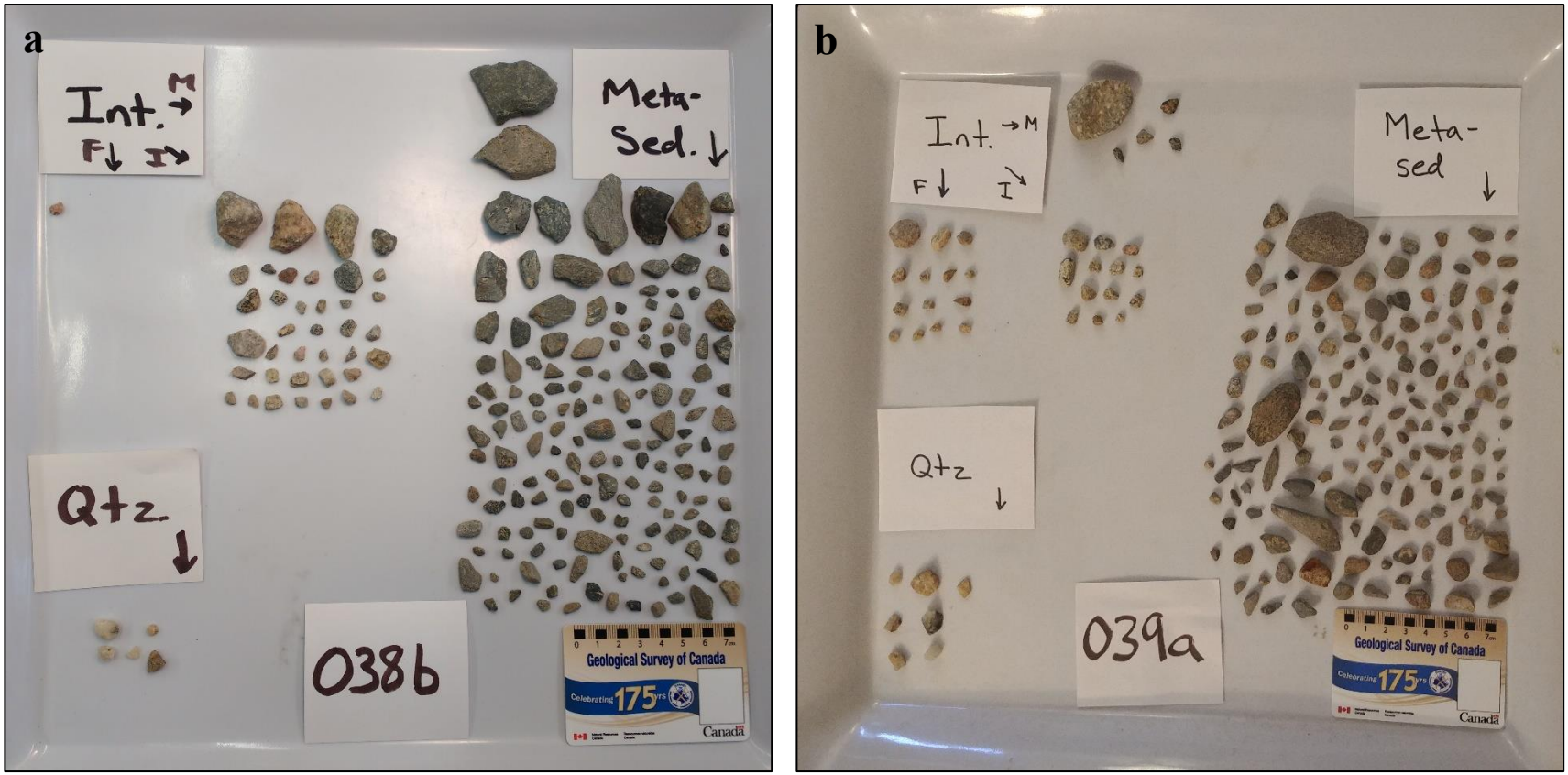

Supplementary Figure 5. 18 (a-b) Till clasts from 2016 sorted by lithology. Sample ID is listed (bottom-centre).
Abbr: F – felsic, I – intermediate, Int – intrusive, M – mafic, Meta-Sed – meta-sedimentary, Qtz – quartz.

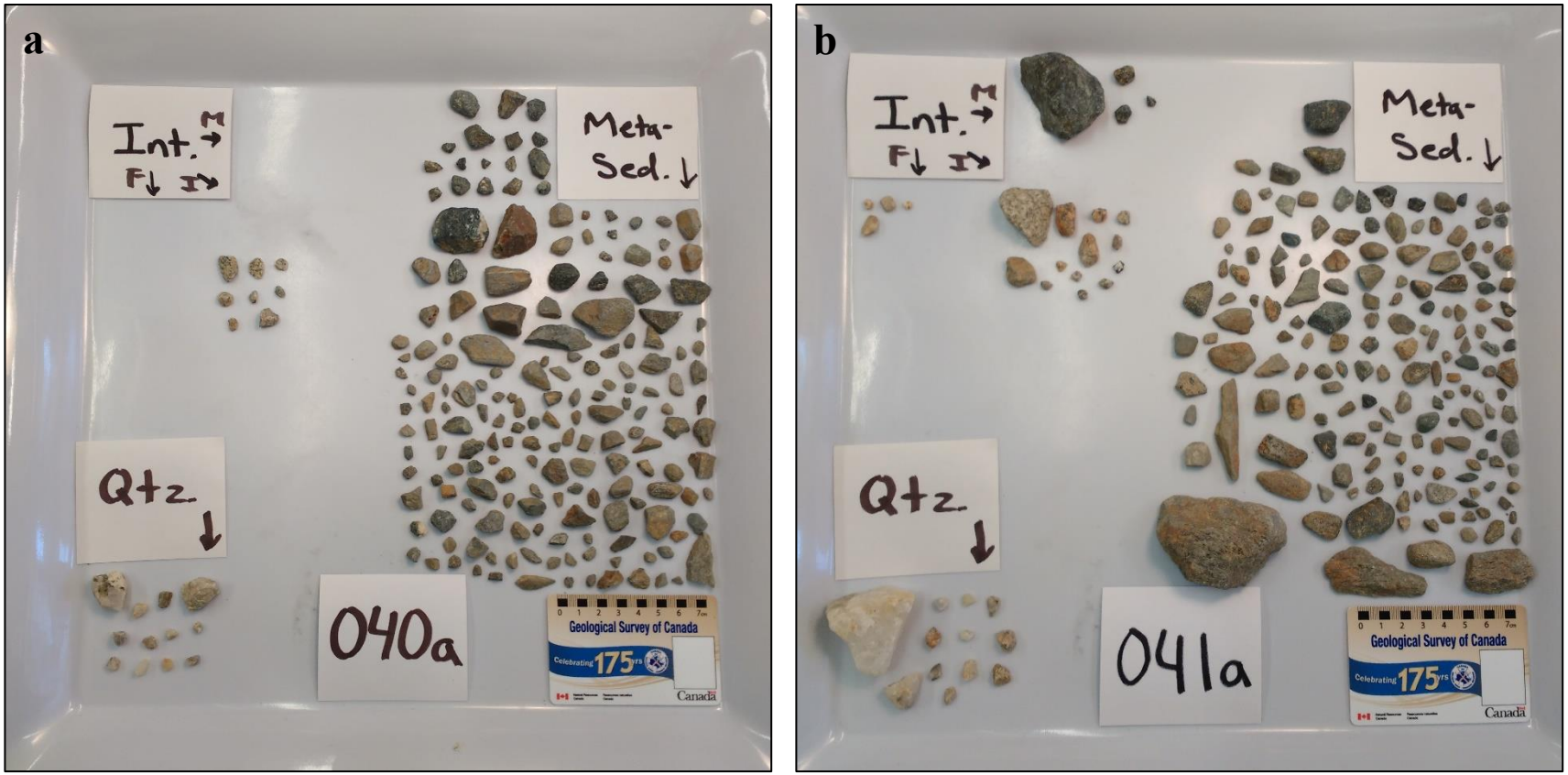

Supplementary Figure 5. 19 (a-b) Till clasts from 2016 sorted by lithology. Sample ID is listed (bottom-centre).
Abbr: F – felsic, I – intermediate, Int – intrusive, M – mafic, Meta-Sed – meta-sedimentary, Qtz – quartz.

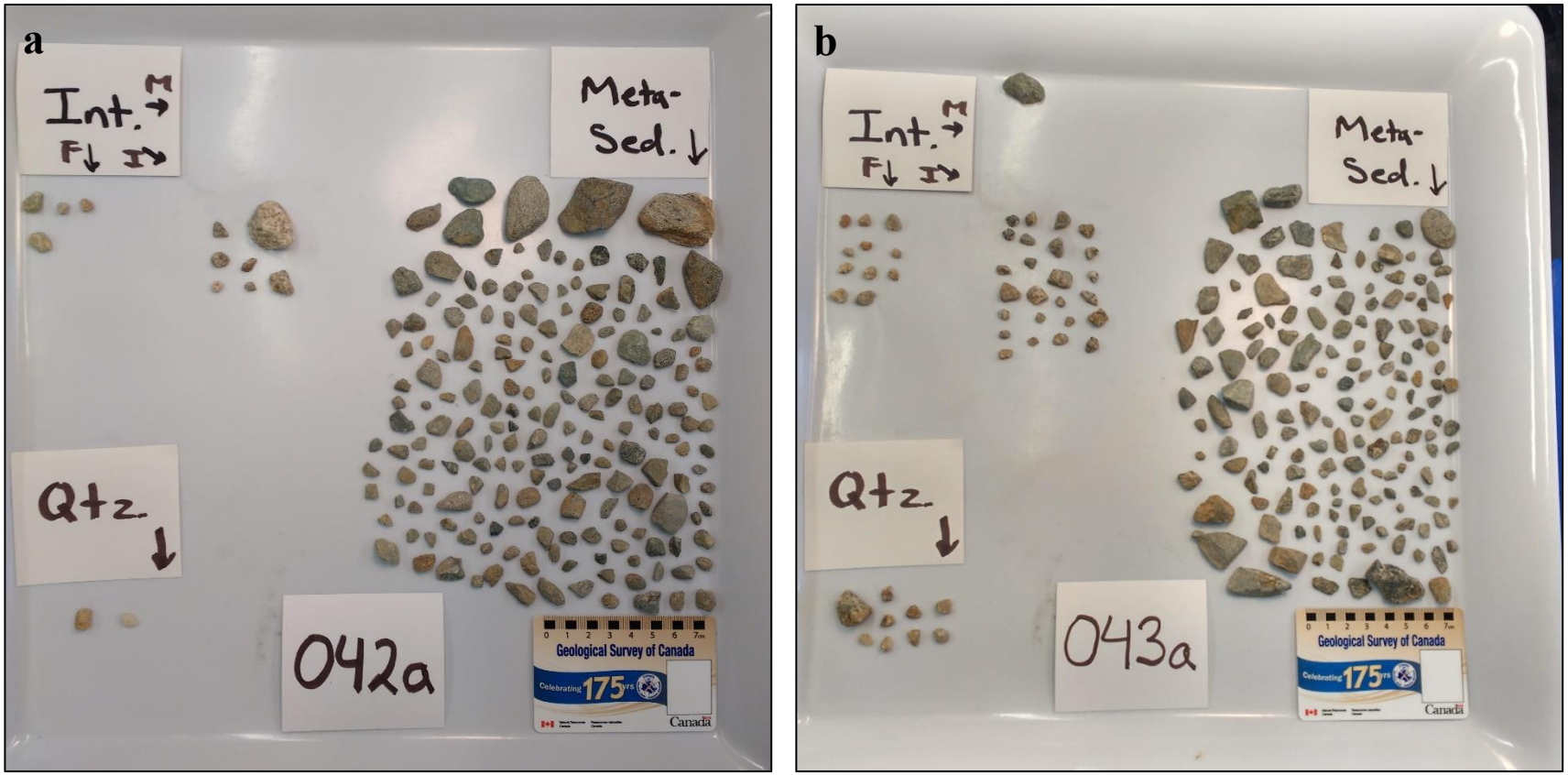

Supplementary Figure 5. 20 (a-b) Till clasts from 2016 sorted by lithology. Sample ID is listed (bottom-centre).
Abbr: F – felsic, I – intermediate, Int – intrusive, M – mafic, Meta-Sed – meta-sedimentary, Qtz – quartz.

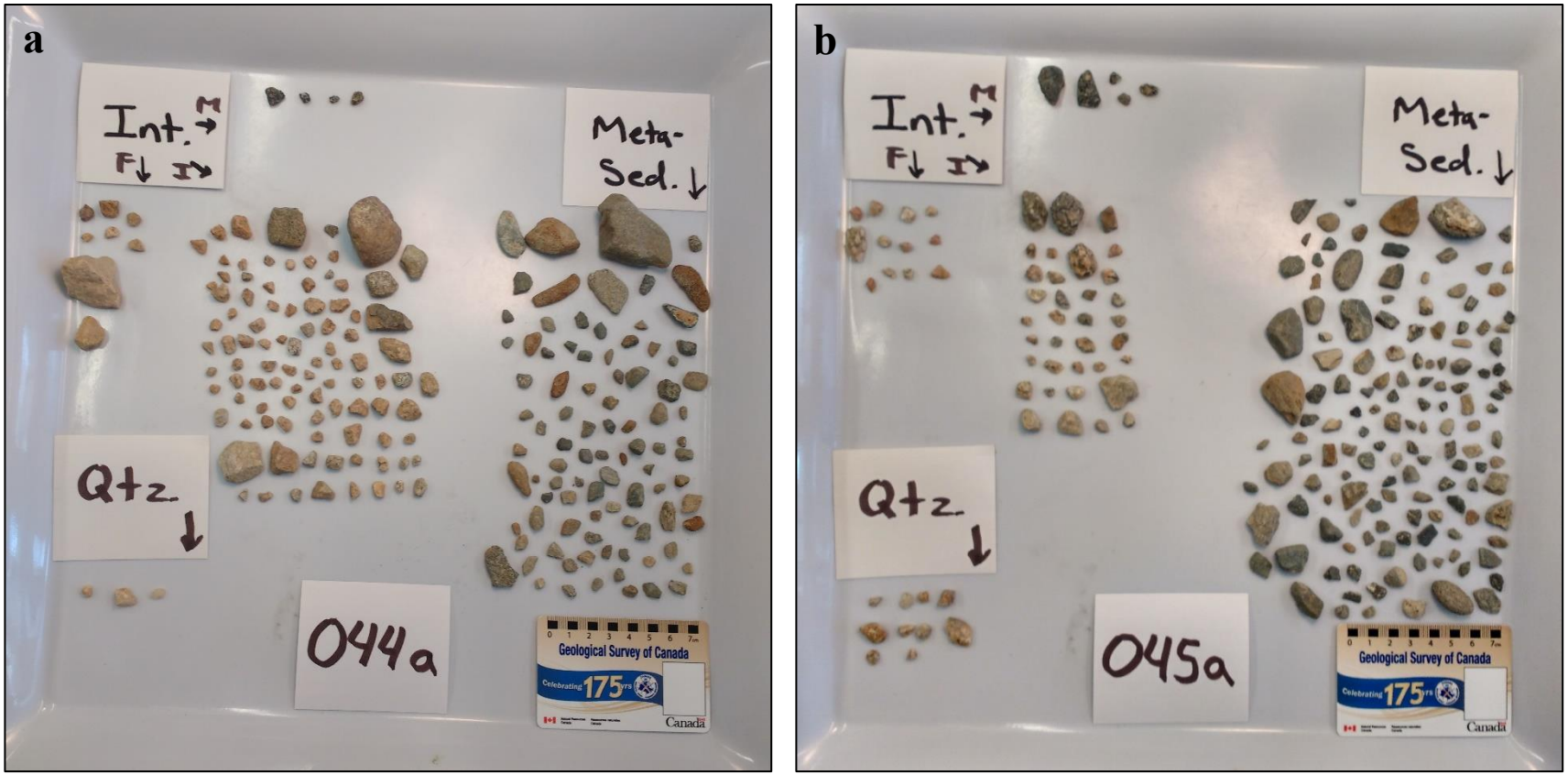

Supplementary Figure 5. 21 (a-b) Till clasts from 2016 sorted by lithology. Sample ID is listed (bottom-centre).
Abbr: F – felsic, I – intermediate, Int – intrusive, M – mafic, Meta-Sed – meta-sedimentary, Qtz – quartz.

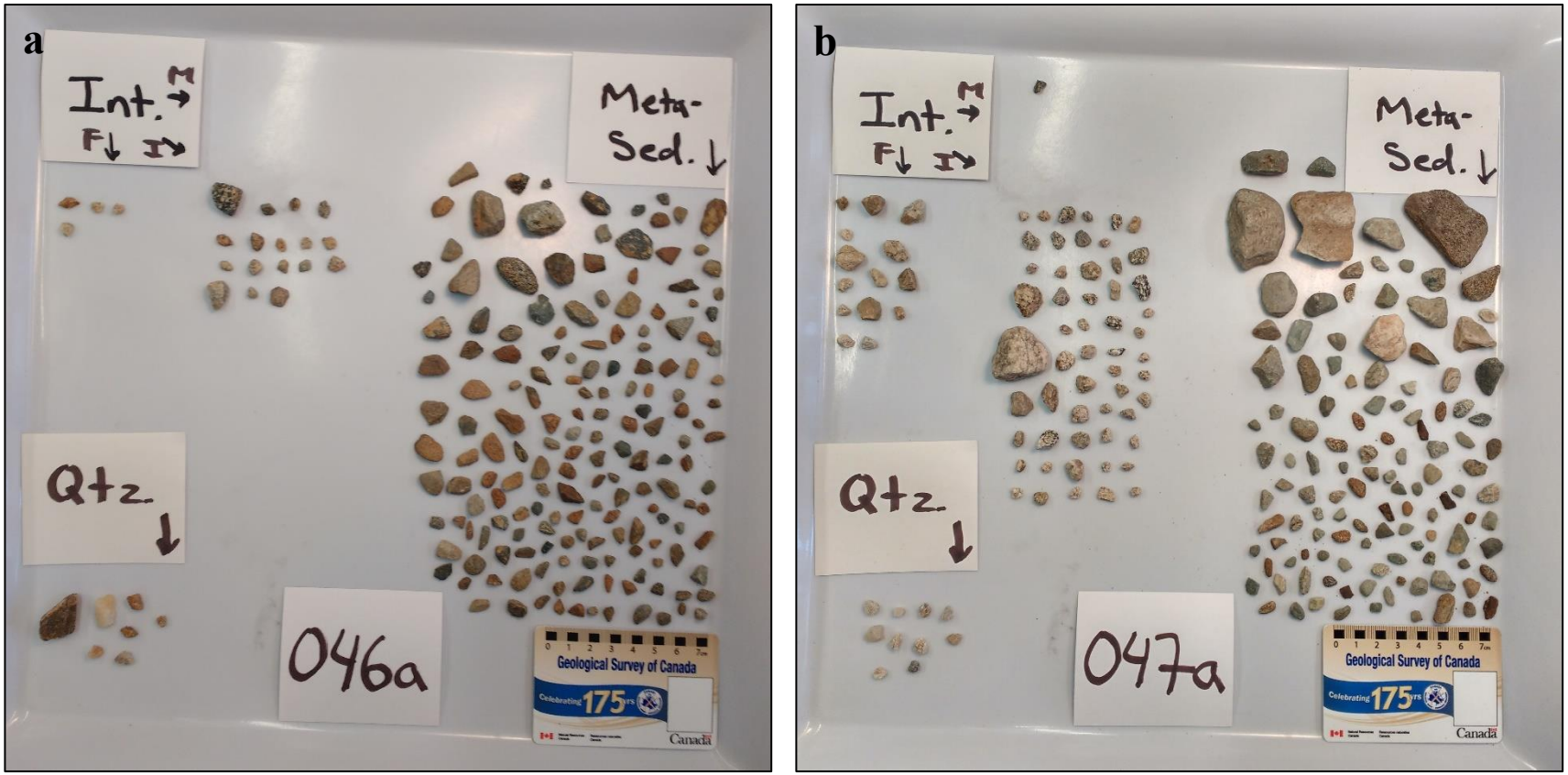

Supplementary Figure 5. 22 (a-b) Till clasts from 2016 sorted by lithology. Sample ID is listed (bottom-centre).
Abbr: F – felsic, I – intermediate, Int – intrusive, M – mafic, Meta-Sed – meta-sedimentary, Qtz – quartz.

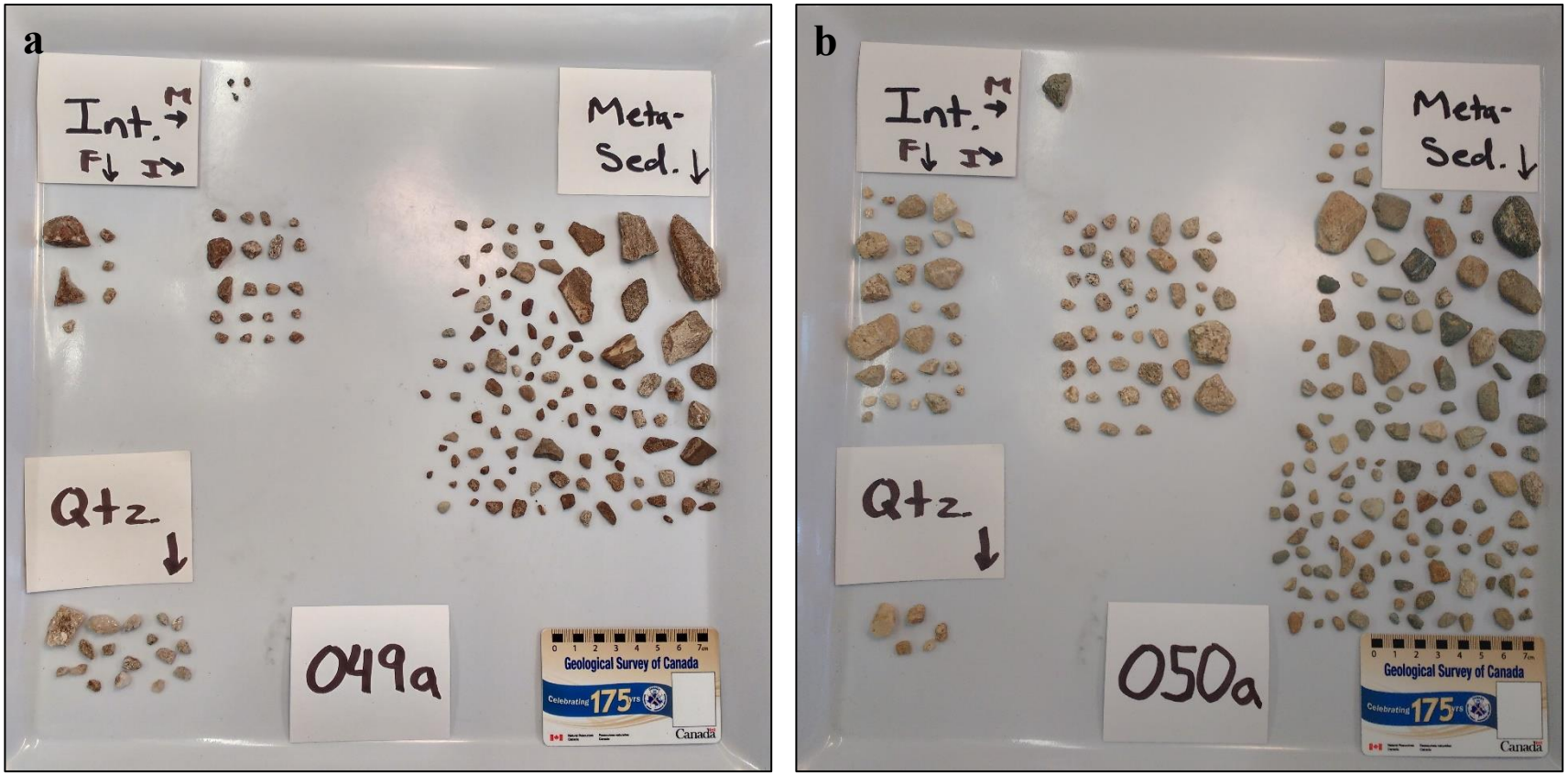

Supplementary Figure 5. 23 (a-b) Till clasts from 2016 sorted by lithology. Sample ID is listed (bottom-centre).
Abbr: F – felsic, I – intermediate, Int – intrusive, M – mafic, Meta-Sed – meta-sedimentary, Qtz – quartz.

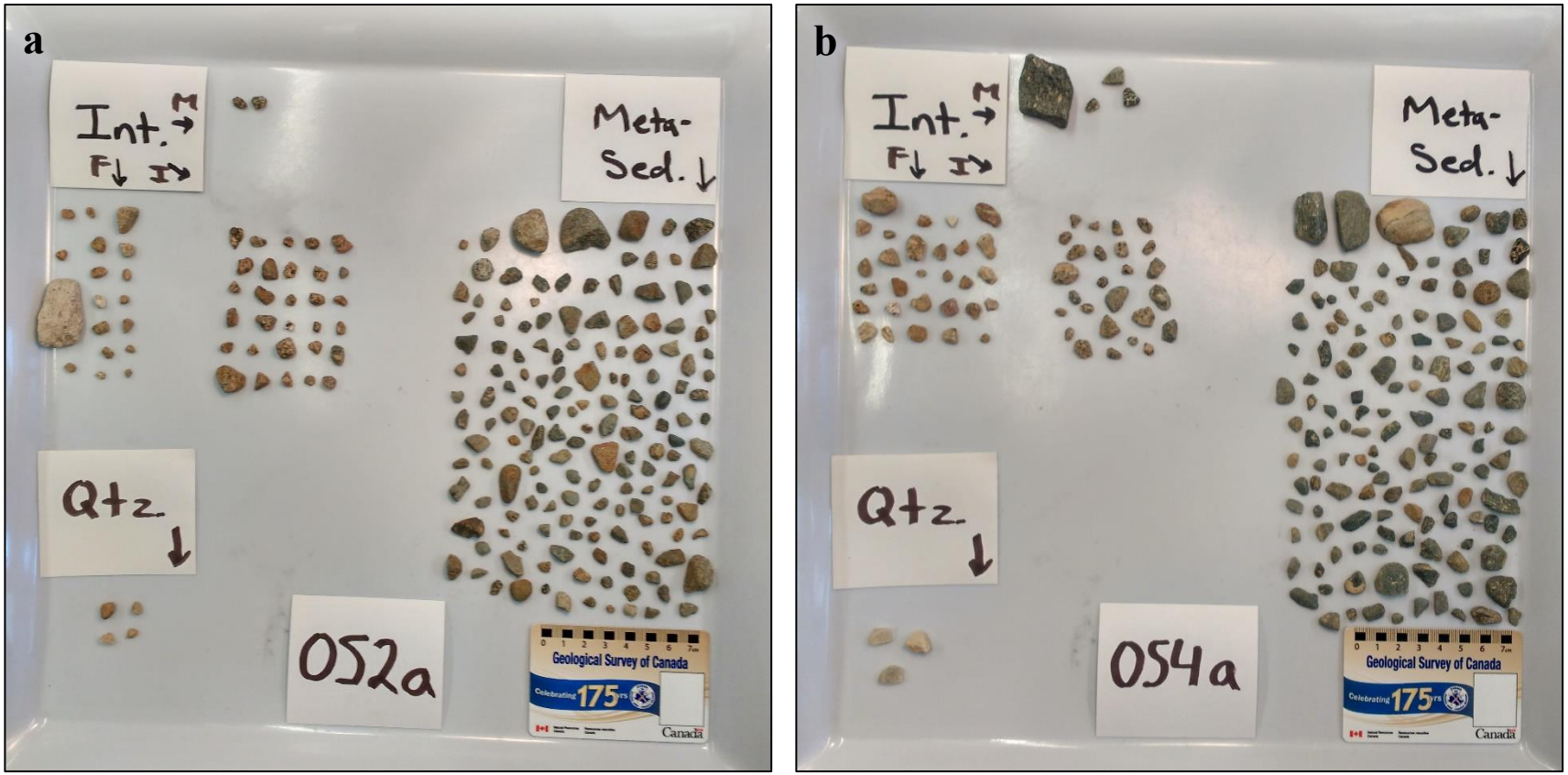

Supplementary Figure 5. 24 (a-b) Till clasts from 2016 sorted by lithology. Sample ID is listed (bottom-centre).
Abbr: F – felsic, I – intermediate, Int – intrusive, M – mafic, Meta-Sed – meta-sedimentary, Qtz – quartz.

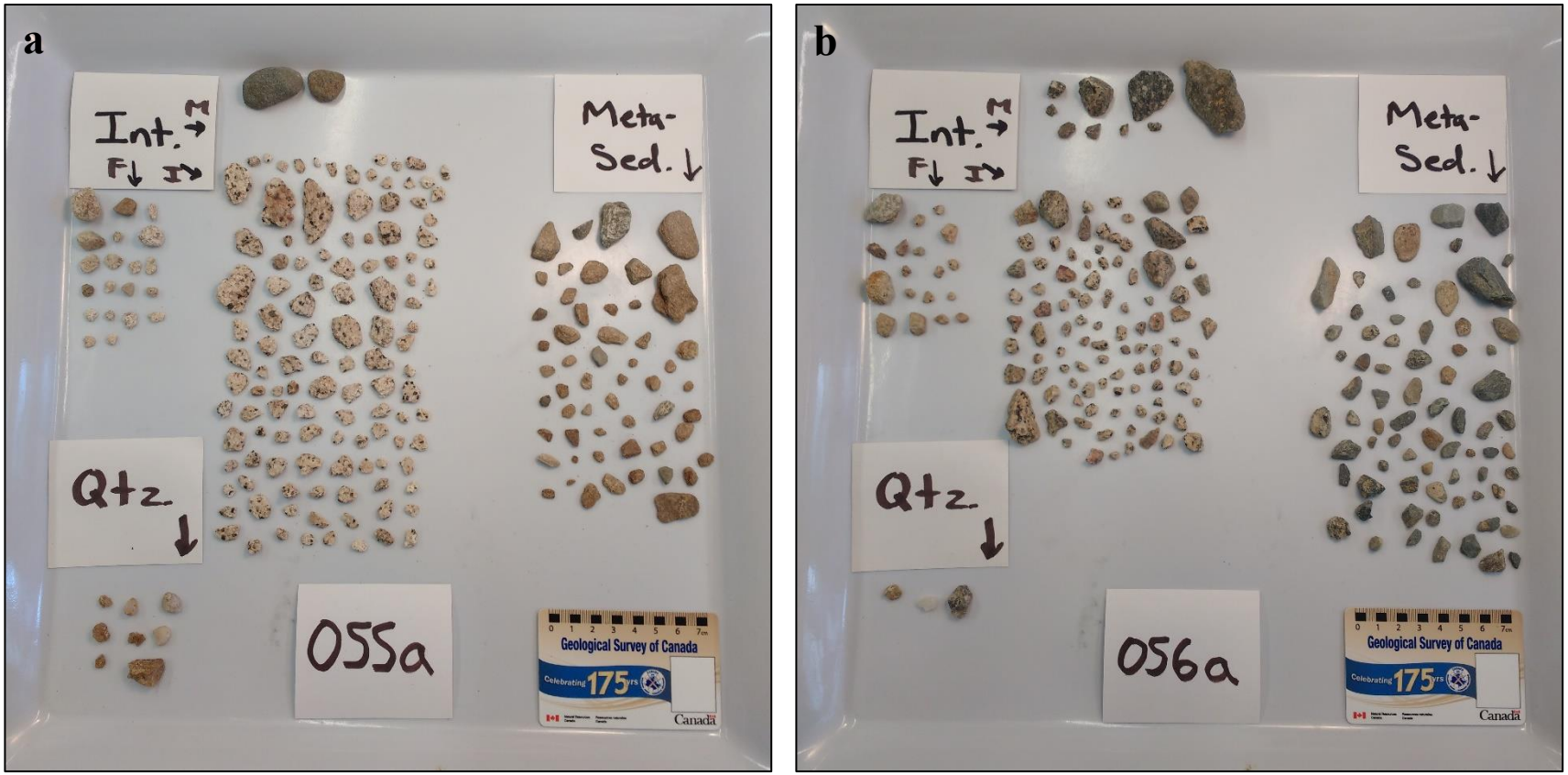

Supplementary Figure 5. 25 (a-b) Till clasts from 2016 sorted by lithology. Sample ID is listed (bottom-centre).
Abbr: F – felsic, I – intermediate, Int – intrusive, M – mafic, Meta-Sed – meta-sedimentary, Qtz – quartz.

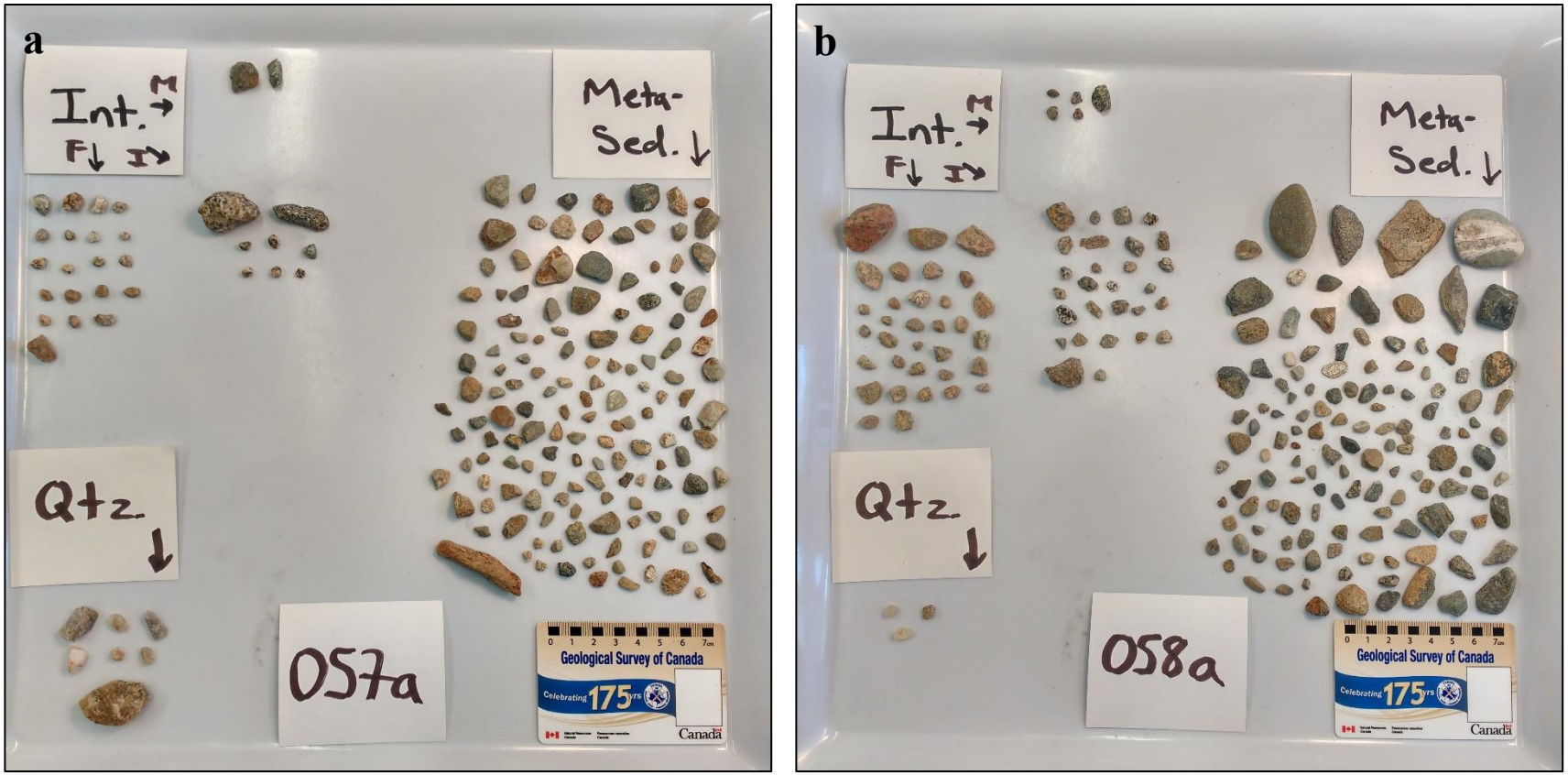

Supplementary Figure 5. 26 (a-b) Till clasts from 2016 sorted by lithology. Sample ID is listed (bottom-centre).
Abbr: F – felsic, I – intermediate, Int – intrusive, M – mafic, Meta-Sed – meta-sedimentary, Qtz – quartz.

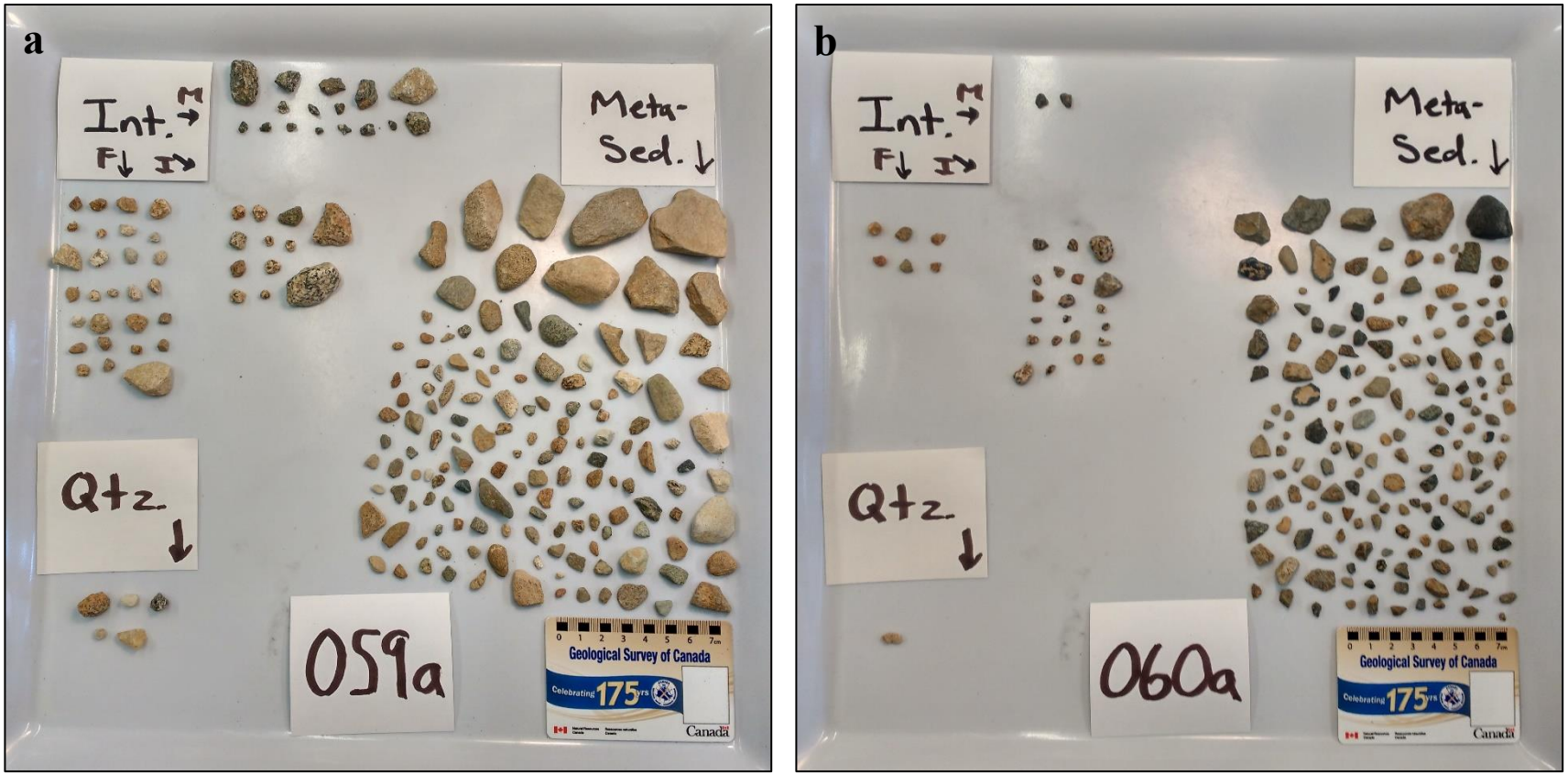

Supplementary Figure 5. 27 (a-b) Till clasts from 2016 sorted by lithology. Sample ID is listed (bottom-centre).
Abbr: F – felsic, I – intermediate, Int – intrusive, M – mafic, Meta-Sed – meta-sedimentary, Qtz – quartz.

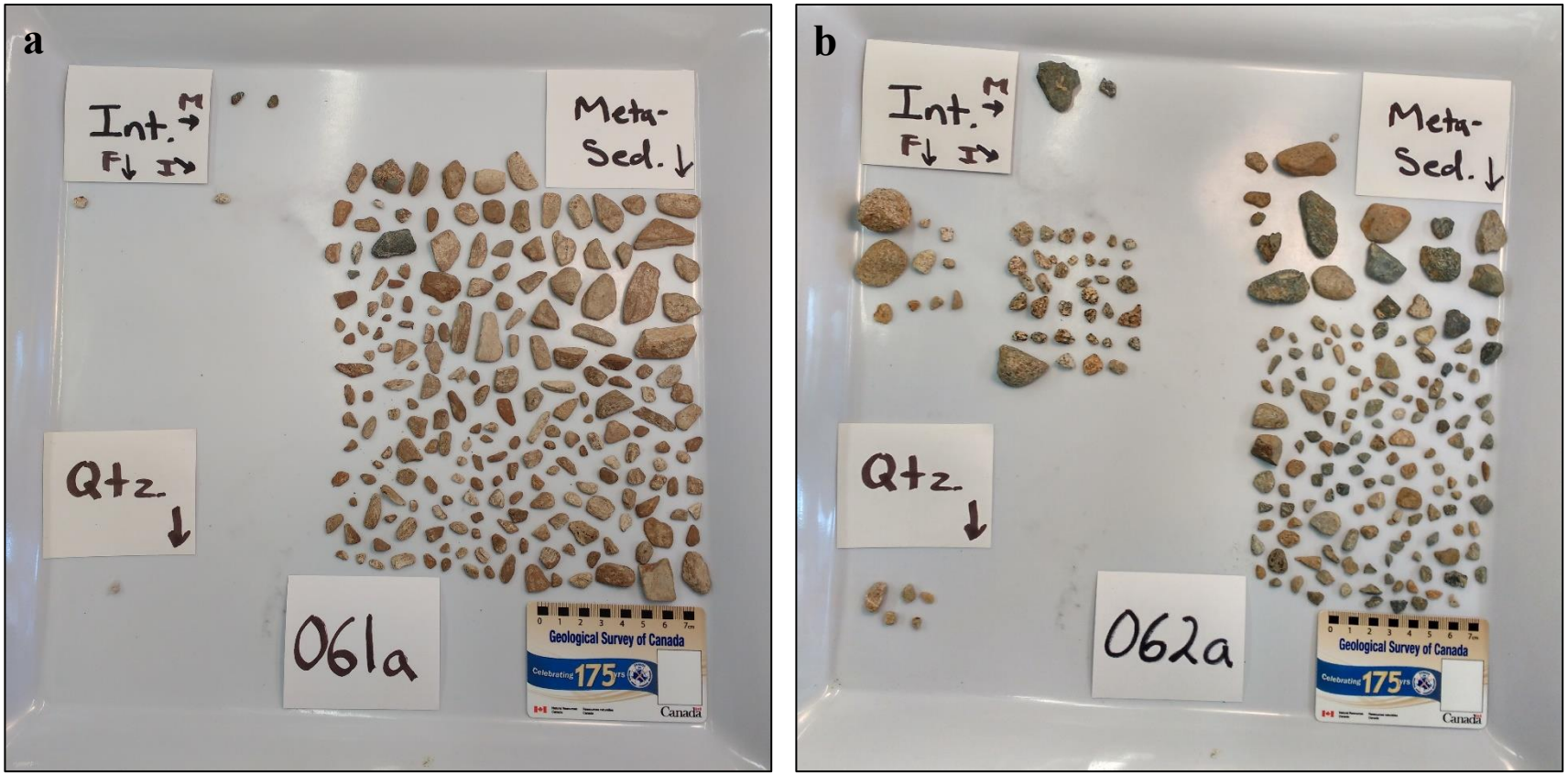

Supplementary Figure 5. 28 (a-b) Till clasts from 2016 sorted by lithology. Sample ID is listed (bottom-centre).
Abbr: F – felsic, I – intermediate, Int – intrusive, M – mafic, Meta-Sed – meta-sedimentary, Qtz – quartz.

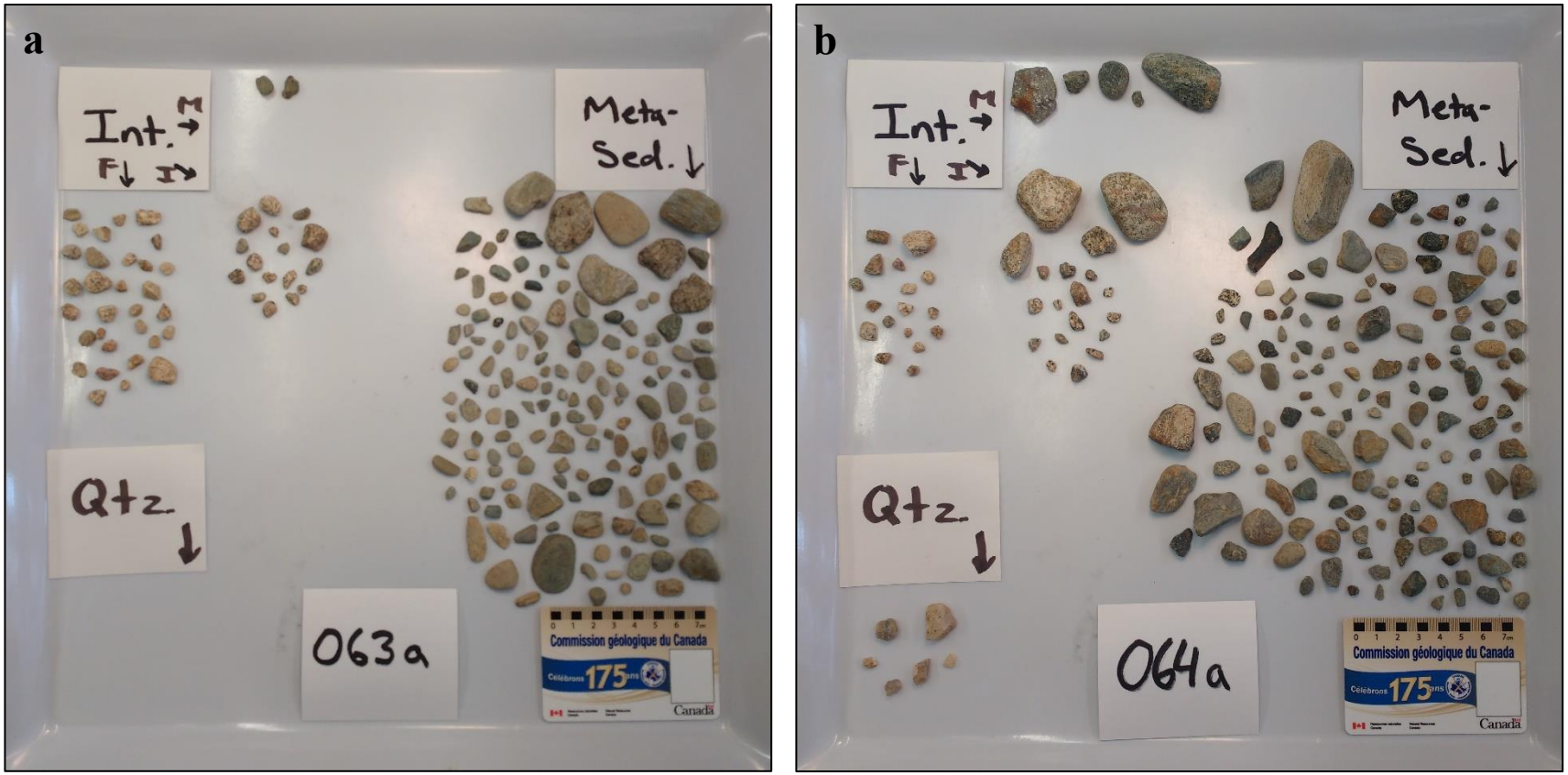

Supplementary Figure 5. 29 (a-b) Till clasts from 2016 sorted by lithology. Sample ID is listed (bottom-centre).
Abbr: F – felsic, I – intermediate, Int – intrusive, M – mafic, Meta-Sed – meta-sedimentary, Qtz – quartz.

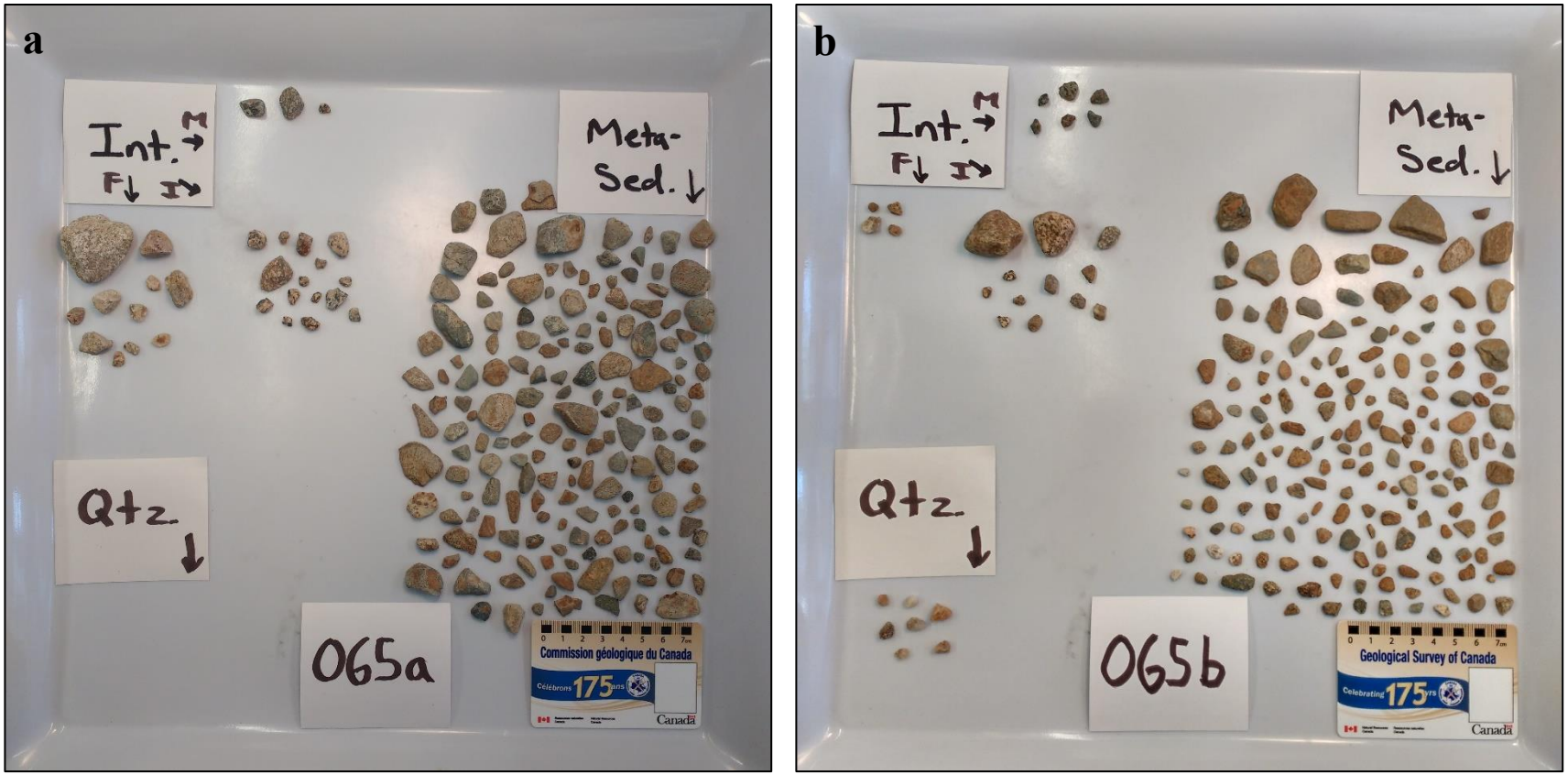

Supplementary Figure 5. 30 (a-b) Till clasts from 2016 sorted by lithology. Sample ID is listed (bottom-centre).
Abbr: F – felsic, I – intermediate, Int – intrusive, M – mafic, Meta-Sed – meta-sedimentary, Qtz – quartz.

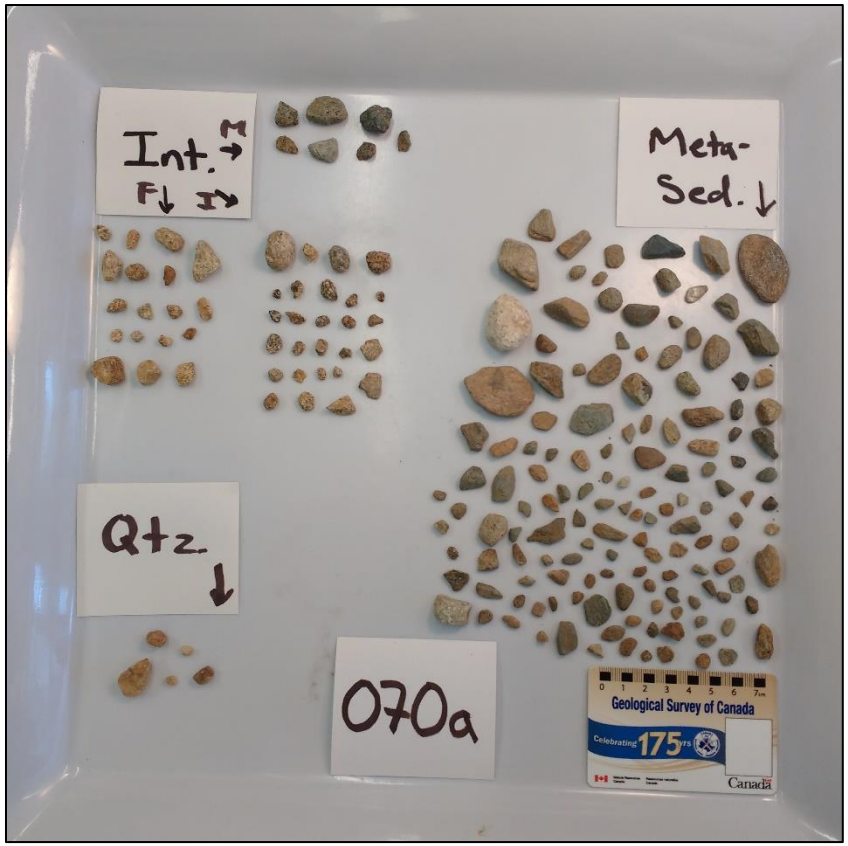

Supplementary Figure 5. 31 (a-b) Till clasts from 2016 sorted by lithology. Sample ID is listed (bottom-centre). Abbr: F – felsic, I – intermediate, Int – intrusive, M – mafic, Meta-Sed – meta-sedimentary, Qtz – quartz.

5.5. Jupyter Notebooks

The following files are available online at:
https://github.com/Caroline-Emily-Taylor/Appendices.git

1. Ch 2 Rose Diagrams All Measurements.ipynb
2. Ch 2 Esker Fabric Analysis.ipynb
3. Ch 2 Elevation of Surficial Units - Histograms and Stats.ipynb
4. Ch 2 Elevation of Surficial Units Stacked Bar Chart Binning.ipynb
5. Ch 2 Elevation - Normalized Stacked Bar Charts.ipynb
6. Ch 2 Major Oxide Boxplots.ipynb
7. Ch 2 Major Oxide Multivariate Analysis.ipynb
8. Ch 3 Minor and Trace Element Multivariate Analysis.ipynb

5.6. Minor and Trace Element Geochemistry QA/QC

5.6.1. Certified Standards

Total average percent relative standard deviation of reference materials is 2.4%, which indicates "excellent" precision (Jenner, 1996). Till 1 and Till 3 CANMET standard data available at https://www.nrcan.gc.ca/our-natural-resources/minerals-mining/mining-resources/till-1-till-2-till-3-and-till-4-certificate-analysis/8137.

Supplementary Table 5. 16 Percent relative standard deviation of CANMET till standard values for minor element measurements (ICP-OES).

SRC Sample ID	Ba (ppm)	Sr (ppm)
Detection limit	1	1
2015 – Till 1		
27	759	324
68	711	306
Average	735.0	315.0
Standard deviation (SD)	33.94	12.73
%Relative SD	4.618	4.041
Ave %RSD	4.329	
2016 – Till 3		
CT-SRC-001	480	307
CT-SRC-027	478	309
CT-SRC-054	476	305
Average	478.0	307.0
Standard deviation (SD)	2.000	2.000
%Relative SD	0.418	0.651
Ave %RSD	0.535	
Total ave %RSD	**2.432**	

Total average percent relative standard deviation of reference materials is 6.0%, which indicates "good" precision (Jenner, 1996). Till 1 and Till 3 CANMET standard data available at https://www.nrcan.gc.ca/our-natural-resources/minerals-mining/mining-resources/till-1-till-2-till-3-and-till-4-certificate-analysis/8137.

Supplementary Table 5. 17 Percent relative standard deviation of CANMET till standard values for trace element measurements (ICP-MS).

SRC Sample ID	Ag (ppm)	Cs (ppm)	Mo (ppm)	Pb (ppm)	Rb (ppm)	W (ppm)
Detection limit	0.02	0.1	0.02	0.1	0.1	0.1
2015 – Till 1						
27	0.40	1.0	0.98	22.0	45.6	1.0
68	0.45	1.1	0.91	22.5	48.5	0.8
Average	0.425	1.05	0.945	22.25	47.05	0.90
Standard deviation (SD)	0.035	0.071	0.049	0.354	2.051	0.141
%Relative SD	8.319	6.734	5.238	1.589	4.358	15.713
Ave %RSD	6.992					
2016 – Till 3						
CT-SRC-001	2.01	2.0	0.87	25.9	54.8	1.5
CT-SRC-027	1.90	2.1	0.84	25.8	56.9	1.0
CT-SRC-054	1.95	2.1	0.85	25.5	55.5	1.4
Average	1.953	2.07	0.853	25.73	55.73	1.30
Standard deviation (SD)	0.055	0.058	0.015	0.208	1.069	0.265
%Relative SD	2.820	2.794	1.790	0.809	1.919	20.352
Ave %RSD	5.080					
Total ave %RSD	**6.036**					

Total average percent relative standard deviation of reference materials is 117.9%, which indicates "insufficient" precision (Jenner, 1996). Till 1 and Till 3 CANMET standard data available at https://www.nrcan.gc.ca/our-natural-resources/minerals-mining/mining-resources/till-1-till-2-till-3-and-till-4-certificate-analysis/8137.

Supplementary Table 5. 18 Percent relative standard deviation of CANMET till standard values for gold measurements (AAS).

SRC Sample ID	Au (ppb)
Detection limit	2
2015 – Till 1	
27	70
68	27
Average	48.5
Standard deviation (SD)	30.4
%Relative SD	62.7
2016 – Till 3	
CT-SRC-001	32
CT-SRC-027	0
CT-SRC-054	0
Average	10.7
Standard deviation (SD)	18.5
%Relative SD	173
Total ave %RSD	**118**

5.6.2. Duplicates

Supplementary Table 5. 19 Minor and trace element values for original and duplicated samples.

Sample ID	Ag (ppm) (original)	Ag (ppm) (duplicate)	Au (ppb) (original)	Au (ppb) (duplicate)	Ba (ppm) (original)	Ba (ppm) (duplicate)	Cs (ppm) (original)	Cs (ppm) (duplicate)	Mo (ppm) (original)
009a	0.20	0.18	4	2	361	374	1.8	1.6	0.42
031a	0.24	0.24	2	<2	474	470	3.5	3.3	0.68
038a	0.18	0.15	<2	<2	351	348	1.7	1.7	2.16
048a	0.19	0.20	<2	<2	376	379	3.4	3.5	1.50
059a	0.20	0.19	<2	<2	444	445	3.5	3.4	1.26
063a	0.47	0.43	<2	<2	385	352	4.8	4.5	1.53
070a	0.43	0.42	18	16	351	352	4.0	4.1	2.17
DS 36	0.24	0.20	3	3	550	545	2.6	2.4	0.66
DS 37	0.15	0.15	<2	7	435	414	1.8	1.9	9.08
ES 18	0.25	0.26	161	158	412	408	2.7	2.8	2.87
SS 13	0.12	0.13	20	27	501	465	2.7	2.8	1.20
SS 3	0.12	0.12	15	3	391	437	1.5	1.7	0.73

Sample ID	Mo (ppm) (duplicate)	Pb (ppm) (original)	Pb (ppm) (duplicate)	Rb (ppm) (original)	Rb (ppm) (duplicate)	Sr (ppm) (original)	Sr (ppm) (duplicate)	W (ppm) (original)	W (ppm) (duplicate)
009a	0.32	8.3	7.6	40.2	38.5	416	436	0.8	0.8
031a	0.63	11.4	10.6	62.8	57.2	362	357	1.5	1.0
038a	1.70	13.1	13.0	35.4	36.5	473	470	1.6	1.3
048a	1.54	16.6	17.1	38.2	38.6	410	415	0.8	0.8
059a	1.18	14.3	13.3	49.9	43.0	411	397	1.3	1.3
063a	1.37	11.9	10.2	58.5	54.0	323	305	1.7	1.4
070a	2.07	20.5	20.0	39.0	38.7	409	409	1.9	1.6
DS 36	0.69	13.4	13.2	76.6	72.4	362	363	0.5	0.5
DS 37	8.76	9.0	9.0	53.1	55.0	422	406	0.5	0.5
ES 18	2.90	26.6	27.5	41.1	42.2	376	374	1.2	1.4

Sample ID	Mo (ppm) (duplicate)	Pb (ppm) (original)	Pb (ppm) (duplicate)	Rb (ppm) (original)	Rb (ppm) (duplicate)	Sr (ppm) (original)	Sr (ppm) (duplicate)	W (ppm) (original)	W (ppm) (duplicate)
SS 13	1.25	15.1	15.7	40.2	43.0	513	477	1.2	1.1
SS 3	0.93	11.7	12.8	31.5	35.8	472	504	0.7	0.7

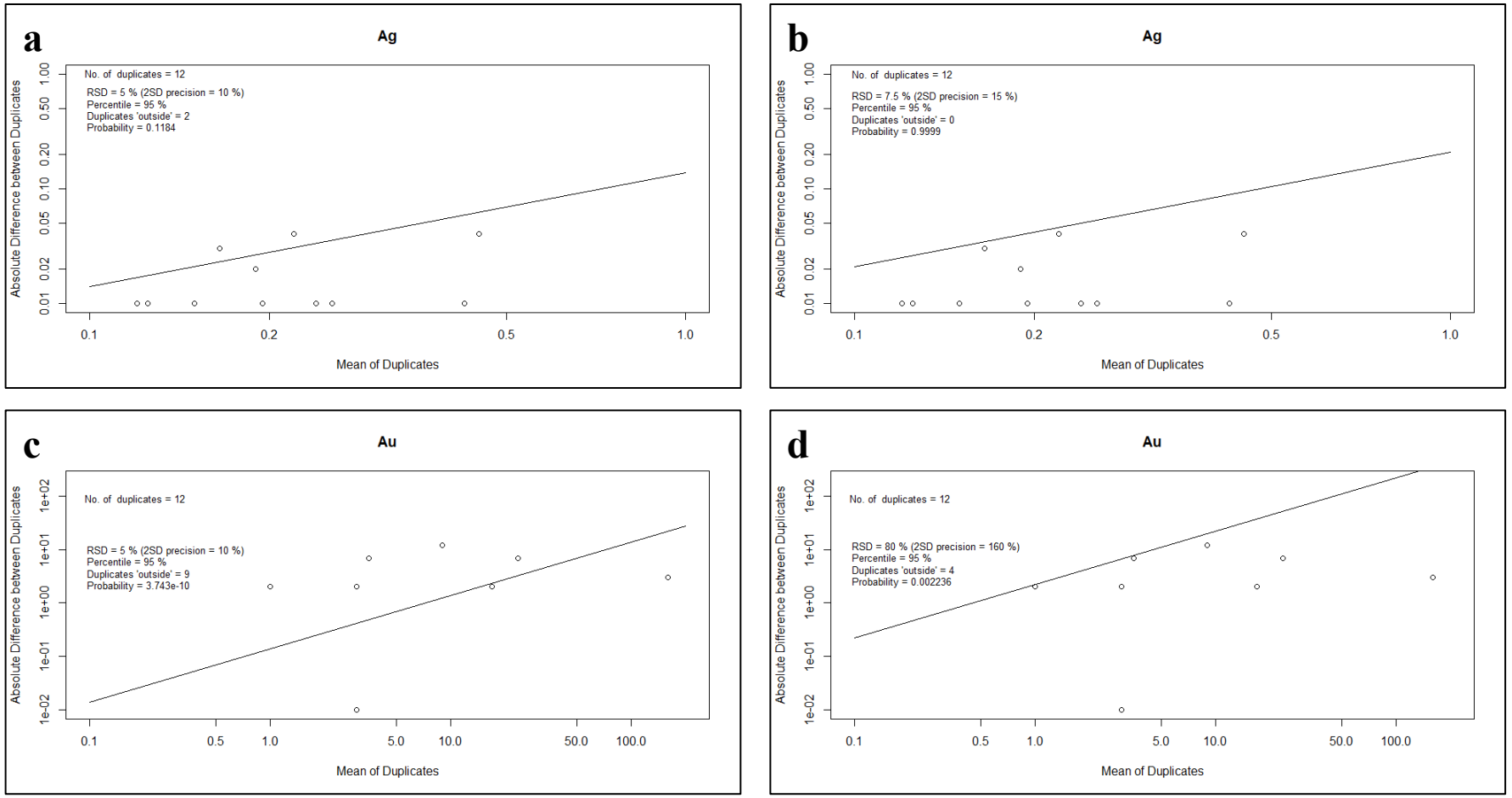

Supplementary Figure 5. 32 (a-d) Thompson-Howarth plots testing the precision of minor and trace element data as outlined by Piercey (2014). Ag measurements show greater than 92.5% precision to a 99% confidence level. Au measurements show greater than 20% precision to a 99% confidence level (excluding values below LOD). Thompson-Howarth plots were generated using the R Statistical package (Garrett and Grunsky, 2003), including ggplot2 (Wickham, 2016).

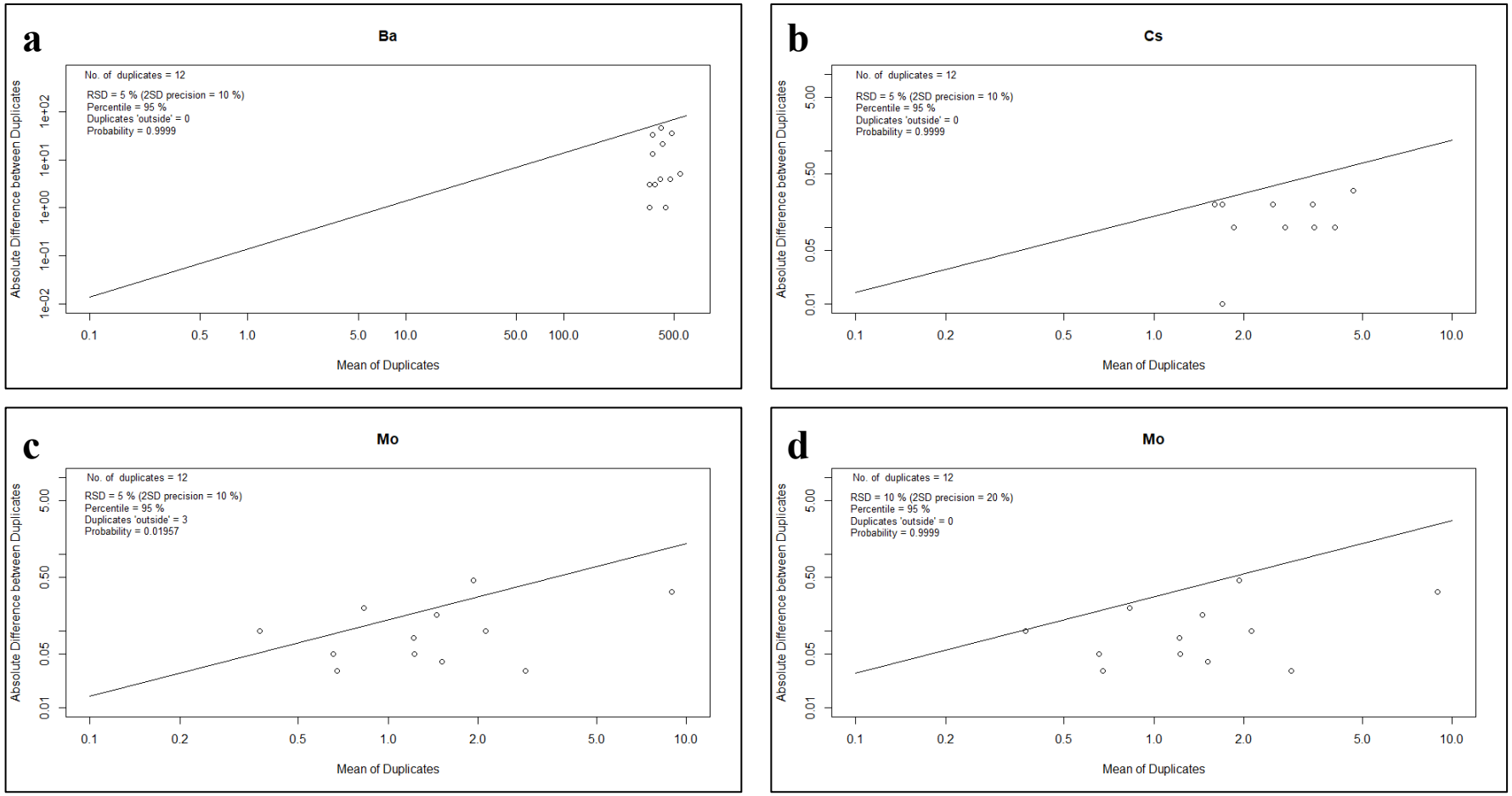

Supplementary Figure 5. 33 (a-d) Thompson-Howarth plots testing the precision of minor and trace element data as outlined by Piercey (2014). Ba and Cs measurements show greater than 95% precision to a 99% confidence level. Mo measurements show greater than 90% precision to a 99% confidence level. Thompson-Howarth plots were generated using the R Statistical package (Garrett and Grunsky, 2003), including ggplot2 (Wickham, 2016).

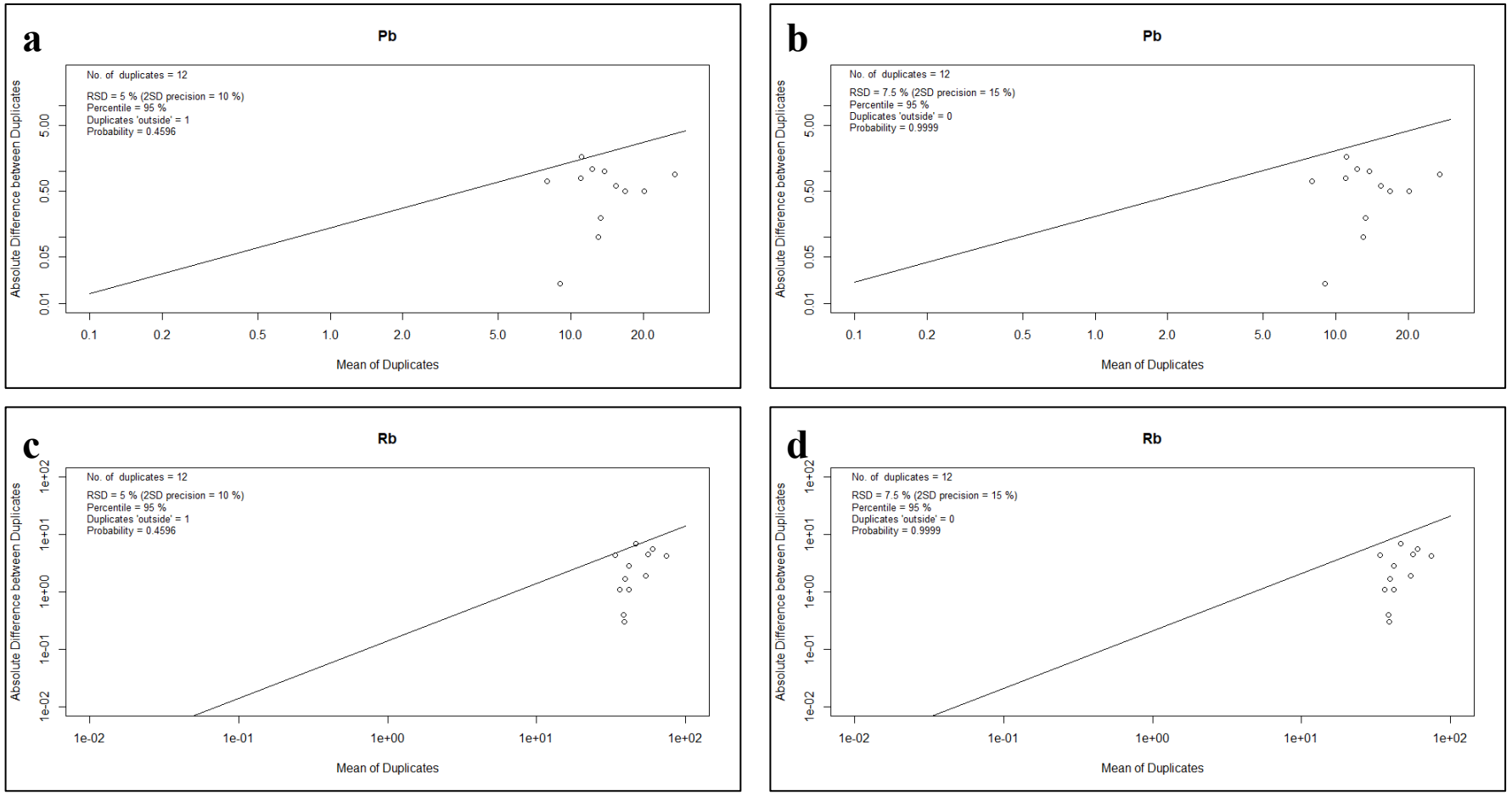

Supplementary Figure 5. 34 (a-d) Thompson-Howarth plots testing the precision of minor and trace element data as outlined by Piercey (2014). Pb and Rb measurements show greater than 92.5% precision to a 99% confidence level. Thompson-Howarth plots were generated using the R Statistical package (Garrett and Grunsky, 2003), including ggplot2 (Wickham, 2016).

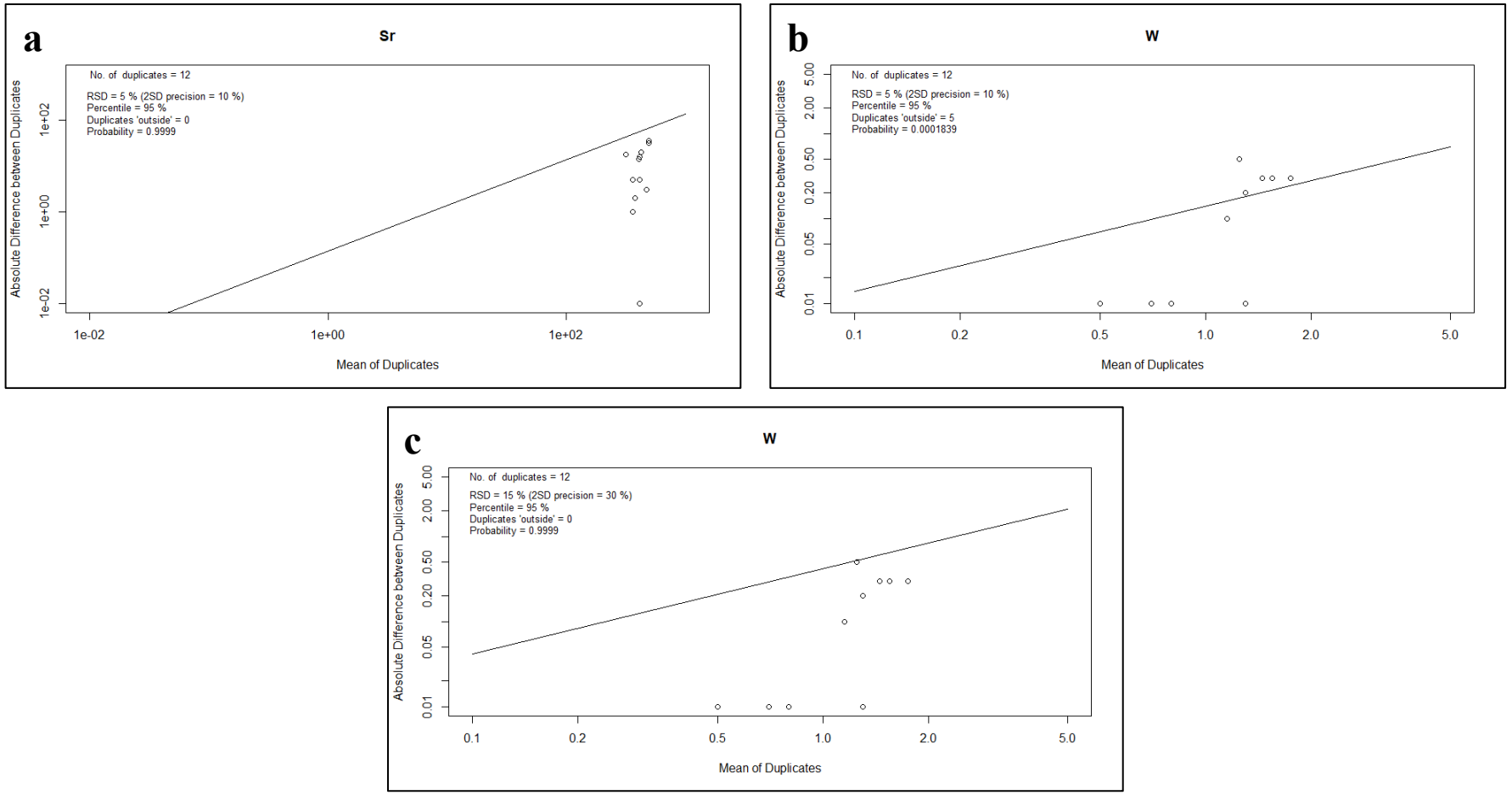

Supplementary Figure 5. 35 (a-c) Thompson-Howarth plots testing the precision of minor and trace element data as outlined by Piercey (2014). Sr measurements show greater than 95% precision to a 99% confidence level. W measurements show greater than 85% precision to a 99% confidence level. Thompson-Howarth plots were generated using the R Statistical package (Garrett and Grunsky, 2003), including ggplot2 (Wickham, 2016).

Supplementary Table 5. 20 Percent variance of minor and trace element values for duplicate samples. Sr measurements is precise to within 10% variance. Ba, Cs, Pb, and Rb are precise to within 15% variance. Ag, Au, Mo, and W measurements show greater than 15% variance. 'Field' duplicates represent samples that were collected twice within close proximity of one another during fieldwork, 'Sample' duplicates represent samples that were split and submitted twice for analysis, and 'Lab' duplicates represent individual samples that were analyzed twice.

Sample ID	Duplicate Type	Ag (ppm) Variance	Au[a] (ppb) Variance	Ba (ppm) Variance	Cs (ppm) Variance	Mo (ppm) Variance	Pb (ppm) Variance	Rb (ppm) Variance	Sr (ppm) Variance	W (ppm) Variance
009a	Field	10.0	50.0	3.6	11.1	23.8	8.5	4.2	4.8	0.0
031a	Sample	0.0	100.0	0.8	5.7	7.4	7.0	8.9	1.4	33.3
038a	Field	16.7	0.0	0.9	0.0	21.3	0.8	3.1	0.6	18.8
048a	Lab	5.3	0.0	0.8	2.9	2.7	3.0	1.0	1.2	0.0
059a	Sample	5.0	0.0	0.2	2.9	6.3	7.0	13.8	3.4	0.0
063a	Sample	8.5	0.0	8.6	6.3	10.5	14.3	7.7	5.6	17.6
070a	Sample	2.3	11.1	0.3	2.5	4.6	2.4	0.8	0.0	15.8
DS 36	Lab	16.7	0.0	0.9	7.7	4.5	1.5	5.5	0.3	0.0
DS 37	Sample	0.0	100.0	4.8	5.6	3.5	0.2	3.6	3.8	0.0
ES 18	Lab	4.0	1.9	1.0	3.7	1.0	3.4	2.7	0.5	16.7
SS 13	Sample	8.3	35.0	7.2	3.7	4.2	4.0	7.0	7.0	8.3
SS 3	Sample	0.0	80.0	11.8	13.3	27.4	9.4	13.7	6.8	0.0

[a]A value of '0' was used for all '<2' measurements.

5.7. Minor & Trace Element Geochemical Analyses

The spatial distribution of minor and trace elements Ba, Cs, Mo, Pb, and Sr is shown in **Supplementary Figure 5. 36**, **Supplementary Figure 5. 37**, **Supplementary Figure 5. 38**, **Supplementary Figure 5. 39**, and **Supplementary Figure 5. 40**, respectively.

As stated in **Chapter 3**, a glacial dispersion train of the element Ba may be present in association with the phengitic white mica bedrock footprint and down-ice from the Canadian Malartic deposit. Glacial dispersion trains of the elements Cs, Mo, Pb, and Sr are unclear and may or may not be present down-ice from the Canadian Malartic deposit.

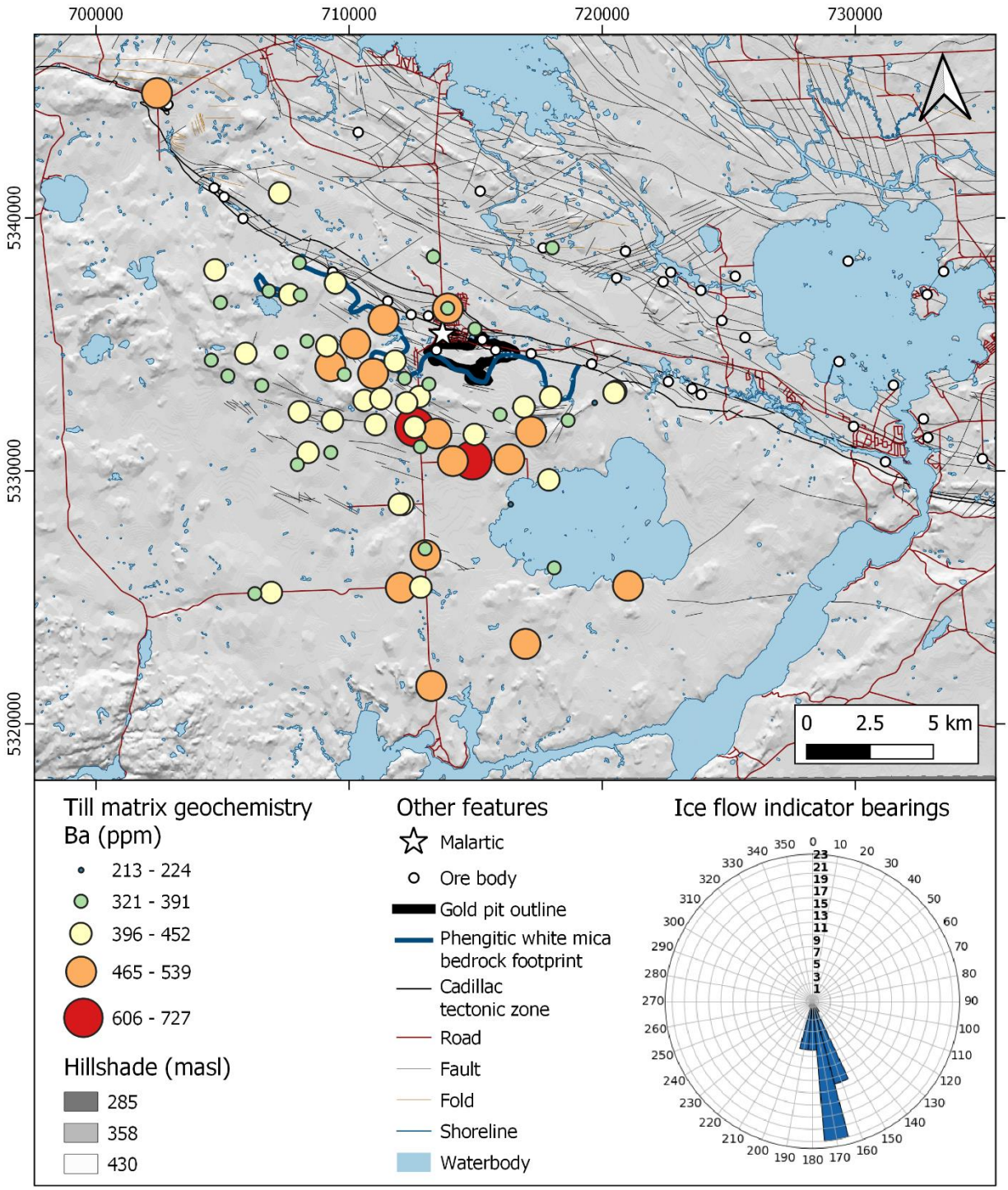

Supplementary Figure 5. 36 Spatial distribution of Ba (ppm) based on till matrix geochemistry (ICP-OES). The phengitic white mica bedrock footprint is after Lypaczewski et al (2019). Waterbodies and hillshade are from Natural Resources Canada (https://maps.canada.ca/czs/index-en.html). Ore bodies, Cadillac tectonic zone, roads, faults, folds, and shorelines are from SIGEOM (https://sigeom.mines.gouv.qc.ca/signet/classes/I1108_afchCarteIntr). Coordinate system: NAD 83, UTM zone 17.

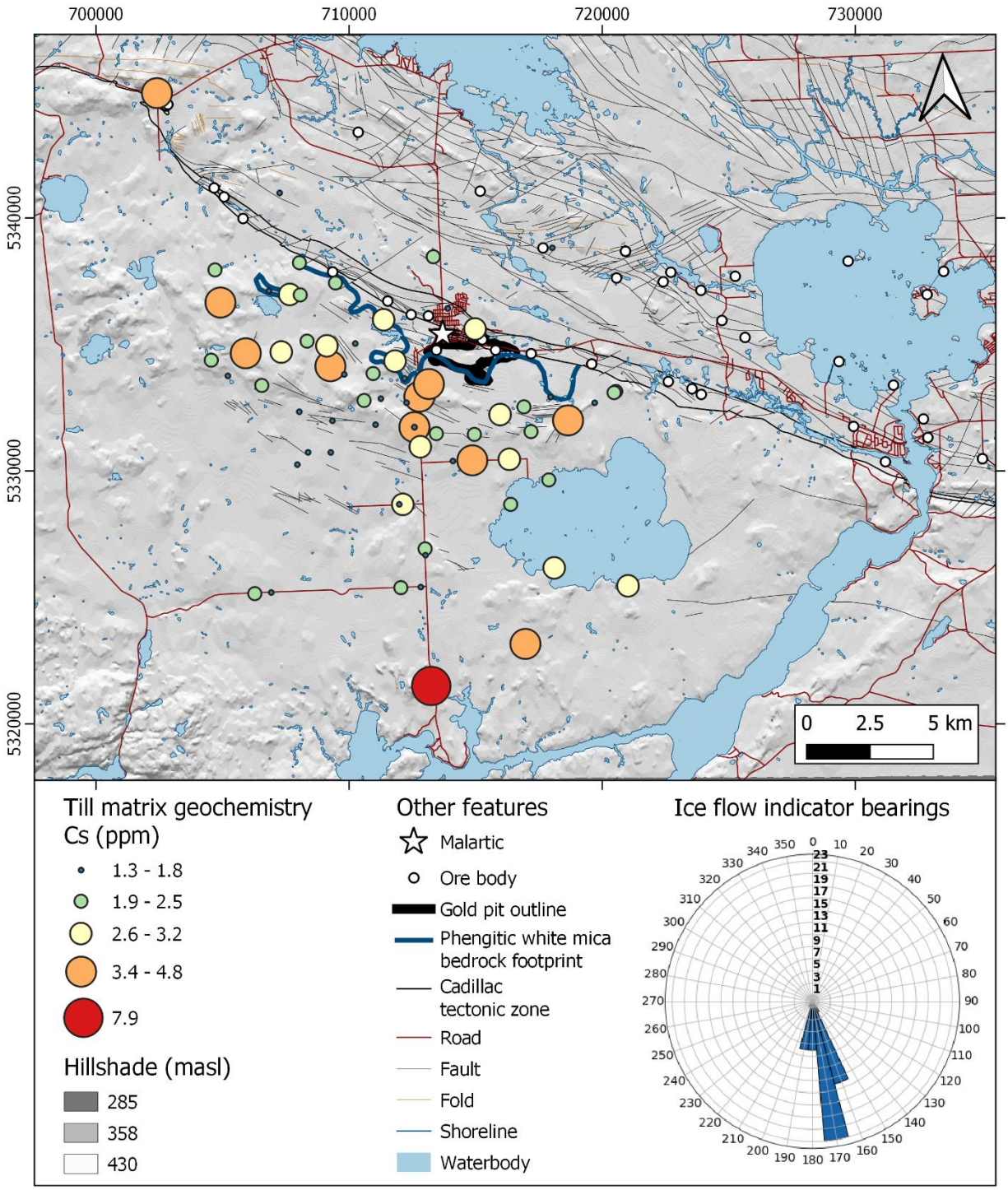

Supplementary Figure 5. 37 Spatial distribution of Ba (ppm) based on till matrix geochemistry (ICP-MS). The phengitic white mica bedrock footprint is after Lypaczewski et al (2019). Waterbodies and hillshade are from Natural Resources Canada (https://maps.canada.ca/czs/index-en.html). Ore bodies, Cadillac tectonic zone, roads, faults, folds, and shorelines are from SIGEOM (https://sigeom.mines.gouv.qc.ca/signet/classes/I1108_afchCarteIntr). Coordinate system: NAD 83, UTM zone 17.

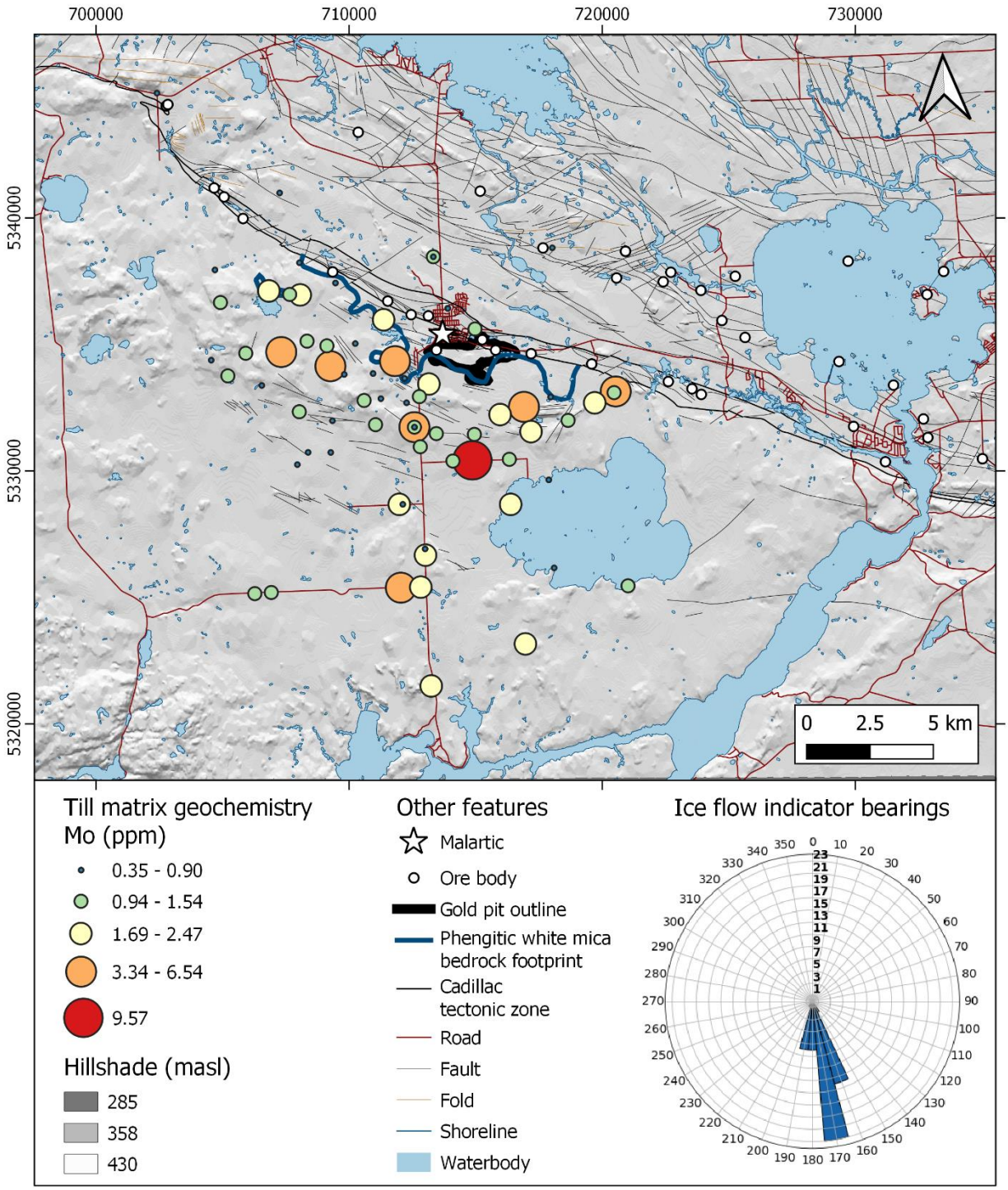

Supplementary Figure 5. 38 Spatial distribution of Mo (ppm) based on till matrix geochemistry (ICP-MS). The phengitic white mica bedrock footprint is after Lypaczewski et al (2019). Waterbodies and hillshade are from Natural Resources Canada (https://maps.canada.ca/czs/index-en.html). Ore bodies, Cadillac tectonic zone, roads, faults, folds, and shorelines are from SIGEOM (https://sigeom.mines.gouv.qc.ca/signet/classes/I1108_afchCarteIntr). Coordinate system: NAD 83, UTM zone 17.

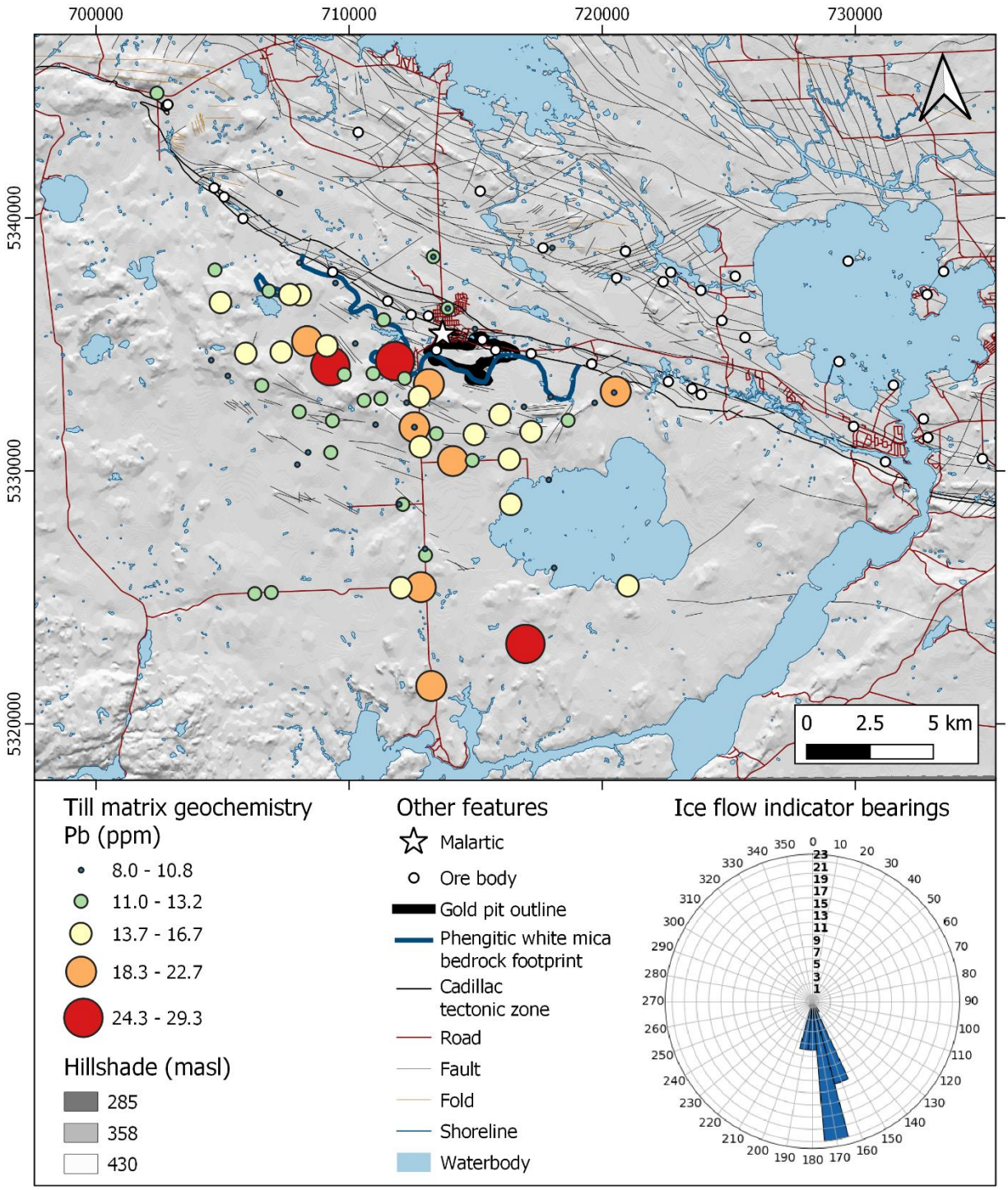

Supplementary Figure 5. 39 Spatial distribution of Pb (ppm) based on till matrix geochemistry (ICP-MS). The phengitic white mica bedrock footprint is after Lypaczewski et al (2019). Waterbodies and hillshade are from Natural Resources Canada (https://maps.canada.ca/czs/index-en.html). Ore bodies, Cadillac tectonic zone, roads, faults, folds, and shorelines are from SIGEOM (https://sigeom.mines.gouv.qc.ca/signet/classes/I1108_afchCarteIntr). Coordinate system: NAD 83, UTM zone 17.

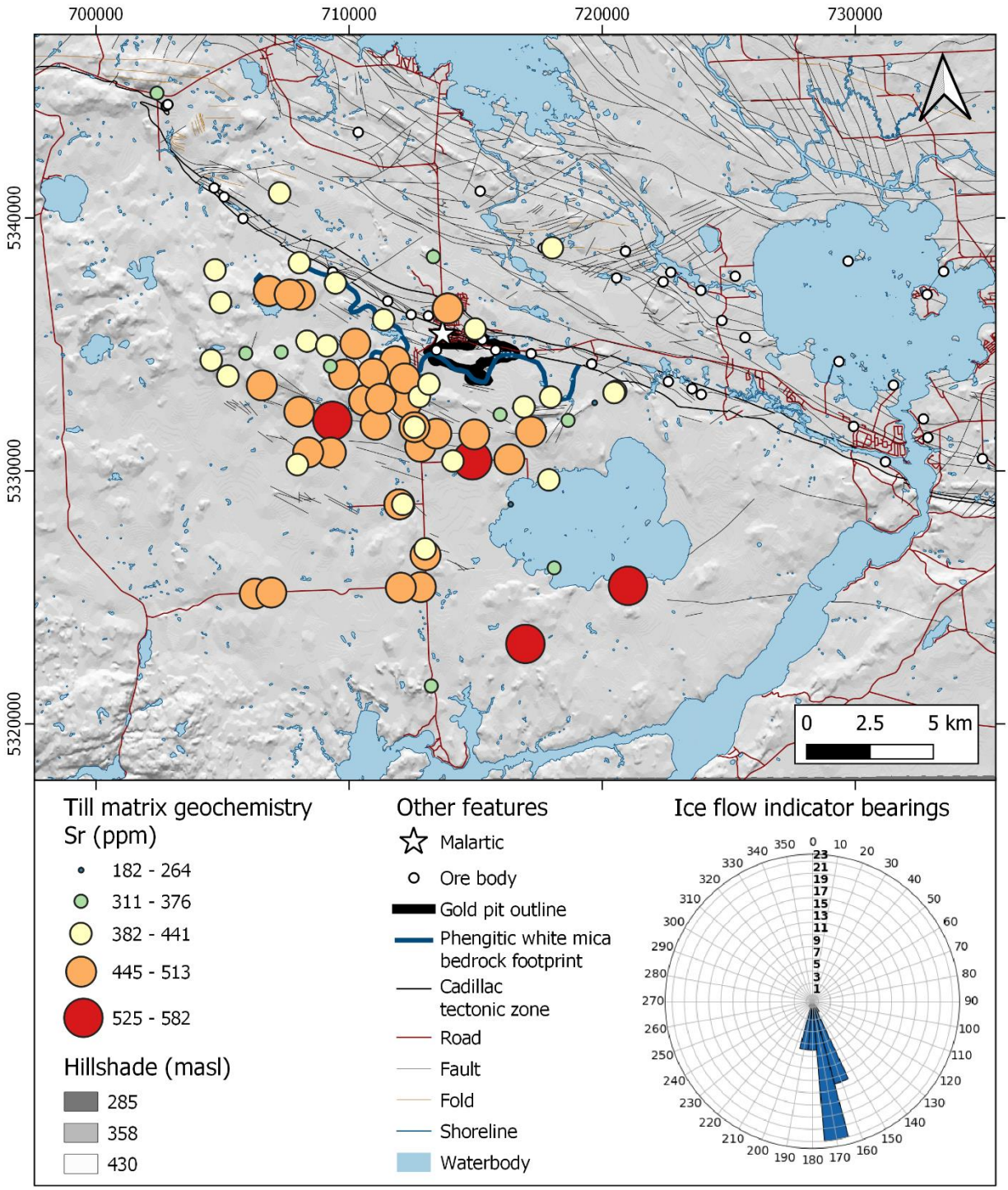

Supplementary Figure 5. 40 Spatial distribution of Sr (ppm) based on till matrix geochemistry (ICP-OES). The phengitic white mica bedrock footprint is after Lypaczewski et al (2019). Waterbodies and hillshade are from Natural Resources Canada (https://maps.canada.ca/czs/index-en.html). Ore bodies, Cadillac tectonic zone, roads, faults, folds, and shorelines are from SIGEOM (https://sigeom.mines.gouv.qc.ca/signet/classes/I1108_afchCarteIntr). Coordinate system: NAD 83, UTM zone 17.

5.8. Gold Grain Counts

Supplementary Table 5. 21 Picked gold grains (≤500 µm) from till: raw counts and normalized counts to 100 g non-magnetic heavy mineral concentrate.

Sample	Total	Reshaped	Modified	Pristine	HMC (g)	Normalized Total	Normalized Reshaped	Normalized Modified	Normalized Pristine
001a	6	4	1	1	11.06	54	36	9	9
004a	1	1	0	0	4.23	24	24	0	0
005a	2	2	0	0	8.37	24	24	0	0
007a	0	0	0	0	7.44	0	0	0	0
009a	6	6	0	0	11.05	54	54	0	0
009b	11	11	0	0	12.19	90	90	0	0
010a	5	4	1	0	12.59	40	32	8	0
011a	9	9	0	0	9.33	96	96	0	0
012a	3	2	1	0	6.38	47	31	16	0
019a	0	0	0	0	7.21	0	0	0	0
021a	9	8	1	0	9.14	98	87	11	0
031a	5	5	0	0	9.13	55	55	0	0
036a	2	2	0	0	4.84	41	41	0	0
038a	2	1	1	0	9.29	22	11	11	0
038b	0	0	0	0	5.10	0	0	0	0
039a	17	10	3	4	11.36	150	88	26	35
040a	1	0	0	1	3.90	26	0	0	26
041a	0	0	0	0	4.88	0	0	0	0
042a	0	0	0	0	4.98	0	0	0	0
043a	0	0	0	0	3.45	0	0	0	0
044a	0	0	0	0	5.82	0	0	0	0
045a	4	3	0	1	6.93	58	43	0	14
046a	0	0	0	0	2.71	0	0	0	0
047a	1	0	1	0	8.69	12	0	12	0
048a	1	1	0	0	7.71	13	13	0	0
049a	0	0	0	0	7.53	0	0	0	0
050a	1	0	1	0	6.77	15	0	15	0
052a	0	0	0	0	3.01	0	0	0	0
054a	1	1	0	0	6.24	16	16	0	0
055a	1	0	1	0	4.50	22	0	22	0

Sample	Total	Reshaped	Modified	Pristine	HMC (g)	Normalized Total	Normalized Reshaped	Normalized Modified	Normalized Pristine
056a	5	4	1	0	10.75	47	37	9	0
057a	1	1	0	0	7.23	14	14	0	0
058a	6	3	2	1	9.88	61	30	20	10
059a	7	3	0	4	3.61	194	83	0	111
060a	2	1	1	0	8.08	25	12	12	0
061a	0	0	0	0	3.19	0	0	0	0
062a	2	0	0	2	3.99	50	0	0	50
063a	0	0	0	0	3.81	0	0	0	0
064a	2	0	0	2	3.95	51	0	0	51
065a	0	0	0	0	4.40	0	0	0	0
065b	2	2	0	0	4.68	43	43	0	0
070a	3	3	0	0	6.16	49	49	0	0
SS 1	15	6	3	6	3.14	478	191	96	191
SS 2	1	1	0	0	14.77	7	7	0	0
SS 3	3	2	1	0	3.40	88	59	29	0
SS 4	0	0	0	0	9.16	0	0	0	0
SS 5	4	3	0	1	15.77	25	19	0	6
SS 6	3	2	0	1	15.10	20	13	0	7
SS 7	6	4	1	1	10.71	56	37	9	9
SS 8	0	0	0	0	5.84	0	0	0	0
SS 9	2	0	1	1	6.89	29	0	15	15
SS 10	2	2	0	0	7.65	26	26	0	0
SS 48	1	1	0	0	12.66	8	8	0	0
SS 11	12	3	3	6	3.92	306	77	77	153
SS 12	0	0	0	0	14.51	0	0	0	0
SS 13	6	4	2	0	7.64	79	52	26	0
SS 19	0	0	0	0	5.76	0	0	0	0
SS 22	3	3	0	0	0.92	326	326	0	0
SS 23	3	2	0	1	7.72	39	26	0	13
SS 48	2	2	0	0	9.18	22	22	0	0
SS 49	9	4	3	2	8.97	100	45	33	22

5.9. Petrography

The following files are available online at:
https://github.com/Caroline-Emily-Taylor/Appendices.git

1. Ch3 Thin Sections Similar to Canadian Malartic Rocks Compressed.pptx
2. Ch3 Thin Sections Dissimilar to Canadian Malartic Rocks Compressed.pptx